Theoretical and Computational Modelling of Compressible and Nonisothermal Viscoelastic Fluids

Alexander Tennyson Mackay

School of Mathematics
Cardiff University

A thesis submitted for the degree of Doctor of Philosophy

August 2018

Abstract

This thesis is an investigation into the modelling of compressible viscoelastic fluids. It can be divided into two parts: (i) the development of continuum models for compressible and nonisothermal viscoelastic fluids using the generalised bracket method and (ii) the numerical modelling of compressible viscoelastic flows using a stabilised finite element method.

We introduce the generalised bracket method, a mathematical framework for deriving systems of transport equations for viscoelastic fluids based on an energy/entropy formulation. We then derive nonisothermal and compressible generalisations of the Oldroyd-B, Giesekus and FENE-P constitutive equations. The Mackay-Phillips (MP) class of dissipative models for Boger fluids is developed within the bracket framework, complimenting the class of phenomenological models that already exist in the literature. Advantages of the MP models are their generality and consistency with the laws of thermodynamics.

A Taylor-Galerkin finite element scheme is used as a basis for numerical simulations of compressible and nonisothermal viscoelastic flow. Numerical predictions for four 2D benchmark problems: lid-driven cavity flow, natural convection, eccentric Taylor-Couette flow and axisymmetric flow past a sphere are presented. In each case numerical comparisons with both empirical and numerical data from the literature are presented and discussed. Numerical drag predictions for the FENE-P-MP model are presented, displaying good agreement with both numerical and experimental data for the drag behaviour of Boger fluids.

Declaration

This work has not been submitted in substance for any other degree or award at this or any other university or place of learning, nor is being submitted concurrently in candidature for any degree or other award.

Signed . . . . (candidate) Date . . . .

STATEMENT 1

This thesis is being submitted in partial fulfilment of the requirements for the degree of PhD.

Signed . . . . (candidate) Date . . . .

STATEMENT 2

This thesis is the result of my own independent work/investigation, except where otherwise stated. Other sources are acknowledged by explicit references. The views expressed are my own.

Signed . . . . (candidate) Date . . . .

STATEMENT 3

I hereby give consent for my thesis, if accepted, to be available for photocopying and for inter-library loan, and for the title and summary to be made available to outside organisations.

Signed . . . . (candidate) Date . . . .

Acknowledgements

Firstly, I would like to thank my supervisor Professor Tim Phillips who has provided guidance throughout my studies. In particular for introducing me to both rheology and computational fluid dynamics. It is incredible that he has been able to find time to see me along with his other PhD students as well as manage his duties as Head of School.

I have had the great pleasure of spending my time as a student with friends and colleagues Scott, Sally, Matthew, Waleed, James. All of you and the other mathematics postgraduates have made my time as a student at the Cardiff School of Mathematics enjoyable. I would like to thank my Uncle who has consistently supported me during my time at Cardiff.

A special thank you to Susanne Claus for her support and advice concerning the implementation of numerical methods using the FEniCS platform.

I would also like to thank the Engineering and Physical Sciences Research Council of the United Kingdom and the Cardiff School of Mathematics for the studentship funding I received.

A special mention to my girlfriend Sophie who I fell in love with during my time at Cardiff University has supported me throughout my PhD. I would like to thank my parents for supporting me throughout my time at Cardiff University, and give a special thanks to my grandfather for encouraging my interest in mathematics and science from a young age.

Lastly, I would like to thank my examiners Professor Rob Poole and Dr Elisabetta De Angelis for taking part in my viva and providing me with useful feedback.

Contents

Chapter 1

Introduction

1.1 Viscoelasticity

Viscoelasticity is a property of rheological or ‘flowing’ materials. As implied by the name, it describes substances that display both viscous and elastic responses to deformation. Examples of viscoelastic fluids are crude oil, molten plastics, blood, toothpaste and shampoo. Unlike Newtonian fluids, viscoelastic fluids exhibit behaviour such as the Barius effect, Weissenberg effect and, in many industrial applications, display shear-thinning and strain-hardening/softening. Macroscopic phenomena observed in polymeric fluids arise because of the elastic response to deformation of large molecular chains suspended within the fluid.

The ability to derive mathematical models that can adequately describe the physical behaviour of viscoelastic fluids is essential to the advancement of the automotive, polymer and food processing industries since experimental methods for optimising industrial applications of viscoelastic fluids are often prohibitively expensive. Moreover, many of these applications are conducted under conditions where large gradients in pressure and temperature occur and therefore the ability to accurately predict flow under non-isothermal conditions is also important.

1.2 Motivation for this Thesis

Over the last 70 years many significant contributions to the study and characterization of a vast collection of polymeric materials have been made. However, theoretical advances in modelling non-isothermal viscoelastic fluids have developed at a more gradual pace.

A plethora of constitutive equations for modelling viscoelastic fluids under incompressible and isothermal conditions exist in the literature. However, derivation of suitable models for compressible and nonisothermal flow problems have received far less attention [13]. In many numerical investigations bespoke rheological models are crafted to suit specific flow problems and therefore are not applicable to more general problems. In polymer processing applications, such as injection modelling and high-speed extrusion, the pressure and flow rate may be large. Furthermore polymer melt flow generally happens at high temperatures where flow parameters and dynamics are a direct result of thermodynamic relationships between state variables. Hence, compressible and nonisothermal effects within the viscoelastic regime may become important and influence resulting flow phenomena. The governing equations for modelling viscoelastic flow are highly nonlinear, often requiring sophisticated numerical methods to solve and considerations of compressibility and temperature variation introduce further complications to an already difficult modelling problem.

Unfortunately, it is not sufficient only to possess knowledge of how the material properties depend on temperature since in many processing applications such as injection moulding, film blowing and wire coating, significant temperature gradients perpendicular to the flow direction arise due to viscous heating. The spatial variation of the material parameters requires a more sophisticated modelling approach than simply time-temperature superposition in order to describe the flow of polymeric liquids more generally. Thus it is necessary to develop a set of evolution equations that are fully non-isothermal and universally valid. This is a formidable mathematical modelling challenge and this thesis is a contribution to the body of literature tackling this problem.

1.3 Historical Overview

Early work to account for temperature dependence of data used the principle of time-temperature superposition [75] to superimpose mechanical property data at different temperatures by means of an experimentally determined shift factor. This was based on extensive experimental evidence of creep and recovery in polymeric liquids and allowed data obtained at one temperature to be used to infer those at another. Of course, this is an empiricism that is not universally valid. Nevertheless, the approach works well for many liquids over a wide range of temperatures. The assumption here is that temperature is a control variable and that a given experiment is performed under isothermal conditions.

Coleman and Noll [20, 21] introduced the concept of a simple fluid in which the stress tensor and heat flux vector at a given material point are expressed as functions of the history of these quantities with diminishing influence as one travels into the past. In this theory the stress tensor and heat flux vector fields of the simple fluid depend on functionals of the deformation gradient and temperature, which are required to satisfy certain continuity and smoothness conditions in order to facilitate mathematical analysis. The complexity of the functionals has meant that the approach has only been implemented in the simplest of situations and so its applicability has been rather limited – for example, to linear viscoelasticity. Its restriction to fluids with fading memory also means that the theory excludes Newtonian fluids [77] and all models that explicitly contain a solvent viscosity since the Newtonian fluid is recovered as the relaxation time tends to zero.

Marucci [61] developed a kinetic model for non-isothermal polymeric solutions based on Hookean dumbbell theory. The spring factor in this non-isothermal theory is assumed to vary linearly with temperature. Gupta and Metzner [40] noted that the additional term in the constitutive equation that accounts for non-isothermal effects has the wrong sign compared with experimental data. They suggested a correction to the model in which the constant stiffness parameter is replaced by a variable stiffness parameter which decays algebraically as temperature increases.

Using an empirical dependence of viscosity on temperature the resulting constitutive equation was used as the basis for numerical simulations by Luo and Tanner [59] and McClelland and Finlayson [62] of film blowing and extrusion, respectively. Wiest [93] extended these ideas to the Rouse model and generalized them to models with a discrete spectrum of relaxation times. However, the resulting constitutive equations are restricted to fluids with a low degree of elasticity which means that they are not particularly suitable for use in many polymer processing situations in which elastic effects are just as important as thermal effects. Sugeng et al. [84] proposed a non-isothermal generalization of the PTT constitutive equation. However, it is restricted to incompressible fluids and suffers from the difficulty in modelling spatial temperature variations in the kinetic theory.

1.4 About this Thesis

This thesis aims to be comprehensive in its approach, covering both theoretical and computational aspects of modelling compressible and nonisothermal viscoelastic fluids. The first part of this thesis (Chapters 2 and 3) is concerned with the derivation of thermodynamically consistent mechanical models for non-Newtonian fluids using the generalised bracket method (or generalised bracket formalism). Compressible and nonisothermal generalisations of the Oldroyd-B and FENE-P models are derived and presented. The main contribution in these chapters will be the derivation of a thermodynamically consistent strain-hardening model for Boger fluids. The aim of this approach is to derive a model capture the relative drag enhancement displayed by Boger fluids (Garduño et al [34]) whilst also being applicable to compressible and nonisothermal flows.

The second part (Chapters 4 - 7) focusses on the numerical modelling of weakly-compressible viscoelastic flow. We address the challenge that arises when computing viscoelastic flows, namely the high Weissenberg number problem, by using a stabilised Taylor-Galerkin finite element method. Computational results for a range of benchmark problems are presented and the combined effects of compressibility and fluid elasticity are assessed.

1.4.1 Outline

In **Chapter 2** we introduce the generalised bracket formulation and derive the general equations governing nonisothermal and compressible viscoelastic flow. In this formulation the Hamiltonian and Helmholtz free energy are presented as the fundamental quantities used to consistently model transport in viscoelastic fluids.

In **Chapter 3** we use the formulation introduced in Chapter 2 to derive compressible forms of the Oldroyd-B, Giesekus and FENE-P models. A new constitutive equations (FENE-P-MP) for modelling Boger fluids is derived. The viscometric behaviour of the derived models is also presented.

In **Chapter 4** we introduce the numerical methods that are used to solve the systems of governing equations derived in Chapter 3. The governing equations are nondimensionalised and an equation of state coupling pressure, density and temperature is introduced into the formulation.

In **Chapter 5** we present numerical results for the lid-driven cavity and natural convection problems. Both are examples of flows with recirculation within a (simple) unit square geometry and are used to benchmark the numerical scheme. Furthermore, we investigate the combined effects of viscoelasticity and compressibility, comparing results to those available in the literature.

In **Chapter 6** we present results for the eccentric Taylor-Couette flow of an extended White-Metzner (EWM) and FENE-P-MP model. Numerical results obtained using those models are compared to those available in the literature.

In **Chapter 7** drag predictions for the flow past a sphere of an (i) Oldroyd-B fluid and (ii) FENE-P-MP fluid are presented along with comparisons to results from the literature.

Finally in **Chapter 8** we present the conclusions from the investigation and discuss avenues future work.

Chapter 2

The Generalised Bracket Formulation

In this chapter we introduce the generalised bracket formulation (GBF) formalism for deriving models for transport in viscoelastic fluids. Sec. 2.1-2.3 provides a summary of the literature on the generalised bracket by Beris & Edwards [8, 29] detailing the theory of equilibrium, nonequilibrium thermodynamics and the bracket description of fluid flow. In Sec. 2.4 we derive an energy balance law based on the general set of governing equations for mass, momentum, entropy and conformation stress. In Sec. 2.5 we introduce Hulsen's thermodynamic admissibility criteria for constitutive laws derived using the generalised bracket. The key points of the generalised bracket method are summarised in Sec. 2.6.

2.1 The Generalised Bracket Formulation: Overview

The continuum mechanics description of fluid dynamics involves modelling fluids based upon separate conservation principles. Hamilton's formulation of Newtonian mechanics provides an alternative method for deriving sets of governing equations for transport in fluids [43]. A fluid system, Ω, at time t can be characterised by a set of state variables

$$\{\rho(\mathbf{x},t), \mathbf{m}(\mathbf{x},t), s(\mathbf{x},t), \mathbf{C}(\mathbf{x},t)\} \tag{2.1.1}$$

where $\mathbf{x} \in \Omega$ and $t > 0$. Here ρ is the density, $\mathbf{m} := \rho\mathbf{u}$ is the momentum, s is the entropy and

$\mathbf{C}$ is the conformation stress tensor. The most common approach to continuum mechanics is to derive evolution equations for each of the variables separately, basing each governing equation on a distinct conservation law. In the generalised bracket method conservation laws for all state variables are derived directly from the first and second laws of thermodynamics using a single equation. The fundamental quantity used in the bracket formulation is the Hamiltonian or total energy, given by

$$H = \int_\Omega h(\rho, \mathbf{u}, s, \mathbf{C})\, d\Omega = \int_\Omega [\mathcal{K}(\rho, \mathbf{u}) + \hat{u}(\rho, s) + w(\mathbf{C})]\, d\Omega \tag{2.1.2}$$

In the absence of any field potential the total energy, h, is divided into three parts: kinetic energy, $\mathcal{K}$, internal energy, $\hat{u}$, and elastic energy, w, where $\mathbf{u}$ is the velocity field.

To model dissipative phenomena such as viscosity or relaxation, one has to consider the effects of mechanical degradation. Temporal evolution of the system depends on the energy available to be converted into mechanical work. Therefore, when modelling dissipative processes within the bracket formulation the total energy (Hamiltonian) is replaced by the *total available energy* or Helmholtz free energy

$$A = \int_\Omega \left[\mathcal{K}(\rho, \mathbf{u}) + w(\mathbf{C}) + \hat{u}(\rho, s) - s(\rho, \mathbf{C})T \right] d\Omega \tag{2.1.3}$$

where T is the absolute temperature defined $T = \frac{\partial h}{\partial s}$. The central principle that underpins the generalised bracket method is that the dynamics of an arbitrary functional, F, are governed by the evolution equation

$$\frac{dF}{dt} = \{[F, A]\}, \tag{2.1.4}$$

where $\{[\cdot,\cdot]\}$ is the generalised bracket and A is the Helmholtz free energy of the system, Ω. The generalised bracket is itself composed of two sub-brackets

$$\{[F, A]\} = \{F, A\} + [F, A]. \tag{2.1.5}$$

The first bracket, $\{\cdot,\cdot\}$, is the Poisson bracket which describes the conservative dynamics of the system. The Poisson bracket has been used in descriptions of particle systems since the development of Hamiltonian mechanics [43]. The Poisson bracket for continuous media was developed by Morrisson and Greene [64] as well as Dzyaloshinskii and Volovick [28]. Later developments were introduced by Beris & Edwards [29]. The second bracket $[\cdot, \cdot]$ describes the nonequilibrium dynamics, specifically viscous dissipation, stress relaxation and non-affine motion. The theory of the dissipative Hamiltonian dynamics was first introduced by Grmela [37] and developed by Kaufman [49] and Morrison [65]. The first application of the dissipative bracket to rheology was done by Grmela [38].

2.2 Equilibrium Thermodynamics: The Poisson Bracket

To introduce the generalised bracket formulation, we begin by considering the dynamics of non-dissipative systems. A reversible process is one in which the system remains in a state of maximum entropy. In practice, completely reversible processes are impossible, however just in the same way as one is first introduced to classical mechanics using 'ideal' conditions (i.e. no friction/ air resistance etc), in order to develop the theory we need to understand non-dissipative phenomena. Let Ω be the domain occupied by a fluid and F is an observable (functional) defined over the state variables on Ω,

$$F = F(\rho(\mathbf{x}, t), \mathbf{m}(\mathbf{x}, t), s(\mathbf{x}, t), \mathbf{C}(\mathbf{x}, t)). \tag{2.2.1}$$

Then the fundamental equation governing non-dissipative fluid transport is given by

$$\frac{dF}{dt} = \{F, A\}, \tag{2.2.2}$$

where A is the Helmholtz free energy. The bracket $\{\cdot, \cdot\}$ is anti-commutative, distributive and satisfies the Jacobi identity. Importantly, if any function, ϕ is constant over phase space then $\{f, \phi\} = 0$ for any f. The Poisson Bracket in *Lagrangian* coordinates is derived by taking the limit as $N \to \infty$ of the expression for the Poisson bracket for N particles (see (A.1.3)) and can be written

$$\{F, A\}_L = \int_\Omega \left[\frac{\delta F}{\delta \Gamma}\frac{\delta A}{\delta \Pi} - \frac{\delta F}{\delta \Pi}\frac{\delta A}{\delta \Gamma}\right] d^3r, \tag{2.2.3}$$

where $\Gamma(\mathbf{r}, t)$ and $\Pi(\mathbf{r}, t)$ are the *Lagrangian* position and momentum vector fields, respectively [8]. Assume that for a viscoelastic medium the observable F is a function of the state variables we wish to model, specifically $\rho(\mathbf{x}, t)$, $\mathbf{m}(\mathbf{x}, t) := \rho\mathbf{u}(\mathbf{x}, t)$, $s(\mathbf{x}, t)$ and $\mathbf{C}(\mathbf{x}, t)$. Use of a chain rule expansion yields

$$\frac{dF}{dt} = \int_\Omega \left[\frac{\delta F}{\delta \rho}\frac{\partial \rho}{\partial t} + \frac{\delta F}{\delta \mathbf{m}} \cdot \frac{\partial \mathbf{m}}{\partial t} + \frac{\delta F}{\delta s}\frac{\partial s}{\partial t} + \frac{\delta F}{\delta \mathbf{C}} : \frac{\partial \mathbf{C}}{\partial t}\right] d\Omega. \tag{2.2.4}$$

In order to obtain working equations, Eq. (2.2.3) must be expressed using a (Cartesian) fixed coordinate frame. An expansion of derivative terms in Eq. (2.2.3) yields

$$\frac{\delta F}{\delta \Gamma_i} = \int_\Omega \left[\frac{\delta F}{\delta \rho}\frac{\delta \rho}{\delta \Gamma_i} + \frac{\delta F}{\delta m_j}\frac{\delta m_j}{\delta \Gamma_i} + \frac{\delta F}{\delta s}\frac{\delta s}{\delta \Gamma_i} + \frac{\delta F}{\delta C_{kj}}\frac{\delta C_{kj}}{\delta \Gamma_i}\right] d\Omega, \tag{2.2.5}$$

$$\frac{\delta F}{\delta \Pi_i} = \int_\Omega \left[\frac{\delta F}{\delta \rho}\frac{\delta \rho}{\delta \Pi_i} + \frac{\delta F}{\delta m_j}\frac{\delta m_j}{\delta \Pi_i} + \frac{\delta F}{\delta s}\frac{\delta s}{\delta \Pi_i} + \frac{\delta F}{\delta C_{kj}}\frac{\delta C_{kj}}{\delta \Pi_i}\right] d\Omega. \tag{2.2.6}$$

Substituting Eq. (2.2.5) and Eq. (2.2.6) into Eq. (2.2.3) and applying integration by parts utilizing the no-slip boundary conditions on $\partial\Omega$, the Eulerian form of the continuous bracket is derived.

$$
\begin{aligned}
\{F,A\}_E = &-\int_{\Omega'} \left[\frac{\delta F}{\delta \rho}\nabla_j\left(\rho\frac{\delta A}{\delta m_j}\right) - \frac{\delta A}{\delta \rho}\nabla_j\left(\rho\frac{\delta F}{\delta m_j}\right)\right] d\Omega \\
&-\int_{\Omega'} \left[\frac{\delta F}{\delta m_k}\nabla_j\left(m_k\frac{\delta A}{\delta m_j}\right) - \frac{\delta A}{\delta m_k}\nabla_j\left(m_k\frac{\delta A}{\delta m_j}\right)\right] d\Omega \\
&-\int_{\Omega'} \left[\frac{\delta F}{\delta s}\nabla_j\left(s\frac{\delta A}{\delta m_j}\right) - \frac{\delta A}{\delta s}\nabla_j\left(s\frac{\delta F}{\delta m_j}\right)\right] d\Omega \\
&-\int_{\Omega'} \left[\frac{\delta F}{\delta C_{ij}}\nabla_k\left(C_{ij}\frac{\delta A}{\delta m_k}\right) - \frac{\delta A}{\delta C_{ij}}\nabla_k\left(C_{ij}\frac{\delta F}{\delta m_k}\right)\right] d\Omega \\
&-\int_{\Omega'} C_{ki}\left[\frac{\delta A}{\delta C_{ij}}\nabla_k\left(\frac{\delta F}{\delta m_j}\right) - \frac{\delta F}{\delta C_{ij}}\nabla_k\left(\frac{\delta A}{\delta m_j}\right)\right] d\Omega \\
&-\int_{\Omega'} C_{kj}\left[\frac{\delta A}{\delta C_{ij}}\nabla_k\left(\frac{\delta F}{\delta m_i}\right) - \frac{\delta F}{\delta C_{ij}}\nabla_k\left(\frac{\delta A}{\delta m_i}\right)\right] d\Omega
\end{aligned}
\tag{2.2.7}
$$

Substituting (2.2.4) and (2.2.7) into Eq. (2.2.2) general dynamic equations for ρ, $\rho\mathbf{u}$, s and $\mathbf{C}$ can be established by comparing coefficients in the expansion[1]. In order to complete the process however, one must establish an expression for the energy functional (Hamiltonian/Helmholtz free energy) in terms of the dynamic variables that have been specified. The simplest form of this expression is obtained through a decomposition of energy into kinetic and stored/potential energy. In the absence of potential fields (gravity/electromagnetism) the Helmholtz free energy can be categorised into two parts: kinetic and internal energy. Beris and Edwards [8] include further discussion of field energy potential terms that can be modelled relatively easily using this method. Classical forms of the expressions for K and $\hat{u}$ are used. Taking derivatives of Eq. (2.1.3) we obtain

$$
\begin{aligned}
\frac{\delta A}{\delta \mathbf{m}} =& \frac{\mathbf{m}}{\rho} = \mathbf{u} \qquad\qquad \frac{\delta A}{\delta s} = T \\
&\frac{\delta A}{\delta \rho} = \frac{\mathbf{m}\cdot\mathbf{m}}{2\rho} + \frac{\partial \hat{u}}{\partial \rho}
\end{aligned}
\tag{2.2.8}
$$

---

[1] For a detailed derivation of Eq. (2.2.7) please see Appendix A (Sec. A.2.3) or alternatively Beris and Edwards [8] p.87-165.

The Volterra derivative of the Hamiltonian with respect to the conformation tensor, $\mathbf{C}$, is dependent on the expression for elastic energy, w, that is chosen. Substituting these expressions into (2.2.7) and comparing coefficients we obtain the system of equations for non-dissipative compressible viscoelastic flow

$$\begin{aligned}\frac{\partial\rho}{\partial t} &= -\nabla\cdot(\rho\mathbf{u})\\ \frac{\partial s}{\partial t} &= -\nabla\cdot(s\mathbf{u})\\ \rho\frac{\partial\mathbf{u}}{\partial t} &= -\nabla p - \rho\mathbf{u}\cdot\nabla\mathbf{u} + 2\nabla\cdot\left(\mathbf{C}\cdot\frac{\partial A}{\partial\mathbf{C}}\right)\\ \frac{\partial\mathbf{C}}{\partial t} &= -\nabla\cdot(\mathbf{u}\mathbf{C}) + \nabla\mathbf{u}\cdot\mathbf{C} + \mathbf{C}\cdot\nabla\mathbf{u}^T\end{aligned} \tag{2.2.9}$$

Pressure is automatically defined as a function of the dynamic variables and derivatives of the internal energy function

$$p := \rho\frac{\partial\hat{u}}{\partial\rho} + s\frac{\partial\hat{u}}{\partial s} + \mathbf{C} : \frac{\partial\hat{u}}{\partial\mathbf{C}} - \hat{u}. \tag{2.2.10}$$

The first three equations in (2.2.9) represent the conservation of mass, entropy (for non-dissipative processes) and momentum (in the absence of diffusion). The non-dissipative description of fluid motion contains no viscous or relaxation terms, hence the viscous stress tensor and relaxation terms in the conformation tensor equation do not appear. Another significant feature of the continuous Poisson bracket is that the *material* and *upper convected* derivatives are the natural time derivatives that arise in the derivation of the balance law for $\mathbf{u}$ and $\mathbf{C}$, respectively. The last equation in (2.2.9) is equivalent to the vanishing Truesdell derivative of $\mathbf{C}$, hence material objectivity is satisfied from the outset.

The system of equations (2.2.9) is adequate for describing compressible fluids such as liquid helium, plasmas and other superfluids that exhibit no dissipative phenomena (viscosity/relaxation). A limitation to the applicability of the Poisson bracket is that it can only describe conservative transport phenomena [8]. In order to adequately model non-equilibrium phenomena such as viscosity and relaxation, Eq. (2.2.2) will have to be modified to include an additional term.

2.3 Non-Equilibrium Thermodynamics and the Generalized Bracket

Around the same time that Hamiltonian mathematics was being developed, mathematicians and physicists were starting to make some headway into understanding irreversible processes. Informally, a reversible process is one that if you could film in action, the footage of it played in reverse is a physical possibility. For example a ball rolling along a smooth (frictionless) flat surface or a spacecraft far away from a gravitational field travelling at a constant velocity. The time reversal of these situations is a physical possibility (another name for this condition is T-symmetry). An irreversible process is one in which time reversal is an impossibility. A ball rolling on a rough surface is a good example of an irreversible thermodynamic process. The ball will be slowed to a halt with the time taken depending on the coefficient of friction between the ball and the surface. The time reversed scenario would show the impossible situation of a ball accelerating from rest due to 'anti-friction' with no real forces acting on it. All real life processes are irreversible i.e. dissipate mechanical energy in some way and it is impossible to reach 100% efficiency. This consideration significantly reduces the total number of possible ways in which a system can behave.

In Section 2.2 we considered the dynamics of continuous media in which the entropy is conserved and the mechanical energy remains constant over time. For real processes however the mechanical energy degrades at a rate proportional to the rate of increase of entropy. This means that our conservation law for entropy has to be generalised to account for *non-decreasing* entropy. For the generalized bracket we must also ensure that $dH/dt = 0$. Using Eq. (2.2.2) we can show that

$$\frac{dH}{dt} = \{H, H\} + [H, H] = 0 \implies [H, H] = 0.$$

In order to satisfy the second law of thermodynamics, the entropy functional

$$S = \int_{\Omega} s d\Omega,$$

must satisfy

$$\frac{dS}{dt} = \{S, H\} + [S, H] \geq 0,$$

which in turn means $[S, H] \geq 0$ as $\{S, H\} = 0$. Throughout this thesis we will use the standard Marrucci definition of the entropy functional

$$S(\rho, \mathbf{C}, T) = \int_{\Omega} \frac{\alpha \rho k_b T}{2} \log \det \left(\frac{K\mathbf{C}}{k_b T} \right) d\Omega, \tag{2.3.1}$$

where α is the mass fraction, k_b is the Boltzmann constant, K is the spring constant (for further explanation of the expression for entropy see Beris and Edwards [8] p.224). Furthermore, the total mass

$$\mathcal{M} \equiv \int_{\Omega} \rho d\Omega,$$

is conserved, even whilst including dissipative effects, therefore

$$\frac{d\mathcal{M}}{dt} = \{\mathcal{M}, H\} + [\mathcal{M}, H] = 0,$$

meaning $[\mathcal{M}, H] = 0$. Given two observables, F and G operating on Ω, the most general form of the dissipation bracket, obeying the first and second laws of thermodynamics, is given by

$$[F, G] = \int_{\Omega} \left[\Xi \left(L \left[\frac{\delta F}{\delta \omega}, \nabla \frac{\delta F}{\delta \omega} \right]; \frac{\delta G}{\delta \omega}; \frac{\delta G}{\delta \omega} \right) - \frac{1}{T} \frac{\delta F}{\delta s} \Xi \left(L \left[\frac{\delta G}{\delta \omega}, \nabla \frac{\delta G}{\delta w \omega} \right]; \frac{\delta G}{\delta \omega}; \frac{\delta G}{\delta \omega} \right) \right] d\Omega, \tag{2.3.2}$$

where $\omega = (\rho, \mathbf{m}, s, \mathbf{C})$ is a vector containing the dynamic variables, $L[\cdot]$ denotes that Ξ is linear with respect to its arguments and Ξ is given by

$$\Xi = \Sigma_{i,j} \left[\hat{A}_{ij} \frac{\delta F}{\delta \omega_i} \frac{\delta G}{\delta \omega_j} + \hat{B}_{ijk} \frac{\delta F}{\delta \omega_i} \nabla_k \left(\frac{\delta G}{\delta \omega_j} \right) + \hat{C}_{ijk} \nabla_k \left(\frac{\delta F}{\delta \omega_i} \right) \frac{\delta G}{\delta \omega_j} + \hat{D}_{ijkl} \nabla_k \frac{\delta F}{\delta \omega_i} \nabla_l \frac{\delta G}{\delta \omega_j} \right]. \tag{2.3.3}$$

Eq. (2.3.2) represents the most general expression for a dissipation bracket consistent with the first and second laws of thermodynamics. In Eq. (2.3.3), $\hat{A}_{ij}$, $\hat{B}_{ijk}$, $\hat{C}_{ijk}$, $\hat{D}_{ijkl}$ are phenomenological coefficient matrices, which depend on the dynamic variables of the system. Beris and Edwards [8] discuss the general forms that these coefficient matrices take when used for modelling a range of fluids and composite rheological materials. Most well-known viscoelastic models can be derived by specifying a non-zero form for each phenomenological tensor. Using an alternative factorisation of the terms in Eq. (2.3.3) we can show that for a general viscoelastic fluid the dissipation bracket takes the form

$$
\begin{aligned}
[F, A] = &- \int_\Omega Q_{ijkl} \nabla_i \left(\frac{\delta F}{\delta m_j} \right) \nabla_k \left(\frac{\delta A}{\delta m_l} \right) d\Omega \\
&+ \int_\Omega \frac{1}{T} \frac{\delta F}{\delta s} Q_{ijkl} \nabla_i \left(\frac{\delta A}{\delta m_j} \right) \nabla_k \left(\frac{\delta A}{\delta m_l} \right) d\Omega \\
&- \int_\Omega \Lambda_{ijkl} \frac{\delta F}{\delta C_{ij}} \frac{\delta A}{\delta C_{kl}} \, d\Omega \\
&+ \int_\Omega \frac{1}{T} \frac{\delta F}{\delta s} \Lambda_{ijkl} \frac{\delta A}{\delta C_{ij}} \frac{\delta A}{\delta C_{kl}} \, d\Omega \\
&- \int_\Omega L_{ijkl} \left(\nabla_i \frac{\delta F}{\delta m_j} \frac{\delta A}{\delta C_{kl}} - \nabla_i \frac{\delta A}{\delta m_j} \frac{\delta F}{\delta C_{kl}} \right) d\Omega \\
&- \int_\Omega \alpha_{ij} \nabla_i \left(\frac{\delta F}{\delta s} \right) \nabla_k \left(\frac{\delta A}{\delta s} \right) d\Omega \\
&+ \int_\Omega \frac{1}{T} \frac{\delta F}{\delta s} \alpha_{ij} \nabla_i \left(\frac{\delta A}{\delta s} \right) \nabla_k \left(\frac{\delta A}{\delta s} \right) d\Omega,
\end{aligned}
\tag{2.3.4}
$$

where $\mathbf{\Lambda}$ and $\mathbf{Q}$ are fourth-order relaxation and viscosity tensors, respectively, $\mathbf{L}$ represents non-affine interactions between the velocity gradient and conformation tensor fields and $\boldsymbol{\alpha}$ is the thermal conductivity matrix (see Sec. 2.4). The forms that the three dissipative tensors can take vary significantly due to the limited number of assumptions used in this formulation. Most importantly $\mathbf{\Lambda}$, $\mathbf{Q}$ and $\mathbf{L}$ have to satisfy the Onsager reciprocal relations and frame indifference principles. In practice this means that the coefficients of $\mathbf{\Lambda}$ are functions of the principle invariants of $\mathbf{C}$ (see [8] p.264-272), the coefficients of $\mathbf{Q}$ are positive constants (see Beris and Edwards [8] p.184) and the coefficients of $\mathbf{L}$ are functions of the invariants of $\mathbf{C}$ and $\nabla \mathbf{u}$ [56].

The generalised bracket for modelling transport in nonisothermal and compressible viscoelastic fluids is obtained by adding Eq. (2.3.4) to Eq. (2.2.7):

$$
\begin{aligned}
\{[F,A]\} = &-\int_{\Omega}\left[\frac{\delta F}{\delta \rho}\nabla_j\left(\rho\frac{\delta A}{\delta m_j}\right)-\frac{\delta A}{\delta \rho}\nabla_j\left(\rho\frac{\delta F}{\delta m_j}\right)\right]d\Omega\\
&-\int_{\Omega}\left[\frac{\delta F}{\delta m_k}\nabla_j\left(m_k\frac{\delta A}{\delta m_j}\right)-\frac{\delta A}{\delta m_k}\nabla_j\left(m_k\frac{\delta A}{\delta m_j}\right)\right]d\Omega\\
&-\int_{\Omega}\left[\frac{\delta F}{\delta \rho}\nabla_j\left(s\frac{\delta A}{\delta m_j}\right)-\frac{\delta A}{\delta s}\nabla_j\left(s\frac{\delta F}{\delta m_j}\right)\right]d\Omega\\
&-\int_{\Omega}\left[\frac{\delta F}{\delta C_{ij}}\nabla_k\left(C_{ik}\frac{\delta A}{\delta m_k}\right)-\frac{\delta A}{\delta C_{ij}}\nabla_k\left(C_{ij}\frac{\delta F}{\delta m_k}\right)\right]d\Omega\\
&-\int_{\Omega}C_{ki}\left[\frac{\delta A}{\delta C_{ij}}\nabla_k\left(\frac{\delta F}{\delta m_j}\right)-\frac{\delta F}{\delta C_{ij}}\nabla_k\left(\frac{\delta A}{\delta m_j}\right)\right]d\Omega\\
&-\int_{\Omega}C_{ki}\left[\frac{\delta A}{\delta C_{ij}}\nabla_k\left(\frac{\delta F}{\delta m_j}\right)-\frac{\delta F}{\delta C_{ij}}\nabla_k\left(\frac{\delta A}{\delta m_j}\right)\right]d\Omega\\
&-\int_{\Omega}Q_{ijkl}\nabla_i\left(\frac{\delta F}{\delta m_j}\right)\nabla_k\left(\frac{\delta A}{\delta m_l}\right)d\Omega\\
&+\int_{\Omega}\frac{1}{T}\frac{\delta F}{\delta s}Q_{ijkl}\nabla_i\left(\frac{\delta A}{\delta m_j}\right)\nabla_k\left(\frac{\delta A}{\delta m_l}\right)d\Omega\\
&-\int_{\Omega}\Lambda_{ijkl}\frac{\delta F}{\delta C_{ij}}\frac{\delta A}{\delta C_{kl}}\,d\Omega\\
&+\int_{\Omega}\frac{1}{T}\frac{\delta F}{\delta s}\Lambda_{ijkl}\frac{\delta A}{\delta C_{ij}}\frac{\delta A}{\delta C_{kl}}\,d\Omega\\
&-\int_{\Omega}L_{ijkl}\left(\nabla_i\frac{\delta F}{\delta M_j}\frac{\delta A}{\delta C_{kl}}-\nabla_i\frac{\delta A}{\delta M_j}\frac{\delta F}{\delta C_{kl}}\right)d\Omega\\
&-\int_{\Omega}\alpha_{ij}\nabla_i\left(\frac{\delta F}{\delta s}\right)\nabla_k\left(\frac{\delta A}{\delta s}\right)d\Omega\\
&+\int_{\Omega}\frac{1}{T}\frac{\delta F}{\delta s}\alpha_{ij}\nabla_i\left(\frac{\delta A}{\delta s}\right)\nabla_k\left(\frac{\delta A}{\delta s}\right)d\Omega.
\end{aligned}
\tag{2.3.5}
$$

Expanding the left-hand side of Eq. (2.1.4) using the chain rule and then comparing like terms with the right-hand side of Eq. (2.3.4) and Eq. (2.2.7) we obtain the differential form of the governing equations for the state variables

$$\frac{\partial \rho}{\partial t} + \nabla \cdot (\rho \mathbf{u}) = 0 \tag{2.3.6}$$

$$\rho\left(\frac{\partial \mathbf{u}}{\partial t} + \mathbf{u} \cdot \nabla \mathbf{u}\right) = -\nabla p + \nabla \cdot \mathbb{T} \tag{2.3.7}$$

$$\frac{\partial s}{\partial t} + \nabla \cdot (s\mathbf{u}) = \frac{1}{T}\mathbf{Q} :: \left(\nabla \mathbf{u} \otimes \nabla \mathbf{u}\right) + \frac{1}{T}\nabla \cdot (\boldsymbol{\alpha} T \nabla T) + \frac{1}{T}\boldsymbol{\Lambda} :: \left(\frac{\delta A}{\delta \mathbf{C}} \otimes \frac{\delta A}{\delta \mathbf{C}}\right) \tag{2.3.8}$$

$$\overset{\triangledown}{\mathbf{C}} + (\nabla \cdot \mathbf{u})\mathbf{C} = -\boldsymbol{\Lambda} : \frac{\delta A}{\delta \mathbf{C}} + \mathbf{L} : \nabla \mathbf{u}, \tag{2.3.9}$$

with $\mathbb{T}$ given by

$$\mathbb{T} = \mathbf{Q} : \nabla \mathbf{u} + 2\frac{\delta A}{\delta \mathbf{C}} \cdot \mathbf{C} + 2\mathbf{L} : \frac{\delta A}{\delta \mathbf{C}}, \tag{2.3.10}$$

where we define

$$\mathbf{A} :: \mathbf{B} = \sum_{i,j,k,l} A_{ijkl} B_{ijkl} \qquad \mathbf{C} \otimes \mathbf{D} = C_{ij} D_{kl}$$

$$\mathbf{a} \cdot \mathbf{b} = \sum_{k} a_k b_k$$

The pressure is defined in terms of the internal energy

$$p = -\hat{u} + \rho\frac{\partial \hat{u}}{\partial \rho} + s\frac{\partial \hat{u}}{\partial s} + \mathbf{C} : \frac{\partial \hat{u}}{\partial \mathbf{C}} \tag{2.3.11}$$

Eq. (2.3.6)-(2.3.10) is the general set of governing equations from which specific viscoelastic fluid models can be derived by specifying a form of the Helmholtz free energy and tensors $\boldsymbol{\Lambda}$, $\mathbf{Q}$ and $\mathbf{L}$ (for further discussion of the general governing equations see [8] p.328-335).

2.4 The Energy Balance Equation

We can now derive an energy balance equation using Eq. (2.3.6)-(2.3.9). The time derivative of the Helmholtz free energy is given by

$$\frac{\partial a}{\partial t} = \frac{\partial}{\partial t}\left(\frac{\rho}{2}\mathbf{u}\cdot\mathbf{u} + \hat{a}(\rho, s, \mathbf{C})\right). \tag{2.4.1}$$

Taking derivatives of $\hat{a}$ w.r.t. t yields

$$\frac{\partial \hat{a}(\rho, s, \mathbf{C})}{\partial t} = \frac{\partial \hat{a}}{\partial \rho}\frac{\partial \rho}{\partial t} + \frac{\partial \hat{a}}{\partial s}\frac{\partial s}{\partial t} + \frac{\partial \hat{a}}{\partial \mathbf{C}} : \frac{\partial \mathbf{C}}{\partial t}. \tag{2.4.2}$$

It can be shown via substitution of Eq. (2.3.6)-(2.3.9) into Eq. (2.4.2), that in the absence of external thermal energy potential, the equation for internal energy is given by

$$\frac{D\hat{a}}{Dt} + (\nabla\cdot\mathbf{u})\hat{a} = \nabla\cdot\mathbf{q} + \hat{\boldsymbol{\sigma}} : \nabla\mathbf{u}, \tag{2.4.3}$$

where

$$\hat{\boldsymbol{\sigma}} = \mathbb{T} - \mathbf{L}\cdot\frac{\delta A}{\delta \mathbf{C}} - p(\nabla\cdot\mathbf{u}), \tag{2.4.4}$$

and $\mathbf{q} = -\boldsymbol{\alpha}\nabla T$. For a more detailed derivation of Eq. (2.4.3) see Sec. (A.4). The thermal conductivity matrix, $\boldsymbol{\alpha}$, is a function of the conformation stress, to the extent dictated by the Cayley-Hamilton theorem (see [8] p.331)

$$\boldsymbol{\alpha} = a_1\mathbf{I} + a_2\mathbf{C} + a_3\mathbf{C}\cdot\mathbf{C}, \tag{2.4.5}$$

where scalar coefficients a_1, a_2 and a_3 are, in general, functions of the invariants of the conformation stress [8]. To ensure non-negative entropy production the following conditions must hold:

$$a_1 \geq 0, \qquad\qquad a_2 + a_3 \geq 0. \tag{2.4.6}$$

The body of theoretical and experimental work suggests thermal conductivity in polymeric fluids is anisotropic under flowing conditions [8, 41]. Experiments on cross-linked elastomers show a significant enhancement in thermal conductivity in the direction of stretch for natural rubber subjected to uniaxial elongation (Tautz [85]). Moreover, Cocci and Picot [19] showed that, for polymeric liquids, thermal conductivity in the direction of strain of the macromolecule was much higher than perpendicular to it. For dilute polymer solutions Van den Brule and Slikkerveer[87] defined a_1 as the anisotropic thermal conductivity of the solvent and a_i $i \in \{2, 3\}$ are given by

$$a_2 = \frac{3\zeta}{2m}\alpha\rho k_b, \qquad a_3 = 0, \tag{2.4.7}$$

where m is the mass of the polymer and ζ is the friction coefficient. A detailed review of the theory behind the derivation of the energy equation was given by Dressler et al. [25] with a discussion of the thermal coefficient matrix on p.124.

In order to avoid complicating the analysis, in the benchmark problems considered in Chapters 5-7 we will assume that the heat condition is purely isotropic i.e.

$$a_1 = \kappa, \qquad a_2 = 0 \qquad a_3 = 0. \tag{2.4.8}$$

It is understood that this assumption does limit the applicability of results to polymeric fluids where strong nonisotropic thermal conductivity is observed and future work should consider this as a major area of development.

2.5 Thermodynamic Consistency and Hulsen's Theorem

Within the context of the generalised bracket theory the governing equation of the conformation tensor takes the form

$$\overset{\triangledown}{\mathbf{C}} + (\nabla \cdot \mathbf{u})\mathbf{C} = \hat{f}_1(\mathbf{C})\mathbf{I} + \hat{f}_2(\mathbf{C})\mathbf{C} + \hat{f}_3(\mathbf{C})\mathbf{C}^2, \tag{2.5.1}$$

where $\hat{f}_i(\mathbf{C})$ $i \in \{1, 2, 3\}$ are general functions of the invariants of $\mathbf{C}$. Hulsen examined the mathematical behaviour of the conformation tensor obeying (2.5.1) and provides us with a condition ensuring the consistency of our model.

Theorem 2.5.1 (Hulsen [46]) *Given that* $\boldsymbol{c}$ *satisfies the differential equation given by* (2.5.1) *and* $\boldsymbol{c}(\boldsymbol{x},0)$ *is positive definite. Then if* $\hat{f}_1(\boldsymbol{c}) > 0$ *and* $\nabla \boldsymbol{u}$ *finite,* $\boldsymbol{c}$ *remains positive definite for all* $t > 0$.

To invoke Hulsen's theorem it is sufficient to analyse the behaviour of $\hat{f}_1(\mathbf{C})$ for positive definite $\mathbf{C}$ (further discussion on Hulsen's theorem and analysis of the conformation tensor is given on p.279 [8] and Hulsen's 1990 paper on conformation tensor theory [46]).

2.6 Summary

We have presented the theory behind the generalised bracket method for deriving viscoelastic fluid models, detailing the theory behind the Poisson bracket (Sec. 2.2) and dissipative bracket (Sec. 2.3). The generalised bracket framework (GBF) formalism is modular and can be summarised 3 steps

- **Module 1**: Choose variables that characterise the state of the system, i.e mass density, ρ, momentum, $\mathbf{m} = \rho\mathbf{u}$, entropy, s and conformation stress $\mathbf{C}$. It is at this stage that the continuum approximation is made.
- **Module 2**: Choose a form of the energy and entropy (or Helmholtz free energy) functional. Throughout this thesis we use the standard Marrucci entropy (Eq. (2.3.1)). The constitutive equation depends on the elastic strain energy and entropy functionals. We consider both linear and nonlinear strain energy formulations when developing the various models detailed in the next Chapter.
- **Module 3**: Choose the form of the phenomenological tensors in the dissipative bracket, ensuring that the dissipative tensors satisfy the Onsager reciprocal relations and the resulting constitutive equation satisfies Hulsen's theorem. In this thesis we make use of the 'non-affine' tensor (Beris and Edwards) to derive a new model for Boger fluids.

These three modules provide a framework for deriving thermodynamically consistent models for transport in viscoelastic fluids. In the next chapter we will present a range of constitutive models for nonisothermal and compressible viscoelastic fluids derived using the generalised bracket framework.

Chapter 3

Compressible and Nonisothermal Models Based on the Generalised Bracket Method

In this Chapter we present a range of viscoelastic models using the generalised bracket framework. In Sec. 3.1.1 we derive general forms of the Maxwell and Oldroyd-B models. Sec. 3.2 presents a constitutive model derived using strain energy for hyperelastic materials formulation and Sec. 3.2.2 presents a derivation of the Leonov model. In Sec. 3.3.1 a generalised bracket method derived FENE-P model is presented. The most important contribution in this chapter is in Sec. 3.3.2, where we present the FENE-P-MP constitutive model for Boger fluids. FENE-P-MP is a generalised bracket method derived model analogous to the swanINNF(q)-FENE-P model by Garduño, Tamaddon-Jahromi & Webster [34, 35] making it a suitable candidate for modelling dilute polymer solutions in high pressure/strain-rate flows.

3.1 Maxwell-Type Models

3.1.1 The Compressible Oldroyd-B Model

Maxwell-type fluids can be modelled within the generalised bracket framework. First of all, it is necessary to specify the form of the Helmholtz free energy. Given a Helmholtz free energy of the form (2.1.2) the system of equations for mass, momentum, entropy and constitutive law are given by Eq. (2.3.6)-(2.3.9). For an Oldroyd-B fluid the extra stress tensor is assumed to comprise polymeric and solvent contributions. In order to capture these two contributions, nonzero forms of $\mathbf{\Lambda}$ and $\mathbf{Q}$ need to be specified [8].

3.1.2 Isothermal Compressible Oldroyd B Model

In the first instance we consider the isothermal case where the fluid parameters (viscosities, relaxation time) are assumed to be independent of temperature. The components of the relaxation tensor are given by

$$\Lambda_{ijkl} = \frac{1}{2nK\lambda_2}(\delta_{jl}C_{ik} + \delta_{jk}C_{il} + \delta_{il}C_{jk} + \delta_{ik}C_{jl}) + \frac{2}{3\alpha K}\left(\frac{1}{\lambda_0} - \frac{1}{\lambda_2}\right)\delta_{ij}C_{kl} \tag{3.1.1}$$

where $\lambda_0 = \lambda_0(T)$ and $\lambda_2 = \lambda_2(T)$ are the relaxation times of the fluid. Essentially λ_0 and λ_2 represent the trace and the traceless stress relaxation time, respectively. n is the number density of the polymers and K is the spring constant. The expression for $\mathbf{\Lambda}$ given by Eq. (3.1.1) satisfies the Onsager reciprocal relations and is positive definite for all positive definite $\mathbf{C}$. For the purposes of this thesis we will only consider fluids characterised by a single relaxation time i.e. $\lambda_0 = \lambda_2 = \lambda$. Several experiments such as dynamic oscillatory shear have shown that polymeric fluids often display a spectra of relaxation times. Therefore the assumption of a single relaxation time characterising a polymeric fluid system results in models that poorly approximate actual material functions. However, it is a necessary assumption required in order to obtain PDEs that can be easily used for computing viscoelastic flow in complex geometries.

Furthermore, Eq. (3.1.1) is one of many forms that $\mathbf{\Lambda}$ can take. The only strict requirement is that the equation for the conformation tensor ensures $\mathbf{C}(\mathbf{x}, t)$ is positive definite $\forall t > 0$. We have chosen this form as it is one of the simpler expressions for relaxation. In reality both the viscosity and relaxation time of a fluid will be functions of pressure and temperature with relationships being uniquely determined for each specific material.

The most general form of the viscosity tensor is given by

$$Q_{ijkl} = \mu_s(\delta_{ik}\delta_{jl} + \delta_{il}\delta_{jk}) + \eta_s(\delta_{ik}\delta_{jl} - \delta_{il}\delta_{jk}) + \kappa'_s\delta_{ij}\delta_{kl} \tag{3.1.2}$$

To satisfy frame indifference (principle of objectivity), η_s has to be set to zero so that

$$Q_{ijkl} = \mu_s(\delta_{ik}\delta_{jl} + \delta_{il}\delta_{jk}) + \kappa'_s\delta_{ij}\delta_{kl} \tag{3.1.3}$$

where $\mu_s = \mu_s(T)$ is the shear viscosity and $\kappa'_s = \kappa'_s(T) = \kappa_s(T) - \frac{2}{3}\mu_s(T)$ is the 'second viscosity'. Using κ'_s instead of the *bulk viscosity* κ_s permits the separation of gradient and divergence free terms in the Newtonian viscosity.

Eq. (3.1.3) provides the most general form of a fourth order viscosity tensor that satisfies the principle of frame indifference and the Onsager reciprocal relations [8]. The subscript 's' denotes that $\mathbf{Q}$ is normally associated with the viscosity of the solvent (Newtonian) component of the fluid. We define the general elastic modulus

$$G = \frac{\mu_p}{\lambda}, \tag{3.1.4}$$

where μ_p is the polymeric viscosity and λ is the relaxation time. Another definition for G that is often used in the literature is

$$G = nk_bT, \tag{3.1.5}$$

where k_b is the Boltzmann constant and T is the temperature. The number density, n, is defined as the mass fraction of the polymers and can be defined in terms of the mass density as $n = \alpha\rho$, where α is a measure of the degree of elasticity per unit mass of the polymeric fluid ([25] p.129/130). It must also be noted that the ability to linearly decompose the stress into viscous terms (dependent on μ_s and $\nabla\mathbf{u}$) and elastic terms (dependent on $\mathbf{C}$) is a non-trivial assumption. The Helmholtz free energy density is given by the sum of the kinetic and internal energy (elastic strain energy, chemical potential etc.) less a *degradation term* proportional to the Boltzmann entropy and temperature (for more details on the relationship between the Hamiltonian and Helmholtz free energy and relationships between the derivatives of the two functionals see [8])

$$A[\rho, \rho\mathbf{u}, s, T, \mathbf{C}] = \int_\Omega a(\rho, \rho\mathbf{u}, T, \mathbf{C})\, d\Omega = \int_\Omega \left(\frac{\rho\mathbf{u}\cdot\rho\mathbf{u}}{2\rho} + \hat{a}(\rho, T, \mathbf{C}) \right) d\Omega \tag{3.1.6}$$

where

$$\hat{a}(\rho, s, T, \mathbf{C}) = a_0(\rho, T) + w(\mathbf{C}) - s(\rho, T, \mathbf{C})T \tag{3.1.7}$$

For a Maxwell fluid the elastic strain energy is given by

$$w(\mathbf{C}) = \frac{\alpha K}{2}(tr\mathbf{C} - 3) \tag{3.1.8}$$

Substituting (3.1.8) and (2.3.1) into (3.1.7) we obtain.

$$\hat{a} = \hat{a}_0(\rho, T) + \frac{\alpha K}{2}(tr\mathbf{C} - 3) - \frac{\alpha\rho k_b T}{2}\log\det\left(\frac{\mathbf{C}K}{\rho k_b T}\right) \tag{3.1.9}$$

The additional term, $\hat{a}_0(\rho, T)$, in Eq. (3.1.9) represents the Helmholtz free energy density for the fluid in the 'rest' state (i.e. not depending on $\mathbf{C}$) of a fluid. Here we have also used α to represent the fraction of mass density represented by the polymeric constituent ($\alpha\rho$ being the 'elasticity density'). It then follows that

$$\frac{\delta A}{\delta\mathbf{C}} = \frac{\alpha K}{2}\mathbf{I} - \frac{\alpha\rho k_b T}{2}\mathbf{C}^{-1} \tag{3.1.10}$$

Substituting (3.1.10) and (3.1.1) into (2.3.9) we can write

$$\boldsymbol{\Lambda} : \frac{\delta A}{\delta \mathbf{C}} = \frac{1}{\lambda}\mathbf{C} - \frac{1}{\lambda}\frac{\alpha\rho k_b T}{K}\mathbf{I}\,, \tag{3.1.11}$$

thus obtaining a dynamic equation for the conformation tensor

$$\overset{\triangledown}{\mathbf{C}} + (\nabla\cdot\mathbf{u})\mathbf{C} = -\frac{1}{\lambda}\left(\mathbf{C} - \frac{G}{\alpha K}\mathbf{I}\right) \tag{3.1.12}$$

Note that in the limit as $\lambda \to \infty$ we have

$$\lim_{\lambda\to\infty} \boldsymbol{\Lambda} : \frac{\delta A}{\delta \mathbf{C}} = 0 \tag{3.1.13}$$

which leaves us with the equation for an elastic solid

$$\overset{\triangledown}{\mathbf{C}} + (\nabla\cdot\mathbf{u})\mathbf{C} = 0 \tag{3.1.14}$$

Additionally the expression for $\mathbb{T}$ is given by

$$\mathbb{T} = (2\mu_s\mathbb{D} + \kappa_s'(\nabla\cdot\mathbf{u})\mathbf{I}) + \alpha K\mathbf{C} - G\mathbf{I} \tag{3.1.15}$$

Rearranging this equation to make $\mathbf{C}$ the subject gives

$$\mathbf{C} = \frac{1}{\alpha\rho K}\mathbb{T} - \frac{1}{\alpha\rho K}(2\mu_s\mathbb{D} + \kappa_s'(\nabla\cdot\mathbf{u})\mathbf{I}) + \frac{k_b T}{K}\mathbf{I} \tag{3.1.16}$$

with upper convected derivative given by

$$\overset{\triangledown}{\mathbf{C}} = \frac{1}{\alpha\rho K}\overset{\triangledown}{\mathbb{T}} - \frac{1}{\alpha\rho K}(2\mu_s\overset{\triangledown}{\mathbb{D}} - 2\kappa_s'(\nabla\cdot\mathbf{u})\mathbb{D}) - 2\frac{k_b T}{K}\mathbb{D} \tag{3.1.17}$$

where $\mathbb{D} = \frac{1}{2}(\nabla\mathbf{u} + \nabla\mathbf{u}^T)$. Substituting Eq. (3.1.16) and Eq. (3.1.17) into Eq. (3.1.12) we obtain

$$\begin{aligned}\left(\frac{1}{\lambda}+(\nabla\cdot\mathbf{u})\right)\mathbb{T}+\overset{\triangledown}{\mathbb{T}} &= 2((G_0-\kappa_s'(\nabla\cdot\mathbf{u}))\mathbb{D}+\mu_s\overset{\triangledown}{\mathbb{D}})+(\nabla\cdot\mathbf{u})(2\mu_s\mathbb{D}+(\kappa_s'(\nabla\cdot\mathbf{u})-G_0)\mathbf{I})\\ &\quad+\frac{2\mu_s}{\lambda}\mathbb{D}+\left[\frac{\kappa_s'}{\lambda}(\nabla\cdot\mathbf{u})+\frac{G_0}{\alpha K\lambda}\right]\mathbf{I}\end{aligned} \tag{3.1.18}$$

which can be written in the form

$$\begin{aligned}\mathbb{T}+\lambda(\overset{\triangledown}{\mathbb{T}}+(\nabla\cdot\mathbf{u})\mathbb{T}) =&2\mu_s\mathbb{D}+2\mu_p\mathbb{D}+\kappa_s'(\nabla\cdot\mathbf{u})-2\kappa_s'\lambda(\nabla\cdot\mathbf{u})\mathbb{D}\\ &+2\lambda\mu_s(\nabla\cdot\mathbf{u})\mathbb{D}+2\lambda\mu_s\overset{\triangledown}{\mathbb{D}}\\ &-\mu_p(\nabla\cdot\mathbf{u})\mathbf{I}+\lambda(\nabla\cdot\mathbf{u})^2\mathbf{I}\end{aligned} \tag{3.1.19}$$

where we have used the fact that $G=\alpha\rho k_bT=\mu_p/\lambda$.

Eq. (3.1.19) represents the most general form of constitutive equation for a compressible Oldroyd-B fluid with a single relaxation time. However, this equation is not in a form that can be used in any practical sense to obtain numerical approximations to viscoelastic flow problems. In order to reduce the equations to a more tractable form we now decompose the total extra stress $\mathbb{T}$ into solvent and polymeric contributions $\mathbb{T}=\boldsymbol{\tau}_s+\boldsymbol{\tau}_p$ where $\boldsymbol{\tau}_s$ and $\boldsymbol{\tau}_p$ satisfy the equations

$$\begin{aligned}\boldsymbol{\tau}_s &= 2\mu_s\mathbb{D}+\kappa_s'(\nabla\cdot\mathbf{u})\mathbf{I}\\ \lambda\overset{\triangledown}{\boldsymbol{\tau}}_p+(1+\lambda(\nabla\cdot\mathbf{u}))\boldsymbol{\tau}_p &= 2\mu_p\left(\mathbb{D}-\frac{1}{2}(\nabla\cdot\mathbf{u})\mathbf{I}\right)\end{aligned} \tag{3.1.20}$$

It can be shown that the expressions in (3.1.20) satisfy (3.1.19) exactly. When the incompressibility condition ($\nabla\cdot\mathbf{u}=0$) is imposed we recover the incompressible form of the

Oldroyd-B constitutive law given by

$$\begin{aligned} \boldsymbol{\tau}_s &= 2\mu_s \mathbb{D} \\ \lambda \overset{\triangledown}{\boldsymbol{\tau}}_p + \boldsymbol{\tau}_p &= 2\mu_p \mathbb{D} \end{aligned} \tag{3.1.21}$$

Eq. (3.1.20) represents a the constitutive equation for an isothermal compressible Oldroyd-B fluid with relaxation time independent of **C**. The system given by Eq. (2.3.6)-(2.3.10) is also capable of modelling viscoelastic fluids with a spectrum of relaxation times. We now consider the extension of Eq. (3.1.20) to the nonisothermal case when the fluid parameters are functions of temperature.

3.1.3 Nonisothermal Compressible Oldroyd B Model

Suppose that the fluid parameters are temperature dependent. The components of the relaxation tensor are given by

$$\Lambda_{ijkl} = \frac{1}{2\alpha\rho K(T)\lambda(T)}(\delta_{jl}C_{ik} + \delta_{jk}C_{il} + \delta_{il}C_{jk} + \delta_{ik}C_{jl}) \tag{3.1.22}$$

The relaxation tensor with components given by (3.1.22) was initially proposed by Dresler et. al [25]. Likewise the components of the viscous dissipation tensor are given by

$$Q_{ijkl} = \mu_s(T)(\delta_{ik}\delta_{jl} + \delta_{il}\delta_{jk}) + \kappa'_s(T)\delta_{ij}\delta_{kl} \tag{3.1.23}$$

where $\kappa'_s(T) = \kappa_s(T) - \frac{2}{3}\mu_s(T)$. Equation (2.3.10) becomes

$$\mathbb{T} = 2\mu_s(T)\mathbb{D} + \kappa'_s(T)(\nabla \cdot \mathbf{u})\mathbf{I} + \alpha\rho K(T)\mathbf{C} - \alpha\rho k_b T\mathbf{I} \tag{3.1.24}$$

Taking the upper-convected derivative of the polymeric stress

$$\boldsymbol{\tau}_p = \alpha\rho K(T)\mathbf{C} - G(T)\mathbf{I} \tag{3.1.25}$$

yields

$$\overset{\triangledown}{\boldsymbol{\tau}}_p = \alpha \frac{D\rho}{Dt} K(T)\mathbf{C} + \alpha\rho\frac{DK(T)}{Dt}\mathbf{C} + \alpha\rho K(T)\,\overset{\triangledown}{\mathbf{C}} - \frac{DG}{Dt}\mathbf{I} + 2G(T)\mathbb{D} \tag{3.1.26}$$

which contains additional terms due to the non-constant temperature and spring constant. Rearranging Eq. (3.1.25) and (3.1.26) and eliminating $\mathbf{C}$ results in the constitutive equation

$$\begin{gathered}\lambda(T)\,\overset{\triangledown}{\boldsymbol{\tau}}_p + \left[1 + \lambda(T)\left(\nabla\cdot\mathbf{u} - \frac{D\ln K(T)}{Dt}\right)\right]\boldsymbol{\tau}_p = G(T)\lambda(T)\left[2\mathbb{D} + \left(\frac{D\ln K(T)}{Dt} - \frac{D\ln(T)}{Dt}\right)\mathbf{I}\right]\\ \boldsymbol{\tau}_s = 2\mu_s(T)\left(\mathbb{D} - \frac{1}{3}(\nabla\cdot\mathbf{u})\mathbf{I}\right) + \kappa(T)(\nabla\cdot\mathbf{u})\mathbf{I}\end{gathered} \tag{3.1.27}$$

Eq. (3.1.27) provides the most general form of the non-isothermal compressible Oldroyd-B constitutive equation for a fluid defined by a single relaxation time[1]. The functional dependence of the viscosity and spring constant are determined experimentally and are dependent on the particular polymer melt/solution under consideration. In the case of incompressible and isothermal flow the model reduces to Eq. (3.1.21). This model differs from the models proposed by Belblidia et al. [13] and Dressler et al. [25] in that additional compressible terms appear on the right-hand side of the polymeric stress equation.

It must be noted that (3.1.27) is not the only form that a compressible extension of the Oldroyd-B model can take. There is some discussion in the literature about additional terms in the phenomenological tensors that may exist (see [8] p.331). However, it is clear that by use of the generalised bracket method the constitutive model represented by (3.1.27) is thermodynamically admissible. Furthermore, in the incompressible limit we obtain an equivalent model to that proposed by Dressler et al. [25] derived using the GENERIC formalism.

The bracket formulation enables us to ensure consistency with thermodynamic principles when extending governing equations for viscoelastic/non-Newtonian fluids to account for

---

[1] A full derivation of the compressible and nonisothermal Maxwell-model is given in Sec. A.3

compressible flow [8, 13]. The major advantage of this approach however lies in its ability to capture a much wider range of stress-strain relations based on the Hamiltonian/Helmholtz free energy. The Oldroyd-B model is derived from a (linear) Hookean strain energy model (Eq. (3.1.8)).

3.1.4 The Giesekus Model

The Giesekus model was first developed within the context of network theory for continua (see [8] p.252). In this model, the effect on a given dumbbell due to the presence of the confining interactions with the other dumbbells. The drag coefficient $\zeta = 4K\lambda$ is replaced by a "mobility tensor"

$$\boldsymbol{\zeta}^{-1} = \frac{1}{\zeta}\left((1-\hat{\alpha})\mathbf{I} + \hat{\alpha}\frac{K}{k_bT}\mathbf{C}\right) \tag{3.1.28}$$

where $\hat{\alpha}$ is an empirical constant which lies within the range $0 \leq \hat{\alpha} \leq 1$. Noting that $1/(2nK\lambda) = 2/(n\zeta)$ the phenomenological tensor, Λ, is then adapted to the form

$$\Lambda_{ijkl} = \frac{2}{n\zeta}\left[4(1-\hat{\alpha})C_{ik}\delta_{jl} + \hat{\alpha}\frac{4nK}{G_0}C_{ik}C_{jl}\right] \tag{3.1.29}$$

which includes higher order correction terms. Note that (3.1.29) still satisfies the Onsager reciprocal relations and thus fits into the class of thermodynamically permissible phenomenological tensors. Eq. (3.1.29) can be substituted into Eq. (2.3.9) to obtain

$$\overset{\triangledown}{C}_{ij} = -\frac{4k_bT}{\zeta}\left((1-\hat{\alpha})\delta_{ik} + \hat{\alpha}\frac{K}{k_bT}C_{ik}\right)\left(\frac{K}{k_bT}C_{kj} - \delta_{kj}\right) \tag{3.1.30}$$

The factor K/k_bT is nondimensional and so Eq. (3.1.30) can be written in terms of the new variable $\tilde{\mathbf{C}} = \frac{K}{k_bT}\mathbf{C}$.

$$\frac{k_bT}{K}\overset{\triangledown}{\tilde{C}}_{ij} = -\frac{4k_bT}{\zeta}\left((1-\hat{\alpha})\delta_{ik} + \hat{\alpha}\tilde{C}_{ik}\right)\left(\tilde{C}_{kj} - \delta_{kj}\right) \tag{3.1.31}$$

The polymeric stress is given by

$$\boldsymbol{\tau}_p = \mathbf{C} - G\mathbf{I} \tag{3.1.32}$$

Taking the upper convected derivative of Eq. (3.1.32)

$$\overset{\triangledown}{\boldsymbol{\tau}}_p = \overset{\triangledown}{\mathbf{C}} + 2G\mathbb{D} \tag{3.1.33}$$

Substituting Eq. (3.1.33) and (3.1.32) into (3.1.31) we arrive at the Giesekus constitutive law

$$\boldsymbol{\tau}_p + \lambda_1 \overset{\triangledown}{\boldsymbol{\tau}}_p + \hat{\alpha}\frac{\lambda_1}{\mu_p}\boldsymbol{\tau}_p^2 = 2\mu_p\mathbb{D} \tag{3.1.34}$$

A compressible form of the Giesekus constitutive relation can also be derived within the generalised bracket framework using the same strain energy formulation and phenomenological tensor. If we include the compressible terms in the conformation tensor equation (Eq. (3.1.31)) it becomes

$$\overset{\triangledown}{\mathbf{C}} + (\nabla \cdot \mathbf{u})\mathbf{C} = -\frac{4k_bT}{\zeta}\left((1-\hat{\alpha})\mathbf{I} + \hat{\alpha}\frac{K}{k_bT}\mathbf{C}\right)\left(\frac{K}{k_bT}\mathbf{C} - \mathbf{I}\right) \tag{3.1.35}$$

Substitution of (3.1.33) and (3.1.32) results in the compressible form of the Giesekus model given by

$$\boldsymbol{\tau}_p + \lambda_1(\overset{\triangledown}{\boldsymbol{\tau}}_p + (\nabla \cdot \mathbf{u})\boldsymbol{\tau}_p) + \hat{\alpha}\frac{\lambda_1}{\mu_p}\boldsymbol{\tau}_p^2 = 2\mu_p\left(\mathbb{D} - \frac{1}{2}(\nabla \cdot \mathbf{u})\mathbf{I}\right) \tag{3.1.36}$$

Note that, similar to the compressible form of the Oldroyd-B model (Eq. (3.1.20)) compressible terms exist on both the left- and right-hand side of the equation. In the next section we will look at a range of more complicated elastic strain energy models and the connection between strain energy formulae for hyperelastic rubber-like solids and nonlinear viscoelastic fluid constitutive laws.

3.1.5 The Extended White-Metzner Model

In an attempt to account for the spectra of relaxation times observed in real polymeric fluids, phenomenological models with non constant relaxation time are often used in the literature. The extended White-Metzner (EWM) model, proposed by Souvaliotis and Beris [81] is the generalised bracket derived variable relaxation time model, similar in form the WM model. However, the EWM model retains an important advantage of the WM model in that it can accurately predict the viscosity and first normal stress difference of any polymeric fluid in a simple shear flow using only a single relaxation time [36]. Furthermore, it guarantees both the evolutionary character of the flow field and non-negative entropy production by the fluid. Specifically, the relaxation time is chosen to a power law of the first invariant of the conformation stress

$$\lambda(T, \mathbf{C}) = \lambda_0 \left(\frac{1}{3} \frac{K}{k_b T} \mathrm{tr}\mathbf{C} \right)^{\gamma} \tag{3.1.37}$$

where $\gamma \geq 0$ is a power law index (not to be confused with the viscometric shear rate, $\dot{\gamma}$). The polymeric viscosity is also of the form (3.1.37) as the since they are directly proportional via the elastic modulus (see Eq. (3.1.4)). The relaxation tensor is given by

$$\Lambda_{ijkl} = \frac{1}{2\alpha\rho K(T)\lambda_0} \left(\frac{1}{3} \frac{K}{k_b T} \mathrm{tr}\mathbf{C} \right)^{-\gamma} (\delta_{jl} C_{ik} + \delta_{jk} C_{il} + \delta_{il} C_{jk} + \delta_{ik} C_{jl}) \tag{3.1.38}$$

where $K(T)\mathrm{tr}\mathbf{C} > 0$ since $\mathbf{C}$ is positive definite and $K(T) > 0$. Substitution of (3.1.38) into (2.3.9) yields the constitutive relation

$$\boldsymbol{\tau}_p + \lambda(T, \mathbf{C})(\overset{\triangledown}{\boldsymbol{\tau}}_p + (\nabla \cdot \mathbf{u})\boldsymbol{\tau}_p) = 2\mu_p(T, \mathbf{C})\mathbb{D} \tag{3.1.39}$$

Eq. (3.1.39) reduces to the isothermal UCM model when $\gamma = 0$.

3.2 Hyperelastic Strain Energy Models

In this section we present a brief discussion of some of the elastic energy models used frequently used in the literature on finite strain theory. One of the more appealing characteristics of the generalised bracket method is that it provides a framework that enables the derivation of continuum models of viscoelastic fluids by utilising elastic energy density formula for hyperelastic materials.

Deriving constitutive laws from strain-energy models ensures that the accuracy of the predictions made by the viscoelastic fluid model directly reflects the applicability of the strain-energy model to the material being modelled. However, a large number of the elastic energy models used in finite strain are themselves phenomenological, one must take care to ensure that the various admissibility criteria in the generalised bracket method are satisfied. Another difficulty with modelling fluids using finite strain energy models is that there is no guarantee that a closed form expression can be obtained from the outset.

In order to proceed let us consider the following. The elastic energy component of the Hamiltonian for a viscoelastic material is a function of the invariants of the conformation tensor i.e.

$$W(\mathbf{C}) = \int_{\Omega} w(I_1(\mathbf{C}), I_2(\mathbf{C}), I_3(\mathbf{C}))\, d\Omega \tag{3.2.1}$$

where $I_k(\mathbf{C})$ ($k \in \{1, 2, 3\}$) are the principal invariants of $\mathbf{C}$. Hyperelastic materials undergo large elastic deformations relative to their reference configuration and are also characterised by a nonlinear relationship between the stress and strain. We now present constitutive models for viscoelastic fluids derived using nonlinear expressions for W in Eq. (3.2.1).

3.2.1 Compressible Mooney-Rivlin Type Model

So far we have discussed compressible viscoelastic models based on elastic strain energy density functions for Hookean-spring like materials. However, the literature on finite strain theory is rich with elastic strain energy density functions [26] for modelling the behaviour of rubber like polymeric materials. For both the UCM and Oldroyd-B models the elastic potential energy is that of a neo-Hookean material i.e. $W(\mathbf{C}) = \frac{\hat{\mu}}{2}(I_1(\mathbf{C}) - 3)$ where $\hat{\mu} = \alpha\rho K$ is the stiffness parameter of the material.

Consider a fluid whose polymeric constituent behaves like a Mooney-Rivlin material i.e. instead of a strain energy directly proportional to $I_1(\mathbf{C})$ the strain energy depends on all three principal invariants

$$w(\mathbf{C}) = \frac{\mu_1}{2}\left(\frac{I_1(\mathbf{C})}{I_3(\mathbf{C})^{\frac{1}{3}}} - 3\right) + \frac{\mu_2}{2}\left(\frac{I_2(\mathbf{C})}{I_3(\mathbf{C})^{\frac{2}{3}}} - 3\right) + \kappa_p'(I_3(\mathbf{C})^{1/2} - 1)^2 \tag{3.2.2}$$

where μ_1 and μ_2 are parameters to be determined empirically. The first and second terms are associated with the stiffness of the polymeric constituent and the third term is a compressible term associated with the bulk viscosity. It is easy to verify that if $I_3(\mathbf{C}) = \det \mathbf{C} = 1$, $\mu_2 = 0$ and $\mu_1 = \alpha\rho K$, then Eq. (3.2.2) reduces to the strain energy for a Maxwell material. Taking the derivative of the Helmholtz free energy functional, with elastic strain energy defined by (3.2.2) we obtain

$$\frac{\delta A}{\delta \mathbf{C}} = -\left(\kappa_p'(I_3^{1/2} - I_3) + \frac{\mu_1 I_1}{6I_3^{4/3}} + \frac{\mu_2 I_2}{3I_3^{5/3}} + \frac{G(T)}{2}\right)\mathbf{C}^{-1} + \left(\frac{\mu_1}{2I_3^{1/3}} + \frac{\mu_2 I_1}{2I_3^{2/3}}\right)\mathbf{I} - \frac{\mu_2}{2I_3^{2/3}}\mathbf{C} \tag{3.2.3}$$

which we write in the form

$$\frac{\delta A}{\delta \mathbf{C}} = g_1(\mathbf{C})\mathbf{C}^{-1} + g_2(\mathbf{C})\mathbf{I} + g_3(\mathbf{C})\mathbf{C}$$

where

$$\begin{aligned} g_1(\mathbf{C}) &= -\left(\kappa_p'(I_3^{1/2} - I_3) + \frac{\mu_1 I_1}{6I_3^{4/3}} + \frac{\mu_2 I_2}{3I_3^{5/3}} + \frac{\alpha\rho k_b T}{2}\right) \\ g_2(\mathbf{C}) &= \left(\frac{\mu_1}{2I_3^{1/3}} + \frac{\mu_2 I_1}{2I_3^{2/3}}\right) \\ g_3(\mathbf{C}) &= -\frac{\mu_2}{2I_3^{2/3}} \end{aligned} \tag{3.2.4}$$

Using the expression given by Eq. (3.2.3) for the energy derivative and Eq. (3.1.1) for the relaxation we obtain

$$\begin{aligned}\mathbf{\Lambda} : \frac{\delta W}{\delta \mathbf{C}} =& \frac{2}{\alpha K}\left(\frac{1}{\lambda_0} g_1(\mathbf{C}) + \frac{1}{3}\left(\frac{1}{\lambda_0} - \frac{1}{\lambda_2}\right)\left[g_2(\mathbf{C})I_1(\mathbf{C}) + g_3(\mathbf{C})(I_1(\mathbf{C}) - 2I_2(\mathbf{C}))\right]\right)\mathbf{I} \\ &+ \frac{2}{\lambda_2 \alpha K} g_2(\mathbf{C})\mathbf{C} \\ &+ \frac{2}{\lambda_2 \alpha K} g_3(\mathbf{C})\mathbf{C}^2\end{aligned} \tag{3.2.5}$$

where we have used the fact that $tr\mathbf{C}^2 = I_1(\mathbf{C}) - 2I_2(\mathbf{C})$. Consider once more the case when relaxation is described via a single relaxation time, λ. In this case Eq. (3.2.5) reduces to

$$\begin{aligned}\mathbf{\Lambda} : \frac{\delta W}{\delta \mathbf{C}} &= \frac{2}{\lambda \alpha K} g_1(\mathbf{C})\mathbf{I} + \frac{2}{\lambda \alpha K} g_2(\mathbf{C})\mathbf{C} + \frac{2}{\lambda \alpha K} g_3(\mathbf{C})\mathbf{C}^2 \\ &= a_1(\mathbf{C})\mathbf{I} + a_2(\mathbf{C})\mathbf{C} + a_3(\mathbf{C})\mathbf{C}^2\end{aligned} \tag{3.2.6}$$

By Hulsen's theorem the physical admissibility of the model depends on the behaviour of $a_1(\mathbf{C}) = \frac{2}{\alpha K} g_1(\mathbf{C})$. Substituting our strain energy expression into Eq. (2.3.9) and Eq. (2.3.10) the governing equations for conformation tensor and stress can be expressed

$$\overset{\triangledown}{\mathbf{C}} + (\nabla \cdot \mathbf{u})\mathbf{C} = -\frac{1}{\lambda \alpha K}\boldsymbol{\tau}_p \tag{3.2.7}$$

where

$$\begin{aligned}\mathbb{T} &= 2\mu_s \mathbb{D} + \kappa_s(\nabla \cdot \mathbf{u})\mathbf{I} + \boldsymbol{\tau}_p \\ \boldsymbol{\tau}_p &= 2g_1(\mathbf{C})\mathbf{I} + 2g_2(\mathbf{C})\mathbf{C} + 2g_3(\mathbf{C})\mathbf{C}^2\end{aligned} \tag{3.2.8}$$

Due to the additional complications introduced when $g_3 \neq 0$ the hyperelastic model cannot be reduced further (i.e. $\mathbf{C}$ cannot be eliminated). However further constraints on μ_1 and μ_2 exist in order to ensure $\boldsymbol{\tau}_p$ is zero when $\mathbf{C}$ is at equilibrium. Using the Cayley-Hamilton Theorem, it can be shown that the right-hand side of the dynamic equation for the conformation tensor can be written in the form

$$\mathbf{\Lambda} : \frac{\delta W}{\delta \mathbf{C}} = -(\alpha_0 + \alpha_2 \alpha_{01}^2)\mathbf{I} + (\alpha_1 + 2\alpha_{01}\alpha_2)\mathbf{C} - \alpha_2 \mathbf{C}^2 \tag{3.2.9}$$

where α_i are functions of the invariants of $\mathbf{C}$ (and also functions of $g_i(\mathbf{C})$) [8]. The parameter α_{01} is specifically chosen to be the ratio α_0/α_1 so that $\mathbf{C} = \alpha_{01}\mathbf{I}$ at equilibrium [8] i.e.

$$\overset{\triangledown}{\mathbf{C}} + (\nabla \cdot \mathbf{u})\mathbf{C} = 0 \qquad \text{when} \quad \mathbf{C} = \alpha_{01}\mathbf{I} \tag{3.2.10}$$

3.2.2 The Leonov Model

Leonov [55] designed single conformation tensor type fluid in order to model thermoplastics. Leonov proposed his model based on an alternative view on the state of stress within a viscoelastic fluid. The elastic strain deformation is not measured from a fixed and equal-for-all-points (global) relaxed state, but one that evolves with the fluid as it deforms. One can adjust the rate at which the rest state "follows" the flow so that in the limit where it doesn't follow the deformation (remains fixed) you have a perfect elastic material and in the limit where the rest state is identical to the deformed state we recover the model for a Newtonian fluid. It should be noted that in Leonov's derivation he identified $\mathbf{C} = \rho\mathbf{c}$ with the finger deformation tensor. In this work we define it as a normalised and averaged dyadic product of the end-to-end distance vector of the elastic chain molecules (see [8] p.213-216). However, this is not something that needs to be investigated in any detail for the purposes of this work as both definitions represent the state of elastic strain in the material and are interchangeably used in the literature [8].

As before we specify a (Helmholtz free) strain energy density functional for the viscoelastic fluid occupying Ω. In Leonov's derivation the elastic strain energy was not specified but rather written as a general function $w(a_1, a_{-1})$ where

$$a_1 = \frac{I_1(\mathbf{C})}{I_3(\mathbf{C})^{1/3}} \qquad a_{-1} = I_{-1} I_3^{1/3}, \tag{3.2.11}$$

$$I_1 = \mathrm{tr}\mathbf{C}, \qquad I_{-1} = \frac{I_2}{I_3}. \tag{3.2.12}$$

In this particular derivation of the model we will consider the case where W is a general linear function of a_1 and a_{-1} and $w = 0$ when $\mathbf{C} = G\mathbf{I}$ as to permit the derivatives of w to be the simplest possible non-trivial functions

$$w(a_1, a_{-1}) = \frac{\mu_1}{2}(a_1 - 3) + \frac{\mu_2}{2}(a_{-1} - 3). \tag{3.2.13}$$

Proceeding in the same manner as before, computing the functional derivatives for A

$$\frac{\delta A}{\delta \mathbf{C}} = \frac{\mu_1}{2}\frac{\partial}{\partial \mathbf{C}}(I_1(\mathbf{C})I_3(\mathbf{C})^{-1/3}) + \frac{\mu_2}{2}\frac{\partial}{\partial \mathbf{C}}(I_1(\mathbf{C})I_3(\mathbf{C})^{-2/3}) - \frac{\alpha\rho k_b T}{2}\frac{\partial}{\partial \mathbf{C}}\log\left(\det\left(\frac{\mathbf{C}K}{\rho k_b T}\right)\right)$$

which can be written in the form

$$\frac{\delta A}{\delta \mathbf{C}} = \left(\frac{\mu_1}{2I_3^{1/3}} + \frac{\mu_2 I_1}{2I_3^{2/3}}\right)\mathbf{I} - \left(\frac{\mu_2}{2I_3^{2/3}}\right)\mathbf{C} - \left(\frac{\mu_1 I_1}{6I_3^{1/3}} + \frac{\mu_2 I_1}{3I_3^{2/3}} + \frac{\alpha k_b T}{2}\right)\mathbf{C}^{-1} \tag{3.2.14}$$

The fourth order tensor $\mathbf{\Lambda}$ takes the form

$$\Lambda_{ijkl} = \frac{2}{G\lambda}(C_{il}C_{kj} + C_{ik}C_{jl}) - \frac{4}{3G_0\lambda}C_{lk}C_{ij} \tag{3.2.15}$$

For further information on the mechanism used to derive the form of the phenomenological tensors see Beris & Edwards p.266-269 [8]. Substituting Eq. (3.2.14) and Eq. (3.2.15) into the expression for the conformation tensor equation in Eq. (2.3.9) we obtain

$$\lambda(\overset{\triangledown}{\mathbf{C}} + \nabla \cdot \mathbf{u}\mathbf{C}) = \mu_1\left(\frac{I_1}{3}\mathbf{C} - \mathbf{C}^2\right) + \mu_2\left(\mathbf{I} - \frac{I_2}{3I_3}\mathbf{C}\right) \tag{3.2.16}$$

which can be rearranged to give the Leonov equation for the conformation tensor

$$\lambda\overset{\triangledown}{\mathbf{C}} + \lambda(\nabla \cdot \mathbf{u})\mathbf{C} = \frac{\mu_2}{G}\mathbf{I} + \frac{1}{G}\left[\mu_1\frac{I_1}{3} - \mu_2\frac{I_2}{3I_3}\right]\mathbf{C} - \frac{\mu_1}{G}\mathbf{C}^2 \tag{3.2.17}$$

Thermodynamic consistency conditions are met if we ensure that μ_1, μ_2 and the spring constant G are all non-negative. The Leonov model is an example of the class of viscoelastic models where the coefficients on the right-hand side of Eq. (2.5.1) are nonlinear functions of the invariants of $\mathbf{C}$. In the next section we will discuss nonlinear dumbbell models. Specifically 'finitely extendible' dumbbell models that capture the polymeric responses for Boger fluids at large extension/shear rates.

3.3 Elastic Dumbbell Models Based on Nonlinear Spring Force Laws

3.3.1 FENE-P, FENE-CR Models

Linearly elastic dumbbells corresponding to the Hookean model of chain-chain conformations yield UCM/Oldroyd-B models. However linear elastic models perform poorly at predicting the behaviour of viscoelastic flows at high deformation rates. As the magnitude of the end-to-end distance vector, $\mathbf{Q}$, approaches the length of the fully extended chain, b, the elastic response deviates drastically from that of a Hookean spring. The Finitely Extended Nonlinear Elastic (FENE) Dumbbell model was developed in the early 1980s [9] in order to model the increased spring force at the full chain length limit. The spring force between two connected beads in a dumbbell reads

$$F(\mathbf{Q}) = \frac{K}{1 - \frac{\mathbf{Q}\cdot\mathbf{Q}}{\mathbf{b}^2}}\mathbf{Q} \tag{3.3.1}$$

where K is the characteristic (small-strain) spring constant. In the limit as $b \to \infty$ it is possible to derive a constitutive equation for the polymeric stress without the need of a closure approximation [52, 69]. For finite values of b it is impossible to derive a single constitutive equation equivalent to FENE theory. The closed form approximation to the model, FENE-P, proposed by Peterlin[52], averages the response of the dumbbells reducing the description of the elastic material to a single conformation tensor. All of the information is contained within the outer product $\mathbf{Q} \otimes \mathbf{Q}$. To obtain a closed form expression for the polymeric strain a self-consistent pre-averaging approximation is used. For simple 2-bead models the conformation tensor can be defined as the second moment

$$C_{ij} = \int Q_i Q_j \Psi \, dR \equiv \langle Q_i Q_j \rangle \tag{3.3.2}$$

the angular brackets denote the configuration space average $\langle \cdot \rangle = \int \cdot \Psi \, dR$, where Ψ is the distribution function (for more detail on the theory behind the distribution function used see [8] p.236-242). As a result the spring force can then be written in terms of the second moment, $\langle \mathbf{QQ} \rangle$.

$$F(\mathbf{Q}) = \frac{K}{1 - \frac{\langle Q^2 \rangle}{b^2}} \mathbf{Q} = \frac{K}{1 - \frac{\mathbf{trc}}{b^2}} \mathbf{Q} \tag{3.3.3}$$

This averaging process reduces the description of polymeric behaviour to the conformation tensor level. To generate the FENE-P model we require the strain energy density function to take the form

$$w(\rho, \mathbf{C}) = -\int_{\Omega} \left[\frac{1}{2} \alpha \rho K b^2 \ln \left(1 - \frac{\mathrm{tr}\mathbf{C}}{b^2} \right) \right] d\Omega \tag{3.3.4}$$

The Helmholtz free energy is then given by the expression

$$A = \int_{\Omega} a_0(\rho, T) + w(\rho, \mathbf{C}) - \frac{\alpha \rho k_b T}{2} \ln \left(\det \left[\frac{\mathbf{C} K}{\rho k_b T} \right] \right) d\Omega \tag{3.3.5}$$

Note that Eq.(3.3.4) is also known as the GENT model in the finite strain theory literature [45]. A further discussion of this and similar strain energy models for hyperelastic solids is given in Section 3.2. Taking the derivative of Eq. (3.3.4) we obtain

$$\frac{\delta w}{\delta \mathbf{C}} = \frac{1}{2} \alpha \rho K f(\mathrm{tr}\mathbf{C}) \mathbf{I} \tag{3.3.6}$$

where $f(\mathrm{tr}\mathbf{C})$ is defined by

$$f(\mathrm{tr}\mathbf{C}) = \frac{1}{1 - \frac{\mathrm{tr}\mathbf{C}}{b(T)^2}} \tag{3.3.7}$$

The relaxation tensor remains the same as for the Oldroyd-B model (Eq. (3.1.1))

$$\Lambda : \frac{\delta A}{\mathbf{C}} = \frac{1}{\lambda} f(\mathrm{tr}\mathbf{C})\mathbf{C} - \frac{G}{\lambda K(T)}\mathbf{I} \tag{3.3.8}$$

Substituting Eq. (3.3.8) into Eq.(2.3.9), the evolution equation for the conformation tensor can be written in the form

$$\overset{\triangledown}{\mathbf{C}} + (\nabla \cdot \mathbf{u})\mathbf{C} = -\frac{1}{\lambda}\left[f(\mathrm{tr}\mathbf{C})\mathbf{C} - \frac{k_b T}{K(T)}\mathbf{I} \right]$$

which can be simplified to

$$\lambda \overset{\triangledown}{\mathbf{C}} + \lambda(\nabla \cdot \mathbf{u})\mathbf{C} + \left[f(\mathrm{tr}\mathbf{C})\mathbf{C} - \frac{k_b T}{K(T)}\mathbf{I} \right] = 0 \tag{3.3.9}$$

The solvent and polymeric stresses are given by

$$\begin{aligned} \boldsymbol{\tau}_s &= 2\mu_s \mathbb{D} \\ \boldsymbol{\tau}_p &= G(f(\mathrm{tr}\mathbf{C})\mathbf{C} - \mathbf{I}) \end{aligned} \tag{3.3.10}$$

We can eliminate $\mathbf{C}$ to obtain a closed form constitutive equation

$$Z\boldsymbol{\tau}_p + \lambda \boldsymbol{\tau}_p - \lambda\left(\boldsymbol{\tau}_p + G\mathbf{I} \right)\frac{D \ln Z}{Dt} = 2\mu_p \mathbb{D} \tag{3.3.11}$$

where

$$Z = 1 + \frac{3}{b}\left(1 + \frac{1}{3G}\mathrm{tr}\boldsymbol{\tau}_p \right)$$

FENE-P performs relatively well as a polymer model for extensional flow problems [52][8][69]. FENE-CR is a variant of a closed form FENE model which can be obtained by modifying

Eq. (3.3.10) to

$$\begin{aligned} \boldsymbol{\tau}_s &= 2\mu_s \mathbb{D} \\ \boldsymbol{\tau}_p &= G f(\mathrm{tr}\mathbf{C})(\mathbf{C} - \mathbf{I}) \end{aligned} \tag{3.3.12}$$

where the function $f(\mathrm{tr}\mathbf{C})$ now multiplies both $\mathbf{C}$ and $\mathbf{I}$ in the constitutive equation. The closure of the FENE constitutive model represented by Eq. (3.3.12) has the advantage of ensuring that $\boldsymbol{\tau}_p = 0$ when $\mathbf{C} = \mathbf{I}$. Although beneficial this is not thermodynamically necessary (see [8] p.246) and modifications can be made to $f(\mathrm{tr}\mathbf{C})$ to achieve the same result. Further discussion of the appropriate forms of the dissipative bracket required to obtain Eq. (3.3.12) can be found in [8] p.242-246, although it is the author's understanding that we are unable to obtain Eq. (3.3.12) using both the standard Marrucci entropy (Eq. (2.3.1)) and strain energy given by Eq. (3.3.4).

3.3.2 The FENE-P-MP Model: Compressible Nonisothermal Dissipative Model

Recently, a new class of models has been proposed that predicts shear-thinning and extensional strain-hardening with the aim of reproducing computationally the levels of drag enhancement that are measured experimentally for the flow of Boger fluids past a sphere. Garduño et al. [34] proposed a new hybrid dissipative model based on a combination of FENE and White-Metzner models. An extensional viscosity that is strain-hardening was found to be a crucial component in the modelling. The viscosity ratio was also found to be an important factor for Boger fluids. The hybrid models were termed swanINNF(q). However, the proposed models are ad-hoc since they were developed to predict certain behaviour by modifying existing models through the inclusion of additional terms without properly addressing the underlying physics. This in turn makes it very difficult to generalise the new constitutive equations to compressible and nonisothemral flows. In this section we present the Mackay-Phillips class of dissipative viscoelastic models. Similar to the swanINNF(q) class a viscoelastic model base is required. In our case the base model depends on the strain energy density function, relaxation and dissipation tensors. The additional terms in the constitutive equation are derived using a nonzero **L** tensor as a source term in the bracket formulation. As a result we are able to derive models with similar rheological properties to swanINNF(q) whilst ensuring thermodynamic consistency and thus allowing generalisation to the modelling of nonisothermal compressible viscoelastic fluids.

In order to make quantitative comparisons with results in the literature we have chosen to present the Mackay-Phillips modification of the FENE-P model (FENE-P-MP). However, the Mackay-Phillips modification can be done to all viscoelastic constitutive equations that can be derived using the generalised bracket method. The resulting constitutive law is similar to swanINNFM(q)-FENE-P model of Garduño et al. [34]. Additional terms appear in the formulation as a result of being derived using the generalised bracket method and, although the additional terms do not play a significant role in viscometric flows, they may become important when predicting complex flows in 2D and 3D.

The strain energy for finitely extensible dumbbells is replaced by the nonlinear equation

$$W(\mathbf{C}) = \int_{\Omega} -\frac{nK(T)b(T)^2}{2T} \ln\left(1 - \frac{\mathrm{tr}\mathbf{C}}{b(T)^2}\right) d\Omega \tag{3.3.13}$$

where b is the square of the maximum extension of the dumbbell, which is taken to be temperature dependent. The Helmholtz free energy is given by

$$A = \int_{\Omega} \left[a_0(\rho, T) - \frac{\alpha\rho K(T)b(T)^2}{2T} \ln\left(1 - \frac{\mathrm{tr}\mathbf{C}}{b(T)}\right) - \frac{\alpha\rho k_b T}{2} \ln(\det\mathbf{C}) \right] d\Omega \tag{3.3.14}$$

The last term is the expression for the Boltzmann entropy. The expressions for $\mathbf{\Lambda}$ and $\mathbf{Q}$ remain the same as for the Maxwell models (Eq. (3.1.22) and (3.1.23)). Consider the following nonzero expression for the non-affine tensor, **L**,

$$L_{ijkl} = \frac{\psi(\dot{\epsilon})}{2} \left\{ C_{ik}\delta_{jl} + C_{il}\delta_{jk} + C_{jk}\delta_{il} + C_{jl}\delta_{ik} \right\} \tag{3.3.15}$$

where

$$\psi(\dot{\epsilon}) = \frac{\phi(\dot{\epsilon}) - 1}{2}, \qquad \phi(\dot{\epsilon}) = \cosh(\lambda_D \dot{\epsilon}) \tag{3.3.16}$$

and

$$\dot{\epsilon} = 3I_3(\mathbb{D})/I_2(\mathbb{D}) \tag{3.3.17}$$

is the generalised extension rate. The tensor $\mathbf{L}$, associated with non-affine motion (stick/slip) within the system, is a crucial ingredient in enabling the model to capture both shear-thinning and strain-hardening behaviour. Through modelling in this way we are able to deduce that strain-hardening effects in the fluid are the result of nonlinear interactions between the conformation tensor and velocity gradient fields. Specifically, polymer chains 'stick' with respect to the solvent around them due to polymer chain entanglement. It can also be noted that for, small values of $\dot{\epsilon}$, ϕ can be approximated by taking the truncated Taylor expansion

$$\cosh(\lambda_D \dot{\epsilon}) \approx 1 + \frac{(\lambda_D \dot{\epsilon})^2}{2} \tag{3.3.18}$$

The evolution equation for the conformation tensor is given by

$$\lambda(T)\left[\overset{\triangledown}{\mathbf{C}} + (\nabla \cdot \mathbf{u})\mathbf{C}\right] = -\left[f(\mathrm{tr}\mathbf{C})\mathbf{C} - \frac{G(T)}{\alpha\rho K(T)}\mathbf{I}\right] + \lambda(T)\psi(\dot{\epsilon})[\mathbf{C}\cdot\mathbb{D} + \mathbb{D}\cdot\mathbf{C}] \tag{3.3.19}$$

and the expression for the extra stress is

$$\mathbb{T} = 2\mu_s(T)\mathbb{D} + \kappa'(T)(\nabla\cdot\mathbf{u})\mathbb{I} + \frac{\phi(\dot{\epsilon})\mu_p(T)}{\lambda(T)}(f(\mathrm{tr}\mathbf{C})\mathbf{C} - G(T)\mathbf{I}) \tag{3.3.20}$$

Note that, unlike the Oldroyd-B/UCM model this expression is nonlinear in $\mathbf{C}$. The governing equations in terms of the solvent and polymeric contributions to the extra stress $\mathbb{T}$ are given by

$$\begin{aligned} \boldsymbol{\tau}_s &= 2\mu_s(T)\mathbb{D} + \kappa_s'(T)(\nabla \cdot \mathbf{u})\mathbf{I} \\ (Z + \lambda(T)\nabla \cdot \mathbf{u})\boldsymbol{\tau}_p + \lambda(T) \overset{\triangledown}{\boldsymbol{\tau}}_p - \lambda(T)\left(\boldsymbol{\tau}_p + G(T)\mathbf{I}\right)\frac{D \ln Z}{Dt} & \\ -\lambda(T)\psi(\dot{\epsilon})[\boldsymbol{\tau}_p \cdot \mathbb{D} + \mathbb{D} \cdot \boldsymbol{\tau}_p] &= 2\phi(\dot{\epsilon})\mu_p(T)\left((\psi(\dot{\epsilon}) + 1)\mathbb{D} - \frac{1}{2}(\nabla \cdot \mathbf{u})\mathbf{I}\right) \end{aligned} \tag{3.3.21}$$

where

$$Z = 1 + \frac{3}{b(T)}\left(1 + \frac{1}{3G(T)}\mathrm{tr}\boldsymbol{\tau}_p\right)$$

The constitutive equations represented by Eq. (3.3.21) is the bracket generated equivalent of the swanINNFM(q)-FENE-P base model. The key difference between the two models is that, by using a non zero $\mathbf{L}$ tensor, the additional terms in the constitutive equation can be justified in a manner consistent with the microscopic model outlined in Chapter 2. Additionally, when $\lambda_D = 0$ ($\phi = 1$) we recover the nonisothermal FENE-P constitutive equation.

Eq. (3.3.21) is nonlinear in $\boldsymbol{\tau}_p$ making analytical solutions very difficult to obtain for non-trivial flow problems. Models such as (3.3.21) are among the class of strong thermodynamically consistent models. By insisting that the fluid parameters such as viscosity and relaxation time are not directly dependent on the rate-of-strain tensor, but rather indirectly by use of the stick/slip tensor, we ensure that the models satisfy both thermodynamic (i.e. corresponding to a non-negative entropy production) and mathematical (i.e. giving rise to evolutionary governing equations) admissibility criteria [8]. Leygue et al. [56] used a nonzero $\mathbf{L}$ tensor to model polymer-chain entanglement and so modelling strain-hardening in this way suggests that polymer-polymer entanglement may be the mechanism behind the observed drag behaviour. However, as Boger fluids are *dilute* we assume that polymer-polymer interaction has a negligible effect on the flow. The observed strain-hardening might be due to other nonlinear elastic behaviour which can only be approximated when using the modelling assumptions of the generalised bracket method. As with any model for viscoelastic fluids there are limitations that must be discussed. The main concern is that the definition of the generalised extension rate as defined by Eq. (3.3.17) is unsuitable for 3D planar extension flows as independence of strain-rate in one axis results in $I_3(\mathbb{D}) = 0$. However a solution can be found by using a 2D approximation and instead using the equation

$$\dot{\epsilon} = 6\frac{\mathbb{D}_{xx}\mathbb{D}_{yy} - \mathbb{D}_{xy}^2}{\mathbb{D}_{xx}^2 + \mathbb{D}_{yy}^2 + 2\mathbb{D}_{xy}^2}, \tag{3.3.22}$$

assuming 2D flow independent of the z-direction. In chapters 4 we present numerical schemes for solving the constitutive equations derived in this chapter for benchmark viscoelastic flow problems. However, first we will present the viscometric data of the models presented thus far.

3.4 Viscometric Behaviour

When investigating a particular constitutive model of a viscoelastic fluid, it important to look at its behaviour under simple types of flow, where the velocity field is known. From these we can compare characteristic behaviour of models.

3.4.1 Shear/Extensional Viscosities & Normal Stress Differences

Shear Viscosity

The shear viscosity (or shear-rate dependent viscosity), $\eta(\dot{\gamma})$, is given by the ratio of the shear stress to the shear rate

$$\eta_{shear}(\dot{\gamma}) = \frac{\sigma_{xy}(t)}{\dot{\gamma}}. \tag{3.4.1}$$

where

$$\dot{\gamma} = \frac{\partial \mathbf{u}}{\partial y} \tag{3.4.2}$$

is the shear rate with units s^{-1}. For a Newtonian fluid the shear viscosity is simply the constant dynamic viscosity of the fluid

$$\sigma_{xy}(t) = \eta_0 \dot{\gamma}_{xy}. \tag{3.4.3}$$

For non-Newtonian fluids in general, this is replaced by

$$\sigma_{xy}(t) = \eta_{shear}(\dot{\gamma}) \dot{\gamma}_{xy}, \tag{3.4.4}$$

where $\eta_{shear}(\dot{\gamma})$ is the apparent shear viscosity and $\dot{\gamma} = |\dot{\gamma}_{xy}|$ is the shear rate. We define the zero-shear viscosity, η_0, and infinite-shear viscosity, η_∞ are the viscosities at the limit of $\dot{\gamma}$ tending to 0 and ∞, respectively. Many Non-Newtonian fluids display shear thinning where $\eta_{shear}(\dot{\gamma}) < \eta_0$ when $\dot{\gamma} > 0$. We nondimensionalise the shear viscosity using so that

$$\eta_{shear}(\dot{\gamma}) \rightarrow \frac{\eta_{shear}(\dot{\gamma})}{\mu_0}, \tag{3.4.5}$$

where $\mu_0 = \mu_p + \mu_s$ is the total (zero-shear) viscosity.

Normal Stresses

The first and second normal stress differences are so-called viscometric functions that are associated with non-Newtonian behaviour

$$\begin{aligned} \sigma_{xx} - \sigma_{yy} &= N_1(\dot{\gamma}), \\ \sigma_{yy} - \sigma_{zz} &= N_2(\dot{\gamma}). \end{aligned} \tag{3.4.6}$$

We nondimensionalise the normal stresses using the total viscosity and relaxation time

$$N_1(\dot{\gamma}) \rightarrow \frac{\lambda N_1(\dot{\gamma})}{\mu_0}, \qquad N_2(\dot{\gamma}) \rightarrow \frac{\lambda N_2(\dot{\gamma})}{\mu_0}, \tag{3.4.7}$$

Extensional Viscosity

The extensional viscosity is given by the ratio of first normal stress difference to extension rate, $\dot{\epsilon}$ (with units s^{-1})

$$\eta_{ext}(\dot{\epsilon}) = \frac{N_1(\dot{\gamma})}{\dot{\epsilon}} = \frac{\sigma_{xx} - \sigma_{yy}}{\dot{\epsilon}} \tag{3.4.8}$$

which can be thought of as fluid's resistance to extensional deformation. The total viscosity, μ_0, is used to scale the extensional viscosity results

$$\eta_{ext}(\dot{\epsilon}) \rightarrow \frac{\eta_{ext}(\dot{\epsilon})}{\mu_0}, \tag{3.4.9}$$

3.4.2 Viscometric Functions for the Oldroyd-B fluid

Steady Simple Shear

For steady simple shear flow $\mathbf{u} = (u, v, w) = (\dot{\gamma}_{xy} y, 0, 0)$ we are able to reduce the constitutive laws for viscoelastic fluids to a system of algebraic equations. For the Oldroyd-B fluid specifically we can solve the equations directly to obtain

$$\begin{aligned} \tau^p_{xx} &= 2\mu_p \lambda \dot{\gamma}^2 \\ \tau^p_{xy} &= \mu_0 \dot{\gamma} \\ \tau^p_{yy} &= 0 = \tau^p_{zz} \end{aligned} \tag{3.4.10}$$

where $\mu_0 = \mu_p + \mu_s$. As displayed in Fig. 3.1 an Oldroyd-B fluid displays constant shear viscosity, a quadratic first normal stress difference and a zero second normal stress difference.

Uniaxial Extension

Consider uniaxial extensional flow $\mathbf{u} = (\dot{\epsilon} x, -\frac{\dot{\epsilon}}{2} y, -\frac{\dot{\epsilon}}{2} z)$ where $\dot{\epsilon}$ is the (constant) extensional rate. For an Oldroyd-B fluid we are able to solve the equations directly to obtain

$$\begin{aligned} \lambda \dot{\tau}^p_{xx} + \tau^p_{xx} - 2\lambda \dot{\epsilon} \tau^p_{xx} &= 2\mu_p \dot{\epsilon} \\ \lambda \dot{\tau}^p_{xy} + \tau^p_{xy} - \frac{\lambda \dot{\epsilon}}{2} \tau^p_{xy} &= 0 \\ \lambda \dot{\tau}^p_{yy} + \tau^p_{yy} + \lambda \dot{\epsilon} \tau^p_{yy} &= -\mu_p \dot{\epsilon} \\ \lambda \dot{\tau}^p_{zz} + \tau^p_{zz} + \lambda \dot{\epsilon} \tau^p_{zz} &= -\mu_p \dot{\epsilon} \end{aligned} \tag{3.4.11}$$

In the steady-state

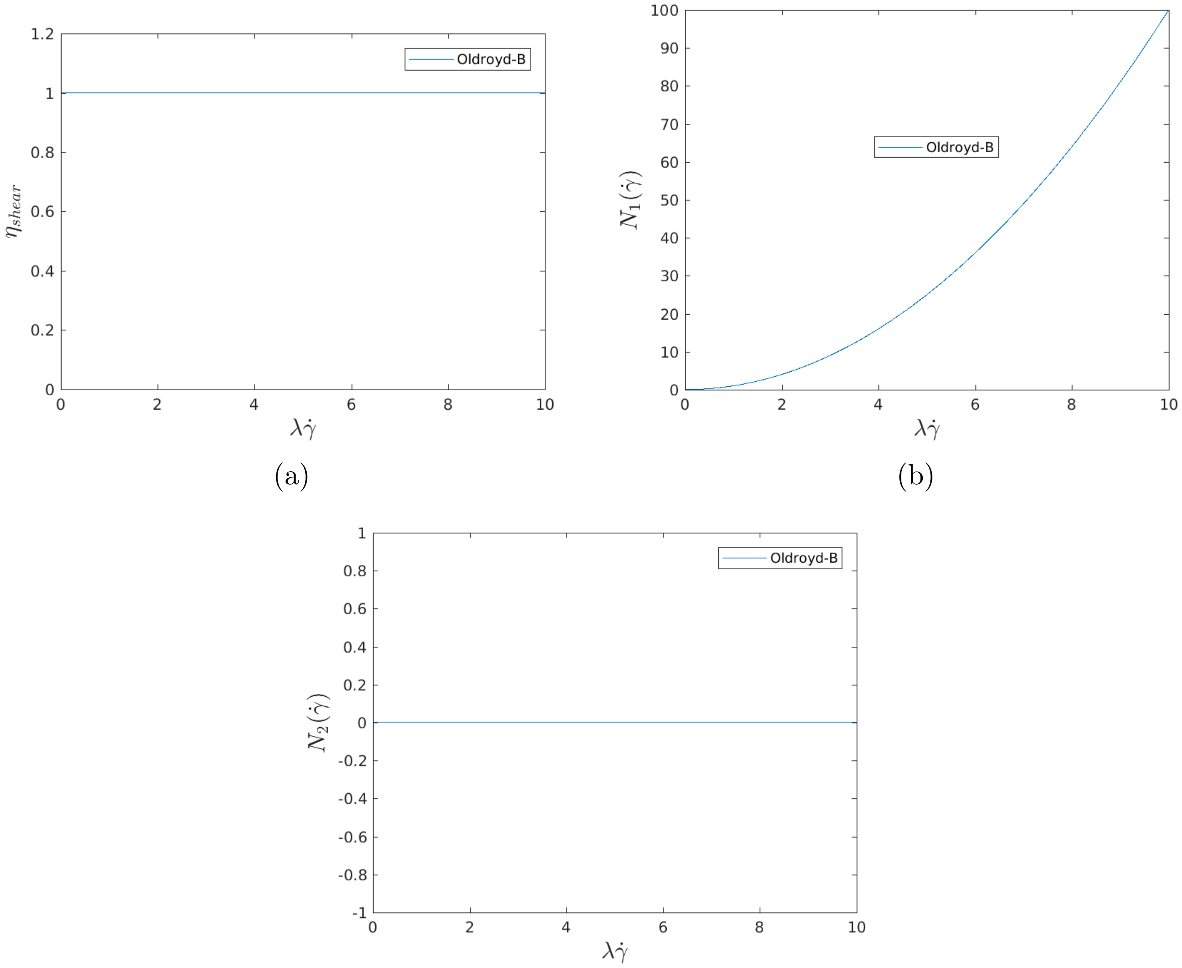

(a) (b)

(c)

Figure 3.1: (a) Shear viscosity, (b) first and (c) second normal stress difference for an Oldroyd-B fluid. $\mu_p/\mu_0 = 0.5$, $\mu_s/\mu_0 = 0.5$, $\lambda = 1s$.

$$\begin{aligned} \tau^p_{xx} &= 2\mu_p\dot{\epsilon}\frac{1}{1-2\lambda\dot{\epsilon}} \\ \tau^p_{xy} &= 0 \\ \tau^p_{yy} &= \tau^p_{zz} = -\mu_p\dot{\epsilon}\frac{1}{1+\lambda\dot{\epsilon}} \end{aligned} \tag{3.4.12}$$

with extensional viscosity

$$\eta_{ext} = 2\mu_p \frac{1}{1 - 2\lambda\dot{\epsilon}} + \mu_p \frac{1}{1 + \lambda\dot{\epsilon}} \tag{3.4.13}$$

The extensional viscosity blows up at $\dot{\epsilon} = \frac{1}{2\lambda}$ as shown in Fig. 3.2. This is of course an unphysical prediction and as a result the Oldroyd-B model can perform poorly when applied to extensional flow problems.

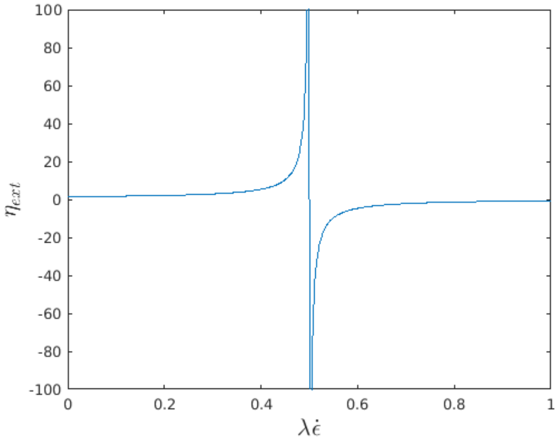

Figure 3.2: Extensional viscosity of the Oldroyd-B fluid, $\mu_s/\mu_0 = \mu_p/\mu_0 = 0.5$, $\lambda = 1s$.

3.4.3 Viscometric Functions for a Giesekus Fluid

Steady Simple Shear

For the Giesekus model, the constitutive equation is given by Eq. (3.1.34) can be reduced to a system of equations

$$\begin{aligned}
&\tau^p_{xx} - 2\lambda\dot{\gamma}\tau^p_{xy} + \frac{\lambda\alpha}{\mu_p}(\tau^p_{xx}\tau^p_{xx} + \tau^p_{xy}\tau^p_{xy}) = 0\\
&\tau^p_{xy} - \lambda\dot{\gamma}\tau^p_{yy} + \frac{\lambda\alpha}{\mu_p}(\tau^p_{xx}\tau^p_{xy} + \tau^p_{xy}\tau^p_{yy}) = \mu_p\dot{\gamma}\\
&\tau^p_{yy} + \frac{\lambda\alpha}{\mu_p}(\tau^p_{yy}\tau^p_{yy} + \tau^p_{xy}\tau^p_{xy}) = 0\\
&\tau^p_{zz} + \frac{\lambda\alpha}{\mu_p}(\tau^p_{zz}\tau^p_{zz}) = 0
\end{aligned} \tag{3.4.14}$$

As shown in Fig. 3.3 the Giesekus fluid displays increasing shear thinning as α is increased and a first normal that is sub-quadratic and decreasing with α. The second normal stress difference also decreases with α.

Uniaxial extension

Substituting $\mathbf{u}$ into Eq. (3.1.34) we obtain the following set of algebraic equations.

$$\begin{aligned}
&\tau^p_{xx} - 2\lambda_1\dot{\epsilon}\tau^p_{xx} + \frac{\lambda\alpha}{\mu_p}(\tau^p_{xx}\tau^p_{xx} + \tau^p_{xy}\tau^p_{xy}) = 2\mu_p\dot{\epsilon}\\
&\tau^p_{xy} - \frac{\lambda_1\dot{\epsilon}}{2}\tau^p_{xy} + \frac{\lambda\alpha}{\mu_p}(\tau^p_{xx}\tau^p_{xy} + \tau^p_{xy}\tau^p_{yy}) = 0\\
&\tau^p_{yy} + \lambda_1\dot{\epsilon}\tau^p_{yy} + \frac{\lambda\alpha}{\mu_p}(\tau^p_{yy}\tau^p_{yy} + \tau^p_{xy}\tau^p_{xy}) = -\mu_p\dot{\epsilon}\\
&\tau^p_{zz} + \lambda_1\dot{\epsilon}\tau^p_{zz} + \frac{\lambda\alpha}{\mu_p}(\tau^p_{zz}\tau^p_{zz}) = -\mu_p\dot{\epsilon}
\end{aligned} \tag{3.4.15}$$

We observe that the Giesekus model does not suffer from the same blow-up issue as the Oldroyd-B model does and predicts finite extensional viscosity

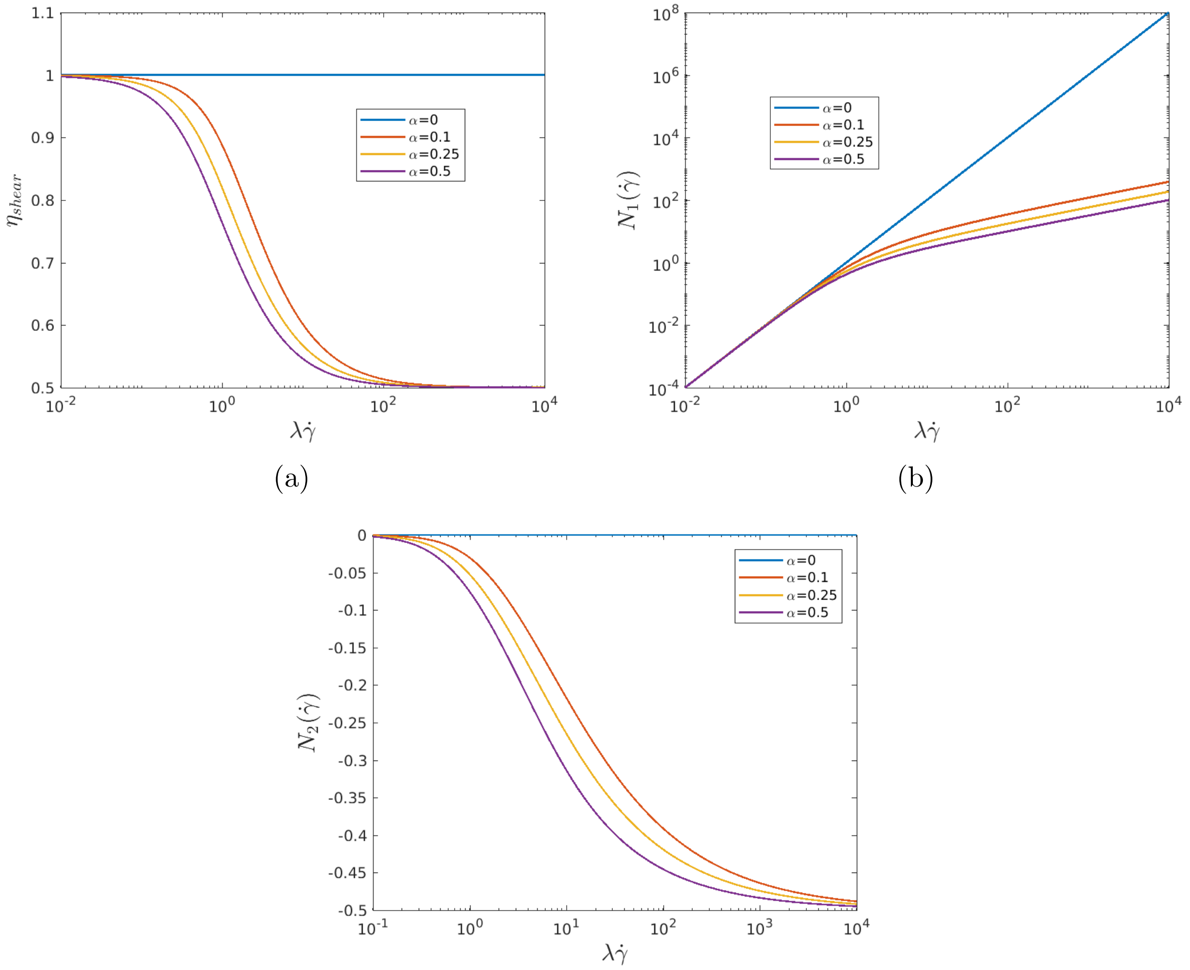

(a)

(b)

(c)

Figure 3.3: (Nondimensionalised) shear viscosity, $\eta_{shear}(\dot{\gamma})$, first normal stress $N_1(\dot{\gamma})$ (left) and log scale (right) for steady shear flow, $\lambda = 1s$, $\mu_p/\mu_0 = 0.5$, $\mu_s/\mu_0 = 0.5$.

3.4.4 Viscometric Functions for a FENE-P Fluid

Steady Simple Shear

Substituting **u** into the steady-state form of Eq. (3.3.10) we obtain the following system

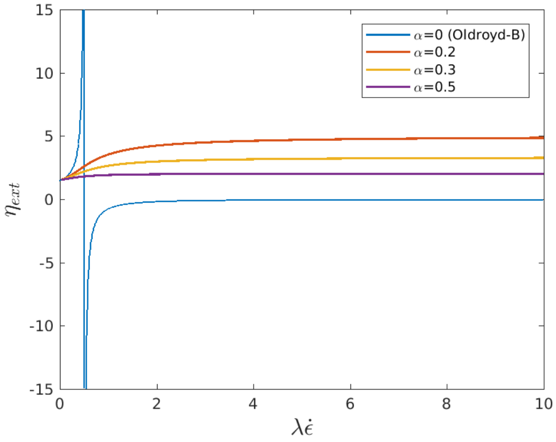

Figure 3.4: Extensional viscosity of the Giesekus fluid $\mu_s/\mu_0 = \mu_p/\mu_0 = 0.5$

$$\begin{aligned}
&-2\lambda\dot{\gamma}C_{xy} + f(\mathrm{tr}\mathbf{C})C_{xx} - 1 = 0 \\
&-\lambda\dot{\gamma}C_{xy} + f(\mathrm{tr}\mathbf{C})C_{xy} = 0 \\
&-\lambda\dot{\gamma}C_{yy} + f(\mathrm{tr}\mathbf{C})C_{yy} - 1 = 0 \\
&-\lambda\dot{\gamma}C_{zz} + f(\mathrm{tr}\mathbf{C})C_{zz} - 1 = 0
\end{aligned} \tag{3.4.16}$$

and

$$\begin{aligned}
\tau^p_{xx} &= \frac{\mu_p}{\lambda}(f(\mathrm{tr}\mathbf{C})C_{xx} - 1) \\
\tau^p_{xy} &= \frac{\mu_p}{\lambda}f(\mathrm{tr}\mathbf{C})C_{xy} \\
\tau^p_{yy} &= \frac{\mu_p}{\lambda}(f(\mathrm{tr}\mathbf{C})C_{yy} - 1)
\end{aligned} \tag{3.4.17}$$

Similar to the Oldroyd-b model (and unlike Giesekus model) the second normal stress difference is identically zero. Another important thing to note is that the zero-shear limit of the viscosity and first normal stress difference increases with b.

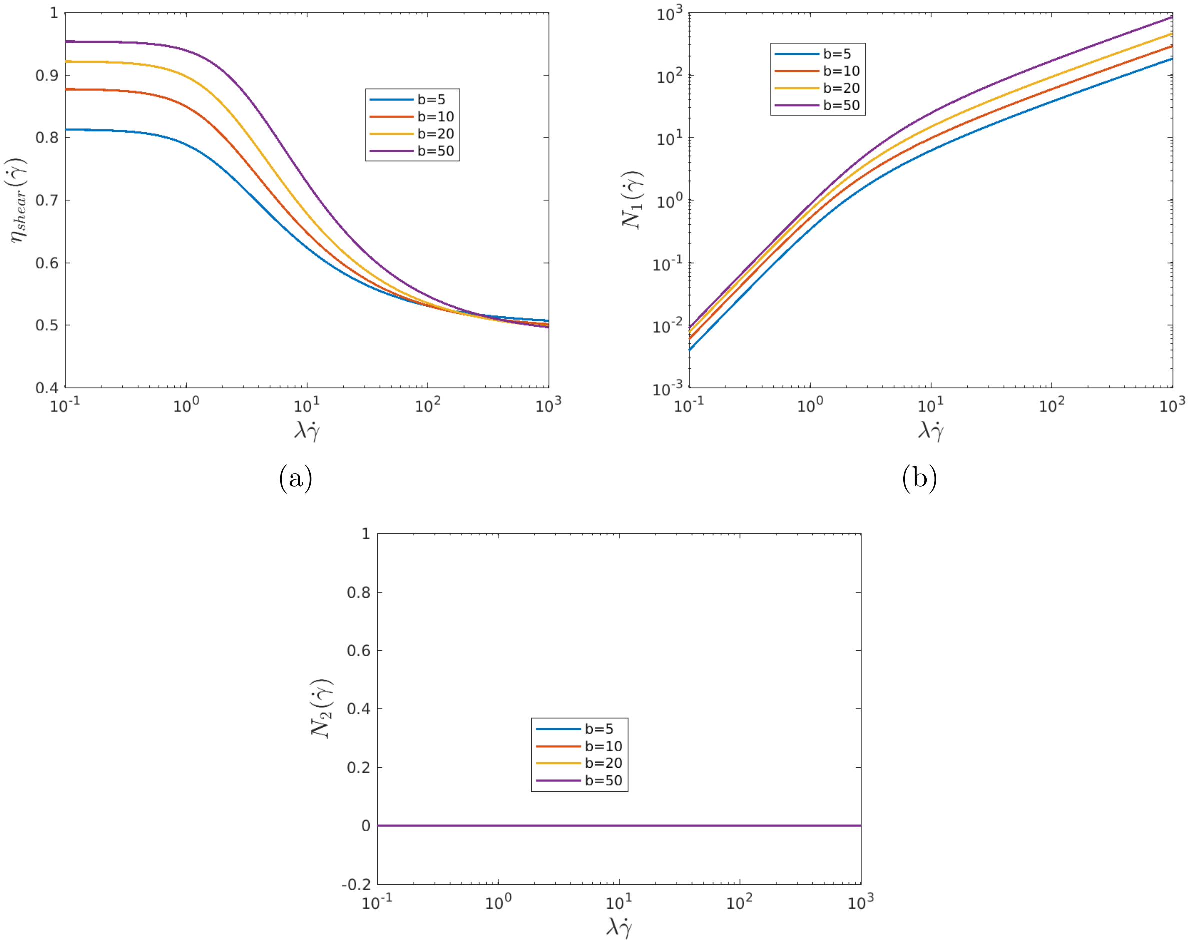

(a) (b)

(c)

Figure 3.5: (a) Shear viscosity, (b) first and (c) second normal stress difference for an FENE-P fluid, $\mu_s/\mu_0 = 0.5$, $\mu_p/\mu_0 = 0.5$, $\lambda = 1s$.

Uniaxial Extension

Substituting $\mathbf{u}$ into Eq. (3.3.10) we obtain the following set of equations for the polymeric stress, $\boldsymbol{\tau}_p$

$$\begin{aligned}
&\lambda\dot{C}_{xx} - 2\lambda\dot{\epsilon}C_{xy} + f(\mathrm{tr}\mathbf{C})C_{xx} - 1 = 0\\
&\lambda\dot{C}_{xy} - \frac{\lambda\dot{\epsilon}}{2}C_{xy} + f(\mathrm{tr}\mathbf{C})C_{xy} = 0\\
&\lambda\dot{C}_{yy} + \lambda\dot{\epsilon}C_{yy} + f(\mathrm{tr}\mathbf{C})C_{yy} - 1 = 0\\
&\lambda\dot{C}_{zz} + \lambda\dot{\epsilon}C_{zz} + f(\mathrm{tr}\mathbf{C})C_{zz} - 1 = 0
\end{aligned} \tag{3.4.18}$$

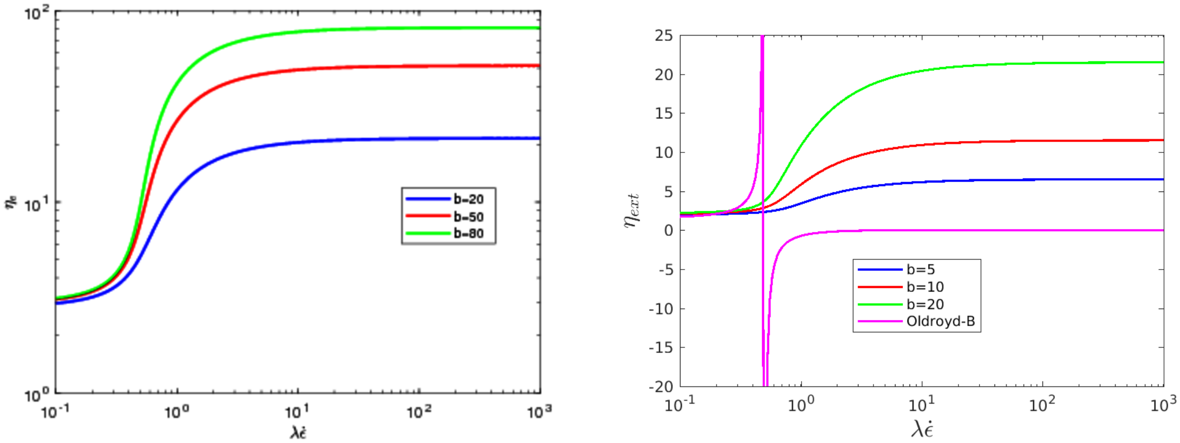

(a) (b)

Figure 3.6: Extensional viscosity of the FENE-P fluid: (a) loglog scale $b = 20, 50, 80$ and (b) comparison with Oldroyd-B.for $b = 5, 10, 20$.

Then the polymeric stress is given by $\boldsymbol{\tau}_p = \mu/\lambda[f(\mathrm{tr}\mathbf{C})\mathbf{C} - \mathbf{I}]$. Fig. 3.6 shows the extensional viscosity for different values of b.

3.4.5 Viscometric Functions for a FENE-P-MP Fluid

Steady Simple Shear

The FENE-P-MP model displays the same shear viscosity and normal stresses as $\phi(\dot{\epsilon}) = 0$ for steady-simple shear and the FENE-P-MP reduces to the FENE-P model and so the $\eta_{shear}(\dot{\gamma})$, $N_1(\dot{\gamma})$ and $N_2(\dot{\gamma})$ are identical and are displayed in Fig. 3.5.

Uniaxial extension

By substituting **u** into (3.3.21) we obtain the following system of equations

$$\begin{aligned}
&Z\tau_{xx} - 2\dot{\epsilon}\psi(\dot{\epsilon})\lambda\tau_{xx} - 2\phi(\dot{\epsilon})\psi(\dot{\epsilon})\mu_p\dot{\epsilon} = 0\\
&Z\tau_{xy} - \frac{\dot{\epsilon}}{2}\psi(\dot{\epsilon})\lambda\tau_{xy} = 0\\
&Z\tau_{yy} + \dot{\epsilon}\psi(\dot{\epsilon})\lambda\tau_{yy} + \phi(\dot{\epsilon})\psi(\dot{\epsilon})\mu_p\dot{\epsilon} = 0\\
&Z\tau_{zz} + \dot{\epsilon}\psi(\dot{\epsilon})\lambda\tau_{zz} + \phi(\dot{\epsilon})\psi(\dot{\epsilon})\mu_p\dot{\epsilon} = 0
\end{aligned} \tag{3.4.19}$$

where

$$Z = 1 + \frac{3}{b}\left(1 + \frac{\lambda}{3\phi(\dot{\epsilon})\mu_p}\boldsymbol{\tau}_p\right) \tag{3.4.20}$$

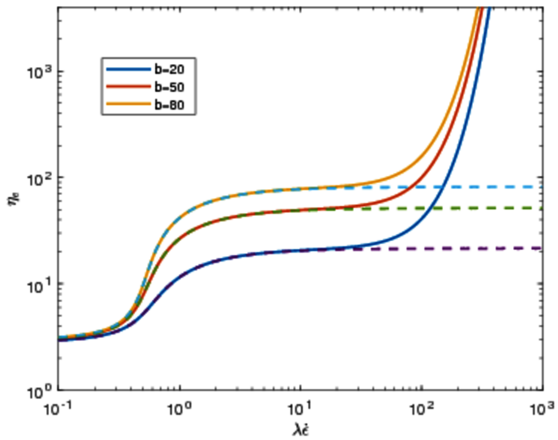

Figure 3.7: Extensional viscosity for the FENE-P-MP model $b = 20, 50, 80$, $\mu_p/\mu_0 = 0.5$, $\mu_s/\mu_0 = 0.5$, $\lambda_D = 0.05$

Fig. 3.7 shows the behaviour of η_e for different values of b with $\lambda_D = 0.05$. Even at small values the dissipation parameter has a significant effect on the extensional viscosity. After an initial increase when $10^{-1} \leq \lambda\dot{\epsilon} \leq 10^0$ a secondary increase in viscosity is observed when $\lambda\dot{\epsilon} > 10^1$. There are, of course limits on the applicability of this models to flows with very high extension rates. Whilst secondary increases in extensional viscosities are observed in Boger

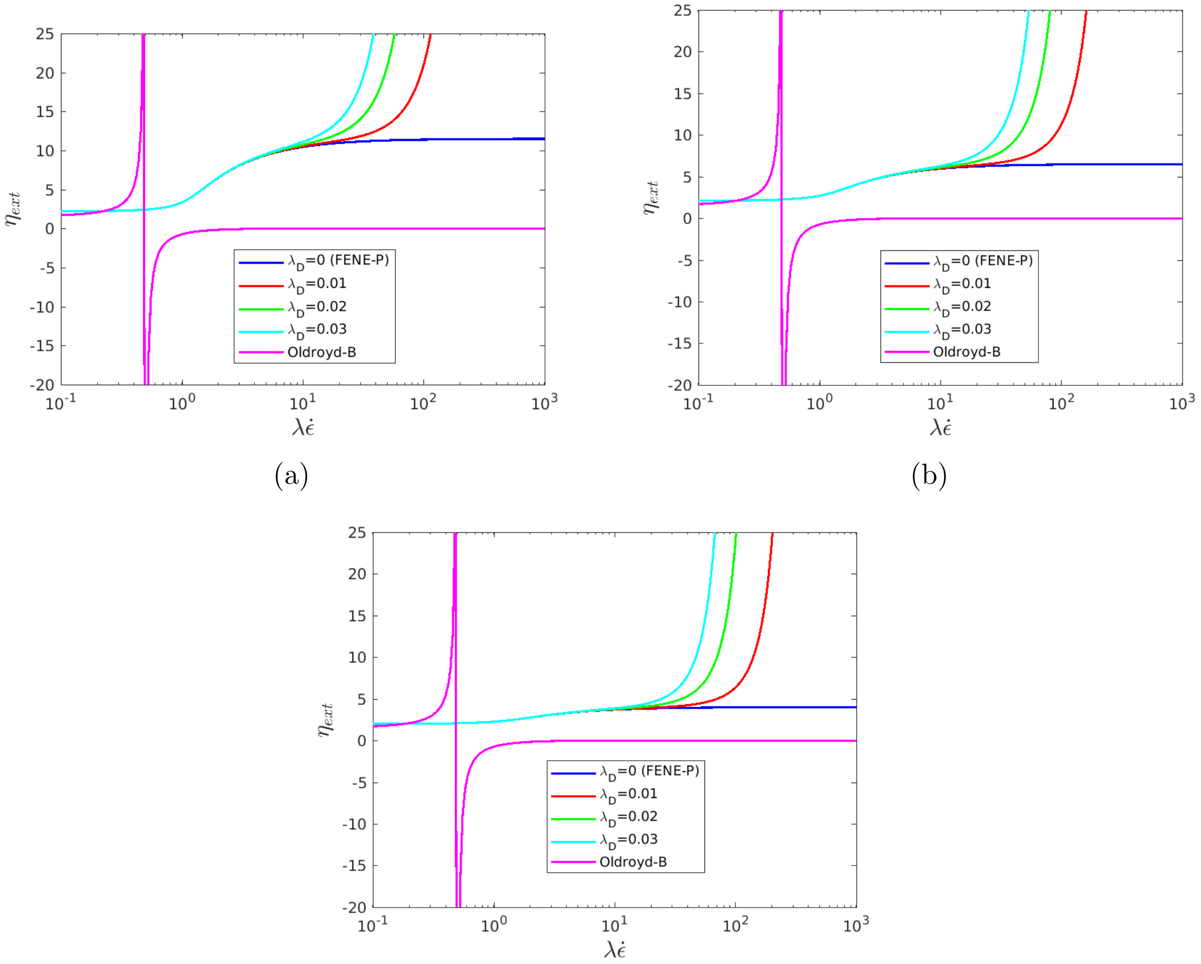

(a)

(b)

(c)

Figure 3.8: Extensional viscosity for the FENE-P-MP model showing the effect of the dissipation parameter λ_D (a) $b = 20$, (b) $b = 10$, (c) $b = 5$, $\mu_p/\mu_0 = 0.5$, $\mu_s/\mu_0 = 0.5$, $\lambda = 1s$

fluids, the FENE-P-MP extensional behaviour may indeed overshoot observed extensional viscosities in Boger fluids. However, as pointed out by Garduño, Tahmaddon-Jahromi and Webster the additional extensional viscosity effects of the dissipation parameter, λ_D, are necessary for capturing drag behaviour of Boger fluid flow past a sphere [34, 35] (see Chapter 7).

3.5 Summary

Models derived using the generalised bracket formulation have been presented. By substitution of the derivatives of specific Helmholtz free energy and dissipative tensor formulations we have derived generalised forms of the Oldroyd-B and Giesekus models. We have also explored nonlinear functions for the elastic energy, using a Mooney-Rivlin type nonlinear strain energy formulation to derive the Leonov model.

The main contribution from this chapter has been the derivation of the FENE-P-MP model (Eq. (3.3.21)) which provides an alternative to the swanINNF(q)-FENE-P model by Garduño and Webster [34, 35]. This should be a welcome contribution to the literature as it begins to bridge the gap between theoretical framework of the generalised bracket method with the predictive power of the phenomenological swanINNF(q) class of models. It also presents the models in a more general form allowing for the application of these constitutive equations to compressible and nonisothermal flow problems. Furthermore, the fact that the dissipative models similar to swanINNF(q) can be derived within the generalised bracket formulation testifies to the broad range viscoelastic constitutive equations that fit within the framework.

Chapter 4

Numerical Method

In chapters 2 and 3 we presented thermodynamically consistent models for viscoelastic fluids, derived using the generalised bracket method. For most nontrivial 2D flows, appropriate numerical methods need to be used to obtain accurate solutions over a range of fluid parameter inputs. The most popular methods for simulating viscoelastic flows are finite volume (FVM), finite element (FEM) and spectral element (SEM) methods. The ultimate goal of these numerical methods is to discretise the problem in both space and time so that the governing system of PDEs can be converted into to a system of algebraic equations. These can then be solved efficiently via available numerical linear algebra techniques.

The finite element method is one of the most popular tools for numerically simulating viscoelastic flows in enclosed geometries. However, the method also presents several numerical difficulties. The constitutive equation is highly nonlinear, with convective and deformation terms that may lead to both local and global oscillations in the numerical approximation. Furthermore, even in the case of smooth solutions it is necessary to satisfy additional compatibility conditions between the velocity and stress interpolation in order to control velocity gradients. Very few elements satisfy these compatibility requirements for velocity-pressure and stress-velocity.

The numerical method presented in this chapter will be used to solve the benchmark 2D flow problems presented in chapters 5, 6 and 7.In Sec. 4.1 we nondimensionalise the general set of

governing equations (Eq. (2.3.6)-(2.3.10)), introducing the Weissenberg, Mach and Reynolds numbers. In Sec. 4.2 we introduce the Taylor-Galerkin temporal discretisation followed by the spatial discretisation (FEM) and weak formulation of the governing equations in Sec. 4.3 and 4.4 respectively. In Sec. 4.5 we motivate the use of numerical stabilisation methods by discussing the high Weissenberg number problem. In Sec. 4.6 we introduce the specific stabilisation methods we will use. The discretised system of equations, algebraic solution methods and implementation are presented in Sections 4.7, 4.8 and 4.9 respectively.
A convergence test for the stabilised numerical scheme is then presented in Sec. 4.10 followed by a summary of the chapter in Sec. 4.11.

4.1 Nondimensionalisation of the Governing Equations

Several fluid parameters appear in the formulation of constitutive models when using the generalised bracket method. Nondimensionalisation is required to reduce the number of parameters in order to make the analysis of the equations easier. For compressible viscoelastic flows three important parameters are the Reynolds number, a measure of the flow inertia, the Mach number, a measure of the flow compressibility, and the Weissenberg number, a measure of the flow elasticity defined

$$Re = \frac{\rho_0 U L}{\mu_0}, \qquad We = \frac{\lambda_0 U}{L} \qquad , Ma = \frac{U}{c_0} \tag{4.1.1}$$

where L is a characteristic length, U ia a characteristic velocity, μ_0 the zero shear total viscosity, λ_0 the relaxation time and c_0 is the compression wave propagation speed of the fluid. For the benchmark problems considered in chapters 5, 6 and 7, we only consider flows at low Mach number ($Ma < 0.2$), where the assumption of weak compressibility is justified [51, 90]. As such, we can make the following assumptions: First, the equation of state coupling density, pressure and temperature is well-approximated by a linear anisothermal model

$$\frac{\partial p}{\partial \rho} = c_0^2 \left(1 + \tilde{\alpha} \frac{T - T_0}{T_0} \right) \tag{4.1.2}$$

where $\tilde{\alpha}$ is a nonisothermal parameter (see Bollada & Phillips [12] for further discussion on the applicability of (4.1.2)).

Secondly, the contribution rate of change of internal energy, $u = u(\rho, T)$ is dominated by the rate of change of temperature rather than density i.e $\frac{Du}{Dt}\Big|_{\rho} \gg \frac{Du}{Dt}\Big|_{T}$ which means that the energy equation can be simplified

$$\frac{Du(\rho, T)}{Dt} = \rho C_p \frac{DT}{Dt} + \frac{Du}{Dt}\Big|_{T} \approx \rho C_p \frac{DT}{Dt} \tag{4.1.3}$$

Thus the energy equation becomes an equation governing temperature evolution within the fluid (see [25] p.122 for further discussion of the approximation given by (4.1.3)). The general set of governing equations are then given by

$$\begin{aligned}
&\rho \frac{D\mathbf{u}}{Dt} = -\nabla p + \mu_s \left(\nabla^2 \mathbf{u} + \frac{1}{3} \nabla (\nabla \cdot \mathbf{u}) \right) + \nabla \cdot \boldsymbol{\tau}_p + \mathbf{F} \\
&\frac{\partial \rho}{\partial t} + \nabla \cdot (\rho \mathbf{u}) = 0 \\
&\boldsymbol{\tau}_p = \mathbf{g}_1(\mathbf{C}, \mathbf{I}) \\
&\mathbf{C} + \lambda(\overset{\triangledown}{\mathbf{C}} + (\nabla \cdot \mathbf{u})\mathbf{C}) + \mathbf{g}_2(\mathbf{C}, \mathbb{D}) = \mathbf{I} \\
&\rho C_p \frac{DT}{Dt} = -\nabla \cdot \mathbf{q} + \mathbb{T} : \nabla \mathbf{u} - p \nabla \cdot \mathbf{u} \\
&\frac{\partial p}{\partial \rho} = c_0^2 \left(1 + \tilde{\alpha} \frac{T - T_0}{T_0} \right)
\end{aligned} \tag{4.1.4}$$

where

$$\mathbf{q} = -\kappa \nabla T \tag{4.1.5}$$

and functions $\mathbf{g}_1$ and $\mathbf{g}_2$ are determined by the model, specifically $w(\mathbf{C})$, $\boldsymbol{\Lambda}$ and $\mathbf{L}$. For example, in the case of Maxwell-type fluids $\mathbf{g}_1$ takes the form

$$\mathbf{g}_1(\mathbf{C},\mathbf{I}) = G\left(\frac{K(T)}{k_bT}\mathbf{C} - \mathbf{I}\right) \tag{4.1.6}$$

where $G = \mu_p(T)/\lambda(T)$. Note that in applications of Maxwell-type fluids in the following chapters it is implicitly assumed that $K(T) = k_bT$ so that we ensure $\mathbf{g}_1 = 0$ when $\mathbf{C} = \mathbf{I}$. The relaxation time, solvent and polymeric viscosity are functionally dependent on temperature. We use the viscosity model given by Wiest and Phan-Thien [94]

$$\mu_p(T) = \mu_{p,0}\exp(-A_{p,0}(T - T_0)/(T_h - T_0)) \tag{4.1.7}$$

where A_0 is the activation energy. In order to be consistent with Eq. (3.1.4) and (3.1.5) we define the relaxation time

$$\lambda(T) = \lambda_0\frac{\exp(-A_{p,0}(T - T_0)/(T_h - T_0))T_0}{T} \tag{4.1.8}$$

In Chapter 6 we also consider the extended White-Metzner model (Souvaliotis and Beris [81]), where the relaxation time and polymeric viscosity explicitly depend both on the conformation stress and temperature $\lambda = \lambda(\mathbf{C}, T)$, $\mu_p = \mu_p(\mathbf{C}, T)$.

To scale the state variables in governing equations, we introduce the dimensionless variables

$$\begin{aligned} \mathbf{u}^* &= \frac{\mathbf{u}}{U} \quad \mathbf{x}^* = \frac{\mathbf{x}}{L} \quad \rho^* = \frac{\rho}{\rho_0} \\ t^* &= \frac{tU}{L} \quad p^* = \frac{pL}{\mu_0 U} \quad \theta = \frac{T - T_0}{T_h - T_0} \\ \boldsymbol{\tau}_p^* &= \frac{L\boldsymbol{\tau}_p}{\mu_0 U} \quad \nabla^* = L\nabla \end{aligned} \tag{4.1.9}$$

where $T_h - T_0$ is the temperature scale of the flow. Using Eq. (4.1.9) we define the following nondimensional groups:

$$\begin{aligned} Re &= \frac{\rho_0 U L}{\mu_0} & We &= \frac{\lambda U}{L} \\ Ma &= \frac{U}{c_0} & \beta_v &= \mu_s/\mu_0 \\ Di &= \frac{\kappa}{\rho_0 C_v U L} & V_h &= \frac{U\mu_0}{\rho_0 C_v L (T_h - T_0)} \end{aligned} \tag{4.1.10}$$

In addition to the parameters defined in Eq. (4.1.1) we have also introduced two new nondimensional parameters that appear in the energy balance equation: the diffusion number Di, and the viscous heating number, V_h. The nondimensional expression for the polymeric viscosity is given by

$$\frac{\mu_p(T)}{\mu_s^0 + \mu_p^0} = (1 - \beta_v)\hat{\psi}(\theta) \tag{4.1.11}$$

and for the relaxation

$$\frac{\lambda(T)U}{L} = We\tilde{\psi}(\theta) \tag{4.1.12}$$

where

$$\hat{\psi}(\theta) = \exp(-A_0\theta) \qquad \tilde{\psi}(\theta) = \exp(-A_0\theta)[\theta(T_h - T_0)/T_0 + 1] \tag{4.1.13}$$

We have used the fact that

$$\lambda_0\left(\frac{T_0}{T}\right) = \lambda_0\left(\left[\frac{T_h - T_0}{T_0}\right]\theta + 1\right)$$

Substituting Eq. (4.1.10) into (4.1.4) and dropping the * notation, the governing equations can then be written in nondimensional form

$$
\begin{aligned}
& Re\rho\frac{D\mathbf{u}}{Dt} = -\nabla p + \left[\beta_v\left(\nabla^2\mathbf{u} + \frac{1}{3}\nabla(\nabla\cdot\mathbf{u})\right) + \nabla\cdot\boldsymbol{\tau}_p\right] + \mathbf{F} \\
& \frac{\partial\rho}{\partial t} + \nabla\cdot(\rho\mathbf{u}) = 0 \\
& \boldsymbol{\tau}_p = \mathbf{g}_1(\mathbf{C},\mathbf{I}) \\
& \mathbf{C} + We\tilde{\psi}(\theta)(\overset{\triangledown}{\mathbf{C}} + (\nabla\cdot\mathbf{u})\mathbf{C}) + \mathbf{g}_2(\mathbf{C},\mathbb{D}) = \mathbf{I} \\
& \rho\frac{D\theta}{Dt} = \nabla\cdot\tilde{\mathbf{q}} + V_h(\mathbb{T} : \nabla\mathbf{u} - p\nabla\cdot\mathbf{u}) \\
& \frac{\partial\rho}{\partial p} = \frac{Ma^2}{Re(1+\tilde{\alpha}\theta)}
\end{aligned}
\tag{4.1.14}
$$

For the incompressible case ($\nabla\cdot\mathbf{u} = 0$), $\rho = \rho_0$, the governing equations take the form

$$
\begin{aligned}
& Re\frac{D\mathbf{u}}{Dt} = -\nabla p + \left[\beta_v\nabla^2\mathbf{u} + \nabla\cdot\boldsymbol{\tau}_p\right] + \mathbf{F} \\
& \nabla\cdot\mathbf{u} = 0 \\
& \frac{D\theta}{Dt} = \nabla\cdot\tilde{\mathbf{q}} + V_h\mathbb{T} : \nabla\mathbf{u} \\
& \boldsymbol{\tau}_p = \mathbf{g}_1(\mathbf{C},\mathbf{I}) \\
& \mathbf{C} + We\tilde{\psi}(\theta)\,\overset{\triangledown}{\mathbf{C}} + \mathbf{g}_2(\mathbf{C},\nabla\mathbf{u}) = \mathbf{I}
\end{aligned}
\tag{4.1.15}
$$

The nondimensional form of the heat flux vector, $\mathbf{q}$ is given by

$$
\tilde{\mathbf{q}} = Di\nabla\theta \tag{4.1.16}
$$

Note: Alternative variable scaling and definitions of nondimensional parameters are used in Sec. 5.3. A description of the alternative nondimensionalisation is given in Sec. 5.3.4. Furthermore, the equations presented here are for reference so that the numerical scheme can be explained. For each of the three benchmark problems further assumptions apply and are stated when used.

4.2 Temporal Discretisation: Taylor-Galerkin Methods

Taylor-Galerkin methods were initially developed for solving convective transport problems for which the governing equations are hyperbolic [69]. The motivation for Taylor Galerkin methods is the desire to derive high-order accurate time-stepping schemes which can be used in conjunction with spatial discretisation methods. To demonstrate the ideas behind this method consider the following prototypical convective transport problem: Let $\phi = \phi(x)$, $x \in [a, b]$, $a, b \in \mathbb{R}$ be a scalar function satisfying

$$\frac{\partial \phi}{\partial t} + u\frac{\partial \phi}{\partial x} = 0 \tag{4.2.1}$$

where u is constant. Assuming ϕ is sufficiently differentiable in time the Taylor expansion up to second order is given by

$$\phi^{n+1} = \phi^n + \Delta t\frac{\partial \phi^n}{\partial t} + \frac{\Delta t^2}{2}\frac{\partial^2 \phi^n}{\partial t^2} + \mathcal{O}(\Delta t^2) \tag{4.2.2}$$

$$\frac{\phi^{n+1} - \phi^n}{\Delta t} + u\frac{\partial \phi^n}{\partial x} = 0 \qquad \text{First Order Approximation (Forward Euler)} \tag{4.2.3}$$

$$\frac{\phi^{n+1} - \phi^n}{\Delta t} + u\frac{\partial \phi^{n+1}}{\partial x} = 0 \qquad \text{First Order Approximation (Backward Euler)} \tag{4.2.4}$$

If we include the second order term, Eq. 4.2.2 can be rearranged to give

$$\frac{\partial \phi^n}{\partial t} = \frac{\phi^{n+1} - \phi^n}{\Delta t} - \frac{\Delta t}{2}\frac{\partial^2 \phi^n}{\partial t^2} + \mathcal{O}(\Delta t^2) \tag{4.2.5}$$

Using Eq. (4.2.1) into we can show that $\frac{\partial}{\partial t} = -u\frac{\partial}{\partial t}$. Therefore we can derive the second-order approximation

$$\frac{\phi^{n+1} - \phi^n}{\Delta t} + u\frac{\partial \phi^n}{\partial x} - \frac{\Delta t u^2}{2}\frac{\partial^2 \phi^n}{\partial x^2} = 0 \tag{4.2.6}$$

The second-order explicit scheme (4.2.6) can be rewritten as a predictor-corrector pair [69]. Thus an equivalent approximation to (4.2.1) is given by

$$\frac{\phi^{n+\frac{1}{2}} - \phi^n}{\Delta t/2} = -u\frac{\partial \phi^n}{\partial x} \tag{4.2.7}$$

$$\frac{\phi^{n+1} - \phi^n}{\Delta t} = -u\frac{\partial \phi^{n+\frac{1}{2}}}{\partial x} \tag{4.2.8}$$

Rearranging Eq. (4.2.7) to make $\phi^{n+\frac{1}{2}}$ the subject and then substituting into Eq. (4.2.8) we obtain Eq. (4.2.6). At each stage of the two-step scheme $\phi^{n+1/2}$ and ϕ^{n+1} can then be solved spatially using a suitable spatial discretisation method. Higher order accurate Taylor-Galerkin time-marching schemes can be derived by including more terms in the Taylor expansion.

4.2.1 A Taylor Galerkin Scheme for Computing Viscous flow

The first scheme presented is the Taylor-Galerkin temporal discretisation for a viscous Newtonian fluid. In this scheme the convective (nonlinear) terms are explicitly calculated using similar steps to Equations (4.2.7) and (4.2.8). The pressure is then determined by combining the Taylor-Galerkin steps with Chorin's projection method. The resulting scheme is given by

$$\begin{aligned}
&\textbf{Step 1a} \quad Re\left(\frac{\mathbf{u}^{n+\frac{1}{2}} - \mathbf{u}^n}{\Delta t/2}\right) = \nabla^2\mathbf{u}^n - Re\mathbf{u}^n\cdot\nabla\mathbf{u}^n - \nabla p^n\\
&\textbf{Step 1b} \quad Re\left(\frac{\mathbf{u}^{*} - \mathbf{u}^n}{\Delta t}\right) = \frac{1}{2}\nabla^2\mathbf{u}^n - Re\mathbf{u}^{n+\frac{1}{2}}\cdot\nabla\mathbf{u}^{n+\frac{1}{2}} - \nabla p^n\\
&\textbf{Step 2} \quad \nabla^2(p^{n+1} - p^n) = \frac{Re}{\Delta t}\nabla\cdot\mathbf{u}^{*}\\
&\textbf{Step 3} \quad Re\left(\frac{\mathbf{u}^{n+1} - \mathbf{u}^{*}}{\Delta t}\right) = -\frac{1}{2}\nabla(p^{n+1} - p^n) + \frac{1}{2}\nabla^2\mathbf{u}^{n+1}
\end{aligned} \tag{4.2.9}$$

Incompressibility is enforced in Step 2. Furthermore, body force terms can also be introduced explicitly (at time $t = t^n$) in steps 1a and 1b. Webster et. al [89] proposed the following modification to the two-step Taylor Galerkin pressure-correction algorithm in order to model unsteady flow of weakly compressible Newtonian fluids

$$\begin{aligned}
&\textbf{Step 1a} \quad Re\rho^n\left(\frac{\mathbf{u}^{n+\frac{1}{2}}-\mathbf{u}^n}{\Delta t/2}\right) = \left(\nabla^2\mathbf{u}^n + \frac{1}{3}\nabla(\nabla\cdot\mathbf{u}^n)\right) - Re\rho^n\mathbf{u}^n\cdot\nabla\mathbf{u}^n - \nabla p^n \\
&\textbf{Step 1b} \quad Re\rho^n\left(\frac{\mathbf{u}^{*}-\mathbf{u}^n}{\Delta t}\right) = \frac{1}{2}\left(\nabla^2\mathbf{u}^n + \frac{1}{3}\nabla(\nabla\cdot\mathbf{u}^n)\right) - Re\rho\mathbf{u}^{n+\frac{1}{2}}\cdot\nabla\mathbf{u}^{n+\frac{1}{2}} - \nabla p^n \\
&\textbf{Step 2} \quad \frac{Ma^2}{Re(1+\tilde{\alpha}\theta^n)}\frac{p^{n+1}-p^n}{\Delta t} = \frac{\Delta t}{2}\nabla^2(p^{n+1}-p^n) - \nabla\cdot(\rho^n\mathbf{u}^*) \\
&\textbf{Step 3} \quad Re\rho^n\left(\frac{\mathbf{u}^{n+1}-\mathbf{u}^*}{\Delta t}\right) = -\frac{1}{2}\nabla(p^{n+1}-p^n) + \frac{1}{2}\left(\nabla^2\mathbf{u}^{n+1} + \frac{1}{3}\nabla(\nabla\cdot\mathbf{u}^{n+1})\right) \\
&\textbf{Step 4} \quad Re\rho^{n+1} = Re\rho^n + \frac{Ma^2}{Re(1+\tilde{\alpha}\theta^n)}(p^{n+1}-p^n)
\end{aligned} \tag{4.2.10}$$

4.2.2 Taylor Galerkin Scheme for Computing Viscoelastic Flow

Taylor Galerkin methods are suitable for numerically simulating compressible and viscoelastic flow due to their efficiency in treating equations of an evolutionary hyperbolic type [69]. In this section we propose an extension of the procedure developed by Belblidia et al. [50, 51] for nonisothermal weakly compressible viscoelastic fluids described by the governing equations Eq. (4.1.14). In the case of incompressible viscoelastic flow the two-step scheme can be written

$$
\begin{aligned}
&\textbf{Step 1a} \qquad Re\left(\frac{\mathbf{u}^{n+\frac{1}{2}}-\mathbf{u}^{n}}{\Delta t/2}\right)=\beta_v\nabla^2\mathbf{u}^n-Re\mathbf{u}^n\cdot\nabla\mathbf{u}^n+\nabla\cdot\boldsymbol{\tau}_p^n-\nabla p^n\\
&\textbf{Step 1b} \qquad Re\left(\frac{\mathbf{u}^{*}-\mathbf{u}^{n}}{\Delta t}\right)=\frac{1}{2}\beta_v\nabla^2\mathbf{u}^n-Re\mathbf{u}^{n+\frac{1}{2}}\cdot\nabla\mathbf{u}^{n+\frac{1}{2}}+\frac{1}{2}\nabla\cdot\boldsymbol{\tau}_p^n-\nabla p^n\\
&\textbf{Step 1c} \qquad \frac{We(\mathbf{C}^{n+\frac{1}{2}}-\mathbf{C}^n)}{\Delta t/2}=[\mathbf{I}-\mathbf{C}-We(\mathbf{u}\cdot\nabla\mathbf{C}-\mathbf{C}\nabla\mathbf{u}+\nabla\mathbf{u}^T\cdot\mathbf{C})-\mathbf{g}_2(\mathbf{C},\nabla\mathbf{u})]^n\\
&\textbf{Step 1d} \qquad \frac{\theta^{n+\frac{1}{2}}-\theta^n}{\Delta t/2}=\nabla\cdot\mathbf{q}^n-\mathbf{u}^n\cdot\nabla\theta^n+V_h\boldsymbol{\sigma}^n:\nabla\mathbf{u}^n\\
&\textbf{Step 2} \qquad \nabla^2(p^{n+1}-p^n)=\frac{Re}{\Delta t}\nabla\cdot\mathbf{u}^*\\
&\textbf{Step 3} \qquad Re\left(\frac{\mathbf{u}^{n+1}-\mathbf{u}^{*}}{\Delta t}\right)=-\frac{1}{2}\nabla(p^{n+1}-p^n)+\frac{1}{2}\beta_v\nabla^2\mathbf{u}^{n+1}+\frac{1}{2}\nabla\cdot\mathbf{C}^{n+1}\\
&\textbf{Step 4} \qquad \frac{We(\mathbf{C}^{n+1}-\mathbf{C}^n)}{\Delta t}+\mathbf{C}^{n+1}=\mathbf{I}-[We(\mathbf{u}\cdot\nabla\mathbf{C}-\mathbf{C}\nabla\mathbf{u}+\nabla\mathbf{u}^T\cdot\mathbf{C})+\mathbf{g}_2(\mathbf{C},\nabla\mathbf{u})]^{n+\frac{1}{2}}\\
&\textbf{Step 5} \qquad \frac{\theta^{n+1}-\theta^n}{\Delta t}=\nabla\cdot\mathbf{q}^{n+1}-\mathbf{u}^{n+\frac{1}{2}}\cdot\nabla\theta^{n+\frac{1}{2}}+V_h\boldsymbol{\sigma}^{n+\frac{1}{2}}:\nabla\mathbf{u}^{n+\frac{1}{2}}
\end{aligned}
\tag{4.2.11}
$$

where $\boldsymbol{\tau}_p^n = \frac{1-\beta_v}{We}(\mathbf{C}^n-\mathbf{I}) =: \mathbf{g}_1(\mathbf{C}^n,\mathbf{I})$. In addition to the steps outlined for the Newtonian fluid the scheme for the incompressible viscoelastic fluid contains two fractional steps for solving the constitutive equation. Moreover the two-step Taylor-Galerkin algorithm for computing nonisothermal and (weakly) compressible viscoelastic flow is given by

$$
\begin{array}{ll}
\textbf{Step 1a} & Re\rho^n\left(\dfrac{\mathbf{u}^{n+\frac{1}{2}}-\mathbf{u}^n}{\Delta t/2}\right)=\beta_v\left(\nabla^2\mathbf{u}^n+\dfrac{1}{3}\nabla(\nabla\cdot\mathbf{u}^n)\right)-Re\mathbf{u}^n\cdot\nabla\mathbf{u}^n+\nabla\cdot\boldsymbol{\tau}_p^n-\nabla p^n \\
\textbf{Step 1b} & \dfrac{We\tilde{\psi}(\theta)(\mathbf{C}^{n+\frac{1}{2}}-\mathbf{C}^n)}{\Delta t/2}=[\mathbf{I}-\mathbf{C}-We(\mathbf{u}\cdot\nabla\mathbf{C}-\mathbf{C}\nabla\mathbf{u}+\nabla\mathbf{u}^T\mathbf{C}+\nabla\cdot\mathbf{u}\mathbf{C})-\mathbf{g}_2(\mathbf{C},\nabla\mathbf{u})]^n \\
\textbf{Step 1c} & \dfrac{\theta^{n+\frac{1}{2}}-\theta^n}{\Delta t/2}=Di\nabla^2\theta^n-\mathbf{u}^n\cdot\nabla\theta^n+V_h\boldsymbol{\sigma}^n:\nabla\mathbf{u}^n-p^n\nabla\cdot\mathbf{u}^n \\
\textbf{Step 2} & Re\rho^n\left(\dfrac{\mathbf{u}^*-\mathbf{u}^n}{\Delta t}\right)=\dfrac{1}{2}\beta_v\left(\nabla^2\mathbf{u}^n+\dfrac{1}{3}\nabla(\nabla\cdot\mathbf{u}^n)\right)-Re\mathbf{u}^{n+\frac{1}{2}}\cdot\nabla\mathbf{u}^{n+\frac{1}{2}}+\nabla\cdot\boldsymbol{\tau}_p^{n+\frac{1}{2}}-\nabla p^n \\
\textbf{Step 3} & \dfrac{Ma^2}{Re(1+\tilde{\alpha}\theta^n)}\dfrac{p^{n+1}-p^n}{\Delta t}=\dfrac{\Delta t}{2}\nabla^2(p^{n+1}-p^n)-\nabla\cdot(\rho^n\mathbf{u}^*) \\
\textbf{Step 4} & \rho^{n+1}=\rho^n+Ma^2(p^{n+1}-p^n) \\
\textbf{Step 5} & Re\rho^n\left(\dfrac{\mathbf{u}^{n+1}-\mathbf{u}^*}{\Delta t}\right)=-\dfrac{1}{2}\nabla(p^{n+1}-p^n)+\dfrac{1}{2}\beta_v\left(\nabla^2\mathbf{u}^n+\dfrac{1}{3}\nabla(\nabla\cdot\mathbf{u}^n)\right) \\
\textbf{Step 6} & \dfrac{We\tilde{\psi}(\theta)(\mathbf{C}^{n+1}-\mathbf{C}^n)}{\Delta t}+\mathbf{C}^{n+1}=[\mathbf{I}-We(\mathbf{u}\cdot\nabla\mathbf{C}-\mathbf{C}\cdot\nabla\mathbf{u}+\nabla\mathbf{u}^T\cdot\mathbf{C}+(\nabla\cdot\mathbf{u})\mathbf{C}) \\
 & \qquad\qquad\qquad\qquad\qquad\qquad -\mathbf{g}_2(\mathbf{C},\nabla\mathbf{u})]^{n+\frac{1}{2}} \\
\textbf{Step 7} & \dfrac{\theta^{n+1}-\theta^n}{\Delta t}=Di\nabla^2\theta^{n+1}-\mathbf{u}^{n+\frac{1}{2}}\cdot\nabla\theta^{n+\frac{1}{2}}+V_h\boldsymbol{\sigma}^{n+\frac{1}{2}}:\nabla\mathbf{u}^{n+\frac{1}{2}}-p^n\nabla\cdot\mathbf{u}^n
\end{array}
\tag{4.2.12}
$$

where $\hat{\mathbb{D}}=\mathbb{D}-\frac{1}{2}(\nabla\cdot\mathbf{u})\mathbf{I}$. Eq. (4.2.12) represents a second-order (in time) discretisation for the system of equations for weakly compressible viscoelastic flow (Eq. (4.1.14)).

4.3 Variational Formulation

In order to write the weak form of the problem, we should introduce some notation. The space of square integrable functions in a domain, Ω, is denoted $L^2(\Omega)$ and the space of functions whose derivatives are square integrable is given by $H^1(\Omega)$. We define the function spaces for the velocity pressure and stress as follows

$$\begin{aligned}
\mathcal{V} =& \left\{ \mathbf{v} \in H^1(\Omega)^2 \right\} \\
\mathcal{V}_0 =& \left\{ \mathbf{v} \in H^1(\Omega)^2 : \mathbf{v} = 0 \,\mathrm{on}\, \partial\Omega \right\} \\
\mathcal{Q} =& \left\{ q \in H^1(\Omega) \right\} \\
\mathcal{Z} =& \left\{ \mathbf{R} = [R_{ij}],\, i, j \in \{1, 2\}, \quad R_{ij} \in H^1(\Omega), \quad R_{ij} = R_{ji} \right\}
\end{aligned} \tag{4.3.1}$$

4.3.1 Incompressible Viscoelastic Flow

We obtain the weak formulation of the time discretised problem as follows: Multiply the momentum balance, mass balance and constitutive equations (4.2.11) by $\mathbf{v} \in \mathcal{V}$, $q, r \in \mathcal{Q}$ and $\mathbf{R} \in \mathcal{Z}$, respectively and integrate over Ω. The weak formulation of Eq. 4.2.11 is as follows: Find $\mathbf{u}^{n+1}, \mathbf{u}^n \in \mathcal{V}$, $p^{n+1}, p^n, \theta^{n+1}, \theta^n \in \mathcal{V}$ and $\mathbf{C}^{n+1}, \mathbf{C}^n \in \mathcal{Z}$ such that

$$
\begin{aligned}
Re\int_{\Omega}\frac{\mathbf{u}^{n+\frac{1}{2}}-\mathbf{u}^{n}}{\Delta t/2}\cdot\mathbf{v}\,d\Omega =&-\beta_v\int_{\Omega}\nabla\mathbf{u}^{n}:\nabla\mathbf{v}\,d\Omega-\int_{\Omega}\mathbf{u}^{n}\cdot\nabla\mathbf{u}^{n}\cdot\mathbf{v}\,d\Omega-\int_{\Omega}\boldsymbol{\tau}_p^{n}:\nabla\mathbf{v}\,d\Omega\\
&-\int_{\Omega}\nabla p^{n}\cdot\mathbf{v}\,d\Omega\\
Re\int_{\Omega}\frac{\mathbf{u}^{*}-\mathbf{u}^{n}}{\Delta t}\cdot\mathbf{v}\,d\Omega =&-\frac{1}{2}\beta_v\int_{\Omega}\nabla\mathbf{u}^{n}\cdot\nabla\mathbf{v}\,d\Omega-\int_{\Omega}\mathbf{u}^{n+\frac{1}{2}}\cdot\nabla\mathbf{u}^{n+\frac{1}{2}}\cdot\mathbf{v}\,d\Omega-\frac{1}{2}\int_{\Omega}\boldsymbol{\tau}_p^{n}:\nabla\mathbf{v}\,d\Omega\\
&-\int_{\Omega}\nabla p^{n}\cdot\mathbf{v}\,d\Omega \qquad\qquad \forall\mathbf{v}\in\mathcal{V}\\
We\int_{\Omega}\frac{\mathbf{c}^{n+\frac{1}{2}}-\mathbf{c}^{n}}{\Delta t/2}:\mathbf{R}\,d\Omega =&-\int_{\Omega}\boldsymbol{\tau}_p^{n}:\mathbf{R}\,d\Omega+\int_{\Omega}\mathbf{I}:\mathbf{R}\,d\Omega\\
&-We\int_{\Omega}(\mathbf{u}\cdot\nabla\mathbf{c}-\mathbf{c}\nabla\mathbf{u}+\nabla\mathbf{u}^{T}\mathbf{c})^{n}:\mathbf{R}\,d\Omega \qquad\qquad \forall\mathbf{R}\in\mathcal{Z}\\
We\int_{\Omega}\frac{\mathbf{c}^{n+1}-\mathbf{c}^{n}}{\Delta t}:\mathbf{R}\,d\Omega =&-\int_{\Omega}\mathbf{c}^{n+1}:\mathbf{R}\,d\Omega+\int_{\Omega}\mathbf{I}:\mathbf{R}\,d\Omega\\
&-We\int_{\Omega}(\mathbf{u}\cdot\nabla\mathbf{c}-\mathbf{c}\nabla\mathbf{u}+\nabla\mathbf{u}^{T}\mathbf{c})]^{n+\frac{1}{2}}:\mathbf{R}\,d\Omega \qquad\qquad \forall\mathbf{R}\in\mathcal{Z}\\
\int_{\Omega}\nabla(p^{n+1}-p^{n})\cdot\nabla q\,d\Omega =&\frac{1}{\Delta t}\int_{\Omega}\mathbf{u}^{*}\cdot\nabla q\,d\Omega \qquad\qquad \forall\mathbf{q}\in\mathcal{Q}\\
Re\int_{\Omega}\frac{\mathbf{u}^{n+1}-\mathbf{u}^{*}}{\Delta t}\cdot\mathbf{v}\,d\Omega =&\frac{1}{2}\beta_v\int_{\Omega}\nabla\mathbf{u}^{n+1}:\nabla\mathbf{v}\,d\Omega-\frac{1}{2}\int_{\Omega}\mathbf{c}^{n+1}:\nabla\mathbf{v}\,d\Omega\\
&-\frac{1}{2}\int_{\Omega}(\nabla p^{n+1}-\nabla p^{n})\cdot\mathbf{v}\,d\Omega \qquad\qquad \forall\mathbf{v}\in\mathcal{V}\\
\int_{\Omega}\frac{\theta^{n+\frac{1}{2}}-\theta^{n}}{\Delta t/2}r\,d\Omega =&-Di\int_{\Omega}\nabla\theta^{n}\cdot\nabla r\,d\Omega-\int_{\Omega}\mathbf{u}^{n}\cdot\nabla\theta^{n}r\,d\Omega\\
&+V_h\int_{\Omega}[\boldsymbol{\sigma}^{n}:\nabla\mathbf{u}^{n}]r\,d\Omega \qquad\qquad \forall\mathbf{v}\in\mathcal{V}\\
\int_{\Omega}\frac{\theta^{n+1}-\theta^{n}}{\Delta t}r\,d\Omega =&-Di\int_{\Omega}\nabla\theta^{n+1}\cdot\nabla r\,d\Omega-\int_{\Omega}\mathbf{u}^{n+\frac{1}{2}}\cdot\nabla\theta^{n+\frac{1}{2}}r\,d\Omega\\
&+V_h\int_{\Omega}[\boldsymbol{\sigma}^{n+\frac{1}{2}}:\nabla\mathbf{u}^{n+\frac{1}{2}}]r\,d\Omega \qquad\qquad \forall r\in\mathcal{Q}
\end{aligned}
\tag{4.3.2}
$$

4.3.2 Weakly Compressible Flow

The weak formulation of Eq. 4.2.11 is as follows: Find $\mathbf{u}^{n+1}, \mathbf{u}^{n} \in \mathcal{V}$, $p^{n+1}, p^{n}, \theta^{n+1}, \theta^{n} \in \mathcal{V}$ and $\mathbf{C}^{n+1}, \mathbf{C}^{n} \in \mathcal{Z}$ such that

$$
\begin{aligned}
Re\int_\Omega \rho^n \frac{\mathbf{u}^{n+\frac{1}{2}}-\mathbf{u}^n}{\Delta t/2}\cdot\mathbf{v}\,d\Omega =& -\beta_v\left(\int_\Omega \nabla\mathbf{u}^n:\nabla\mathbf{v}\,d\Omega+\frac{1}{3}\int_\Omega(\nabla\cdot\mathbf{u}^n)(\nabla\cdot\mathbf{v})\,d\Omega\right)\\
&-Re\int_\Omega \mathbf{u}^n\cdot\nabla\mathbf{u}^n\cdot\mathbf{v}\,d\Omega-\int_\Omega \boldsymbol{\tau}_p^n:\nabla\mathbf{v}\,d\Omega-\int_\Omega\nabla p^n\cdot\mathbf{v}\,d\Omega \qquad \forall\mathbf{v}\in\mathcal{V}\\
We\int_\Omega \tilde{\psi}(\theta)\frac{\mathbf{c}^{n+\frac{1}{2}}-\mathbf{c}^n}{\Delta t/2}:\mathbf{R}\,d\Omega =& -\int_\Omega \mathbf{c}^n:\mathbf{R}\,d\Omega+\int_\Omega\mathbf{I}:\mathbf{R}\,d\Omega\\
&-We\int_\Omega\tilde{\psi}(\theta)(\mathbf{u}\cdot\nabla\mathbf{c}-\mathbf{c}\nabla\mathbf{u}+\nabla\mathbf{u}^T\mathbf{c}+\nabla\cdot\mathbf{u}\mathbf{c})^n:\mathbf{R}\,d\Omega \qquad \forall\mathbf{R}\in\mathcal{Z}\\
\int_\Omega\rho^n\frac{\theta^{n+\frac{1}{2}}-\theta^n}{\Delta t/2}r\,d\Omega =& -Di\int_\Omega\nabla\theta^n\cdot\nabla r\,d\Omega-\int_\Omega\mathbf{u}^n\cdot\nabla\theta^n r\,d\Omega\\
&+V_h\int_\Omega[\boldsymbol{\sigma}^n:\nabla\mathbf{u}^n]r\,d\Omega \qquad \forall\mathbf{v}\in\mathcal{V}\\
Re\int_\Omega\rho^n\frac{\mathbf{u}^*-\mathbf{u}^n}{\Delta t}\cdot\mathbf{v}\,d\Omega =& -\frac{1}{2}\beta_v\left(\int_\Omega\nabla\mathbf{u}^n:\nabla\mathbf{v}\,d\Omega+\frac{1}{3}\int_\Omega(\nabla\cdot\mathbf{u}^n)(\nabla\cdot\mathbf{v})\,d\Omega\right)\\
&-\int_\Omega\mathbf{u}^{n+\frac{1}{2}}\cdot\nabla\mathbf{u}^{n+\frac{1}{2}}\cdot\mathbf{v}\,d\Omega-\frac{1}{2}\int_\Omega\boldsymbol{\tau}_p^n:\nabla\mathbf{v}\,d\Omega\\
&-\int_\Omega\nabla p^n\cdot\mathbf{v}\,d\Omega \qquad \forall\mathbf{v}\in\mathcal{V}\\
We\int_\Omega\tilde{\psi}(\theta)\frac{\mathbf{c}^{n+1}-\mathbf{c}^n}{\Delta t}:\mathbf{R}\,d\Omega =& -\int_\Omega\mathbf{c}^{n+1}:\mathbf{R}\,d\Omega+\int_\Omega\mathbf{I}:\mathbf{R}\,d\Omega\\
&-We\int_\Omega\tilde{\psi}(\theta)(\mathbf{u}\cdot\nabla\mathbf{c}-\mathbf{c}\nabla\mathbf{u}+\nabla\mathbf{u}^T\mathbf{c}+\nabla\cdot\mathbf{u}\mathbf{c})]^{n+\frac{1}{2}}:\mathbf{R}\,d\Omega \qquad \forall\mathbf{R}\\
\int_\Omega\frac{Ma^2}{Re(1+\tilde{\alpha}\theta^n)\Delta t}(p^{n+1}-p^n)q\,d\Omega+&\int_\Omega\frac{\Delta t}{2}\nabla(p^{n+1}-p^n)\cdot\nabla q\,d\Omega\\
=& Re\left(\int_\Omega\rho^n\nabla\cdot\mathbf{u}^*q\,d\Omega+\int_\Omega\nabla\rho^n\cdot\mathbf{u}^*q\,d\Omega\right) \qquad \forall\mathbf{q}\in\mathcal{Q}\\
Re\int_\Omega\rho^n\frac{\mathbf{u}^{n+1}-\mathbf{u}^*}{\Delta t}\cdot\mathbf{v}\,d\Omega =& -\frac{1}{2}\beta_v\left(\int_\Omega\nabla\mathbf{u}^{n+1}:\nabla\mathbf{v}\,d\Omega+\frac{1}{3}\int_\Omega(\nabla\cdot\mathbf{u}^{n+1})(\nabla\cdot\mathbf{v})\,d\Omega\right)\\
&-\frac{1}{2}\int_\Omega\boldsymbol{\tau}_p^{n+1}:\nabla\mathbf{v}\,d\Omega-\frac{1}{2}\int_\Omega(\nabla p^{n+1}-\nabla p^n)\cdot\mathbf{v}\,d\Omega \qquad \forall\mathbf{v}\in\mathcal{V}\\
\int_\Omega\rho^n\frac{\theta^{n+1}-\theta^n}{\Delta t}r\,d\Omega =& -Di\int_\Omega\nabla\theta^{n+1}\cdot\nabla r\,d\Omega-\int_\Omega\mathbf{u}^{n+\frac{1}{2}}\cdot\nabla\theta^{n+\frac{1}{2}}r\,d\Omega\\
&+V_h\int_\Omega[\boldsymbol{\sigma}^{n+\frac{1}{2}}:\nabla\mathbf{u}^{n+\frac{1}{2}}]r\,d\Omega \qquad \forall r\in\mathcal{Q}
\end{aligned}
\tag{4.3.3}
$$

4.4 Spatial Discretisation: FEM

4.4.1 The Finite Element Method: A Brief Overview

Since the dawn of numerical computing, the finite element method has become an increasingly useful technique that has been widely used by engineers. The first textbooks on FEM were published in the 1970s and several popular texts have been published since. Courant [22] is usually credited with having first published the finite element method in an appendix of a paper focussed on Ritz-Rayleigh methods.

Using the definition formulated by Ciarlet [18] we define a finite element as a triple (K, Σ, P) where

- $K \subset \mathbb{R}^n$ is the element domain with Lipschitz continuous boundary ∂K
- Σ is a finite set of linear forms over $C^\infty(K)$. The set Σ is said to be the degrees of freedom of the finite element
- P is the set of nodal variables (basis or dual of Σ)

The first step in the finite element method is to derive the variational form of the PDE, which consists of bilinear and linear forms:

$$a(u, v) = L(v) \qquad \forall v \in V \tag{4.4.1}$$

where u is being solved for and v is a test function. The domain, Ω, over which we wish to solve the PDE is meshed using a shape function K. On each element functions are represented via the coefficients of basis Σ, or degrees of freedom (dof). A set of algebraic equations are then formed by evaluating Eq. (4.4.1) on each degree of freedom (interpolation point) i.e. $a(\phi_i, \psi_j)$ and $L(\psi_j)$ have to be evaluated for each $\phi_i, \psi_j \in P$. PDEs solved using FEM require boundary conditions. These can either be strong, such as Dirichlet boundary conditions which fix some of the coefficients eliminating the corresponding equations, or weak, such as Neumann conditions that are assembled through the variational form.

Implementing the finite element method can be summarised using the following algorithm

1) Derive the variational formulation of governing equation

2) Formulate mesh

3) Create degrees of freedom (dof) on mesh

4) Evaluate $a(i, j) = L(j)$ for $i, j \in$ dofs (generate linear system of equations)

5) Apply Dirichlet boundary conditions

6) Perform algebraic solve

4.4.2 Galerkin Finite Element Discretisation of the Governing Equations

Under the considerations outlined in Sec. 4.4.1 we can construct conforming finite element spaces $\mathcal{V}_h \subset \mathcal{V}$, $\mathcal{Q}_h \subset \mathcal{Q}$ and $\mathcal{Z}_h \subset \mathcal{Z}$ in the usual manner. These discrete function spaces are chosen so that they satisfy the Ladyzhenskaya–Babuška–Brezzi (LBB) or inf-sup condition. The LBB condition is necessary and sufficient for guaranteeing the well posedness of solutions of the discrete problem. The velocity, pressure and stress spaces are subject to the following compatibility conditions

$$\inf_{q_h \in \mathcal{Q}_h} \sup_{\mathbf{v}_h \in \mathcal{V}_h} \frac{(q_h, \nabla \cdot \mathbf{v}_h)}{||q_h||_{\mathcal{Q}_h} ||\mathbf{v}||_{\mathcal{V}_h}} > \beta_1 > 0 \tag{4.4.2}$$

$$\inf_{\mathbf{v}_h \in \mathcal{V}_h} \sup_{\boldsymbol{\tau}_p \in \mathcal{Z}_h} \frac{(\mathbf{R}_h, \mathcal{D}(\mathbf{v}_h))}{||\mathbf{R}_h||_{\mathcal{Z}_h} ||\mathbf{v}_h||_{\mathcal{V}_h}} > \beta_2 > 0 \tag{4.4.3}$$

Numerous types of finite element basis functions exist in the literature. However, one of the difficulties in solving the governing equations for viscoelastic flow is finding compatible basis functions for the pressure velocity and stress in order to satisfy the LBB condition. In this thesis we will restrict ourselves to three types of compatible finite elements suitable for modelling viscoelastic flow; namely $P1$ piecewise linear continuous Lagrangian elements for pressure, density and temperature, $P2$ piecewise quadratic for velocity and $P1$ discontinuous

Lagrangian elements for stress. In the implementation of DEVSS stabilisation (see Sec. 4.6.1) we will make use of the space of discontinuous functions over Ω constructed using $P0$ elements.

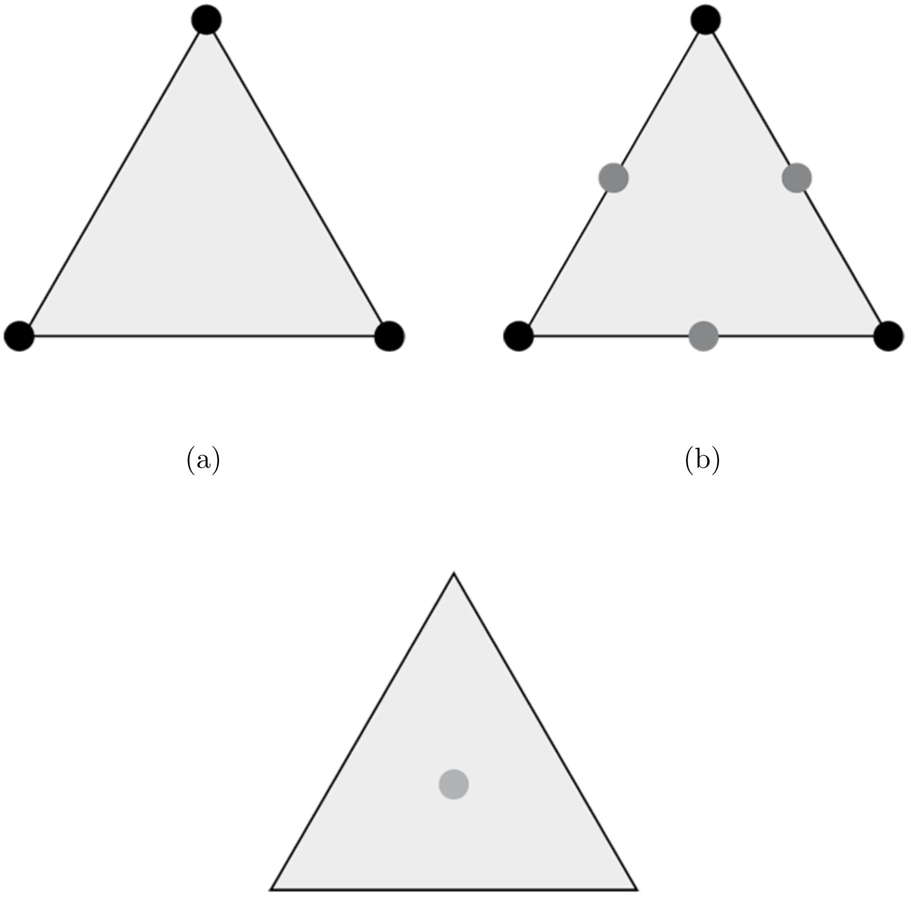
(a)

(b)

(c)

Figure 4.1: (a) Piecewise linear P1, (b) piecewise quadratic P2 and (c) piecewise constant P0 elements

4.5 The High Weissenberg Number Problem (HWNP)

When trying to numerically solve hyperbolic constitutive equations such as UCM and Oldroyd-B, most of the standard polynomial interpolation methods fail to converge for frustratingly low Weissenberg numbers. Further examination reveals that the cause of numerical divergence is due to growing spurious oscillations brought about by dominating advection terms. To demonstrate this problem, consider the following 1D example

$$\frac{\partial \phi}{\partial t} + a(x)\frac{\partial \phi}{\partial x} - b(x)\phi = \frac{1}{We}\phi \tag{4.5.1}$$

where $a(x), b(x) > 0$ with boundary condition $\phi(0,t) = 1$. This equation represents a field that is convected with velocity $a(x)$ and grows exponentially at a rate $b(x) - We^{-1}$. Here $a(x)$ represents the velocity field $\mathbf{u}$, and $b(x)$ plays the role of the velocity gradient $\nabla\mathbf{u}$ in the UCM/Oldroyd-B equation. The solution to (4.5.1) is given by

$$\phi(x) = \int_x^0 \exp\left(\frac{b(s) - We^{-1}}{a(s)}\right) ds \tag{4.5.2}$$

We can solve (4.5.1) numerically using the explicit scheme

$$\frac{\phi_j^{n+1} - \phi_j^n}{\Delta t} = -a_j\frac{\phi_j^n - \phi_{j-1}^n}{\Delta x} + b_j\phi_j^n + \frac{1}{We}\phi_j^n \tag{4.5.3}$$

where $a_j = a(x_j)$ and $b_j = b(x_j)$.

$$\phi_j^{n+1} = \left[1 - \frac{\Delta t a_j}{\Delta x} + \Delta t\left(b_j - \frac{1}{We}\right)\right]\phi_j^n + \frac{a_j\Delta t}{\Delta x}\phi_{j-1}^n \tag{4.5.4}$$

It is clear that the numerical solution blows up unless the terms in the rectangular parenthesis are less than unity in magnitude i.e.

$$\Delta t\left[\frac{a_j}{\Delta x} - b_j + \frac{1}{We}\right] \geq 0 \tag{4.5.5}$$

which in turn implies that either $We < 1/b_j$ or

$$\Delta x \leq \frac{a_j}{b_j - We^{-1}} \tag{4.5.6}$$

This condition holds at each interpolation point x_j. This stability criterion can be interpreted as follows: the spatial profile $\phi(x,t)$ is exponential, therefore every convection scheme based on polynomial interpolation of the fluxes underestimates the flux at the right edge of every computational cell [31]. This failure to balance the convective term with the multiplicative growth rate leads to numerical blow-up. Suitably accurate discretisation schemes and stabilisation methods are required in order to obtain solutions over a wider range of We and are outlined in the following sections.

4.6 Stabilisation

4.6.1 DEVSS and DEVSS-G

The Discrete Elastic Viscous Stress Splitting (DEVSS) scheme introduced by Guénette and Fortin [39] does not require a change of variables and can be implemented at the weak formulation stage of the discretisation.

Incompressible Flow

In the case where $\nabla \cdot \mathbf{u} = 0$, the momentum equation can be expressed in the form

$$\begin{aligned} &Re\frac{D\mathbf{u}}{Dt} + \nabla p + \gamma_u(\nabla^2\mathbf{u} - \nabla \cdot \mathbf{D}) + \beta\nabla^2\mathbf{u} - \nabla \cdot \boldsymbol{\tau}_p = 0 \\ &\mathbf{D} - (\nabla\mathbf{u} + \nabla\mathbf{u}^T) = 0 \end{aligned} \tag{4.6.1}$$

where γ_u is the DEVSS stabilisation parameter. At the continuous level, it is clear that the term in red is equal to zero because $\nabla \cdot \mathbf{D} = \nabla^2\mathbf{u}$. This is not true when the solution space for $\mathbf{D}$ is lower order than that of the derivative space for the velocity solution, $\mathbf{u}$. As a result, in regions of high deformation rate where stress gradients are largest the DEVSS term stabilises the solution.

Compressible Flow

In compressible flow we propose the following extension to the DEVSS formulation (4.6.1)

$$\begin{aligned}
&\rho\frac{D\mathbf{u}}{Dt} + \nabla p + \gamma_u\left(\nabla^2\mathbf{u} + \frac{1}{3}\nabla(\nabla\cdot\mathbf{u}) - \nabla\cdot\mathbf{D}\right) + \beta_v\left(\nabla^2\mathbf{u} + \frac{1}{3}\nabla(\nabla\cdot\mathbf{u})\right) - \nabla\cdot\boldsymbol{\tau}_p = 0\\
&\mathbf{D} - \left(\nabla\mathbf{u} + \nabla\mathbf{u}^T - \frac{2}{3}(\nabla\cdot\mathbf{u})\mathbf{I}\right) = 0
\end{aligned} \tag{4.6.2}$$

In both cases $\boldsymbol{\tau}_p$ is determined by the constitutive equation.

4.6.2 Streamline Upwinding - SU and SUPG

As outlined in section 4.5, spurious oscillations generated by use of central difference methods or Galerkin finite elements for advection dominated equations are an unwelcome nuisance. In order to combat this problem Brooks & Hughes [14] developed the so-called streamlined-upwind/Petrov-Galerkin (SUPG) formulation. A 1D model example to demonstrate the SUPG method is given in the next section.

SUPG Example 1D

Consider the advection-diffusion equation

$$\begin{aligned}
-\epsilon u''(x) + bu'(x) = 0 \qquad & x\in[0,1]\\
u(0)=1, u(1)=0 \qquad &
\end{aligned} \tag{4.6.3}$$

The exact solution of this problem is given by $u_e(x) = (e^{b/\epsilon} - e^{bx/\epsilon})/(e^{b/\epsilon} - 1)$. Let

$$\begin{aligned} V &= \{v \in H^1(0,1) : v(0) = 1,\, v(1) = 0\} \\ W &= H_0^1(0,1) \end{aligned} \tag{4.6.4}$$

The weak form of (4.6.3) is: Find $u \in V$ such that

$$\epsilon\langle u', v'\rangle + b\langle u', v\rangle = 0, \qquad \forall v \in W \tag{4.6.5}$$

where

$$\langle a, b\rangle = \int_0^1 ab\, dx \tag{4.6.6}$$

Define $a(u,v) = \epsilon\langle u', v'\rangle + b\langle u', v\rangle$, the weak form can be rewritten: Find $u \in V$ such that $a(u,v) = 0$ for all $v \in W$. If we approximate the solution using piecewise linear functions

$$u^h(x) = \sum_{i=1}^{N} U_i \phi_i(x) \tag{4.6.7}$$

and choose the test function according to

$$v^h(x) = \phi_j(x) \qquad j = 1, \ldots, N \tag{4.6.8}$$

then the solution to (4.6.5) can be approximated by the solution of the linear system of equations

$$\mathbf{A}\underline{\mathbf{U}} = \underline{\mathbf{0}} \tag{4.6.9}$$

where

$$A_{ij} = a(\phi_j, \phi_i) \tag{4.6.10}$$

and

$$\mathbf{A} = \frac{\epsilon}{h}\begin{pmatrix} 2 & -1+\frac{\gamma}{2} & 0 & \cdots & 0 \\ -1-\frac{\gamma}{2} & 2 & -1+\frac{\gamma}{2} & \cdots & \vdots \\ 0 & -1-\frac{\gamma}{2} & 2 & \ddots & 0 \\ \vdots & & \ddots & \ddots & -1+\frac{\gamma}{2} \\ 0 & \cdots & 0 & -1-\frac{\gamma}{2} & 2 \end{pmatrix} \tag{4.6.11}$$

For the SUPG method, the test function, v_k is replaced by

$$\tilde{v}_k = v_k + h_k v_k' \tag{4.6.12}$$

The SUPG stabilised formulation of (4.6.5) is: : Find $u \in V$ such that

$$a(u_k, \tilde{v}_k) = 0, \qquad \forall v \in W \tag{4.6.13}$$

The discrete problem can then be written

$$\tilde{\mathbf{A}}\underline{\mathbf{U}} = \underline{\mathbf{0}} \tag{4.6.14}$$

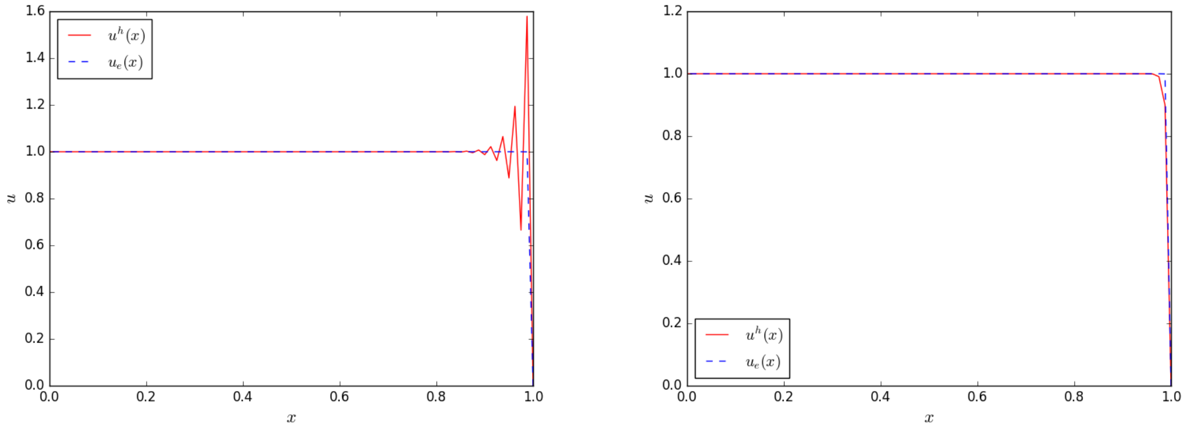

(a) (b)

Figure 4.2: Finite element/difference solution to the problem. (a) unstabilised and (b) SUPG stabilised. $b = 60$, $\epsilon = 0.1$, $h = 0.0125$

As seen in Fig. 4.2 (a) if $\epsilon = 0$ or $\frac{\epsilon}{hb}$ falls below some critical size then the problem is advection dominated and the finite element/difference approximation to the solution develops spurious oscillations. This always occurs unless unless the exact solution is globally smooth [10]. However, when the SUPG weighted test functions are used in the formulation the oscillations are suppressed. Figure 4.2 (b) shows the SUPG stabilised solution.

SUPG For Viscoelastic Flows

For 2D or 3D viscoelastic flow problems the weak formulation of the constitutive equation (4.1.14) using SUPG weighted test functions can be written

$$\int_\Omega \left(\mathbf{C}_h + We(\overset{\triangledown}{\mathbf{C}}_h + (\nabla \cdot \mathbf{u}_h)\mathbf{C}_h) + \mathbf{g}_2(\mathbf{C}_h, \mathbb{D}_h) - \mathbf{I} \right) : \tilde{\mathbf{R}}_h \, d\Omega = 0 \tag{4.6.15}$$

where $\tilde{\mathbf{R}}$ is the augmented test function defined by

$$\tilde{\mathbf{R}}_h = \mathbf{R}_h + |h| \frac{\mathbf{u}_h}{|\mathbf{u}_h|} \cdot \nabla \mathbf{R} \tag{4.6.16}$$

where $|h|$ is the cell diameter of the finite element. The first application of streamlined-upwind methods to viscoelastic flows was performed by Marchal & Crochet [60] in 1987. The authors used both the SUPG method and streamlined upwind (SU) method for the stress, however, they found that the consistent SUPG integration of the constitutive equation produced errors in the calculation of stick-slip flow and flow through an abrupt contraction. Crochet and Legat [23] concluded that the failure of SUPG to prevent numerical breakdown was due to errors occurring at the sharp corners within the flow. They substantiated this claim by illustrating that SUPG method was both stable and accurate for solving UCM flows around a sphere and through a corrugated tube.

For problems with smooth boundaries both high order accuracy and stability for the stress solution can be obtained. For problems with singularities the augmented test function, $\tilde{\mathbf{R}}$, collapses to the standard Galerkin test function near the boundary and spurious oscillations will occur. A review of the SUPG method for viscoelastic flows can be found by Phillips and

Owens [69] p.177-182.

4.6.3 Log Conformation Tensor Representation

The most significant development concerning the HWNP is the development of the log-conformation tensor representation proposed by Fattal & Kupfermen [30, 31]. Some of the difficulties associated with exponential stress profiles can be remedied by solving for the (matrix) logarithm of the conformation tensor, $\log(\mathbf{C})$ (recall that any symmetric positive-definite (SPD) matrix can be diagonalized, $A = R\Lambda R^T$, and that $\log A = R \log \Lambda R^T$). Moreover positivity of the conformation tensor is guaranteed by a formulation based on $\log \mathbf{C}$. For incompressible flow the following theorem holds

Theorem 4.6.1 *Let $\boldsymbol{u}$ be a divergence-free velocity field and let $\boldsymbol{C}$ be the positive-definite conformation tensor. Then, $\nabla \boldsymbol{u}$ can be (locally) decomposed as*

$$\nabla \boldsymbol{u} = \Omega + B + N \boldsymbol{C}^{-1} \tag{4.6.17}$$

where $\Omega(\nabla \boldsymbol{u}, \boldsymbol{C})$ and $N(\nabla \boldsymbol{u}, \boldsymbol{C})$ are anti-symmetric pure rotations and B is symmetric, traceless and commutes with the conformation tensor $\boldsymbol{C}$.

We can then show that if $\mathbf{C}$ satisfies a constitutive equation of the form (4.1.15), and $\mathbf{g}_2$ is dependent on $\mathbf{C}$ only , then $\boldsymbol{\psi} := \log \mathbf{C}$ satisfies the equation

$$We\left(\frac{\partial \boldsymbol{\psi}}{\partial t} + (\mathbf{u} \cdot \nabla)\boldsymbol{\psi} - (\boldsymbol{\psi}\Omega - \Omega\boldsymbol{\psi}) - 2\boldsymbol{B}\right) + e^{-\boldsymbol{\psi}}(\mathbf{g}_2(e^{\boldsymbol{\psi}}) - \mathbf{I}) = 0 \tag{4.6.18}$$

where Ω is the anti-symmetric part of $\nabla \mathbf{u}$ defined in Theorem 4.6.1 and $\mathbf{B} = \frac{1}{2}(\nabla \mathbf{u} + \nabla \mathbf{u}^T) =: \mathbb{D}$ (for further details see Fattal and Kupferman [30]). The improvement in numerical stability for finite element method solutions to Eq. (4.6.18) allows for much higher Weissenberg numbers to be attained.

The development of a log-conformation tensor representation for compressible viscoelastic flows is (unfortunately) outside the scope of this thesis. A future development aimed at improving the numerical scheme outlined in Sec. 4.7 is the extension of the log-conformation tensor representation to compressible flows. Due to the difficulties presented by removing the divergence free condition for $\mathbf{u}$, this is by no means an easy task as analogues of the various tensors used in the decomposition of the velocity gradient will have to be derived and this remains an open problem.

4.6.4 Orthogonal Projection Stabilisation

In recent years, projection based stabilisation techniques have been considered as a computationally efficient means of treating the high Weissenberg instability [16, 88]. Consider the explicit Euler time discretisation of the general constitutive equation in (4.1.14)

$$\frac{We(\mathbf{C}^{n+1} - \mathbf{C}^{n})}{\Delta t} = [\mathbf{I} - \mathbf{C} - We\mathbf{F}(\mathbf{u}, \mathbf{C}) - \mathbf{g}(\nabla \mathbf{u}, \mathbf{C})]^{n} \tag{4.6.19}$$

where $\mathbf{F}$ is given by

$$\mathbf{F}(\mathbf{u}, \mathbf{C}) = \mathbf{u} \cdot \nabla \mathbf{C} - \mathbf{C}\nabla \mathbf{u} + \nabla \mathbf{u}^{T}\mathbf{C} + (\nabla \cdot \mathbf{u})\mathbf{C} \tag{4.6.20}$$

and $\mathbf{g}$ is model dependent. If we define $\mathscr{Z}$ as the suitable function space for $\mathbf{C}$, the weak formulation can than be written in terms of an inner product

$$\frac{We}{\Delta t}\langle \mathbf{C}^{n+1} - \mathbf{C}^{n}, \mathbf{R}\rangle = \langle [\mathbf{I} - \mathbf{C} - We\mathbf{F}(\mathbf{u}, \mathbf{C})]^{n} - \mathbf{g}(\nabla \mathbf{u}, \mathbf{C}), \mathbf{R}\rangle \qquad \forall \mathbf{R} \in \mathscr{Z} \tag{4.6.21}$$

The discrete approximation of (4.6.21) can be written in the form

$$\frac{We}{\Delta t}\langle \mathbf{C}_{k}^{n+1} - \mathbf{C}_{k}^{n}, \mathbf{R}\rangle = \langle [\mathbf{I} - \mathbf{C}_{k} - We\mathbf{F}(\mathbf{u}_{k}, \mathbf{C}_{k}) - \mathbf{g}(\nabla \mathbf{u}_{k}, \mathbf{C}_{k})]^{n}, \mathbf{R}\rangle \qquad \forall \mathbf{R}_{k} \in \mathscr{Z}_{k} \tag{4.6.22}$$

where $\mathbf{u}_{k} \approx \mathbf{u}$ on some element $k \in \mathcal{T}$ (see next section for details of the discrete solution spaces used). Local projection stabilisation for the discrete problem can be described as follows: Let P_{k} be the L^{2} projection onto an appropriate finite element space, either of velocity, elastic stress or pressure without boundary conditions. Let $P_k^{\perp} = I - P_k$ be the orthogonal projection, where I is the identity mapping, i.e.

$$P^{\perp}(\mathbf{u}_k) = \int_{\Omega} (\mathbf{u}_k - \hat{\mathbf{u}}_k) \cdot \mathbf{v}_k \, d\Omega \qquad \forall \mathbf{v}_k \in \mathcal{V} \tag{4.6.23}$$

where $\hat{\mathbf{u}}_k$ is the L^2 projection of $\mathbf{u}$ onto a lower order function space (for further details on the fluctuation operator, $P^{\perp}(\cdot)$ see Castillo et al. [3] and Ganesan et al. [33]). To stabilise the computations of the conformation stress we add the numerical diffusion term

$$\mathbf{S}_{\boldsymbol{\tau}_p}(\mathbf{C}, \mathbf{R}) = \sum_{k \in \mathcal{T}}^{N_P} h_k \langle c_1 \kappa_k \nabla \mathbf{C}, \nabla \mathbf{R} \rangle + \sum_{k \in \mathcal{T}}^{N_P} h_k \langle c_2 \kappa_k \nabla \cdot \mathbf{C}, \nabla \cdot \mathbf{R} \rangle \tag{4.6.24}$$

to the right-hand side of (4.6.22) where κ_k is the scalar fluctuation operator defined by

$$\kappa_k^{n+1} = \left\| P^{\perp} \left[\frac{We}{\Delta t} (\mathbf{C}_k^{n+1} - \mathbf{C}_k^n) + \mathbf{C}_h^n + We \mathbf{F}^n(\nabla \mathbf{u}_k, \mathbf{C}_k) + \mathbf{g}(\nabla \mathbf{u}_k^n, \mathbf{C}_k^n) - \mathbf{I} \right] \right\| \tag{4.6.25}$$

and c_1, c_2 are user chosen parameters. It is clear that, in the elements where $\mathbf{C}_k^n$ satisfies the discretised form of the constitutive equation, $\kappa_k = 0$. Thus the stabilised formulation of the discrete problem (4.6.22) can be written

$$\frac{We}{\Delta t} \langle \mathbf{C}_k^{n+1} - \mathbf{C}_k^n, \mathbf{R} \rangle + \mathbf{S}_{\boldsymbol{\tau}_p}^{n+1} = \langle [\mathbf{I} - \mathbf{C}_k - We \mathbf{F}(\mathbf{u}_k, \mathbf{C}_k) - \mathbf{g}(\nabla \mathbf{u}), \mathbf{C})]^n, \mathbf{R} \rangle \qquad \forall \mathbf{R}_k \in \mathcal{Z}_k \tag{4.6.26}$$

4.7 Bilinear Forms and Discretised Systems

4.7.1 Incompressible Flow

Eq. (4.3.2) can be expressed using bilinear forms as follows: For a given $(\mathbf{u}_h^0, D_H^0)$, p^0 and $\boldsymbol{\tau}_{p,h}^0$, find $(\mathbf{u}_h, D_h)^{n+\frac{1}{2}} \in \mathcal{V}_h \times \mathcal{Z}_{d,h}$, $\boldsymbol{\tau}_p^{n+\frac{1}{2}} \in \mathcal{Z}_h$, $\theta^{n+\frac{1}{2}} \in \mathcal{Q}_h$, $(\mathbf{u}_h, D)_h^* \in \mathcal{V}_h \times \mathcal{Z}_{d,h}$, $p_h^{n+1} \in \mathcal{Q}_h$, $(\mathbf{u}_h, D_h)^{n+1} \in \mathcal{V}_h \times \mathcal{Z}_h$,$\boldsymbol{\tau}_p^{n+1} \in \mathcal{Z}_h$ and $\theta_h^{n+1} \in \mathcal{Q}_h$ such that

$$
\begin{aligned}
Re\left(\frac{\mathbf{u}_h^{n+\frac12}-\mathbf{u}_h^n}{\Delta t/2},\mathbf{v}_h\right)+\gamma_u\left(\mathbf{a}(\mathbf{u}_h^{n+\frac12},\mathbf{v}_h)-\mathbf{c}(\mathcal{D}_h^{n+\frac12},\mathbf{v}_h)\right) &= -\beta_v\mathbf{a}(\mathbf{u}_h^n,\mathbf{v}_h)-Re\,\mathbf{b}(\mathbf{u}_h^n;\mathbf{u}_h^n,\mathbf{v}_h)\\
&\quad+\mathbf{c}(\boldsymbol{\tau}_{p,h}^n,\mathbf{v}_h)-\mathbf{d}(p_h^n,\mathbf{v}_h) \qquad \forall \mathbf{v}_h\in\mathcal{V}_h\\
(\mathcal{D}_h^{n+\frac12},\hat{\mathbf{R}}_h)-\mathbf{e}(\mathbf{u}_h^{n+\frac12},\mathbf{R}_h) &=0 \qquad \forall\mathbf{R}_h\in\mathcal{Z}_{d,h}\\
We\left(\frac{\mathbf{C}_h^{n+\frac12}-\mathbf{C}_h^n}{\Delta t/2},\mathbf{R}_h\right)+\mathbf{S}_{\boldsymbol{\tau}_p}(\mathbf{C}_h^{n+\frac12},\mathbf{R}_h) &= -(\mathbf{c}_h^n,\mathbf{R}_h)+(\mathbf{I},\mathbf{R}_h)\\
&\quad -We\mathbf{f}(\mathbf{u}_h^n;\mathbf{C}_{p,h}^n,\mathbf{R}_h) \qquad \forall\mathbf{R}_h\in\mathcal{Z}_h\\
\left(\frac{\theta_h^{n+\frac12}-\theta_h^n}{\Delta t/2},r_h\right) &= \mathbf{g}(\mathbf{q}_h^n,r)-\mathbf{m}(\mathbf{u}_h^n;\theta_h^n,r_h)\\
&\quad +V_h\mathbf{n}(\beta_v;\mathbf{u}_h^n;\boldsymbol{\tau}_{p,h}^n,r_h) \qquad \forall r_h\in\mathcal{Q}_h\\
Re\left(\frac{\mathbf{u}_h^*-\mathbf{u}_h^n}{\Delta t},\mathbf{v}_h\right)+\gamma_u\left(\mathbf{a}(\mathbf{u}^*,\mathbf{v})-\mathbf{c}(\mathcal{D}_h^*,\mathbf{v}_h)\right) &= -\frac{\beta_v}{2}\mathbf{a}(\mathbf{u}_h^n,\mathbf{v}_h)-Re\,\mathbf{b}(\mathbf{u}_h^{n+\frac12};\mathbf{u}_h^{n+\frac12},\mathbf{v}_h)\\
&\quad+\mathbf{c}(\boldsymbol{\tau}_{p,h}^{n+\frac12},\mathbf{v}_h)-\mathbf{d}(p_h^n,\mathbf{v}_h)\qquad\forall\mathbf{v}_h\in\mathcal{V}_h\\
(\mathcal{D}_h^*,\mathbf{R}_h)-\mathbf{e}(\mathbf{u}_h^*,\mathbf{R}_h)&=0\qquad\forall\mathbf{R}_h\in\mathcal{Z}_{d,h}\\
\mathbf{g}(p^{n+1}-p^n,q)&=\frac{Re}{\Delta t}\mathbf{d}(q,\mathbf{u}^*)\qquad\forall\mathbf{q}_h\in\mathcal{Q}_h\\
Re\left(\frac{\mathbf{u}_h^{n+1}-\mathbf{u}_h^*}{\Delta t},\mathbf{v}_h\right)+\gamma_u\left(\mathbf{a}(\mathbf{u}_h^{n+1},\mathbf{v}_h)-\mathbf{c}(\mathcal{D}_h^{n+1},\mathbf{v}_h)\right)+\frac{\beta_v}{2}\mathbf{a}(\mathbf{u}_h^{n+1},\mathbf{v}_h) &= -\frac12\mathbf{d}(p_h^{n+1}-p_h^n,\mathbf{v}_h)\\
(\mathcal{D}_h^{n+1},\mathbf{R}_h)-\mathbf{e}(\mathbf{u}_h^{n+1},\mathbf{R}_h)&=0\qquad\forall\mathbf{R}_h\in\mathcal{Z}_{d,h}\\
We\left(\frac{\mathbf{C}_h^{n+1}-\mathbf{C}_h^n}{\Delta t},\mathbf{R}_h\right)+\mathbf{S}_{\boldsymbol{\tau}_p}(\mathbf{C}_h^n,\mathbf{R}_h)&=-(\mathbf{C}_h^{n+1}:\hat{\mathbf{R}}_h)+(\mathbf{I},\mathbf{R}_h)\\
&\quad-We\mathbf{f}(\mathbf{u}_h^{n+\frac12};\mathbf{C}_h^{n+\frac12},\mathbf{R}_h)\qquad\forall\mathbf{R}_h\in\mathcal{Z}_h\\
\left(\frac{\theta_h^{n+1}-\theta_h^n}{\Delta t},r_h\right)&=\mathbf{g}(\mathbf{q}^n,r_h)-\mathbf{m}(\mathbf{u}_h^{n+\frac12};\theta_h^{n+\frac12},r_h)\\
&\quad+V_h\mathbf{n}(\beta_v;\mathbf{u}_h^{n+\frac12};\boldsymbol{\tau}_h^{n+\frac12},r_h)\qquad\forall\mathbf{r}_h\in\mathcal{Q}_h
\end{aligned}
\tag{4.7.1}
$$

where

$$
\begin{aligned}
&(\mathbf{u},\mathbf{v}) = \int_\Omega \mathbf{u}\cdot\mathbf{v}\,d\Omega \qquad (\boldsymbol{\tau},\mathbf{R}) = \int_\Omega \boldsymbol{\tau} : \mathbf{R}\,d\Omega \\
&\mathbf{a}(\mathbf{u},\mathbf{v}) = \int_\Omega \nabla\mathbf{u} : \nabla\mathbf{v}\,d\Omega \qquad \mathbf{b}(\hat{\mathbf{u}};\mathbf{u},\mathbf{v}) = \int_\Omega \hat{\mathbf{u}}\cdot\nabla\mathbf{u}\cdot\mathbf{v}\,d\Omega \\
&\mathbf{c}(\boldsymbol{\tau},\mathbf{v}) = \int_\Omega \nabla\cdot\boldsymbol{\tau}\cdot\mathbf{v}\,d\Omega = -\int_\Omega \boldsymbol{\tau} : \nabla\mathbf{v}\,d\Omega \\
&\mathbf{d}(p,\mathbf{v}) = \int_\Omega \nabla p\cdot\mathbf{v}\,d\Omega = -\int_\Omega p\nabla\cdot\mathbf{v}\,d\Omega \\
&\mathbf{e}(\mathbf{u},\mathbf{R}) = \int_\Omega \frac{1}{2}(\nabla\mathbf{u}+\nabla\mathbf{u}^T) : \mathbf{R}\,d\Omega \\
&\mathbf{f}(\mathbf{u};\boldsymbol{\tau},\mathbf{R}) = \int_\Omega (\mathbf{u}\cdot\nabla\boldsymbol{\tau} - \boldsymbol{\tau}\cdot\nabla\mathbf{u}^T - \nabla\mathbf{u}\cdot\boldsymbol{\tau}) : \mathbf{R}\,d\Omega \\
&\mathbf{g}(p,q) = \int_\Omega \nabla p\cdot\nabla q\,d\Omega
\end{aligned}
\tag{4.7.2}
$$

The DEVSS stabilisation terms are highlighted in red and $\mathbf{S}_{\boldsymbol{\tau}_p}(\mathbf{C},\mathbf{R})$ is the Orthogonal projection stabilisation term defined in Eq. (4.6.24). The exact formulation, including nondimensional parameters used is dependent on (i) the scaling used and (ii) parameter dependence on temperature. In the benchmark problems presented in Chapters 5 and 6 variations of the scheme (4.7.1) are used to solve for velocity, stress, pressure and temperature, all of which have the same underlying structure.

Let $\{\boldsymbol{\phi}_i\}$, $i = 1,\ldots N_V$, $\{\zeta_k\}$, $k = 1,\ldots N_Q$, and $\{\boldsymbol{\xi}_r\}$, $r = 1,\ldots N_Z$, be the basis functions for $\mathcal{V}_h$, $\mathcal{Q}_h$ and $\mathcal{Z}_h$, respectively, and let ζ, $\boldsymbol{\phi}$ and $\boldsymbol{\xi}$ be scalar, vector and tensor basis functions, respectively. The discrete solution functions are given by

$$
\begin{aligned}
&\mathbf{u}_h^n(x,y) = \sum_{j=1}^{N_V} \mathbf{U}_j^n \boldsymbol{\phi}_j(x,y) \qquad p_h^n(x,y) = \sum_{j=1}^{N_Q} P_j^n \zeta_j(x,y) \\
&\mathbf{C}_{p,h}^n(x,y) = \sum_{j=1}^{N_Z} \mathbf{T}_j^n \boldsymbol{\xi}_j(x,y) \qquad D_h^n(x,y) = \sum_{j=1}^{N_Z} \mathbf{D}_j^n \boldsymbol{\xi}_j(x,y) \\
&\theta_h^n(x,y) = \sum_{j=1}^{N_{Q_T}} \hat{\theta}_j^n \zeta_j(x,y)
\end{aligned}
\tag{4.7.3}
$$

where $\mathbf{U}_j^n$, $j = 1, \dots N_V$, $\mathbf{P}_j^n$, $\hat{\theta}_j^n$, $j = 1, \dots N_Q$ and $\mathbf{T}_j^n$, ..., $s = 1, \dots N_V$ are the nodal values of the dependent variables at time-step $t = t^n$. For each j, P_j^n, $\mathbf{U}_j^n$ and $\mathbf{T}_j^n$ are a real-valued scalars. Since $\mathbf{u}_h^n$ and $\boldsymbol{\tau_{p}}_h^n$ represent vector and tensor valued functions respectively, we can define $\hat{\mathbf{U}}_{j_v}^n \in \mathbb{R}^2$ for each $j_v \in \{1, \dots, N_v/2\}$, and $\hat{\mathbf{T}}_{j_z}^n \in \mathbb{R}^{2\times 2}$ $j_z \in \{1, \dots, N_Z/4\}$ so that

$$\begin{aligned} \mathbf{U}_j^n \boldsymbol{\phi}_j(x,y) &= \hat{U}_{j_v}^{k,n} \phi_j^k(x,y) \\ \mathbf{T}_j^n \boldsymbol{\xi}_j(x,y) &= \hat{T}_{j_z}^{kl,n} \xi_j^{kl}(x,y) \qquad k,l \in \{1,2\} \end{aligned} \tag{4.7.4}$$

For example, $\mathbf{U}_1^n = \hat{U}_{1_v}^{1,n}$, $\mathbf{U}_2^n = \hat{U}_{1_v}^{2,n}$, $\mathbf{U}_3^n = \hat{U}_{2_v}^{1,n}$, $\mathbf{U}_4^n = \hat{U}_{2_v}^{2,n}$ etc. The same system is used to label the tensor basis functions so $\mathbf{T}_1^n = \hat{T}_{1_v}^{11,n}$, $\mathbf{T}_2^n = \hat{T}_{1_z}^{12,n}$, $\mathbf{T}_3^n = \hat{T}_{1_z}^{21,n}$, $\mathbf{T}_4^n = \hat{T}_{1_z}^{22,n}$. Using this notation will aid with explaining how the various matrices are constructed. Setting $\mathbf{v}_h = \boldsymbol{\phi}_i$, $q_h = \zeta_k$ and $\psi_h = \boldsymbol{\xi}_r$ and substituting (4.7.3) into (4.7.1) generates a system of linear algebraic equations:

Velocity Half-Step

$$\begin{aligned} &\sum_{j=1}^{N_V} [2Re(\boldsymbol{\phi}_j, \boldsymbol{\phi}_i) + \Delta t[\gamma_u(\mathbf{a}(\boldsymbol{\phi}_j, \boldsymbol{\phi}_i)) - \mathbf{e}(\boldsymbol{\phi}_j, \boldsymbol{\xi}_r)]]\mathbf{U}_j^{n+\frac{1}{2}} + \Delta t \sum_{j=1}^{N_Z} [(\boldsymbol{\xi}_j, \boldsymbol{\xi}_k) - \mathbf{c}(\boldsymbol{\xi}_j, \boldsymbol{\phi}_i)]\mathbf{D}_j^{n+\frac{1}{2}} \\ &\quad = \sum_{j=1}^{N_V} [2Re(\boldsymbol{\phi}_j, \boldsymbol{\phi}_i) - \Delta t[\beta \mathbf{a}(\boldsymbol{\phi}_j, \boldsymbol{\phi}_i) + Re\mathbf{b}(\mathbf{u}_h^n; \boldsymbol{\phi}_j, \boldsymbol{\phi}_i)]]\mathbf{U}_j^n + \Delta t \sum_{j=1}^{N_Z} \mathbf{c}(\boldsymbol{\xi}_j, \boldsymbol{\phi}_i)\mathbf{T}_j^n \\ &\quad - \Delta t \sum_{j=1}^{N_Q} \mathbf{d}(\zeta_j, \boldsymbol{\phi}_i)\mathbf{P}_j^n \end{aligned} \tag{4.7.5}$$

Stress Half-Step

$$\begin{aligned} 2We \sum_{j=1}^{N_Z} (\boldsymbol{\xi}_j, \boldsymbol{\xi}_i)\mathbf{T}_j^{n+\frac{1}{2}} + \sum_{j=1}^{N_Z} \mathbf{s}(\boldsymbol{\xi}_j, \boldsymbol{\xi}_i) =& (2We - \Delta t) \sum_{j=1}^{N_Z} (\boldsymbol{\xi}_j, \boldsymbol{\xi}_i)\mathbf{T}_j^n + \sum_{j=1}^{N_V} (\boldsymbol{\phi}_j, \boldsymbol{\xi}_i) \\ &- We\Delta t \sum_{j=1}^{N_Q} \mathbf{f}(\mathbf{u}_h^n; \boldsymbol{\xi}_j, \boldsymbol{\xi}_i)\mathbf{T}_j^n \end{aligned} \tag{4.7.6}$$

Predictor Step

$$\begin{aligned}
&\sum_{j=1}^{N_V}[Re(\boldsymbol{\phi}_j,\boldsymbol{\phi}_i)+\Delta t[\gamma_u(\mathbf{a}(\boldsymbol{\phi}_j,\boldsymbol{\phi}_i))-\mathbf{e}(\boldsymbol{\phi}_j,\boldsymbol{\xi}_r)]]\mathbf{U}_j^* + \Delta t\sum_{j=1}^{N_Z}[(\boldsymbol{\xi}_j,\boldsymbol{\xi}_k)-\mathbf{c}(\boldsymbol{\xi}_j,\boldsymbol{\phi}_i)]\mathbf{D}_j^* \\
&\quad=\sum_{j=1}^{N_V}[Re(\boldsymbol{\phi}_j,\boldsymbol{\phi}_i)-\Delta t\frac{\beta}{2}\mathbf{a}(\boldsymbol{\phi}_j,\boldsymbol{\phi}_i)\mathbf{U}_j^n-\Delta t Re\sum_{j=1}^{N_V}\mathbf{b}(\mathbf{u}_h^{n+\frac{1}{2}};\boldsymbol{\phi}_j,\boldsymbol{\phi}_i)\mathbf{U}_j^{n+\frac{1}{2}}+\Delta t\sum_{j=1}^{N_Z}\mathbf{c}(\boldsymbol{\xi}_j,\boldsymbol{\phi}_i)\mathbf{T}_j^{n+\frac{1}{2}} \\
&\quad-\Delta t\sum_{j=1}^{N_Q}\mathbf{d}(\zeta_j,\boldsymbol{\phi}_i)\mathbf{P}_j^n
\end{aligned} \tag{4.7.7}$$

Pressure Correction

$$\sum_{j=1}^{N_Q}\mathbf{g}(\zeta_j,\zeta_i)P_j^{n+1}=\sum_{j=1}^{N_Q}\mathbf{g}(\zeta_j,\zeta_i)P_j^n+\frac{Re}{\Delta t}\sum_{j=1}^{N_V}\mathbf{d}(\boldsymbol{\phi}_j,\zeta_i)\mathbf{U}_j^n \tag{4.7.8}$$

Velocity Full Step

$$\sum_{j=1}^{N_V}[Re(\boldsymbol{\phi}_j,\boldsymbol{\phi}_i)+\Delta t\frac{\beta}{2}(\mathbf{a}(\boldsymbol{\phi}_j,\boldsymbol{\phi}_i))]\mathbf{U}_j^{n+1}=\sum_{j=1}^{N_V}[Re(\boldsymbol{\phi}_j,\boldsymbol{\phi}_i)-\Delta t\frac{1}{2}\sum_{j=1}^{N_Q}\mathbf{d}(\zeta_j,\boldsymbol{\phi}_i)(\mathbf{P}_j^{n+1}-\mathbf{P}_j^n) \tag{4.7.9}$$

Stress Full Step

$$\begin{aligned}
(We+\Delta t)\sum_{j=1}^{N_Z}(\boldsymbol{\xi}_j,\boldsymbol{\xi}_i)\mathbf{T}_j^{n+1} =& We\sum_{j=1}^{N_Z}(\boldsymbol{\xi}_j,\boldsymbol{\xi}_i)\mathbf{T}_j^n+\sum_{j=1}^{N_V}(\boldsymbol{\phi}_j,\boldsymbol{\xi}_i) \\
&-We\Delta t\sum_{j=1}^{N_Q}\mathbf{f}(\mathbf{u}_h^n;\boldsymbol{\xi}_j,\boldsymbol{\xi}_i)\mathbf{T}_j^n
\end{aligned} \tag{4.7.10}$$

Eq. (4.7.5)-(4.7.10) can be expressed in matrix form as the following set of matrix equations:

$$\begin{bmatrix} 2Re\mathbf{M}^V+\Delta t\gamma_v\mathbf{A} & -\Delta t\gamma_v\mathbf{C} \\ -\Delta t\mathbf{E} & \Delta t\mathbf{M}^Z \end{bmatrix}\begin{bmatrix}\mathbf{U}^{n+\frac{1}{2}} \\ \mathbf{D}^{n+\frac{1}{2}}\end{bmatrix}=\begin{bmatrix}\tilde{\boldsymbol{\mathcal{F}}}_1^u \\ 0\end{bmatrix} \tag{4.7.11}$$

where $\tilde{\boldsymbol{\mathcal{F}}}$ is the right-hand side of (4.7.5)

$$2We\mathbf{M}^Z\mathbf{T}^{n+\frac{1}{2}} + \mathbf{S}_1^{n+1/2} = [(2We - \Delta t)\mathbf{M}^Z - We\mathbf{F}^n]\mathbf{T}^n + 2(1-\beta_v)\mathbf{E}\mathbf{U}^n \tag{4.7.12}$$

$$\begin{bmatrix} Re\mathbf{M}^V + \Delta t\gamma_v\mathbf{A} & -\Delta t\gamma_v\mathbf{C} \\ -\Delta t\mathbf{E} & \Delta t\mathbf{M}^Z \end{bmatrix} \begin{bmatrix} \mathbf{U}^* \\ \mathbf{D}^* \end{bmatrix} = \begin{bmatrix} \tilde{\boldsymbol{\mathcal{F}}}_2^u \\ 0 \end{bmatrix} \tag{4.7.13}$$

$$\mathbf{G}P^{n+1} = \mathbf{G}P^n + \frac{Re}{\Delta t}D^T U^* \tag{4.7.14}$$

$$\begin{bmatrix} Re\mathbf{M}^V + \Delta t\gamma_v\mathbf{A} & -\Delta t\gamma_v\mathbf{C} \\ -\Delta t\mathbf{E} & \Delta t\mathbf{M}^Z \end{bmatrix} \begin{bmatrix} \mathbf{U}^{n+1} \\ \mathbf{D}^{n+1} \end{bmatrix} = \begin{bmatrix} \tilde{\boldsymbol{\mathcal{F}}}_3^n \\ 0 \end{bmatrix} \tag{4.7.15}$$

$$(We + \Delta t)\mathbf{M}^Z\mathbf{T}^{n+1} + \mathbf{S}_1^{n+1} = [We\mathbf{M}^Z - We\mathbf{F}^{n+\frac{1}{2}}]\mathbf{T}^n + 2(1-\beta_v)\mathbf{E}\mathbf{U}^{n+\frac{1}{2}} \tag{4.7.16}$$

where

$$\begin{aligned}
M_{ij}^V &= (\boldsymbol{\phi}_j, \boldsymbol{\phi}_i) = \int_\Omega \boldsymbol{\phi}_j \cdot \boldsymbol{\phi}_i \, d\Omega \\
M_{ij}^Z &= (\boldsymbol{\xi}_j, \boldsymbol{\xi}_i) = \int_\Omega \boldsymbol{\xi}_j : \boldsymbol{\xi}_i \, d\Omega \\
M_{ij}^Q &= (\zeta_j, \zeta_i) = \int_\Omega \zeta_j \zeta_i \, d\Omega \\
A_{ij} &= \mathbf{a}(\boldsymbol{\phi}_j, \boldsymbol{\phi}_i) = \int_\Omega \nabla\boldsymbol{\phi}_j : \nabla\boldsymbol{\phi}_i \, d\Omega \\
B_{ij}^n &= \mathbf{b}(\hat{\mathbf{u}}^n; \boldsymbol{\phi}_j, \boldsymbol{\phi}_i) = \int_\Omega \hat{\mathbf{u}}^n \cdot \nabla\boldsymbol{\phi}_j \cdot \boldsymbol{\phi}_i \, d\Omega \\
C_{ij} &= \mathbf{c}(\boldsymbol{\xi}_j, \boldsymbol{\phi}_i) = -\int_\Omega \boldsymbol{\xi}_j : \nabla\boldsymbol{\phi}_i \, d\Omega \\
D_{ij} &= \mathbf{d}(\zeta_j, \boldsymbol{\phi}_i) = \int_\Omega \nabla\zeta_j \cdot \boldsymbol{\phi}_i \, d\Omega = -\int_\Omega \zeta_j \nabla \cdot \boldsymbol{\phi}_i \, d\Omega \\
E_{ij} &= \mathbf{e}(\boldsymbol{\phi}_j, \boldsymbol{\xi}_i) = \int_\Omega \frac{1}{2}(\nabla\boldsymbol{\phi}_j + \nabla\boldsymbol{\phi}_j^T) : \boldsymbol{\xi}_i \, d\Omega \\
F_{ij} &= \mathbf{f}(\mathbf{u}; \boldsymbol{\xi}_j, \boldsymbol{\xi}_i) = \int_\Omega (\mathbf{u} \cdot \nabla\boldsymbol{\xi}_j - \boldsymbol{\xi}_j \cdot \nabla\mathbf{u}^T - \nabla\mathbf{u} \cdot \boldsymbol{\xi}_j) : \boldsymbol{\xi}_i \, d\Omega \\
G_{ij} &= \mathbf{g}(\zeta_j, \zeta_i) = \int_\Omega \nabla\zeta_j \cdot \nabla\zeta_i \, d\Omega \\
M_{ij} &= \mathbf{m}(\mathbf{u}; \zeta_j, \zeta_i) = \int_\Omega \boldsymbol{\phi}_j \cdot \nabla\theta r \, d\Omega \\
N_i &= \mathbf{n}(\beta_v; \mathbf{u}; \boldsymbol{\tau}_p, \zeta_i) = \int_\Omega [(\beta_v \mathbb{D} + \boldsymbol{\tau}_p) : \nabla\mathbf{u}]\zeta_i \, d\Omega
\end{aligned} \tag{4.7.17}$$

$\tilde{\boldsymbol{\mathcal{F}}}_i^u$ $i = 1, 2, 3$ is the right-hand side of Eq. (4.7.5), (4.7.7) and (4.7.9), respectively. The orthogonal projection stabilisation matrix is given by

$$S_{ij} = \mathbf{s}(\boldsymbol{\xi}_j, \boldsymbol{\xi}_i) \tag{4.7.18}$$

Equations (4.7.11)-(4.7.16) represent the fully discretised form of the governing equations (4.1.15).

4.7.2 Compressible Flow

Eq. (4.3.3) can be expressed using bilinear forms as follows: For a given $(\mathbf{u}_h^0, \mathbf{D}_h^0)$, ρ_h^0 p_h^0 and $\mathbf{C}_h^0$, find $(\mathbf{u}_h, \mathbf{D}_h)^{n+\frac{1}{2}} \in \mathcal{V}_h \times \mathcal{Z}_{d,h}$, $\mathbf{C}_h^{n+\frac{1}{2}} \in \mathcal{Z}_h$, $(\theta_h^{n+\frac{1}{2}}, \Theta^{n+\frac{1}{2}}) \in \mathcal{Q}_h$, $(\mathbf{u}, \mathbf{D})^* \in \mathcal{V} \times \mathcal{Z}$, $p_h^{n+1} \in \mathcal{Q}_h$, $\rho_h^{n+1} \in \mathcal{Q}_h$, $(\mathbf{u}_h, \mathbf{D}_h)^{n+1} \in \mathcal{V}_h \times \mathcal{Z}, \mathbf{C}_h^{n+1} \in \mathcal{Z}_h$ and $\theta_h^{n+1} \in \mathcal{Q}_h$ such that

(4.3.3) can be expressed using bilinear forms

$$
\begin{aligned}
Re\left(\rho_h^n \frac{\mathbf{u}_h^{n+\frac{1}{2}} - \mathbf{u}_h^n}{\Delta t/2}, \mathbf{v}_h\right) + \gamma_u \left(\hat{\mathbf{a}}(\mathbf{u}_h^{n+\frac{1}{2}}, \mathbf{v}_h) - \mathbf{c}(\mathbf{D}_h^{n+\frac{1}{2}}, \mathbf{v}_h)\right) &= -\beta_v \hat{\mathbf{a}}(\mathbf{u}_h^n, \mathbf{v}_h) - \mathbf{b}(\mathbf{u}_h^n; \mathbf{u}_h^n, \mathbf{v}_h) - \mathbf{c}(\boldsymbol{\tau}_{p,h}^n, \mathbf{v}) \\
&\quad - \mathbf{d}(p_h^n, \mathbf{v}_h) \qquad \forall \mathbf{v}_h \in \mathcal{V} \\
\left(\left[\mathbf{D}_h - \frac{1}{2}\left(\nabla \mathbf{u}_h + \nabla \mathbf{u}_h^T - \frac{2}{3}(\nabla \cdot \mathbf{u}_h)\mathbf{I}\right)\right]^{n+\frac{1}{2}}, \hat{\mathbf{R}}_h\right) &= 0 \qquad \forall \mathbf{R}_h \in \mathcal{Z}_{d,h} \\
We\left(\frac{\mathbf{C}_h^{n+\frac{1}{2}} - \mathbf{C}_h^n}{\Delta t/2}, \hat{\mathbf{R}}_h\right) &= -(\mathbf{C}_h^n, \hat{\mathbf{R}}_h) + (\mathbf{I}, \hat{\mathbf{R}}) \\
&\quad - We\mathbf{f}(\mathbf{u}_h^n; \mathbf{C}_h^n, \mathbf{R}_h) \qquad \forall \mathbf{R}_h \in \mathcal{Z}_h \\
Re\left(\rho_h^n \frac{\mathbf{u}_h^* - \mathbf{u}_h^n}{\Delta t}, \mathbf{v}_h\right) + \gamma_u \left(\hat{\mathbf{a}}(\mathbf{u}_h^*, \mathbf{v}_h) - \mathbf{c}(\mathcal{D}_h^*, \mathbf{v}_h)\right) &= -\frac{\beta_v}{2} \mathbf{a}(\mathbf{u}_h^n, \mathbf{v}_h) - \mathbf{b}(\mathbf{u}_h^{n+\frac{1}{2}}; \mathbf{u}_h^{n+\frac{1}{2}}, \mathbf{v}_h) \\
&\quad - \mathbf{c}(\boldsymbol{\tau}_h^{n+\frac{1}{2}}, \mathbf{v}_h) - \mathbf{d}(p_h^n, \mathbf{v}_h) \qquad \forall \mathbf{v}_h \in \mathcal{V}_h \\
\left(\left[\mathbf{D}_h - \frac{1}{2}\left(\nabla \mathbf{u}_h + \nabla \mathbf{u}_h^T - \frac{2}{3}(\nabla \cdot \mathbf{u}_h)\mathbf{I}\right)\right]^{*}, \hat{\mathbf{R}}_h\right) &= 0 \qquad \forall \mathbf{R}_h \in \mathcal{Z}_{d,h} \\
We\left(\frac{\mathbf{C}_h^{n+1} - \mathbf{C}_h^n}{\Delta t}, \hat{\mathbf{R}}_h\right) &= -(\mathbf{C}_h^{n+1} : \mathbf{R}) + (\mathbf{I}, \hat{\mathbf{R}}_h) \\
&\quad - We\mathbf{f}(\mathbf{u}_h^{n+\frac{1}{2}}; \mathbf{C}_h^{n+\frac{1}{2}}, \hat{\mathbf{R}}_h) \qquad \forall \mathbf{R}_h \in \mathcal{Z}_h \\
\frac{Ma^2}{Re\Delta t}(\vartheta^n(p_h^{n+1} - p_h^n), q_h) + \frac{\Delta t}{2}\mathbf{g}(p_h^{n+1} - p_h^n, q_h) &= -\left(\mathbf{h}_1(\rho_h^n; \mathbf{u}_h^*, q_h) + \mathbf{h}_2(\rho_h^n; \mathbf{u}_h^*, q_h)\right) \qquad \forall q_h \in \\
Re\left(\rho_h^n \frac{\mathbf{u}_h^{n+1} - \mathbf{u}_h^*}{\Delta t}, \mathbf{v}_h\right) + \gamma_u \left(\hat{\mathbf{a}}(\mathbf{u}_h^{n+1}, \mathbf{v}_h) - \mathbf{c}(\mathbf{D}_h^{n+1}, \mathbf{v}_h)\right) &= -\frac{\beta_v}{2} \mathbf{a}(\mathbf{u}_h^n, \mathbf{v}_h) + \frac{1}{2}\mathbf{d}(p_h^{n+1} - p_h^n, \mathbf{v}_h) \qquad \forall \\
\left(\left[\mathbf{D}_h - \frac{1}{2}\left(\nabla \mathbf{u}_h + \nabla \mathbf{u}_h^T - \frac{2}{3}(\nabla \cdot \mathbf{u}_h)\mathbf{I}\right)\right]^{n+1}, \mathbf{R}_h\right) &= 0 \qquad \forall \mathbf{R}_h \in \mathcal{Z}_{d,h}
\end{aligned}
\tag{4.7.19}
$$

where we adapt some of the definitions of bilinear forms used in Eq. (4.7.1) to account for the extra compressible terms. The bilinear form $\hat{\mathbf{a}}$ is defined

$$\hat{\mathbf{a}}(\mathbf{u},\mathbf{v}) = \int_\Omega \nabla\mathbf{u} : \nabla\mathbf{v}\, d\Omega + \frac{1}{3}\int_\Omega (\nabla\cdot\mathbf{u})(\nabla\cdot\mathbf{v})\, d\Omega \tag{4.7.20}$$

and we define three new bilinear forms $\hat{\mathbf{d}}$, $\mathbf{h}_1$ and $\mathbf{h}_2$ such that

$$\begin{gathered}\mathbf{h}_1(\rho^n;\mathbf{u}^*,q) = \int_\Omega \rho^n\nabla\cdot\mathbf{u}^* q\, d\Omega \qquad \mathbf{h}_2(\rho^n;\mathbf{u}^*,q) = \int_\Omega \nabla\rho^n\cdot\mathbf{u}q\, d\Omega \\ \hat{\mathbf{d}}(p,r) = -\int_\Omega (\nabla\cdot p) r\, d_\Omega = \int_\Omega p\cdot\nabla r\, d\Omega\end{gathered} \tag{4.7.21}$$

Additionally ϑ is defined

$$\vartheta^n = \frac{1}{1+\tilde{\alpha}\theta^n} \tag{4.7.22}$$

In the momentum equation usual inner product $(\cdot,\cdot)$ is replaced by a weighted inner product $(\rho^n\cdot,\cdot)$.

Velocity Half-Step

$$\begin{aligned}&\sum_{j=1}^{N_V}[2Re(\boldsymbol{\phi}_j,\boldsymbol{\phi}_i) + \Delta t[\gamma_u(\hat{\mathbf{a}}(\boldsymbol{\phi}_j,\boldsymbol{\phi}_i)) - \hat{\mathbf{e}}(\boldsymbol{\phi}_j,\boldsymbol{\xi}_r)]]\mathbf{U}_j^{n+\frac{1}{2}} + \Delta t\sum_{j=1}^{N_Z}[(\boldsymbol{\xi}_j,\boldsymbol{\xi}_k) - \mathbf{c}(\boldsymbol{\xi}_j,\boldsymbol{\phi}_i)]\mathbf{D}_j^{n+\frac{1}{2}} \\ &\quad = \sum_{j=1}^{N_V}[2Re(\boldsymbol{\phi}_j,\boldsymbol{\phi}_i) - \Delta t[\beta\mathbf{a}(\boldsymbol{\phi}_j,\boldsymbol{\phi}_i) + Re\,\mathbf{b}(\mathbf{u}_h^n;\boldsymbol{\phi}_j,\boldsymbol{\phi}_i)]]\mathbf{U}_j^n + \Delta t\sum_{j=1}^{N_Z}\mathbf{c}(\boldsymbol{\xi}_j,\boldsymbol{\phi}_i)\mathbf{T}_j^n \\ &\quad - \Delta t\sum_{j=1}^{N_Q}\mathbf{d}(\zeta_j,\boldsymbol{\phi}_i)\mathbf{P}_j^n\end{aligned} \tag{4.7.23}$$

Stress Half-Step

$$\begin{aligned}2We\sum_{j=1}^{N_Z}(\boldsymbol{\xi}_j,\boldsymbol{\xi}_i)\mathbf{T}_j^{n+\frac{1}{2}} =&(2We-\Delta t)\sum_{j=1}^{N_Z}(\boldsymbol{\xi}_j,\boldsymbol{\xi}_i)\mathbf{T}_j^n+\sum_{j=1}^{N_V}(\boldsymbol{\phi}_j,\boldsymbol{\xi}_i)\\ &-We\Delta t\sum_{j=1}^{N_Q}\mathbf{f}(\mathbf{u}_h^n;\boldsymbol{\xi}_j,\boldsymbol{\xi}_i)\mathbf{T}_j^n\end{aligned}\tag{4.7.24}$$

Predictor Step

$$\begin{aligned}&\sum_{j=1}^{N_V}[Re(\boldsymbol{\phi}_j,\boldsymbol{\phi}_i)+\Delta t[\gamma_u(\mathbf{a}(\boldsymbol{\phi}_j,\boldsymbol{\phi}_i))-\hat{\mathbf{e}}(\boldsymbol{\phi}_j,\boldsymbol{\xi}_r)]]\mathbf{U}_j^*+\Delta t\sum_{j=1}^{N_Z}[(\boldsymbol{\xi}_j,\boldsymbol{\xi}_k)-\mathbf{c}(\boldsymbol{\xi}_j,\boldsymbol{\phi}_i)]\mathbf{D}_j^*\\ &\quad=\sum_{j=1}^{N_V}[Re(\boldsymbol{\phi}_j,\boldsymbol{\phi}_i)-\Delta t\frac{\beta}{2}\hat{\mathbf{a}}(\boldsymbol{\phi}_j,\boldsymbol{\phi}_i)\mathbf{U}_j^n-\Delta tRe\sum_{j=1}^{N_V}\mathbf{b}(\mathbf{u}_h^{n+\frac{1}{2}};\boldsymbol{\phi}_j,\boldsymbol{\phi}_i)\mathbf{U}_j^{n+\frac{1}{2}}+\Delta t\sum_{j=1}^{N_Z}\mathbf{c}(\boldsymbol{\xi}_j,\boldsymbol{\phi}_i)\mathbf{T}_j^{n+\frac{1}{2}}\\ &\quad-\Delta t\sum_{j=1}^{N_Q}\mathbf{d}(\zeta_j,\boldsymbol{\phi}_i)\mathbf{P}_j^n\end{aligned}\tag{4.7.25}$$

Pressure Correction

$$\begin{aligned}\sum_{j=1}^{N_Q}\left[\frac{Ma^2}{\Delta t}(\vartheta^n\zeta_j,\zeta_i)+\frac{\Delta t}{2}\mathbf{g}(\zeta_j,\zeta_i)\right]P_j^{n+1}=&\sum_{j=1}^{N_Q}\left[\frac{Ma^2}{\Delta t}(\zeta_j,\zeta_i)+\frac{\Delta t}{2}\mathbf{g}(\zeta_j,\zeta_i)\right]P_j^n\\ &-\sum_{j=1}^{N_V}[\mathbf{h}_1(\rho_h^n;\boldsymbol{\phi}_j,\zeta_i)+\mathbf{h}_2(\rho_h^n;\boldsymbol{\phi}_j,\zeta_i)]\mathbf{U}_j^*\end{aligned}\tag{4.7.26}$$

Velocity Full Step

$$\sum_{j=1}^{N_V}[Re(\boldsymbol{\phi}_j,\boldsymbol{\phi}_i)+\Delta t\frac{\beta}{2}(\hat{\mathbf{a}}(\boldsymbol{\phi}_j,\boldsymbol{\phi}_i))]\mathbf{U}_j^{n+1}=\sum_{j=1}^{N_V}[Re(\boldsymbol{\phi}_j,\boldsymbol{\phi}_i)-\Delta t\frac{1}{2}\sum_{j=1}^{N_Q}\mathbf{d}(\zeta_j,\boldsymbol{\phi}_i)(\mathbf{P}_j^{n+1}-\mathbf{P}_j^n)\tag{4.7.27}$$

Stress Full Step

$$\begin{aligned}(We+\Delta t)\sum_{j=1}^{N_Z}(\boldsymbol{\xi}_j,\boldsymbol{\xi}_i)\mathbf{T}_j^{n+1} =& We\sum_{j=1}^{N_Z}(\boldsymbol{\xi}_j,\boldsymbol{\xi}_i)\mathbf{T}_j^{n}+\sum_{j=1}^{N_V}(\boldsymbol{\phi}_j,\boldsymbol{\xi}_i)\\ &-We\Delta t\sum_{j=1}^{N_Q}\mathbf{f}(\mathbf{u}_h^n;\boldsymbol{\xi}_j,\boldsymbol{\xi}_i)\mathbf{T}_j^{n}\end{aligned} \tag{4.7.28}$$

Eq. (4.7.23)-(4.7.28) can be expressed in matrix form as the following set of matrix equations:

$$\begin{bmatrix} 2Re\mathbf{M}^V+\Delta t\gamma_v\mathbf{A} & -\Delta t\gamma_v\mathbf{C} \\ -\Delta t\hat{\mathbf{E}} & \Delta t\mathbf{M}^Z \end{bmatrix}\begin{bmatrix}\mathbf{U}^{n+\frac{1}{2}}\\ \mathbf{D}^{n+\frac{1}{2}}\end{bmatrix}=\begin{bmatrix}\tilde{\boldsymbol{\mathcal{F}}}_1^u\\ 0\end{bmatrix} \tag{4.7.29}$$

$$2We\mathbf{M}^Z\mathbf{T}^{n+\frac{1}{2}}=[(2We-\Delta t)\mathbf{M}^Z-We\hat{\mathbf{F}}^n]\mathbf{T}^n+\hat{\mathbf{I}} \tag{4.7.30}$$

$$\begin{bmatrix} Re\mathbf{M}^V+\Delta t\gamma_v\mathbf{A} & -\Delta t\gamma_v\mathbf{C} \\ -\Delta t\hat{\mathbf{E}} & \Delta t\mathbf{M}^Z \end{bmatrix}\begin{bmatrix}\mathbf{U}^{*}\\ \mathbf{D}^{*}\end{bmatrix}=\begin{bmatrix}\tilde{\boldsymbol{\mathcal{F}}}_2^u\\ 0\end{bmatrix} \tag{4.7.31}$$

$$\left(\frac{Ma^2}{\Delta t}\mathbf{M}_\vartheta^Q+\frac{\Delta t}{2}\mathbf{G}\right)P^{n+1}=\left(\frac{Ma^2}{\Delta t}\mathbf{M}_\vartheta^Q+\frac{\Delta t}{2}\mathbf{G}\right)P^{n}-\left(\mathbf{H}^{1,\rho}+\mathbf{H}^{2,\rho}\right)\mathbf{U}^* \tag{4.7.32}$$

$$\begin{bmatrix} Re\mathbf{M}^V+\Delta t\gamma_v\mathbf{A} & -\Delta t\gamma_v\mathbf{C} \\ -\Delta t\hat{\mathbf{E}} & \Delta t\mathbf{M}^Z \end{bmatrix}\begin{bmatrix}\mathbf{U}^{n+1}\\ \mathbf{D}^{n+1}\end{bmatrix}=\begin{bmatrix}\tilde{\boldsymbol{\mathcal{F}}}_3^n\\ 0\end{bmatrix} \tag{4.7.33}$$

$$(We+\Delta t)\mathbf{M}^Z\mathbf{T}^{n+\frac{1}{2}}=[We\mathbf{M}^Z-We\hat{\mathbf{F}}^{n+\frac{1}{2}}]\mathbf{T}^{n+\frac{1}{2}}+\hat{\mathbf{I}} \tag{4.7.34}$$

where $\tilde{\boldsymbol{\mathcal{F}}}_i^u$ $i=1,2,3$ is the right-hand side of (4.7.23), (4.7.25) and (4.7.27), respectively. In addition to the matrices defined in equations (4.7.17) additional matrices for the compressible scheme are defined as follows:

$$
\begin{aligned}
&\hat{E}_{ij} = \mathbf{e}(\boldsymbol{\phi}_j, \boldsymbol{\xi}_i) = \int_\Omega \frac{1}{2}(\nabla\boldsymbol{\phi}_j + \nabla\boldsymbol{\phi}_j^T) : \boldsymbol{\xi}_i \, d\Omega \\
&\hat{F}_{ij} = \mathbf{f}(\mathbf{u}; \boldsymbol{\xi}_j, \boldsymbol{\xi}_i) = \int_\Omega (\boldsymbol{\phi}_l \cdot \nabla\boldsymbol{\xi}_j - \boldsymbol{\xi}_j \cdot \nabla\boldsymbol{\phi}_l^T - \nabla\boldsymbol{\phi}_l \cdot \boldsymbol{\xi}_j + \nabla \cdot \mathbf{u}\boldsymbol{\xi}_j) : \boldsymbol{\xi}_i \, d\Omega \\
&G_{ij} = \mathbf{g}(\zeta_j, \zeta_i) = \int_\Omega \nabla\zeta_j \cdot \nabla\zeta_i \, d\Omega \qquad (4.7.35) \\
&H_{ij}^{\rho_h^n,1} = \mathbf{h}_1(\rho_h^n; \boldsymbol{\phi}_j, \zeta_i) = \int_\Omega \rho_{h,j}^n \zeta_j \nabla \cdot \boldsymbol{\phi}_j \zeta_i \, d\Omega \\
&H_{ij}^{\rho_h^n,2} = \mathbf{h}_2(\rho_h^n; \boldsymbol{\phi}_j, \zeta_i) = \int_\Omega \nabla\zeta_j \cdot \nabla\zeta_i \, d\Omega
\end{aligned}
$$

4.8 Solving the Discretised System

4.8.1 The Conjugate Gradient Method

The conjugate gradient (CG) method is a fast and efficient iterative method for solving symmetric linear systems of equations. It was first derived and introduced by Hestenes and Stiefel in 1952 as part of a generalisation of a class of iterative algorithms for linear systems including Gaussian elimination [44]. Finding the solution, $\mathbf{x}$, to the system $A\mathbf{x} = \mathbf{b}$ can be thought of as the minimisation of the unary quadratic form

$$f(\mathbf{x}) = \frac{1}{2}\mathbf{x}^T A\mathbf{x} - \mathbf{b}^T\mathbf{x} + \gamma \qquad (4.8.1)$$

where γ is a constant vector. The gradient of f is given by

$$\nabla f(\mathbf{x}) = A\mathbf{x} - \mathbf{b} \qquad (4.8.2)$$

Symmetric positive definiteness ensures that f is convex and thus has a *unique minimum.* It follows that

$$\mathbf{x}\,\text{minimiser of}\,f \iff \nabla f(\mathbf{x}) = 0 \iff A\mathbf{x} = \mathbf{b} \qquad (4.8.3)$$

When the eigenvalues of A lie within distinct clustered groups CG converges extremely rapidly, often in fewer than n steps. The Krylov subspace of dimension of order n is given by

$$\mathcal{K}_n = \text{span}\{\mathbf{b}, A\mathbf{b}, \ldots, A^{n-1}\mathbf{b}\} \tag{4.8.4}$$

The conjugate method is the archetype of a Krylov space solver: an orthogonal projection method which satisfies a minimality condition. CG generates a sequence of vectors $\mathbf{x}_n \in \mathcal{K}_n$ that converges to the solution of the linear system $A\mathbf{x} = \mathbf{b}$. The aim is to minimize the energy norm of the error vector $\mathbf{e} = \mathbf{x}_k - \mathbf{x}$ denoted $||\mathbf{e}||_A$, where $||.||_A$ is the *energy norm* defined

$$||\mathbf{e}||_A = \sqrt{\mathbf{e}^T A\mathbf{e}} \tag{4.8.5}$$

Ensuring A-orthogonality of vectors $\mathbf{v}_k = \mathbf{x}_k - \mathbf{x}_{k-1}$ guarantees that the minimum is achieved in at most n-steps.

The Conjugate Gradient (CG) Algorithm

1) Choose initial guess $\mathbf{x}_0$ and compute $\mathbf{r}_0 = \mathbf{b} - A\mathbf{x}_0$. Set $\mathbf{p}_0 = \mathbf{r}_0$

2) For $k = 1, 2, 3, \ldots$, compute

$$\begin{aligned}
\alpha_k &= ||\mathbf{r}_{k-1}||^2 / \mathbf{p}_{k-1}^T A\mathbf{p}_{k-1} \\
\mathbf{x}_k &= \mathbf{x}_{k-1} + \alpha_k \mathbf{p}_{k-1} \\
\mathbf{r}_k &= \mathbf{r}_{k-1} - \alpha_k \mathbf{p}_{k-1} \\
\beta_k &= ||\mathbf{r}_k||^2 / ||\mathbf{r}_{k-1}||^2 \\
\mathbf{p}_k &= \mathbf{r}_k + \beta_k \mathbf{p}_{k-1}
\end{aligned} \tag{4.8.6}$$

Until $||\mathbf{b} - A\mathbf{x}_n||$ is below some tolerance

The step length α_n is chosen so that $\mathbf{r}_n$ is orthogonal to $\mathbf{r}_{n-1}$. It can then be shown (by induction) that successive residuals generated at each step of the conjugate gradient algorithm are orthogonal to all previous residuals in the sequence

$$\mathbf{r}_n^T \mathbf{r}_j = 0, \quad j < n \tag{4.8.7}$$

Additionally the search directions, $\mathbf{p}_n$, are A-conjugate

$$\mathbf{p}_n^T A \mathbf{p}_j = 0, \quad j < n \tag{4.8.8}$$

4.8.2 Preconditioners For The CG Algorithm

The rate of convergence of the CG method depends on the size of the condition number, $\kappa(\mathbf{A})$ (definition given in [63] p.493). If the eigenvalues of A are not close to one another then CG converges slowly. Convergence speed can be improved by way of preconditioning the system with a suitable nonsingular matrix P^{-1}. Preconditioners are chosen such that the resulting system,

$$P^{-1}\mathbf{A}\mathbf{x} = P^{-1}\mathbf{b} \tag{4.8.9}$$

is better suited for the CG algorithm. The precondtioner matrix, P is usually chosen to be an approximation to $\mathbf{A}$, albeit one easier to invert, with $P^{-1}\mathbf{A}$ having eigenvalues clustered close to unity.

The Preconditioned Conjugate Gradient (CG) Algorithm

1) Choose initial guess $\mathbf{x}_0$ and compute $\mathbf{r}_0 = \mathbf{b} - \mathbf{A}\mathbf{x}_0$.

2) Solve $P\mathbf{z}_0 = \mathbf{r}_0$. Set $\mathbf{p}_0 = \mathbf{z}_0$.

3) For $k = 1, 2, 3, \ldots$, compute

$$\begin{aligned}
\alpha_k &= \mathbf{r}_{k-1}^T \mathbf{z}_{n-1} / \mathbf{p}_{k-1}^T A \mathbf{p}_{k-1} \\
\mathbf{x}_k &= \mathbf{x}_{k-1} + \alpha_k \mathbf{p}_{k-1} \\
\mathbf{r}_k &= \mathbf{r}_{k-1} - \alpha_k A \mathbf{p}_{k-1} \\
\mathbf{z}_k &= P^{-1} \mathbf{r}_k \\
\beta_k &= ||\mathbf{r}_k||^2 / ||\mathbf{r}_{k-1}||^2 \\
\mathbf{p}_k &= \mathbf{r}_k + \beta_k \mathbf{p}_{k-1}
\end{aligned} \tag{4.8.10}$$

Until $||\mathbf{b} - A\mathbf{x}_k||$ is below some tolerance.

4.9 Implementation Using FEniCS

FEniCS is an open-source (LGPLv3) computing platform enabling straightforward implementation of the finite element method. The FEniCS Python/C++ interface allows different ways to access the core functionality, ranging from low-level to very high-level access [27]. Finite element meshes can be created using *Mesh.h* tools along with a large variety of finite element basis functions. Codes are written using Unified Form Language (UFL) [27] allowing the user to easily translate the weak formulation into Python/C++ syntax which then call FEniCS routines to assemble local and global linear systems. The resulting global systems are then solved using CG routines available from PETSc libraries. Having both high level functionality and allowing the user access to more fine-grained control of the solution process reduces the lines of code required to implement the numerical scheme.

4.10 Convergence Test for Numerical Scheme

We now present a convergence test for the two-step Taylor-Galerkin finite element scheme for incompressible (4.2.11) and compressible (4.2.12) algorithms for computations of viscoelastic flow. Artificial body force terms are added to the momentum and constitutive equations such that the exact solution of the velocity, stress and pressure are given by

$$u_x(x,y,t) = xf(t) \tag{4.10.1}$$

$$u_y(x,y,t) = -yf(t) \tag{4.10.2}$$

$$p(x,y,t) = \text{constant} \tag{4.10.3}$$

$$C_{xx}(x,y,t) = xf(t) + 1 \tag{4.10.4}$$

$$C_{xy}(x,y,t) = (x+y)f(t) \tag{4.10.5}$$

$$\tau_{yy}(x,y,t) = yf(t) + 1 \tag{4.10.6}$$

where $f(t)$ is a smooth time-dependent function given by

$$f(t) = \exp(-t)\sin(2\pi t) \tag{4.10.7}$$

It is clear that equations (4.10.1)-(4.10.6) do not satisfy the momentum equation and Oldroyd-B constitutive law. Forcing terms are required in order to ensure zero residual between the left and right hand sides. The body force terms are given by

$$\mathbf{F}_u = Re\left(\frac{\partial \mathbf{u}}{\partial t} + \mathbf{u}\cdot\nabla\mathbf{u}\right) + \nabla p - \nabla\cdot\boldsymbol{\tau} - \beta\nabla^2\mathbf{u} \tag{4.10.8}$$

$$\mathbf{F}_{\boldsymbol{\tau}} = \boldsymbol{\tau} + We\left(\frac{\partial \boldsymbol{\tau}}{\partial t} + \mathbf{u}\cdot\nabla\boldsymbol{\tau} - \nabla\mathbf{u}\cdot\boldsymbol{\tau} - \boldsymbol{\tau}\cdot\nabla\mathbf{u}^T\right) - (1-\beta)(\nabla\mathbf{u} + \nabla\mathbf{u}^T) \tag{4.10.9}$$

We use the manufactured solutions to measure the convergence rate of the proposed numerical schemes for both incompressible and compressible flow. The computational error is evaluated in velocity, stress, pressure and temperature by considering the L^2 and H^1 norms in space and l^∞ and l^2 norms in time. Use of these norms gives a sense of spatial and temporal accuracy of the solutions. The definition of the norms we consider are given by

$$\begin{aligned}
||e_{\mathbf{u}}||_{0,\infty} &= \sup_{n=1,2,..N} ||\mathbf{u}^e(t^n) - \mathbf{u}^h(t^n)||_{L^2}(\Omega) \\
||e_{\mathbf{u}}||_{0,0} &= \left(\int_0^T ||\mathbf{u}^e(t^n) - \mathbf{u}^h(t^n)||^2_{L^2}(\Omega) \right)^{1/2} \\
||e_{\mathbf{u}}||_{1,\infty} &= \sup_{n=1,2,..N} ||\mathbf{u}^e(t^n) - \mathbf{u}^h(t^n)||_{H^1}(\Omega) \\
||e_{\mathbf{u}}||_{1,0} &= \left(\int_0^T ||\mathbf{u}^e(t^n) - \mathbf{u}^h(t^n)||^2_{H^1}(\Omega) \right)^{1/2}
\end{aligned} \tag{4.10.10}$$

At each level of mesh refinement the governing equations are solved with $Re = 0.5$, $We = 0.25$, $\beta_v = 0.75$, $\Delta t = h^2$. The stabilisation parameters are chosen to be $c_1 = 0.1$, $c_2 = 0.05$ and DEVSS stabilisation coefficient is $\gamma_u = 0.5$. The time-step is chosen as to ensure CFL conditions are met.

4.10.1 Incompressible Taylor-Galerkin Numerical Scheme

We first present the convergence of the incompressible Taylor-Galerkin numerical scheme (4.2.11).

Figures 4.3(a)-(c) show that the incompressible scheme demonstrates the desired convergence rate.

4.10.2 Compressible & Nonisothermal Taylor-Galerkin Scheme

For the compressible scheme, in addition to the exact solution given by (4.10.1)-(4.10.6) we require two additional prescribed solutions for density and temperature

$$\begin{aligned}
\rho(x,y) &= 1 \\
T(x,y,t) &= (x+y)f(t)
\end{aligned} \tag{4.10.11}$$

In simulations the pressure and density are chosen so that they satisfy the equation state.

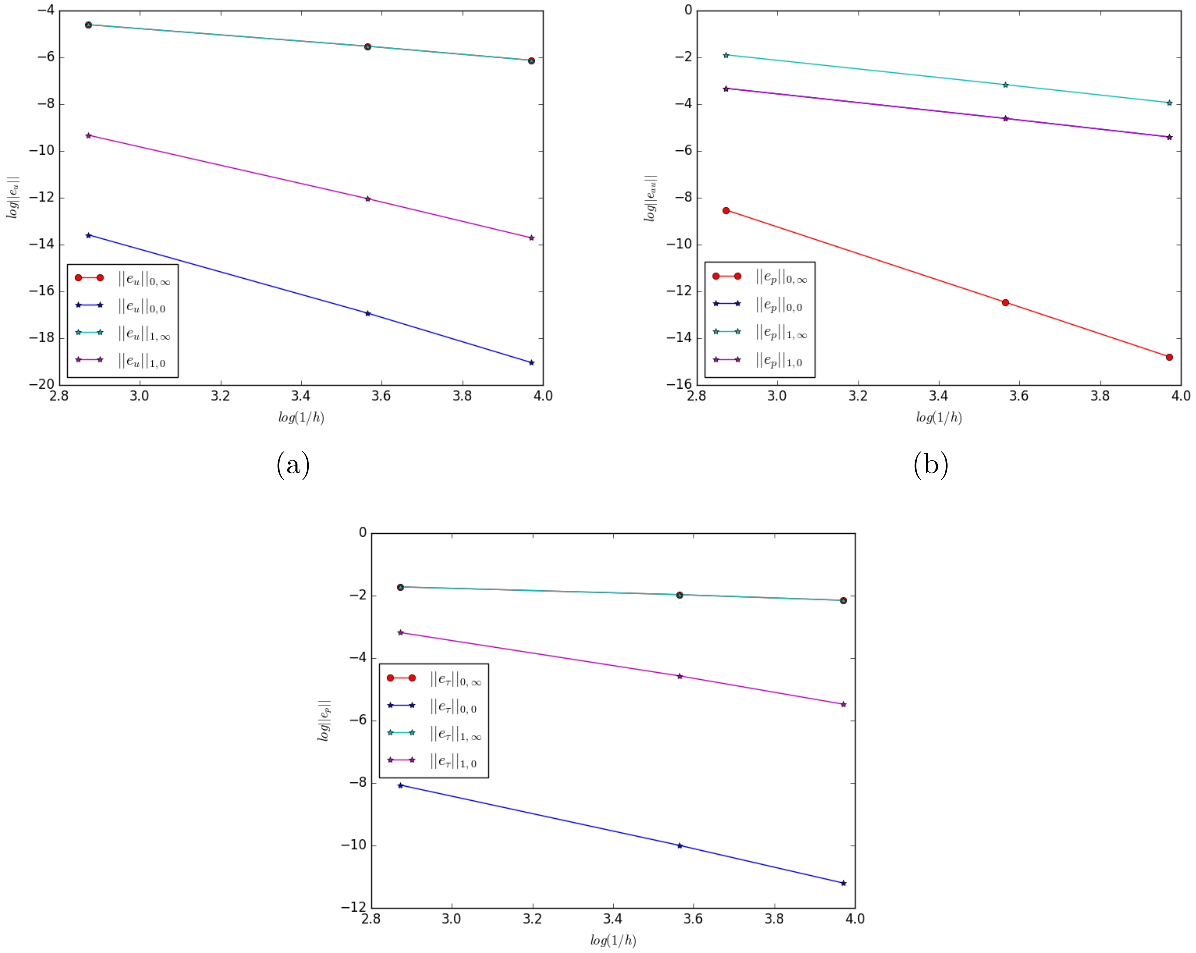

(a)

(b)

(c)

Figure 4.3: Convergence test for incompressible flow numerical scheme ((4.2.11)) (a) $\mathbf{u}$, (b) p and (c) $\boldsymbol{\tau}_p = (1 - \beta_v)/We(\mathbf{C} - \mathbf{I})$.

The additional body force term for the temperature equation is given by

$$\mathbf{F}_\theta = \frac{\partial T}{\partial t} + \mathbf{u} \cdot \nabla T - Di\nabla^2 T - \boldsymbol{\sigma} : \nabla \mathbf{u} \tag{4.10.12}$$

Figures 4.4 (a)-(d) show the convergence for the compressible numerical scheme. The convergence rate for the velocity is the fastest and demonstrates the smallest error for a given norm. Both (4.2.11) and (4.2.12) display the expected rate of convergence in velocity, pressure, stress and temperature as well good agreement with the exact solution.

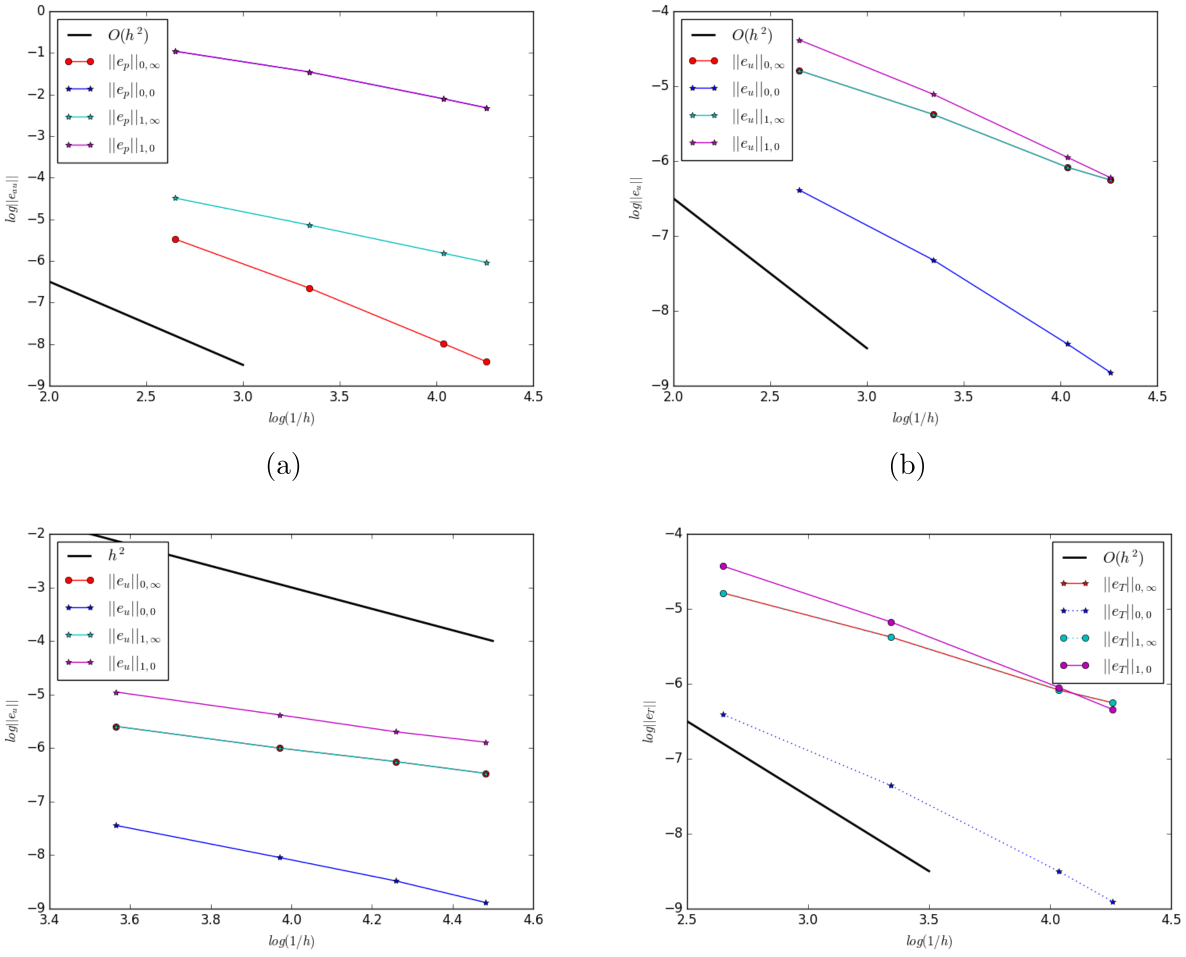

(a) (b)

(c) (d)

Figure 4.4: Convergence test for compressible flow numerical scheme ((4.2.12)) (a) $\mathbf{u}$, (b) p, (c) $\boldsymbol{\tau}_p = (1-\beta_v)/We(\mathbf{C}-\mathbf{I})$ and (d) θ.

4.11 Summary

The numerical method for computing incompressible and compressible viscoelastic flow has been introduced. The governing equations are discretised temporally using a Taylor-Galerkin time marching scheme. At each stage the solutions are approximated spatially using Taylor-Hood elements for velocity and pressure and piecewise linear discontinuous elements for conformation stress. To stabilise the computations the DEVSS formulation is used and orthogonal projection terms are included in the weak formulation. For computations of weakly compressible flow the original forms of the DEVSS formulation have been adapted to provide control over the additional divergence terms in the momentum and stress equations. The resulting solution method for solving the governing equations are coded in Python and mesh generation, local and global matrix assembly are automated using FEniCS/DOLFIN finite element tools. Finally, the stabilised Taylor-Galerkin/finite element scheme for (both incompressible and compressible) show the expected rate of convergence.

Chapter 5

Flows in the Unit Square

5.1 Introduction

In this chapter we consider two benchmark CFD problems with the same physical domain. The flow of a compressible Oldroyd-B fluid is analysed so that comparisons between the incompressible and weakly compressible schemes can be made. In Section 5.2 a solution to the lid-driven cavity flow problem is presented. In Section 5.3 we present an investigation into the buoyancy-driven flow between flat plates (natural convection flow). In both sections the domain, mesh and numerical method are described and solutions for both incompressible and compressible flow are analysed and compared to results from the literature.

5.2 Lid Driven Cavity Flow

Viscoelastic fluids exhibit qualitatively different behaviour to Newtonian fluids under the same flow conditions. Examples of this can be seen in phenomena such as rod-climbing, the Barius effect, siphoning and secondary flows. The difference in behaviour is due to the fact that stress in a viscoelastic fluid is dependent on the strain history, and not solely on the current strain.

The compressibility of the flow is characterised by the flow Mach number, $Ma = U/c_0$.

A Mach number of zero corresponds to an incompressible flow. In many applications of both Newtonian and non-Newtonian flows, Mach number effects are often ignored. However in the processing of polymeric fluids, compression and expansion due to heat/pressure are phenomena that need to be well understood and controlled. Despite this fact the importance of compressibility in non-Newtonian flows has received little coverage in the literature to date. In this section, we consider the flow of an Oldroyd-B fluid in a lid-driven cavity. The lid driven cavity problem is one of the benchmark problems in both Newtonian and non-Newtonian fluid mechanics used to analyse the performance of numerical solution schemes. The 2D geometry, interesting flow behaviour and the plentiful supply of numerical predictions in the literature make it an ideal test problem to study the efficiency of new numerical schemes. We will investigate numerical solutions to both compressible and incompressible Oldroyd-B flow using the Taylor-Galerkin finite element schemes outlined in Chapter 4.

5.2.1 Historical Overview of the Lid Driven Cavity Problem

Viscoelastic flows are present in a wide range of modern day industrial applications of complex fluids. Examples include food production, oil recovery, drug delivery, ink-jet printing, injection moulding and polymer processing. Physical experiments are often costly and impractical and therefore theoretical and computational analysis of viscoelastic flow is a vital tool in the improvement of these industrial processes. Several models exist for viscoelastic fluids such as Oldroyd-B, Giesekus, PTT, FENE-P, FENE-CR. The inherent sophistication of the mathematical models mean that numerical methods are required to obtain solutions to viscoelastic flow problems. Even in simple geometries viscoelastic flows exhibit complex behaviour including transient flow patterns and complex secondary flows [88]. Numerical simulations are a cheap alternative to physical experiments and enable us to make flow predictions that would otherwise be impossible to obtain. Since the 1970s improvements have been made to both the accuracy and computational efficiency of numerical simulations of polymeric fluids. The main contributing factor to this improvement is the increase in computer processing power. However, several hurdles have been overcome in both modelling and numerical analysis.

A large percentage of the literature on non-Newtonian flow is limited to incompressible and isothermal problems. Well-known predictor-corrector schemes such as Chorin's projection method rely on the divergence-free velocity field condition in order to update the velocity at each time step. However enforcing the incompressibility condition results in the pressure becoming a Lagrange multiplier and therefore any thermodynamic information about the pressure is lost [13]. In industrial polymer processing operations, such as injection moulding and high-speed extrusion, pressure, flow rate and temperature variation may be large. Hence, compressibility effects within the viscoelastic regime may become important and influence resulting flow phenomena. The difference between incompressible and compressible flows is determined by the propagation speed of longitudinal waves, c, which couples density with pressure via an equation of state. For incompressible fluids the speed of sound is infinite whereas for compressible fluids the speed is finite. In recent years some work has been done to develop numerical schemes for compressible flow. Keshtiban and Webster [50] developed a Taylor-Galerkin scheme and used it to successfully obtain solutions to several benchmark problems for viscoelastic flow.

Numerical investigations of fluid transport problems involve finding solutions to coupled systems of equations governing momentum, density, pressure and extra-stress (state variables). In the case of Newtonian flow, the extra-stress can be expressed as a linear function of the rate of strain tensor. For viscoelastic flow the extra-stress tensor satisfies its own governing equation (constitutive law) and cannot be eliminated by direct substitution. Furthermore, if the fluid is assumed to be incompressible the density is constant and can be parametrised. In the more general case fluid density is governed by the conservation of mass equation and an equation of state. Detailed theoretical analysis of the laws governing compressible & nonisothermal viscoelastic fluid transport have been undertaken by Beris & Edwards [8, 29] and Bollada & Phillips [13].

A major difficulty for all numerical simulations of viscoelastic flow is the so-called high Weissenberg number problem (HWNP) (see Sec. 4.5), which is the failure of numerical schemes to attain mesh converged solutions to even simple flow problems. Consistent viscoelastic models capturing time dependent relaxation effects use objective derivatives in the constitutive equations, such as the upper convected derivative $(\overset{\triangledown}{\cdot})$. At high Weissenberg numbers, the presence of deformation terms in these derivatives result in steep exponential profiles that are not well captured by polynomial interpolation functions. Errors resulting from the failure to properly balance deformation with convection leads to convergence failure for most numerical solution schemes unless further stabilisation techniques are employed. In order to overcome these challenges, several stabilisation methods have been proposed.

A commonly used technique for combatting the spurious oscillations that arise due to the advection-dominated constitutive equation is the Streamline Upwind Petrov Galerkin (SUPG) method of Brooks and Hughes [14] (see Sec. 4.6.2). SUPG was first implemented to stabilise Oldroyd-B flow calculations by Marchal and Crochet [60]. A similar technique was used by Guénette and Fortin [39] for the analysis of PTT fluids. Another stabilisation widely used is Elastic Viscous Stress Splitting (EVSS), first proposed by Rajanopalan et al. [76]. EVSS was successful in stabilising finite element method solutions to flow between eccentrically rotating cylinders, a benchmark problem greatly affected by the high Weissenberg number problem due to sharp velocity gradients arising in the narrow gap (see Section 6.2 for more details). Subsequently a variety of similar methods have been developed such as Discrete Elastic Viscous Stress Splitting (DEVSS) [39], Explicitly Elliptic Momentum Equation (EEME) [76], DEVSS-G [15] and Discontinuous Galerkin (DG) methods [32]. A large volume of literature concerning stabilised finite element methods for viscoelastic flow can be found. In most cases, finite element methods are stabilised by adding (artificial) mesh-dependent terms to the standard Galerkin approximation equation.

Fattal and Kupferman introduced the log-conformation representation (LCR) method, in which the constitutive equation is reformulated as an equation for the logarithm of the conformation matrix. Using log-conformation representation ensures the stress tensor remains symmetric positive during computations. Similar techniques have been proposed such as the square-root conformation tensor formulation (SRCR), proposed by Balci et al. [2], and the kernel conformation tensor formulation, proposed by Alfonso et al. [1].

In recent years further advancements have been made in overcoming the HWNP for finite element approximations of Oldroyd-B flow. Venkatesan and Ganesan [88] developed a three-field formulation based on one-level Local Projection Stabilisation (LPS) when investigating Oldroyd-B flow in a wide channel. Using enriched approximation spaces and control terms in order to stabilise the constitutive and momentum equations they were able to compute solutions to the benchmark problems flow past a sphere and lid-driven cavity flow for a wide range of Reynolds and Weissenberg numbers.

In this section we consider the flow of both an incompressible ($Ma = 0$) and *compressible* ($Ma > 0$) Oldroyd-B fluid in the unit square (the so called lid-driven cavity problem). The temporal solution scheme implemented is the second-order Taylor-Galerkin pressure-correction scheme detailed in Chapter 4.Numerical results for incompressible flow will be used to benchmark the Taylor-Galerkin pressure correction scheme. Compressible flow dynamics are then analysed over a range of Reynolds, Weissenberg and Mach numbers. Mach numbers in the range $0.001 \leq Ma \leq 0.1$ are considered. Computations are stabilised using DEVSS and orthogonal projection stabilisation with the traditional DEVSS formulation being adapted in order to account for the compressible terms in the strain-rate tensor.

The numerical scheme is implemented on a single CPU desktop using for the coarse meshed approximation and advanced supercomputer RAVEN for the fine mesh. Packages from the FEniCS/DOLFIN finite element library are used in order to build the meshes and spatially discretise the stabilised equations at each time-step. The resulting linear systems of equations are then solved using PETSc Krylov Solver.

5.2.2 Domain & Mesh

The fluid is contained in a square cavity $\Omega = [0, 1] \times [0, 1]$, bounded by solid walls with the top boundary moving in a rightward direction. The boundary is denoted by $\partial\Omega$ with $\partial\Omega = \partial\Omega_1 \cup \partial\Omega_2$. $\partial\Omega_i$, $i \in \{1, 2\}$ are subsets of the boundary, $\partial\Omega_1$ representing the moving lid (top boundary), and $\partial\Omega_2$ the no-slip boundary. Fig. 5.1 illustrates the problem geometry.

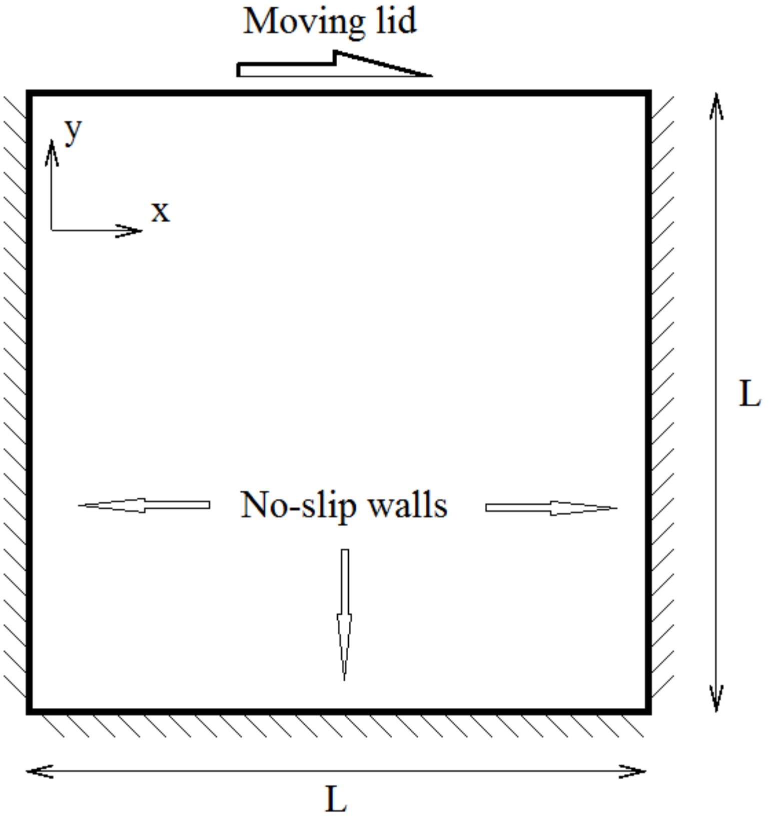

Figure 5.1: Geometry of the 2D lid driven cavity problem

Viscoelastic fluids cannot sustain steep deformations near the upper corners and therefore the lid velocity needs to be regularised such that $\nabla \mathbf{u}$ vanishes at $(0,1)$ and $(1,1)$. Accordingly we use the velocity profile proposed by Venkatesan & Ganesan [88]

$$u_x(x,1,t) = 8[1+\tanh(8(t-0.5))]x^2(1-x)^2 \qquad u_y(x,1,t) = 0 \tag{5.2.1}$$

The velocity is ramped so that $\mathbf{u} \approx (0,0)$ when $t=0$. We also impose that $\boldsymbol{\tau}^p_{ij} = 0$ for $i,j = \{1,2\}$. The average velocity of the lid, $\hat{U}$, is given by

$$\hat{U} = \int_0^1 u_x(x,1,t)\,dx = \frac{4}{15}[1+\tanh(8(t-0.5))] \rightarrow \frac{8}{15} \qquad \text{as}\, t \rightarrow \infty \tag{5.2.2}$$

Sousa et al. [80] showed that the use of this regularisation significantly reduces the strength of the main recirculation region. In order to better mimic the unregularized problem, weaker regularisations can be used so that the fluid is moving at maximum velocity on a larger percentage of the wall.

Finite Element Mesh

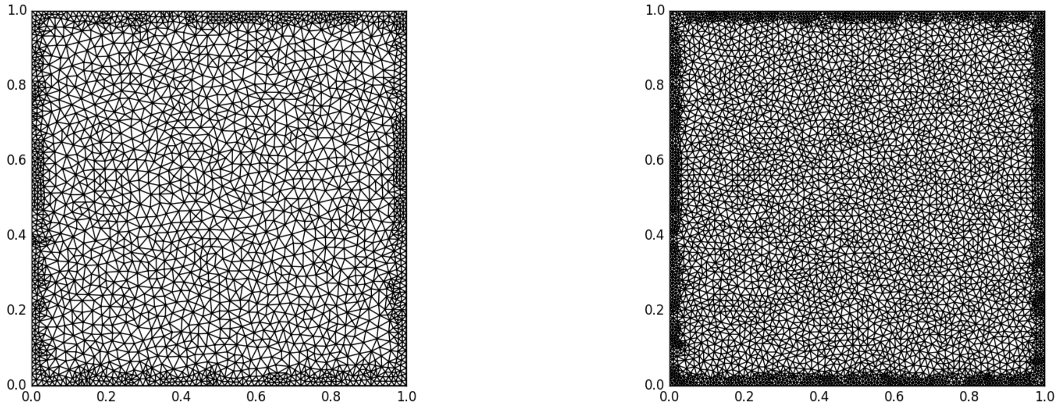

(a) $M1$ (b) $M2$

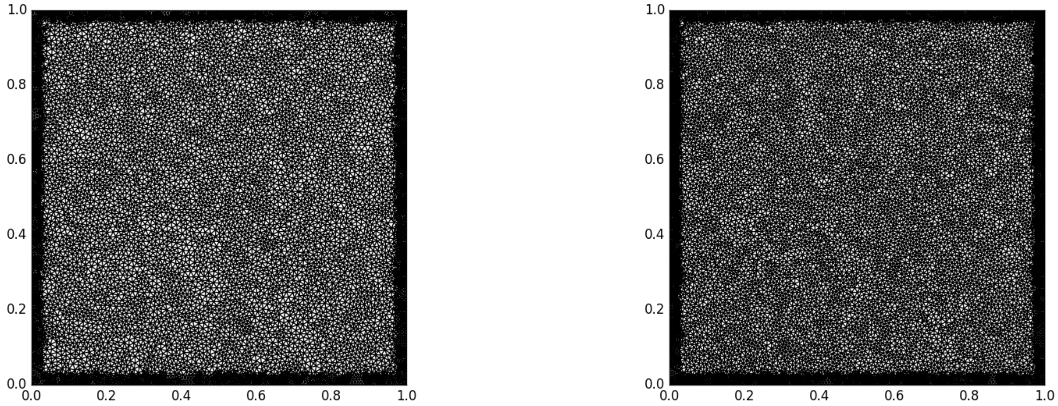

(c) $M3$ (d) $M4$

Figure 5.2: Lid driven cavity: Finite element meshes $M1$ to $M4$.

Mesh	Cells	h_{min}	h_{max}	$DoF(p)$	$DoF(\mathbf{u})$	$DoF(\mathbf{C})$	time/iteration
M1	3535	0.011091	0.039751	1854	14484	21726	0.94
M2	7813	0.007575	0.026512	4069	31900	47850	2.36
M3	13889	0.005321	0.019885	7118	56248	84372	4.36
M4	31024	0.003617	0.013257	15836	125390	188085	7.24

Table 5.1: Lid driven cavity flow: Mesh characteristics $M1$-$M4$

The domain, Ω is decomposed into triangular elements. Fig. 5.2 shows meshes $M1$ to $M4$ and Table 5.1 gives the mesh characteristics. The refinement method used is similar to the technique used by Venkastesan and Ganesan [88] where the cells with centres within $0.05/L$ of the boundary are divided in two by connecting the mid-point of the longest side to the opposite vertex. The cell adjacent to the refined element is also subdivided in the same way to prevent the creation of a hanging node.

5.2.3 Stabilisation

For simulations of both incompressible and compressible flow we use DEVSS (Sec. 4.6.1) with $\gamma_u = 1 - \beta_v$ and orthogonal projection stabilisation (Sec. 4.6.4) with $c_1 = 0.05$ and $c_2 = 0.01$.

5.2.4 Incompressible Flow

In the first instance we consider the incompressible flow of an Oldroyd-B fluid (Eq. (3.1.21)). The nondimensionalised governing equations are given by Eq. (4.1.15) with

$$\mathbf{g}_1(\mathbf{C}, \mathbf{I}) = \frac{1-\beta_v}{We}(\mathbf{C} - \mathbf{I}) \qquad \mathbf{g}_2(\mathbf{C}, \nabla\mathbf{u}) = 0 \tag{5.2.3}$$

and the temporal solution scheme (4.2.11). The fully discretised numerical scheme is given by Eq. (4.7.11)-(4.7.16). The flow behaviour is analysed for $Re = 0$ (inertia-free) up to $Re = 50$ and $0 \leq We \leq 1.0$. All simulations other than the grid independence test are solved on the medium refined mesh $M3$.

5.2.5 Weakly Compressible Viscoelastic Lid Driven Cavity Problem

For the weakly compressible flow of an Oldroyd-B fluid the governing equations are given by Eq. (4.1.14) with g_1 and g_2 given by Eq. (5.2.3). We implement the numerical scheme in Sec. 4.7.2. The flow behaviour is examined for Mach numbers ranging from $Ma = 0.001 - 0.1$ ($c_0 = 10 - 1000$ for $U = 1$). A Mach number of 0.1 may have significant compressible effects whereas a flow with $Ma = 0.001$ (or $c_0 = 1000$m/s for our experiments) behaves effectively as an incompressible fluid. The values of Re and We will be kept the same range as for incompressible flow simulations to allow for quantitative comparison of the compressible effects. Furthermore, for the lid-driven cavity the effects due to temperature gradients in the flow are small in comparison to the impact of the moving lid. As such we will only consider the isothermal equations (setting $\theta = 0$) compressible effects on the flow alone can be investigated (the full nonisothermal model is considered in both Sec. 5.3 and Chapter 6).

5.2.6 Results and Discussion

The flow profiles, stress components, elastic and kinetic energy profiles are presented and analysed. A grid dependency test must be done in order demonstrate that the solutions are mesh convergent. Another common technique employed to analyse the rheological behaviour of polymeric/solvent fluids is the analysis of the energy profile of the flow. For both compressible and incompressible flow the kinetic and elastic energies are given by:

$$E_{kinetic} = \frac{1}{2}\int_{\Omega} \rho \mathbf{u} \cdot \mathbf{u} d\Omega \tag{5.2.4}$$

$$E_{elastic} = \int_{\Omega} \mathrm{tr}(\mathbf{C}) d\Omega \tag{5.2.5}$$

For incompressible flow the (nondimensonalised) density is equal to 1. However, in the case of compressible flow the density has to be evaluated at every point in the computational domain and therefore cannot be factorised out of the integral. The stream function is defined by

$$\psi(x, y, t) = \int_A^P u\,dy - v\,dx \tag{5.2.6}$$

where A and P are points with coordinates (x, y). Alternatively ψ satisfies the differential equation

$$\nabla^2\psi = \frac{\partial u}{\partial y} - \frac{\partial v}{\partial x} \tag{5.2.7}$$

where

$$\mathbf{u} = (u, v) = \left(\frac{\partial \psi}{\partial y}, -\frac{\partial \psi}{\partial x}\right) \tag{5.2.8}$$

The stream function is used to measure both the strength and location of the eye of recirculation in the flow.

Mesh Convergence

First we compare the kinetic and elastic energy profiles for the meshes shown in Fig. 5.2 in order to demonstrate the mesh convergence of the solution. The grid independence test is assurance that the solution is independent of the approximation space used in the numerical scheme. Fig. 5.3 shows the steady state mesh grid values and the relative size of the fluctuation operator, κ where we have defined

$$\kappa = \left(\int_\Omega |\kappa_h|^2 d\Omega\right)^{1/2} \tag{5.2.9}$$

and

$$||\boldsymbol{\tau}|| = \left(\int_\Omega |\hat{\tau}_h|^2 d\Omega\right)^{1/2} \tag{5.2.10}$$

where $\hat{\tau}_h = \frac{\tau_{xx,h}+\tau_{xy,h}+\tau_{yy,h}}{3}$

Furthermore, Figure 5.4 shows the mesh convergence of the solution for $Re = 1$, $Ma = 0.001$ and $We = 0.5$ for the compressible flow problem. We observe that the results tend to a constant value as the number of interpolation points increases.

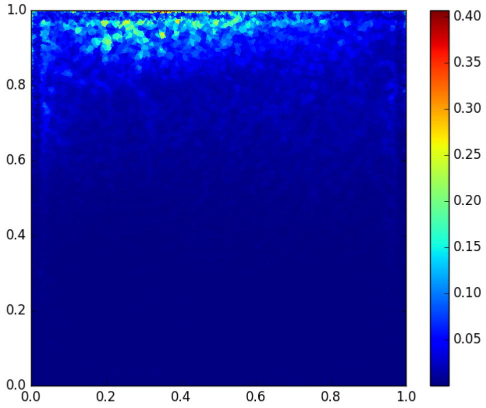

(a)

Figure 5.3: Lid driven cavity flow: (a) Comparison of κ and $||\boldsymbol{\tau}||$ (a) and (b) plot of κ at $t = 2.0$ ($Re = 0$, $We = 0.5$, $\beta_v = 0.5$.)

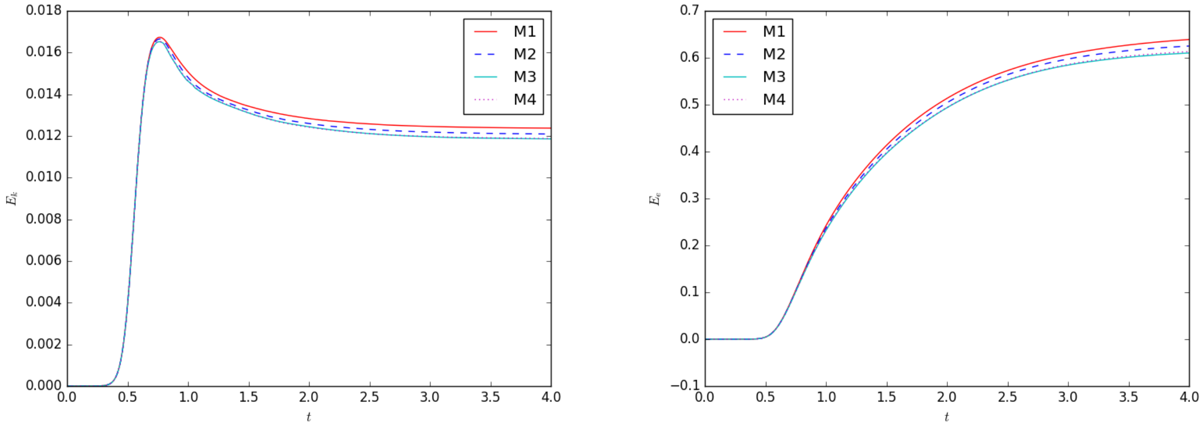

(a) (b)

Figure 5.4: Lid-driven Cavity Flow: Mesh convergence test, kinetic (a) and elastic (b) energy profiles for meshes $M1$-$M4$ ($We = 0.5$, $Re = 1.0$)

Figures 5.4 (a) and (b) show that the error control terms are much smaller in $L^2(\Omega)$ norm than the stress and localised to the region near the top boundary.

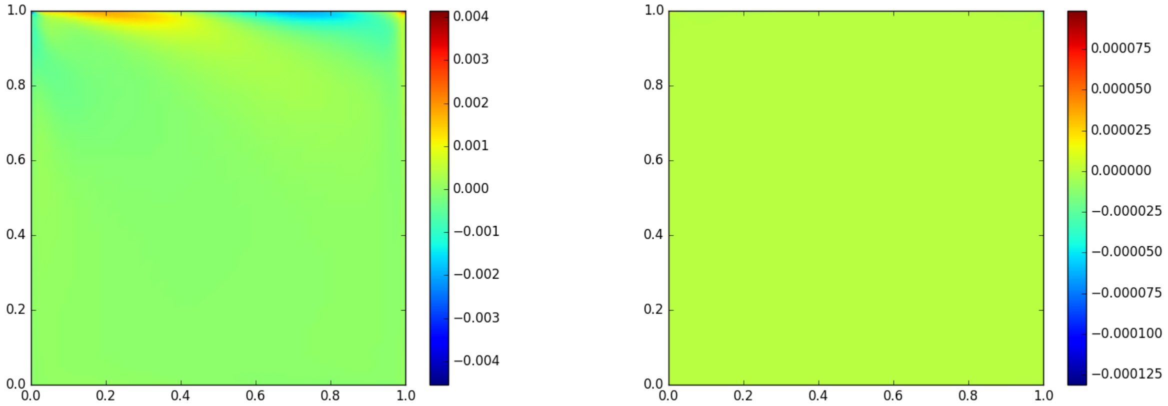

(a) $(\mathbf{D} - \nabla \mathbf{u})_{xx}/||\mathbf{D}_{xx}||$ (b) $(\mathbf{D} - \nabla \mathbf{u})_{xy}/||\mathbf{D}_{xy}||$

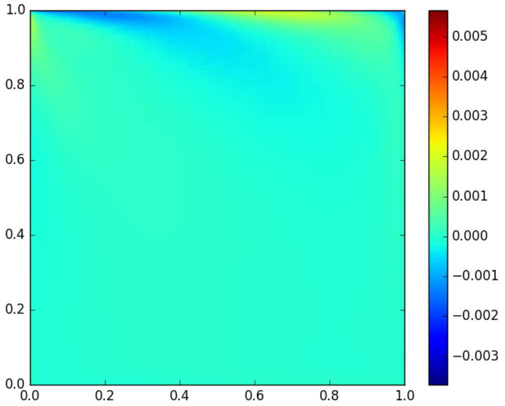

(c) $(\mathbf{D} - \nabla \mathbf{u})_{yy}/||\mathbf{D}_{yy}||$

Figure 5.5: Lid-driven cavity flow: DEVSS numerical diffusion

Incompressible Flow

The results generated using the scheme outlined in Section 4.7.1 agree with results in the literature [31, 80, 88]. Steady state isostreams for $We = 0.5$, $Re = 0$ are displayed in Fig. 5.6 and velocity components are shown in Fig. 5.7. There is a significant build-up of viscoelastic stress in the region near the upper right corner at the re-entry point of the flow, pushing the eye of rotation to the left. Table 5.2.6 shows that results for location and minimum value of the stream function are in good agreement with results in the literature [16, 70, 80, 88]. Figure 5.5 shows the regions of the domain where DEVSS stabilisation terms are largest.

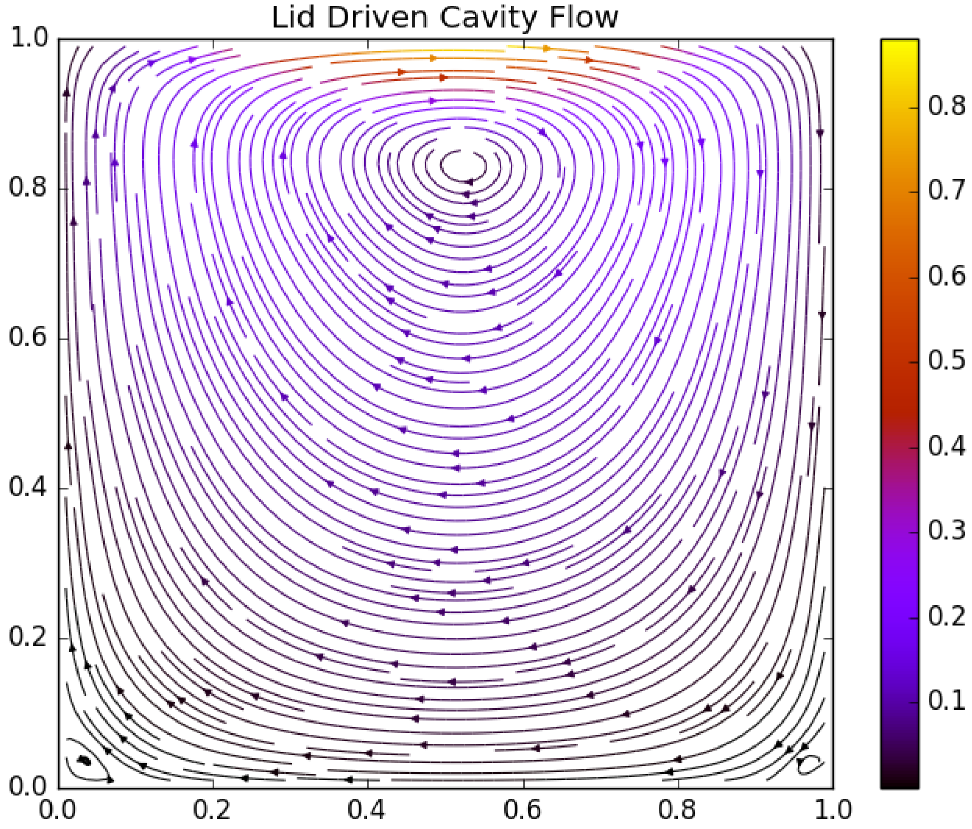

Figure 5.6: Lid driven cavity flow: isostreams at $t = 10.0$. $Re = 0$, $We = 0.5$ at $t = 5.0$.

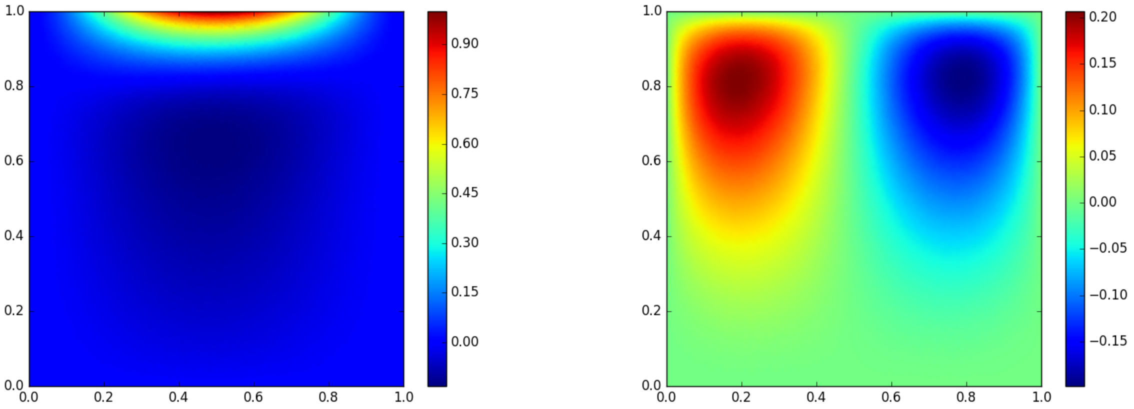

Figure 5.7: Lid driven cavity flow: (a) u_x and (b) u_y $We = 0.5$, $\beta = 0.5$, $Re = 0$ at $t = 10.0$

The regions of the flow where DEVSS stabilisation additions to the approximation equation are most significant are along the top boundary.

Reference	ψ_{min}	x_{min}	y_{min}
Current work	-0.0692665	0.486	0.800
Venkatesan et. al. [88]	-0.0697739	0.470	0.798
Pan et. al. [70]	-0.0700056	0.469	0.798
Sousa et. al. [80]	-	0.467	0.801
Castillo et. al.[16]	-	0.470	0.800

Table 5.2: Incompressible lid driven cavity flow: Comparison of minimum value of stream function and its location with results in the literature for $We = 0.5$. (Table reference [88])

Compressible Flow

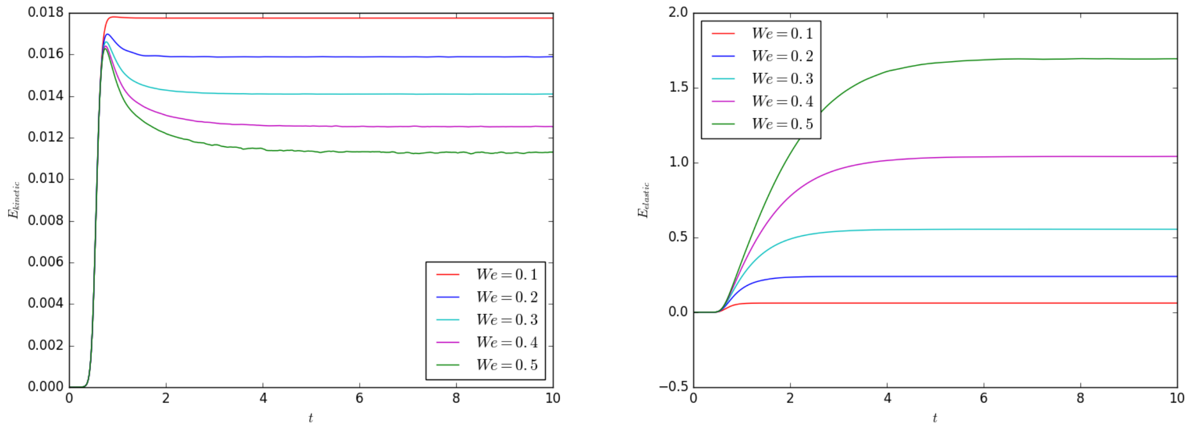

Figure 5.8: Lid-driven cavity Flow: (a) kinetic and (b) elastic energy for $We \in \{0.1, 0.2, 0.3, 0.4, 0.5\}$ and $Re = 5$ and $Ma = 0.01$

Simulations for the compressible flow were generated for $Ma = 0.001, 0.01, 0.1$. At these Mach numbers little distinguishes the qualitative behaviour of flow from the incompressible case but quantitative comparisons of kinetic, elastic energy, centre of rotation and minimum value of the stream function. Lower Mach numbers were tested but simulations of the lid-driven cavity produced significant errors in the density approximation.

The three components of steady-state viscoelastic extra-stress profiles are shown in Figure 5.10. The stress component τ_{xx} has a boundary layer along the upper boundary whilst τ_{xy} and τ_{yy} display large gradients in the upper right-hand corner. It is also observed that the symmetry of the flow is broken due to elastic effects. This is due to the asymmetry of the normal stress values. The eye of the recirculation region shifts upstream. However, this trend is weakened when the Reynolds number is increased above zero.

Figure 5.9 shows the kinetic and elastic energy profiles of the flow for different Ma. As is the case for incompressible flow, the steady state kinetic energy of the fluid is reduced as the Weissenberg number is increased and stored elastic energy is significantly increased. Varying the Mach number in the range $0 \leq Ma \leq 0.1$ doesn't change the underlying behaviour. However, when the Mach number reaches 0.1 unstable behaviour in the flow persists for the first few seconds altering the kinetic energy profile (shown in Fig. 5.14).

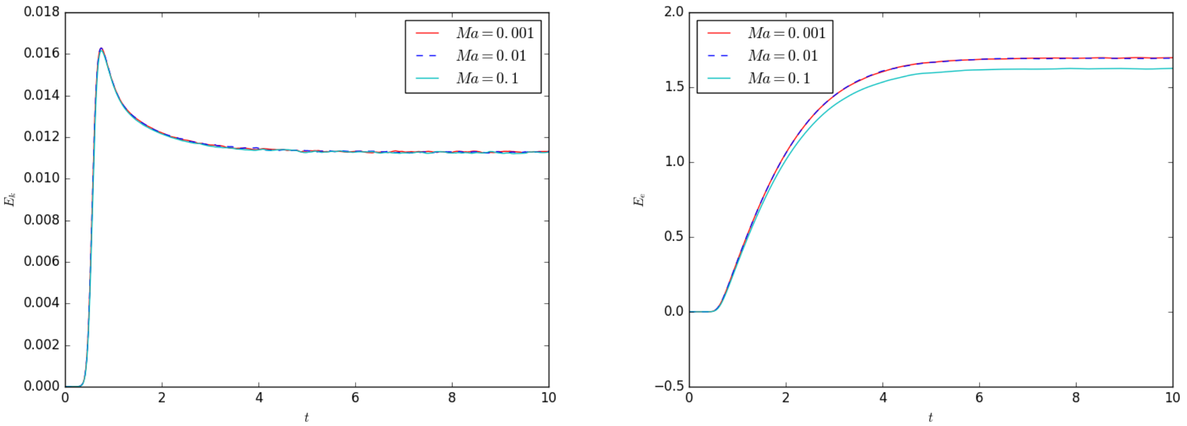

Figure 5.9: Lid-driven cavity Flow: (a) kinetic and (b) elastic energy for $Ma \in \{0.001, 0.01, 0.1\}$, $Re = 1$ and $We = 0.3$

The underlying qualitative behaviour of the flow is the same for both the compressible and incompressible case. The Weissenberg number is the largest contributing factor to the energy profile. The kinetic energy grows as the lid accelerates, reaching a peak between $t = 0.5$ and $t = 1.5$ before falling to a steady state value. The elastic energy grows reaching a plateau proportional to the Weissenberg number. The Weissenberg number has little impact on the peak kinetic energy, which remains close to the steady state value for the Newtonian case.

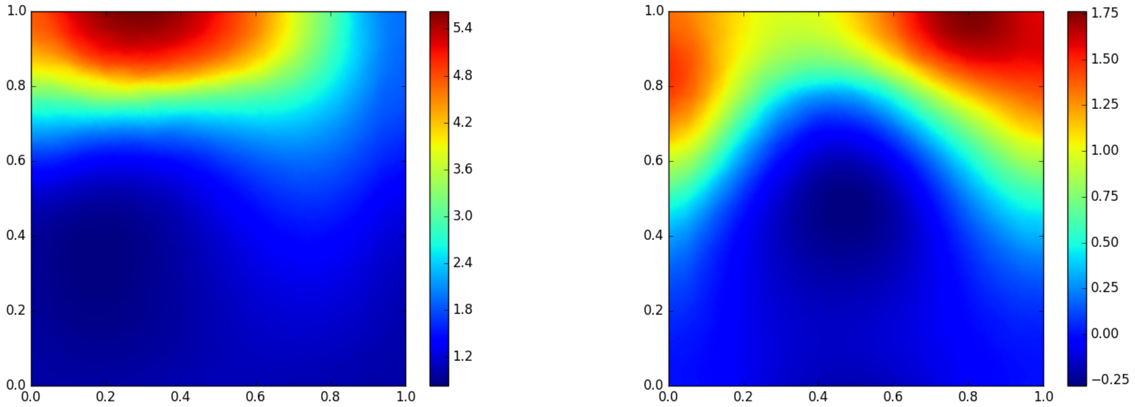

(a) τ_{xx} (b) τ_{xy}

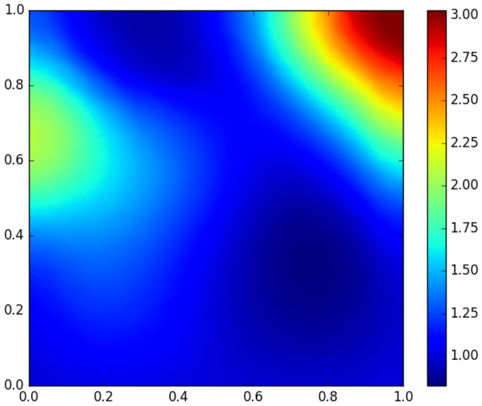

(c) τ_{yy}

Figure 5.10: Lid driven cavity flow : (a) τ_{xx}, (b) τ_{xy}, (c) τ_{yy} $We = 0.5$, $\beta = 0.5$, $Re = 1$, $Ma = 0.01$.

Compressibility does have a noticeable impact on the kinetic and elastic energy profiles. Increasing Ma increases the peak and steady-state kinetic energy and also increases the elastic energy. Figure 5.14 shows the steady state value of the kinetic and elastic energy increasing with Mach number.

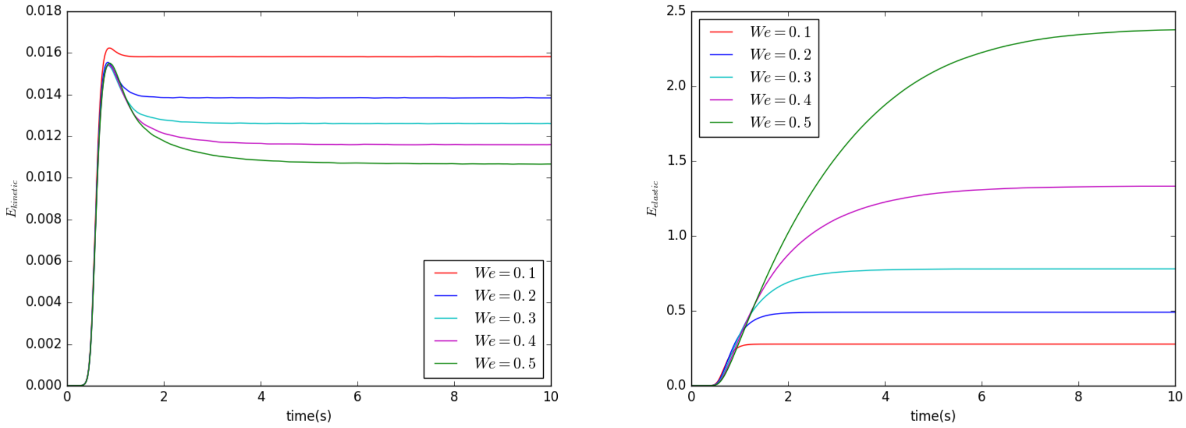

(a)

(b)

Figure 5.11: Lid-driven cavity Flow: Kinetic and elastic energy for $We \in \{0.1, 0.2, 0.3, 0.4, 0.5\}$ and $Re = 1$ and $Ma = 0.01$

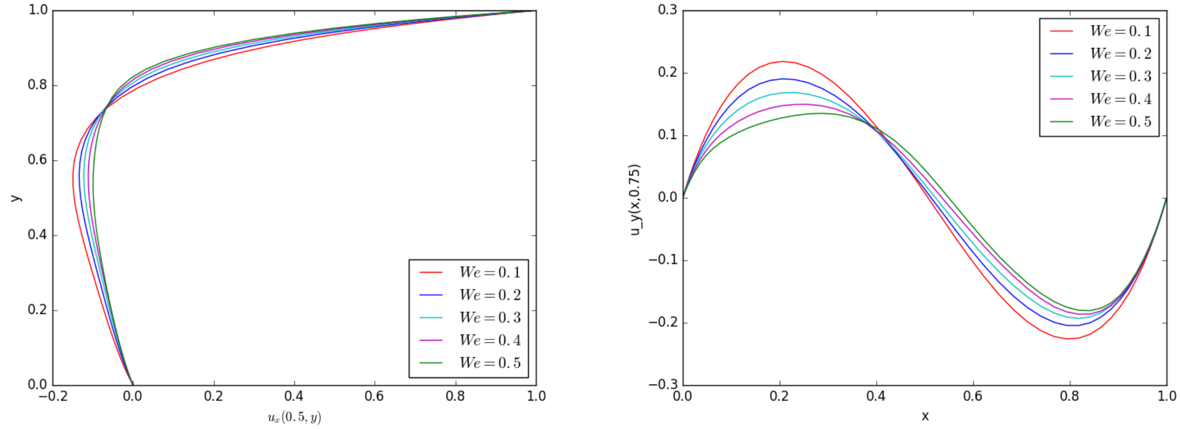

(a) τ_{yy}

(b) τ_{yy}

Figure 5.12: Lid-driven cavity Flow: Cross-section of velocity components for $We \in \{0.1, 0.2, 0.3, 0.4, 0.5\}$ and $Re = 1$ and $Ma = 0.01$

Ma	ψ_{min}	x_{min}	y_{min}
0.001	-0.06428	0.48621	0.81236
0.01	-0.05998	0.48923	0.82663
0.1	-0.05316	0.49112	0.8353

Table 5.3: Compressible lid-driven cavity flow: Dependence of the minimum value of stream function on Ma for $Re = 1$, $We = 0.5$ $Ma = 0.01 - 0.1$

Without inertia the recirculation vortex in the flow is symmetrical about the line $x = 0.5$ if the fluid is Newtonian. Elastic effects cause this symmetry to be broken. As the Weissenberg number is increased the location of the eye moves progressively away from the centre in the direction opposite to the movement of the lid.

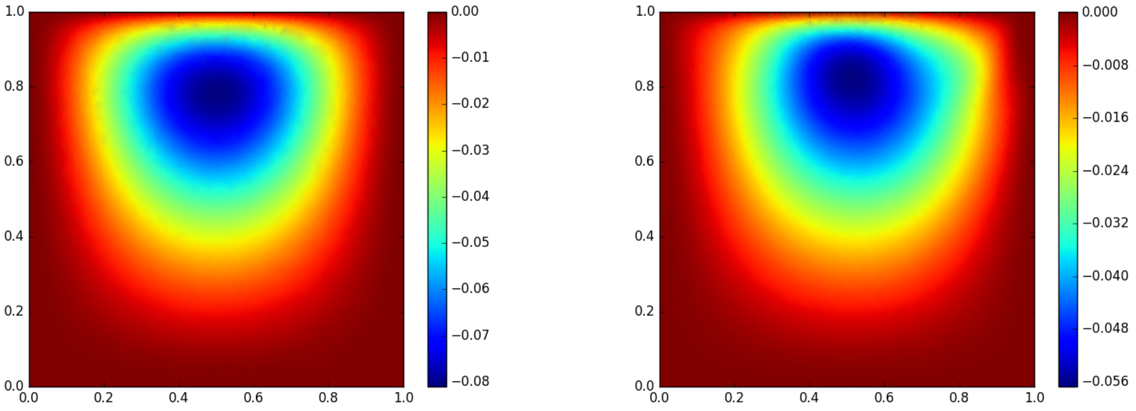

(a) (b)

Figure 5.13: Lid-driven cavity flow: The stream function for (a) $We = 0.1$ and (b) $We = 0.5$ ($Re = 0$ and $Ma = 0.01$)

The kinetic energy is unaffected by changes in Ma and the elastic energy is decreased as Ma is increased meaning viscoelasticity and compressibility have opposite effects on the elastic energy. However at low Mach numbers the results are close to those for incompressible flow. The minimum value of the stream function is the measure used for quantitative comparisons with investigations in the literature. For inertia-less Newtonian flow the eye of rotation remains in a central location. As the Weissenberg number increases the location of the minimum of the stream function shifts leftward and the symmetry of the flow is progressively broken. However, as the Reynolds number is increased, the eye of rotation shifts back towards the centre line $x = 0.5$. Increased compressibility also causes the eye of rotation to shift toward the centre line although the effect is relatively small at low Mach numbers.

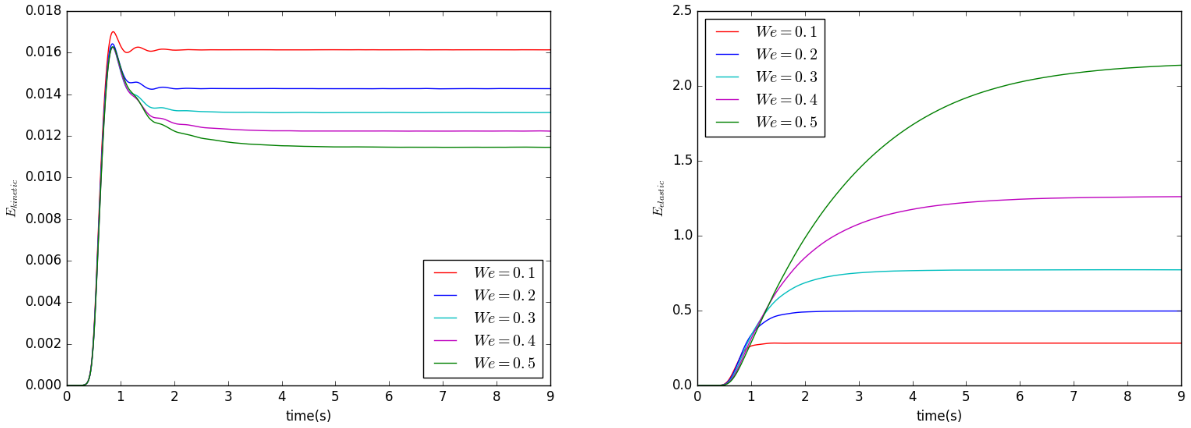

(a) (b)

Figure 5.14: Lid-driven cavity flow: Compressible flow kinetic (a) and elastic (b) energy profiles $We \in \{0.1, 0.2, 0.3, 0.4, 0.5\}$ and $Re = 5$ and $Ma = 0.1$

Ma/We	0.1	0.25	0.5	0.75	1.0
0.001	-0.081305	-0.071771	-0.064276	-0.048152	-0.04250580
0.01	-0.081209	-0.0709576	-0.05998	-0.044981	-0.03763765
0.1	-0.081122	-0.069468	-0.053160	-	-

Table 5.4: Compressible lid driven cavity flow: Comparison of ψ_{min} for $We \in \{0.1, 0.25, 0.5, 0.75, 1.0\}$, $Re = 0$ $Ma \in \{0.001, 0.01, 0.1\}$, $t = 15$.

Ma/We	0.1	0.25	0.5	0.75	1.0
0.001	(0.4922,0.8255)	(0.4897,0.8206)	(0.4842,0.8123)	(0.4806,0.8116)	(0.4746,0.8095)
0.01	(0.4927,0.8255)	(0.4902,0.8205)	(0.4862,0.8266)	(0.4816,0.81)	(0.4760,)
0.1	(0.4931,0.8265)	(0.4917,0.82)	(0.4811,0.8353)	-	-

Table 5.5: Compressible lid driven cavity flow: Comparison of ψ_{min} location for different Weissenberg numbers $Re = 0$ $Ma \in \{0.001, 0.01, 0.1\}$, $t = 15$.

Ma/Re	1	5	10	25	50
0.001	-0.06428	-0.06226	-0.059243	-0.058138	-0.057459626
0.01	-0.05998	-0.062233	-0.059233	-0.058118	-0.05741772
0.1	-0.05316	-0.05298	-0.05265	-	-

Table 5.6: Compressible lid-driven cavity flow: Comparison of ψ_{min} for different Reynolds numbers, $We = 0.5$ $Ma \in \{0.001, 0.01, 0.1\}$, $t = 15$.

Ma/Re	0	5	10	25	50
0.001	(0.486205,0.81236)	(0.48862,0.7866)	(0.4903,0.7686)	(0.4916,0.7458)	(0.4955,0.7215)
0.01	(0.48923,0.82663)	(0.4905,0.7925)	(0.4915,0.7726)	(0.4918,0.7425)	(0.4925,0.7495)
0.1	(0.49112,0.8353)	(0.4918,0.8236)	(0.4925,0.8056)	-	-

Table 5.7: Compressible lid-driven cavity flow: Comparison of ψ_{min} location for different Mach numbers $We = 0.5$, $\beta_v = 0.5$ $Ma \in \{0.001, 0.01, 0.1\}$, $t = 15$.

Compressibility has far less of an impact on the strength and location of the eye of rotation than relaxation time. However, to the extent that it does affect the flow, the results show that it weakens the symmetry-breaking effects of relaxation. Tables 5.4-5.6 show the values and minimum locations of the stream function. In the cases $Re = 25$ and $Re = 50$ for $Ma = 0.1$ the eye of rotation did not reach a steady-state value.

5.3 Natural Convection Flow of an Oldroyd-B Fluid

Nonisothermal flows are of significant interest to both science and industrial manufacturing. Examples of these flows can be found in nuclear reactor systems, geological flows, fire control, polymer processing applications and food production and more. In these cases sufficiently good models for the transport of heat energy need to be coupled with the momentum and constitutive laws to predict flow behaviour.

This section will be organised as follows: A historical overview and literature survey of natural convection flow problem is given in Sec. 5.3.1. A description of the domain and finite element mesh will be given in Section 5.3.2. The governing equations for the incompressible and compressible models will be given in Sections 5.3.4 and 5.3.5, respectively. In both cases the dimensional and nondimensional forms of the equations will be presented along with a description of the nondimensional parameters such as the Rayleigh, Ra, and Prandtl, Pr, numbers. Sections 5.3.4 and 5.3.5 will also cover the weak formulation of the governing equations. Stabilisation techniques for the Galerkin finite element method will be discussed in Section 5.3.3, specifically an adaptation of the DEVSS stabilisation described in section 4.6.1. The computational results are then presented in Sec. 5.3.6.

5.3.1 Historical Overview of the Natural Convection Flow Problem

Modern developments in the understanding of buoyancy driven flows came in the period just after the Second World War [68]. However, it took nearly two decades before a satisfactory description of the problem was discovered and accurate computational models started to appear.

Nonisothermal convection flows are difficult to model because of the complex coupling between the momentum and thermal fields. These types of problems are classified as either forced convection, where the flow is generated by some external pump or fan, or as natural convection, where the flow is a result of density gradients within the flow. Buoyancy-driven flows are either categorised as external (free convection) or internal (natural convection) [68]. The earliest work on natural convection in a completely enclosed geometry was done by Lewis [82], who performed an investigation into ‘foam-like’ insulating materials consisting of gas-filled cells dispersed throughout a solid material. Heat transfer through gas layers in rectangular geometries composed of adiabatic horizontal walls and was first investigated by Batchelor [4, 68]. It was shown that the flow regime within the cavity was dependent on the height to width ratio L/D and the Rayleigh number [4]. For low values of Ra the investigation concluded that conduction was the dominant mode of heat transfer. In the asymptotic limit, $L/D \to \infty$, conduction was also found to be the only means of heat transport.

The first comprehensive study into this class of flow problems was undertaken by Ostrach [66]. It was also pointed out by Ostrach [67] that internal convection flow problems are more complex than external convection flows. The reason for this is that the boundary layer forms an enclosed region around the core of the flow. In turn the flow is dependent on the boundary layer and vice versa. At large Rayleigh numbers the interaction between the two results in the onset of turbulence [68].

With the development of numerical computing methods, simulation of 2D flows in enclosed geometries such as natural convection have become a frequent topic of research papers in applied mathematics. The vast majority of the literature consists of studies of Newtonian flow at Rayleigh numbers ranging from $10^3 - 10^7$, where the solutions provide good predictions of low viscosity/large length scale buoyancy-driven flows. However, the literature on non-Newtonian convective heat flow problems is sparse with very few publications considering fully viscoelastic models. An investigation into power law fluids by Kim et. al [48] found that heat transfer was intensified as the power-law index is increased. An experimental study by Pittman et. al [74] showed that the rheological properties of a fluid are a significant determining factor for its thermal convective properties.

In this investigation we consider the problem of buoyancy driven flow of an Oldroyd-B fluid in a square cavity whose vertical sides are kept at (different) constant temperatures (Dirichlet boundary conditions) and whose horizontal sides are partially insulated (Neumann boundary conditions). Governing equations for both incompressible and weakly compressible flows are analysed. For the incompressible problem, the Boussinesq approximation is used to describe the buoyancy forces.

5.3.2 Domain & Mesh

The domain for the problem is identical to that of the lid-driven cavity (outlined in Sec. 5.2.2). In the case of natural convection flow the regions of Ω with the largest shear rates, and thus largest discontinuities in the finite element approximations of $\nabla \mathbf{u}$ are closest to the boundary Γ. A uniform mesh is generated by dividing the unit square into N equally spaced intervals and triangulating using either left or right diagonals of each square. A node positioned at (x^i, y^i) in the uniform mesh is mapped to (ξ^i, η^i) using the following equations

$$\begin{aligned} \xi^i &= \frac{1}{2}(1 - \cos(\pi x^i)) \\ \eta^i &= y \end{aligned} \tag{5.3.1}$$

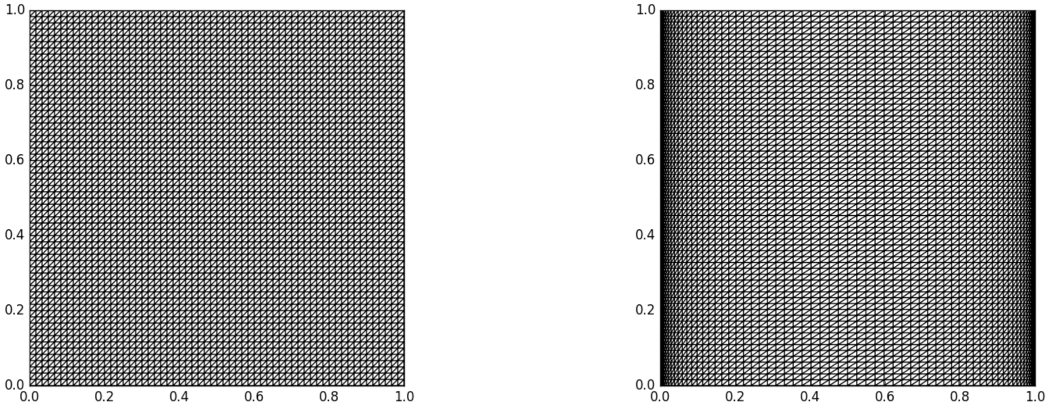

(a) (b)

Figure 5.15: Uniform (a) vs non-uniform (b) 64×64 (M2) mesh over $\Omega = [0, L] \times [0, L]$, $L = 1$

Mapping the location of the element vertices using Eq. (5.3.1) concentrates the interpolation points close to the left and right walls. Characteristics of the different meshes used are given in Table 5.8.

Mesh	Cells	h_{min}	h_{max}	$DoF(p)$	$DoF([\mathbf{u}, \mathbf{D}])$	$DoF(\boldsymbol{\tau}_p)$	$DoF(\theta)$
M1	4608	0.02086	0.03877	2401	60290	28227	2401
M2	8192	0.01564	0.02909	4225	107010	49923	4225
M3	12800	0.01251	0.02327	6561	167042	77763	6561
M4	18432	0.010420	0.019394	9409	240386	111747	9409

Table 5.8: Natural convection flow: characteristics of the finite element meshes - coarse ($M1$) to fine ($M4$)

Mesh	time/iteration (s)
M1	1.812
M2	3.372
M3	6.152
M4	9.504

Table 5.9: Natural convection flow: CPU run time per iteration (timestep) on coarse ($M1$) to fine ($M4$) meshes

The time/iteration is the mean of time taken per timestep loop when the compressible solution scheme (see Sec. 5.3.5) is implemented on a single CPU desktop.

5.3.3 Stabilisation

Just as in Section 5.2.3 we use a combination of DEVSS and local projection stabilisation. For all computations the stabilisation parameters are chosen to be $\gamma_u = 1 - \beta_v$, $c_1 - 0.1$ and $c_2 = 0.05$

5.3.4 Incompressible Flow w/ Boussinesq Approximation

For natural convection flow an alternative scaling is used as we now have to consider a body force in the governing equations.

Governing Equations & Boundary Conditions

In the first case we investigate the incompressible flow problem. Invoking the *Boussinesq approximation*, thermophysical properties of the fluid are assumed to be constant (i.e. no equation of state coupling pressure, density and temperature required). The density is assumed to have *linear dependence on temperature* and the compressible effects are contained within the body force term by using the

$$\rho = \rho_0(1 - \beta(T - T_c)) \tag{5.3.2}$$

where ρ_0 is the density at a reference temperature T_c. By invoking the Boussinesq approximation we are also able to fully couple the momentum and temperature equations. The governing system of equations are given by (4.1.4) with an additional body force term added to the right-hand side of the momentum equation. We impose the divergence-free velocity condition and therefore the governing system can be written

$$\begin{aligned}
&\nabla \cdot \mathbf{u} = 0 \\
&\frac{D\mathbf{u}}{D\mathbf{t}} = -\frac{1}{\rho}\nabla p + \nu \nabla^2 \mathbf{u} + \frac{1}{\rho}\nabla \cdot \boldsymbol{\tau}_p + g\beta(T - T_c)\mathbf{k} \\
&\boldsymbol{\tau}_p = \mathbf{g}_1(\mathbf{C}, \mathbf{I}) \qquad (5.3.3) \\
&\mathbf{C} + \lambda(T)(\overset{\triangledown}{\mathbf{C}} + (\nabla \cdot \mathbf{u})\mathbf{C}) + \mathbf{g}_2(\mathbf{C}, \mathbb{D}) = \mathbf{I} \\
&\rho C_p \frac{DT}{Dt} = -\nabla \cdot \mathbf{q} + \mathbb{T} : \nabla \mathbf{u}
\end{aligned}$$

where $\nu = \mu/\rho_0$is the kinematic viscosity and $\mathbf{k} = (0, -1)$. As discussed in Sec. 2.4 the form of $\mathbf{q}$ is dependent on the thermal conductivity matrix, $\boldsymbol{\alpha}$. We will assume that the thermal conductivity is isotropic, therefore

$$\mathbf{q} = -\kappa \nabla T \qquad (5.3.4)$$

Furthermore the constitutive equation we consider is the Oldroyd-B model

$$\mathbf{g}_1 = \frac{1 - \beta_v}{We}(\mathbf{C} - \mathbf{I}) \qquad \mathbf{g}_2 = 0 \qquad (5.3.5)$$

The boundary conditions for the problem are given by

$$\begin{aligned}
&u(t, x, 0) = u(t, x, L) = 0 = u(t, 0, y) = u(t, L, y) \\
&T(t, 0, y) = T_l(t) \quad T(t, L, y) = T_c \qquad (5.3.6) \\
&\frac{\partial T}{\partial t}(t, x, L) = hT
\end{aligned}$$

where $T_l(t)$ and T_c are temperatures at the hot (left) and cold (right) walls, respectively. The left wall is heated from an initial temperature T_0 to T_h using a smooth ramping function

$$T_l(t) = T_0 + \frac{1}{2}(T_h - T_0)(1 + \tanh(8(t - 0.5))) \tag{5.3.7}$$

Throughout these simulations we will set

$$T_0 = 300K \qquad\qquad T_h = 350K \tag{5.3.8}$$

The appropriate parameter scalings required for nondimensionalisation in natural convection flow differ from those outlined in Sec. 4.1. This is because the thermal diffusivity, defined

$$\alpha = \frac{\kappa}{\rho C_p} \tag{5.3.9}$$

is much more important than the dynamic viscosity in determining the flow behaviour. Using the following change of variables

$$\begin{aligned}
&x^* = \frac{x}{L}, \quad y^* = \frac{y}{L}, \quad \mathbf{u}^* = \frac{\mathbf{u}L}{\alpha} \\
&p^* = \frac{pL^2}{\rho\alpha^2}, \quad \mathbf{C}^* = \mathbf{C}\frac{L^2}{\rho\alpha\nu}, \quad t^* = t\frac{\alpha}{L^2} \\
&\theta = \frac{T - T_c}{T_h - T_c}
\end{aligned} \tag{5.3.10}$$

The governing equations are given by

Substituting (5.3.10) into (5.3.3) results in the following dimensionless set of governing equations

$$\begin{aligned}
\nabla \cdot \mathbf{u} &= 0 \\
\frac{D\mathbf{u}}{Dt} &= -\nabla p + Pr[\beta_v \nabla^2 \mathbf{u} + \nabla \cdot \boldsymbol{\tau}_p] + RaPr\theta\mathbf{k} \\
\mathbf{C} + We\,\overset{\triangledown}{\mathbf{C}} &= \mathbf{I} \\
\frac{D\theta}{Dt} &= \nabla^2\theta + V_h \mathbb{T}^n : \nabla\mathbf{u}
\end{aligned} \tag{5.3.11}$$

where * notation has been dropped. The respective boundary conditions are given by

$$\begin{aligned}
&u(t,x,0) = u(t,x,1) = 0 = u(t,0,y) = u(t,1,y) \\
&\theta(t,0,y) = \theta_h(t) \quad \theta(t,1,y) = 1 \\
&\frac{\partial \theta}{\partial \mathbf{n}}(t,x,1) = Bi\theta
\end{aligned} \tag{5.3.12}$$

where the dimensionless groups are given by

$$\begin{aligned}
&Ra = \frac{L^3\beta g}{\nu\alpha}(T_h - T_c), \quad Pr = \frac{\nu}{\alpha} \\
&We = \frac{\lambda\alpha}{L^2}, \quad V_h = \frac{\alpha^2\mu}{(T_h - T_c)\kappa L^2}, \quad Bi = \frac{Lh_c}{\kappa}
\end{aligned} \tag{5.3.13}$$

and h_c is the heat transfer coefficient. The Rayleigh number is the nondimensional number associated with the convection in the fluid. Beyond a critical value, heat transfer in a fluid is dominated by convection. We choose the boundary condition for the hot wall Γ_3 to smoothly increase from $\theta = 0$ up to $\theta = 1$ when $0 \leq t \leq 1$.

Solution Method

As in Section 5.2.4, the discrete finite element spaces are chosen so that LBB conditions are satisfied. This means Taylor-Hood elements for velocity and pressure, discontinuous piecewise linear elements for stress and continuous linear elements for temperature. The resulting systems of algebraic equations are given by

Velocity Half-Step

$$\begin{aligned}\sum_{j=1}^{N_V}[2(\boldsymbol{\phi}_j,\boldsymbol{\phi}_i)+\Delta t[\gamma_u(\mathbf{a}(\boldsymbol{\phi}_j,\boldsymbol{\phi}_i))-\mathbf{e}(\boldsymbol{\phi}_j,\boldsymbol{\xi}_r)]]\mathbf{U}_j^{n+\frac{1}{2}}+\Delta t\sum_{j=1}^{N_Z}[(\boldsymbol{\xi}_j,\boldsymbol{\xi}_k)-\mathbf{c}(\boldsymbol{\xi}_j,\boldsymbol{\phi}_i)]\mathbf{D}_j^{n+\frac{1}{2}}&\\ =\sum_{j=1}^{N_V}[2(\boldsymbol{\phi}_j,\boldsymbol{\phi}_i)-\Delta t[Pr\beta\mathbf{a}(\boldsymbol{\phi}_j,\boldsymbol{\phi}_i)+\mathbf{b}(\mathbf{u}_h^n;\boldsymbol{\phi}_j,\boldsymbol{\phi}_i)]]\mathbf{U}_j^n+Pr\Delta t\sum_{j=1}^{N_Z}\mathbf{c}(\boldsymbol{\xi}_j,\boldsymbol{\phi}_i)\mathbf{T}_j^n&\\ -\Delta t\sum_{j=1}^{N_Q}\mathbf{d}(\zeta_j,\boldsymbol{\phi}_i)\mathbf{P}_j^n+RaPr\sum_{j=1}^{N_V}(\zeta_j,\boldsymbol{\phi}_i)\boldsymbol{\theta}_i k_i&\end{aligned}\tag{5.3.14}$$

Stress Half-Step

$$\begin{aligned}2We\sum_{j=1}^{N_Z}(\boldsymbol{\xi}_j,\boldsymbol{\xi}_i)\mathbf{T}_j^{n+\frac{1}{2}}+\sum_{j=1}^{N_Z}\mathbf{s}(\boldsymbol{\xi}_j,\boldsymbol{\xi}_i)=&(2We-\Delta t)\sum_{j=1}^{N_Z}(\boldsymbol{\xi}_j,\boldsymbol{\xi}_i)\mathbf{T}_j^n+\sum_{j=1}^{N_V}(\boldsymbol{\phi}_j,\boldsymbol{\xi}_i)\\ &-We\Delta t\sum_{j=1}^{N_Q}\mathbf{f}(\mathbf{u}_h^n;\boldsymbol{\xi}_j,\boldsymbol{\xi}_i)\mathbf{T}_j^n\end{aligned}\tag{5.3.15}$$

Temperature Half-Step

$$\sum_{j=1}^{N_Q}[2(\zeta_j,\zeta_i)+\Delta t[\mathbf{d}(\zeta_j,\boldsymbol{\phi}_i)]\boldsymbol{\theta}_j^{n+\frac{1}{2}}=\sum_{j=1}^{N_V}[2(\zeta_j,\zeta_i)-\Delta t[\mathbf{g}(\zeta_j,\zeta_i)]]\boldsymbol{\theta}_j^n+\Delta t\sum_{j=1}^{N_Z}\mathbf{n}(\mathbf{u}_h^n;\mathbf{C}_{p,h}^n\boldsymbol{\xi}_j,\zeta_i)\tag{5.3.16}$$

Predictor Step

$$
\begin{aligned}
&\sum_{j=1}^{N_V}[(\boldsymbol{\phi}_j,\boldsymbol{\phi}_i)+Pr\Delta t[\gamma_u(\mathbf{a}(\boldsymbol{\phi}_j,\boldsymbol{\phi}_i))-\mathbf{e}(\boldsymbol{\phi}_j,\boldsymbol{\xi}_r)]]\mathbf{U}_j^{*}+\Delta t\sum_{j=1}^{N_Z}[(\boldsymbol{\xi}_j,\boldsymbol{\xi}_k)-\mathbf{c}(\boldsymbol{\xi}_j,\boldsymbol{\phi}_i)]\mathbf{D}_j^{*}\\
&\quad=\sum_{j=1}^{N_V}[(\boldsymbol{\phi}_j,\boldsymbol{\phi}_i)-Pr\Delta t\frac{\beta}{2}\mathbf{a}(\boldsymbol{\phi}_j,\boldsymbol{\phi}_i)\mathbf{U}_j^{n}-\Delta t\sum_{j=1}^{N_V}\mathbf{b}(\mathbf{u}_h^{n+\frac{1}{2}};\boldsymbol{\phi}_j,\boldsymbol{\phi}_i)\mathbf{U}_j^{n+\frac{1}{2}}+Pr\Delta t\sum_{j=1}^{N_Z}\mathbf{c}(\boldsymbol{\xi}_j,\boldsymbol{\phi}_i)\mathbf{T}_j^{n+\frac{1}{2}}\\
&\quad-\Delta t\sum_{j=1}^{N_Q}\mathbf{d}(\zeta_j,\boldsymbol{\phi}_i)\mathbf{P}_j^{n}+RaPr\sum_{j=1}^{N_V}(\zeta_j,\boldsymbol{\phi}_i)\boldsymbol{\theta}_i F_i^{g}
\end{aligned}
\tag{5.3.17}
$$

Pressure Correction

$$
\sum_{j=1}^{N_Q}\mathbf{g}(\zeta_j,\zeta_i)P_j^{n+1}=\sum_{j=1}^{N_Q}\mathbf{g}(\zeta_j,\zeta_i)P_j^{n}+\frac{1}{\Delta t}\sum_{j=1}^{N_V}\mathbf{d}(\boldsymbol{\phi}_j,\zeta_i)\mathbf{U}_j^{n}
\tag{5.3.18}
$$

Velocity Full Step

$$
\sum_{j=1}^{N_V}[(\boldsymbol{\phi}_j,\boldsymbol{\phi}_i)+\Delta tPr\frac{\beta}{2}(\mathbf{a}(\boldsymbol{\phi}_j,\boldsymbol{\phi}_i))]\mathbf{U}_j^{n+1}=\sum_{j=1}^{N_V}[(\boldsymbol{\phi}_j,\boldsymbol{\phi}_i)-\frac{\Delta t}{2}\sum_{j=1}^{N_Q}\mathbf{d}(\zeta_j,\boldsymbol{\phi}_i)(\mathbf{P}_j^{n+1}-\mathbf{P}_j^{n})
\tag{5.3.19}
$$

Stress Full Step

$$
\begin{aligned}
(We+\Delta t)\sum_{j=1}^{N_Z}(\boldsymbol{\xi}_j,\boldsymbol{\xi}_i)\mathbf{T}_j^{n+1}=&We\sum_{j=1}^{N_Z}(\boldsymbol{\xi}_j,\boldsymbol{\xi}_i)\mathbf{T}_j^{n}+\sum_{j=1}^{N_V}(\boldsymbol{\phi}_j,\boldsymbol{\xi}_i)\\
&-We\Delta t\sum_{j=1}^{N_Q}\mathbf{f}(\mathbf{u}_h^{n};\boldsymbol{\xi}_j,\boldsymbol{\xi}_i)\mathbf{T}_j^{n}
\end{aligned}
\tag{5.3.20}
$$

Temperature Full Step

$$\sum_{j=1}^{N_Q}[(\zeta_j,\zeta_i)+\Delta t[\mathbf{d}(\zeta_j,\boldsymbol{\phi}_i)]\boldsymbol{\theta}_j^{n+\frac{1}{2}}=\sum_{j=1}^{N_V}[(\zeta_j,\zeta_i)-\Delta t[\mathbf{g}(\zeta_j,\zeta_i)]]\boldsymbol{\theta}_j^{n}+\Delta t\sum_{j=1}^{N_Z}\mathbf{n}(\mathbf{u}_h^n;\boldsymbol{\tau}_{p,h}^n\boldsymbol{\xi}_j,\zeta_i) \tag{5.3.21}$$

where $k_i = -1 + (-1)^i$. The bilinear forms are defined in in Eq. (4.7.2) with the additional bilinear forms in the temperature update steps given by

$$\begin{aligned}(\theta, r) &= \int_\Omega \theta r \, d\Omega \\ \mathbf{m}(\mathbf{u},\theta,r) &= \int_\Omega \mathbf{u}\cdot\nabla\theta r \, d\Omega \\ \mathbf{n}(\beta_v;\mathbf{u};\boldsymbol{\tau}_p,r) &= \int_\Omega [(\beta_v\mathbb{D}+\boldsymbol{\tau}_p):\nabla\mathbf{u}] r \, d\Omega\end{aligned} \tag{5.3.22}$$

Eq. (5.3.14)-(5.3.21) can be expressed in matrix form as the following set of matrix equations:

$$\begin{bmatrix}\mathbf{M}^V+\Delta t Pr\beta_v\mathbf{A} & -\Delta t\gamma_v\mathbf{C}^Z\\ -\Delta t\mathbf{E} & \Delta t\mathbf{M}^Z\end{bmatrix}\begin{bmatrix}\mathbf{U}^{n+\frac{1}{2}}\\ \mathbf{D}^{n+\frac{1}{2}}\end{bmatrix}=\begin{bmatrix}\tilde{\boldsymbol{\mathcal{F}}}_1^u\\ 0\end{bmatrix} \tag{5.3.23}$$

$$2We\mathbf{M}^Z\mathbf{T}^{n+\frac{1}{2}}+\mathbf{S}_1^{n+1/2}=[(2We-\Delta t)\mathbf{M}^Z-We\mathbf{F}^n]\mathbf{T}^n+\hat{\mathbf{I}} \tag{5.3.24}$$

$$(\mathbf{M}^Q+\Delta t\mathbf{A}^Q)\boldsymbol{\theta}^{n+\frac{1}{2}}=\tilde{\boldsymbol{\mathcal{F}}}_2^\theta \tag{5.3.25}$$

$$\begin{bmatrix}\mathbf{M}^V+\Delta t Pr\beta_v\mathbf{A}^V & -\Delta t\gamma_v\mathbf{C}^Z\\ -\Delta t\mathbf{E}^V & \Delta t\mathbf{M}^Z\end{bmatrix}\begin{bmatrix}\mathbf{U}^{*}\\ \mathbf{D}^{*}\end{bmatrix}=\begin{bmatrix}\tilde{\boldsymbol{\mathcal{F}}}_2^u\\ 0\end{bmatrix} \tag{5.3.26}$$

$$\mathbf{G}^Q\boldsymbol{P}^{n+1}=\mathbf{G}^Q\boldsymbol{P}^{n}+\frac{1}{\Delta t}D^T\mathbf{U}^* \tag{5.3.27}$$

$$\begin{bmatrix}\mathbf{M}^V+\Delta t Pr\beta_v\mathbf{A}^V & -\Delta t\gamma_v\mathbf{C}^Z\\ -\Delta t\mathbf{E}^V & \Delta t\mathbf{M}^Z\end{bmatrix}\begin{bmatrix}\mathbf{U}^{n+1}\\ \mathbf{D}^{n+1}\end{bmatrix}=\begin{bmatrix}\tilde{\boldsymbol{\mathcal{F}}}_3^u\\ 0\end{bmatrix} \tag{5.3.28}$$

$$(We + \Delta t)\mathbf{M}^{Z}\mathbf{T}^{n+1} + \mathbf{S}_{1}^{n+1} = [We\mathbf{M}^{Z} - We\mathbf{F}^{n+\frac{1}{2}}]\mathbf{T}^{n+\frac{1}{2}} + \hat{\mathbf{I}} \tag{5.3.29}$$

$$(\mathbf{M}^{Q} + \Delta t\mathbf{A}^{Q})\boldsymbol{\theta}^{n+1} = \tilde{\boldsymbol{\mathcal{F}}}_{2}^{\theta} \tag{5.3.30}$$

5.3.5 Weakly Compressible Flow

We now consider buoyancy-driven flow using a weakly compressible variable density formulation. The motivation behind using this method is to circumvent the use of the Boussinesq approximation. In doing so we can permit a larger range of density and temperature variation within the flow. The incompressibility constraint is relaxed and consider the full set of governing equations given by Eq. (4.1.14). We use the equation of state given by Eq. (4.1.2) to couple density, pressure and temperature.

Governing Equations & Discretisation

In order to fully couple the momentum and energy conservation laws we need an equation of state relating density and temperature. Implicit in the weakly compressible Taylor Galerkin scheme is the relation between density and pressure

$$p + B = B\rho^m \tag{5.3.31}$$

This isothermal equation of state is empirically derived and is suitable for polymer melts and solutions and other liquids under the linear approximation ($m = 1$). In that case

$$\frac{\partial p}{\partial \rho} = \frac{(B + p)m}{\rho} = c_0^2 \tag{5.3.32}$$

In the linear case we effectively use the relationship

$$p = c_0^2(\rho) - B \tag{5.3.33}$$

where c_0 is the speed of sound. The nonisothermal extension to this equation is defining

$$\rho = \tilde{\rho}\frac{\hat{\beta}_0}{\hat{\beta}_1 + \hat{\beta}_2 T} \tag{5.3.34}$$

where β_i $i \in \{1, 2, 3\}$ are parameters to be determined empirically.

So the equation of state is extended to

$$p = c_0^2 \rho \left(\frac{\hat{\beta}_0}{\hat{\beta}_1 + \hat{\beta}_2 T} \right) - B \tag{5.3.35}$$

and can be written in the form

$$\frac{\partial p}{\partial \rho} = c_0^2 \left(\frac{\hat{\beta}_0}{\hat{\beta}_1 + \hat{\beta}_2 T} \right) \tag{5.3.36}$$

The dimensional governing equations are given by

$$\begin{aligned}
&\rho \frac{D\mathbf{u}}{Dt} = -\nabla p + \mu_s(T) \left(\nabla^2 \mathbf{u} + \frac{1}{3} \nabla (\nabla \cdot \mathbf{u}) \right) + \nabla \cdot \boldsymbol{\tau}_p + g\rho \mathbf{k} \\
&\frac{\partial \rho}{\partial t} + \nabla \cdot (\rho \mathbf{u}) = 0 \\
&\boldsymbol{\tau}_p = \frac{\mu_p(T)}{\lambda(T)} (\mathbf{C} - \mathbf{I}) \\
&\mathbf{C} + \lambda(T) (\overset{\triangledown}{\mathbf{C}} + (\nabla \cdot \mathbf{u}) \mathbf{C}) = \mathbf{I} \\
&\rho C_p \frac{DT}{Dt} = -\nabla \cdot \mathbf{q} + \mathbb{T} : \nabla \mathbf{u} - p \nabla \cdot \mathbf{u} \\
&\frac{\partial p}{\partial \rho} = c_0^2 \left(\frac{\hat{\beta}_0}{\hat{\beta}_1 + \hat{\beta}_2 T} \right)
\end{aligned} \tag{5.3.37}$$

with boundary conditions

$$\begin{aligned}
&u(t, x, 0) = u(t, x, L) = 0 = u(t, 0, y) = u(t, L, y) \\
&T(t, 0, y) = T_h(t) \quad T(t, L, y) = T_c \quad T(t, x, 0) = T_c + (1 - x/L)(T_h - T_c) \\
&\frac{\partial T}{\partial t}(t, x, L) = h_c T
\end{aligned} \tag{5.3.38}$$

We use the same nondimensionalisation parameters for length, velocity, stress and temperature as the incompressible case (defined in Eq. (5.3.10)) along with the additional nondimensional density $\rho^* = \frac{\rho}{\rho_0}$. Substituting nondimensional variables into (5.3.37) results in a parametrised set of governing equations for the weakly compressible viscoelastic fluid.

The set of governing equations for the nonisothermal compressible system is therefore be given by

$$
\begin{aligned}
&\rho\frac{D\mathbf{u}}{Dt} = -\nabla p + Pr\left[\beta\left(\nabla^2\mathbf{u} + \frac{1}{3}\nabla(\nabla\cdot\mathbf{u})\right) + \nabla\cdot\boldsymbol{\tau}_p\right] + RaPr\tilde{\rho}\frac{\beta_0}{\beta_1+\beta_2\theta}\mathbf{k}\\
&\frac{\partial\rho}{\partial\rho} + \nabla\cdot(\rho\mathbf{u}) = 0\\
&\mathbf{C} + We\tilde{\psi}(\theta)(\overset{\triangledown}{\mathbf{C}} + (\nabla\cdot\mathbf{u})\mathbf{C}) = \mathbf{I}\\
&\rho\frac{D\theta}{Dt} = \nabla^2\theta + V_{h^1}\mathbb{T}:\nabla\mathbf{u} - V_{h^2}p\nabla\cdot\mathbf{u}\\
&\frac{\partial\rho}{\partial p} = Ma^2\left(\hat{\alpha}_1 + \hat{\alpha}_2\theta\right)
\end{aligned}
\tag{5.3.39}
$$

where

$$
\begin{aligned}
Ra = \frac{L^3 g}{\nu\alpha}(T_h - T_c), \quad Pr = \frac{\nu}{\alpha}, \quad We = \frac{\lambda_0\alpha}{L^2}, \quad Ma = \frac{\alpha}{c_0 L}\\
V_{h^1} = \frac{\alpha^2\mu}{(T_h - T_c)\kappa L^2}, \quad V_{h^2} = \frac{\alpha^3\rho_0}{(T_h - T_c)\kappa L^2}
\end{aligned}
\tag{5.3.40}
$$

and

$$
\hat{\alpha}_1 = \frac{\hat{\beta}_1 + T_0}{\hat{\beta}_0} \qquad \hat{\alpha}_2 = \frac{\hat{\beta}_2}{\hat{\beta}_0}
\tag{5.3.41}
$$

We also define $\nu = \mu/\rho_0$ and $\alpha = \frac{\kappa}{\rho_0 C_p}$. The quantity V_{h^1} represents the usual viscous heating coefficient and V_{h^2} is the parameter that describes the heat contributed by expansion.

5.3.6 Results & Discussion

Mesh Convergence

First we assess mesh convergence by comparing the kinetic energy profiles for meshes $M1$-$M4$. Figure 5.16 shows the mesh convergence properties of the numerical solution when $We = 0.25$ and $\beta_v = 0.5$.

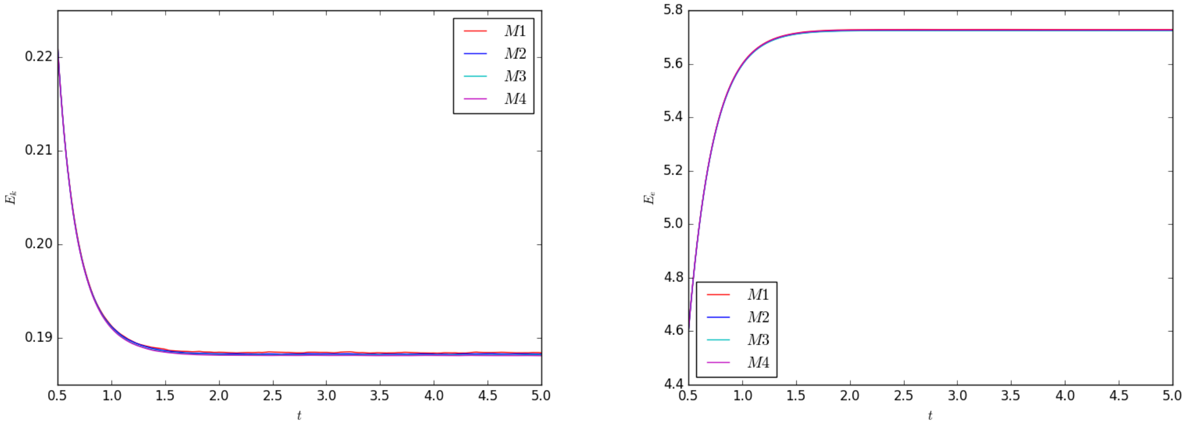

(a) (b)

Figure 5.16: Natural convection flow: (a) kinetic and (b) elastic energy profile for meshes $M1$, $M2$, $M3$ and $M4$. $We = 0.25$, $\beta_v = 0.5$ and $Ra = 10^3$ $\Delta t = h_{min}^2$

Figure 5.16 shows the kinetic energy (calculated using Eq. (5.2.4)) of the flow for $We = 0.25$ and $\beta_v = 0.5$ for meshes $M1$-$M4$. Numerical experiments for the following sections are all performed using mesh $M3$.

Incompressible Flow

The numerical predictions for incompressible Oldroyd-B flow are shown in Figures 5.17-5.23. As t increases from 0 the temperature of the left wall increases, resulting in thermal disequilibrium and a (clockwise) circular flow is induced. As a result the kinetic energy rapidly increases as the flow starts reaching a peak between $t = 0$ and $t = 1$ before reducing to a steady-state level. Elasticity has no significant effect on the maximum value of the kinetic energy but the steady-state kinetic energy/maximum flow speed decreases with Weissenberg number. The elastic energy increases from zero reaching a steady-state before $t = 5$ with the steady-state value increasing with Weissenberg number. The results presented would suggest that viscoelastic fluids could be useful in limiting heat transfer in flows where convection is the dominant mode of heat transfer. However the Rayleigh numbers considered ($Ra \leq 10^4$) means that the scope of this research is limited to highly viscous flows over small length scales. Further work should be done to investigate the effect of relaxation time on flows with larger Rayleigh numbers. A suggested experiment could be tracking heat flow for a range of solvent liquids with and without polymer additives in a similar manner to Pittman et. al [74]. The dramatic change in kinetic energy predicted in this work would suggest a substantial difference in flow rate between polymeric and non-polymeric fluids.

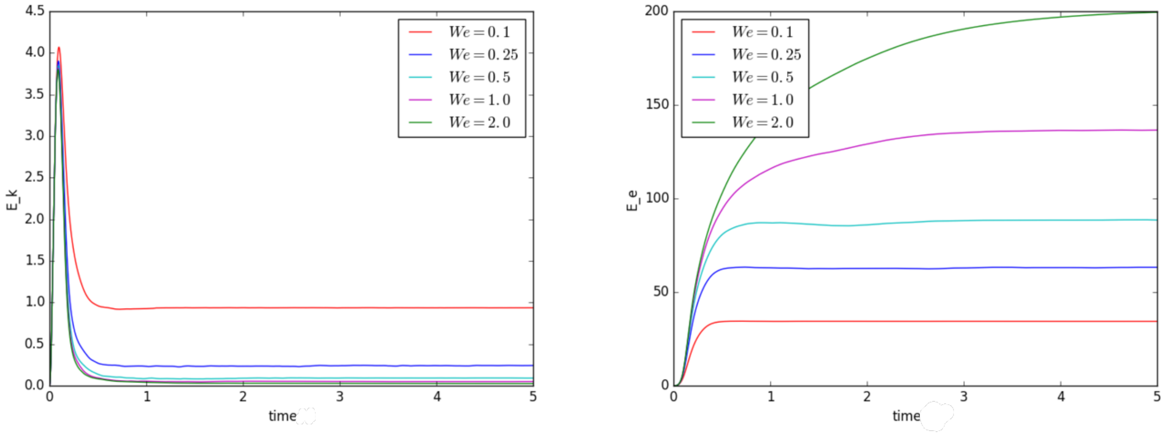

(a) (b)

Figure 5.17: Natural convection flow: Long term kinetic and elastic energy profiles $We \in \{0.1, 0.25, 0.5, 1.0, 2.0\}$; $\beta_v =$ and $Ra = 10^3$

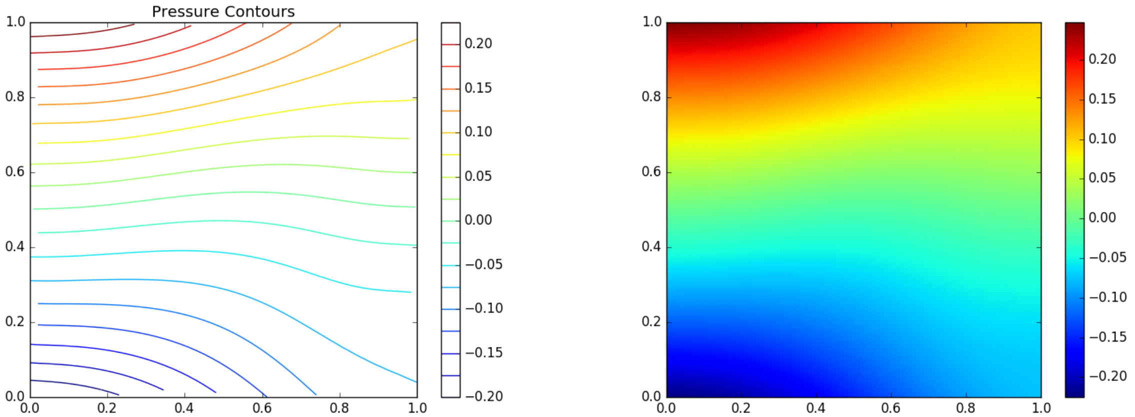

(a) (b)

Figure 5.18: Natural convection flow: Pressure field $Ra = 1000$, $Pr = 1.0$, $We = 0.1$,

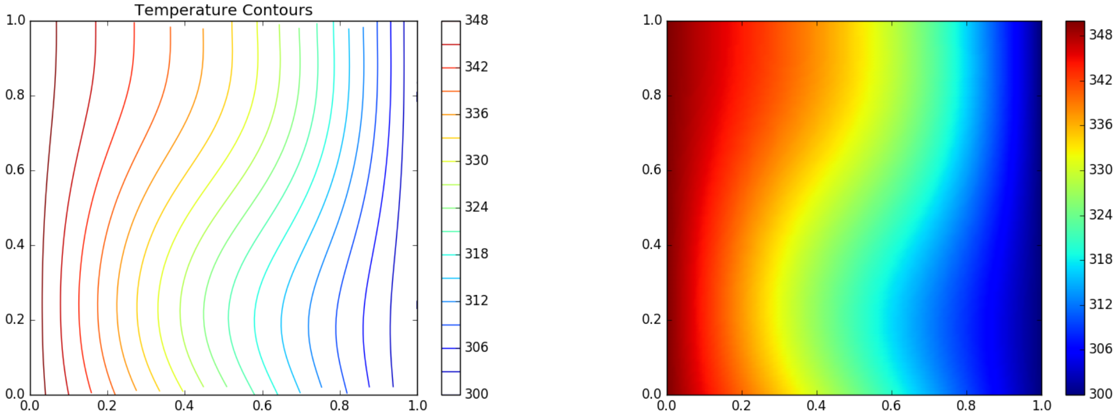

(a) (b)

Figure 5.19: Natural convection flow: Temperature solutions at $t = 1.5$, $Ra = 1000$, $Pr = 0.1$, $We = 0.1$

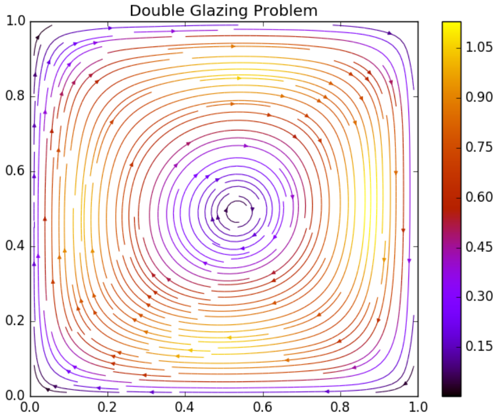

Figure 5.20: Natural convection flow: Velocity field for $Ra = 1000$, $Pr = 1.0$, $We = 1.0$, $t = 1.5$

Weakly Compressible Flow

Unfortunately, we were unable to obtain valid results for the compressible flow problem and solution scheme outlined in Sec. 5.3.5. Despite using both DEVSS and orthogonal projection stabilisation (see Sec. 4.6, the region near the left wall displays considerable variations in temperature and density over short length scales and numerical blowup cannot

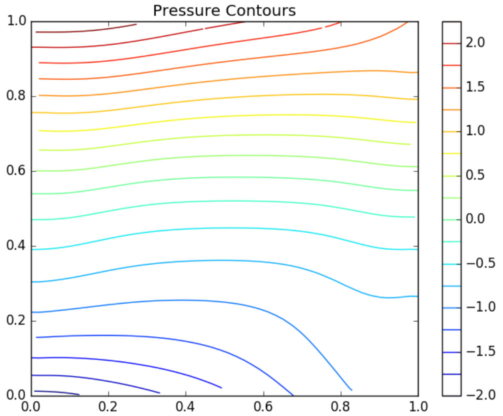

Figure 5.21: Natural convection flow: Pressure field $Ra = 10000$, $Pr = 1.0$, $We = 0.5$.

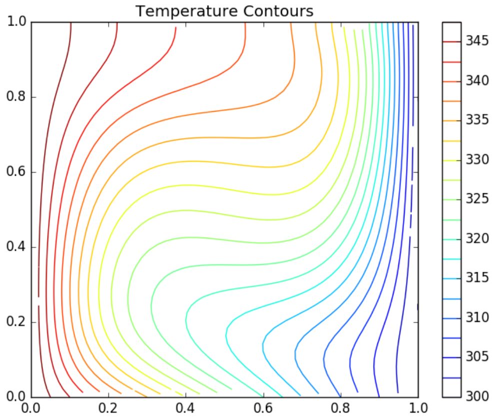

Figure 5.22: Natural convection flow: Plots of $T = T_c + \theta(T_h - T_c)$, $T_h = 350K$, $T_c = 300K$. $Ra = 10000$, $Pr = 1.0$, $We = 1.0$, $t = 1.5$

be avoided. Although this is disappointing result, this is at least a starting point for future work. Subsequent investigations should concern finding more suitable stabilisation methods for problems of buoyancy driven weakly compressible viscoelastic flows, comparing the results to those obtained when the Boussinesq approximation is invoked.

Viscoelasticity and Heat Transfer

The Weissenberg number has a significant impact on the speed of the flow and, as a result, the temperature distribution of the fluid in both the steady and unsteady state. Two metrics

$We\backslash Ra$	10^2	10^3	2×10^3	5×10^3	10^4
0	1.5664	7.315	9.365	13.569	18.256
0.1	0.8663	2.624	3.568	4.211	5.545
0.25	0.6842	2.235	3.144	3.464	4.101
0.5	0.41824	1.43	2.001	2.336	3.266
1.0	0.27299	1.036	1.563	1.803	3.001
2.0	0.19033	0.7822	1.233	1.633	-

Table 5.10: Natural convection flow: steady-state values of max$|\mathbf{u}|$, $Pr = 2$, $\beta_v = 0.5$.

$We\backslash Ra$	10^2	10^3	2×10^3	5×10^3	10^4
0	1.1011	1.1574	1.3422	1.8554	2.2852
0.1	1.0952	1.1102	1.1823	1.4024	1.7852
0.25	1.0565	1.0824	1.1211	1.2566	1.5472
0.5	1.0319	1.0556	1.0688	1.0998	1.2997
1.0	1.0224	1.0423	1.0511	1.0787	1.1152
2.0	1.0169	1.0282	1.0422	1.0657	1.1011

Table 5.11: Natural convection flow: steady-state values of $\bar{Nu}$, $Pr = 2$, $\beta_v = 0.5$.

are used to measure the rate of heat transfer. The first is the average Nusselt number defined

$$\bar{Nu} = \int_0^1 \frac{\partial T}{\partial n}(0, y)\, dy, \tag{5.3.42}$$

which measures overall heat transfer. An approximation of the normal derivative on the hot wall in Eq. (5.3.42) is made using the approximation

$$\frac{\partial T}{\partial n}(0, y) = \frac{T(h_{0,y}, y) - T(0, y)}{h_{0,y}} \tag{5.3.43}$$

where $h_{0,y}$ is the length of the cell adjacent to the left boundary in the x-direction. The second measurement considered is the steady-state maximum flow speed. Each is calculated for different We and Ra with Pr and other parameters fixed.

As We is increased the steady-state flow speed is reduced. Table 5.10 shows the maximum flow speed attained for various Ra and We. the maximum flow speed increases with Rayleigh number and decreases as We is increased. Furthermore, Tab. 5.11 shows the value of $\bar{Nu}$

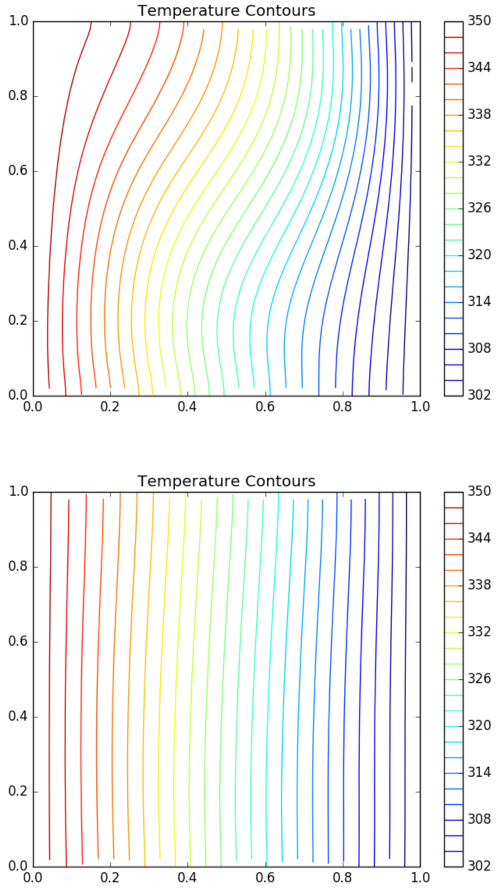

Figure 5.23: Natural convection Flow: Steady-state $T = T_c + \theta(T_h - T_c)$, $T_h = 350K$, $T_c = 300K$ $We = 0$ (a) and $We = 1.0$ (b) and $Ra = 10^3$

over the same range of Ra and We. Whilst $\bar{Nu}$ increases with Ra, the elasticity parameter counteracts this effect in a strong way. For example, at $Ra = 10^4$ $\bar{Nu} = 2.28$ for Newtonian flow ($We = 0$). This reduces to $\bar{Nu} = 1.1011$ when $We = 2.0$ Fig. 5.23 shows the effect on steady-state temperature of We at $Ra = 10^3$. Although further numerical study is required these trends would suggest that elasticity has a negative effect on the capacity of a fluid to transfer heat via convection, especially for flows at low Rayleigh numbers.

$\Delta t \backslash Ra$	10^2	10^3	10^4	10^5	10^6	10^7
0.000125	Stable	Stable	Stable	0.492	0.4	DNC
0.00025	Stable	Stable	Stable	0.492	0.38	DNC
0.0005	Stable	Stable	Stable	0.472	0.36	DNC
0.001	Stable	Stable	Stable*	0.456	0.265	DNC
0.002	Stable	Stable	0.871	0.448	0.264	DNC
0.004	Stable	Stable	0.830	0.448	0.266	DNC
0.008	Stable	Stable	0.731	0.416	0.268	DNC
0.016	Stable	Stable	0.672	0.38	0.248	DNC
0.032	Stable	Stable	0.608	0.32	0.256	DNC
0.064	Stable	1.024	0.64	0.384	0.288	DNC

Table 5.12: Stability of the numerical scheme: timestep size vs Rayleigh number on mesh $M3$; $We = 0.5$, $\beta_v = 0.5$

Stability of Numerical Scheme

The convergence properties of the numerical scheme are heavily dependent on the choice of timestep, Δt. Despite using semi-implicit formulation and suitable non-uniform mesh refinement, Taylor-Galerkin/Finite Element methods fail to converge for $Ra \geq 10^5$ at even modest Weissenberg numbers ($Pr = 1$). We conclude that unless improvements in the stabilisation methods are made, the Taylor-Galerkin finite element numerical scheme is limited for flows up to $We = 2.0$ and $Ra \approx 10^4$.

Table 5.12 shows the convergence properties of the numerical scheme for varying choices of Δt and Ra. The number in the table indicate the time at which numerical blowup occurs. When $Ra = 10^7$ the solution failed to converge in the first time-iteration independent of the choice of Δt.

5.4 Summary

In this chapter we have presented solutions to benchmark problems of 2D flows of Oldroyd-B fluids in a unit square. The Taylor-Galerkin finite element scheme has performed relatively well compared to similar schemes in the literature over the range of Re and We outlined and the results presented are in good agreement with results from similar studies in the literature.

5.4.1 Lid-Driven cavity

The results for incompressible flow are in good agreement with results by Venkatesan et. al [88] and Castillo [16]. Numerical simulations of weakly compressible Oldroyd-B lid-driven cavity flow is new territory and there are no results in the literature (known to the author) with which to compare the results from Sec. 5.2.6. The scheme demonstrated good stability characteristics for $0.001 < Ma < 0.1$ and results for very low Mach numbers were close to the incompressible results. Compressibility reduces the magnitude of ϕ_{min}, but otherwise does not have a significant impact on the qualitative behaviour of the flow. Future work should focus on obtaining numerically stable solutions for a larger range of Mach and Weissenberg numbers (i.e. $Ma > 0.1$ and $We > 2.0$). At larger Weissenberg numbers fluid compressibility may have a more significant impact on the flow behaviour.

5.4.2 Natural Convection Flow

For the Double Glazing Problem, future work should focus on analysing the impact of viscoelasticity on flow stability, which would require simulations at higher Rayleigh numbers. The reduction in kinetic energy by relaxation effects implies, at least intuitively, that viscoelastic fluids exhibit a strong potential for increasing the critical Rayleigh number of the flow. However, the finite element numerical scheme did not perform well for $Ra > 10^4$ for modest values of We. Future work should focus on the implementation of alternative numerical schemes, such as SEM or FVM that could potentially be able to produce results over a wider range of parameter values.

Furthermore, another major disappointment is that the compressible flow solver did not yield results. Future work should revisit the problem as the author feels that important insights can be gained by comparing the Boussinesq approximation and the equation of state as a model for buoyancy driven flow.

Chapter 6

Flow between Eccentrically Rotating Cylinders

6.1 Introduction

In this chapter, we use the numerical scheme presented in Chapter 4 to numerically simulate the flow between eccentrically rotating cylinders. We compare the predictions of two thermodynamically derived models: the extended White Metzner (EWM) model and the FENE-P-MP model. In Sec. 6.2 a review of the literature on eccentrically rotating cylinders is presented. The domain and boundary conditions are presented in Sec. 6.3. In Sec. 6.4 the numerical scheme for incompressible flow is benchmarked and results are compared to those from the literature. In Sec. 6.5.2 we present the compressible constitutive models for EWM and FENE-P-MP models. A discussion of the parameter values used in the compressible flow simulations is also given. The results are then presented in Sec 6.5.4 and a summary is given in Sec. 6.6.

6.2 Literature Survey

Lubricants reduce wear and vibration in bearing systems by preventing contact between moving parts. The physical characteristics of lubricants are a crucial determining factor in the performance and longevity of lubricated systems such as car engines and axles. As a consequence lubrication theory is of particular interest to the automotive industry. The flow between eccentrically rotating cylinders is of particular interest in the mathematical modelling of journal bearing lubrication [69] since it is an idealised problem that retains important elements of the engineering problem.

Journal bearing systems are an intricate part of a large number of industrial and commercial mechanical devices. The working temperature of bearing systems can vary widely within the flow and has a huge impact on performance of the system overall [57]. Thermal analysis of dynamically loaded bearings (journal bearings) is an invaluable tool in the design of bearing systems and lubricants [57]. Polymers are added to mineral oils to make multi-grade oils. This was originally done to weaken the dependence of viscosity on temperature [69]. The addition of elastic polymer chains in Newtonian lubricants results in a viscoelastic mixture. The effect of viscoelastic relaxation on the journal bearing has been a subject of interest in many investigations. Real journal bearing systems operate at high rates of rotation where the flow Mach number is large enough to be in a weakly compressible regime. Furthermore, the compressibility of a lubricant has been shown to play a significant role in the load bearing capacity of a journal bearing [12].

From a mathematical standpoint, the flow between eccentrically rotating cylinders is an attractive benchmark problem because of its closed geometry, free from sharp boundaries [69]. Several comprehensive numerical investigations of the statically and dynamically loaded bearing problem have been performed by Phillips, Bollada and Davies [11, 13, 12, 42, 57, 69], and is a commonly visited benchmark problem in CFD. Phillips and Roberts [73] showed that, at high eccentricities the predicted reaction forces exerted on the journal by a UCM fluid during rotation are significantly larger than for Newtonian fluids.

Beris et al. [6, 7] calculated the flow between eccentrically rotating cylinders for UCM and PTT fluids using spectral/finite element methods. Davies and Li [24] investigated the effects of temperature-thinning and pressure-thickening using an incompressible White-Metzner model. They found that, at high eccentricities, pressure-thickening dominates the viscosity behaviour due to the enormous pressure gradients generated across the narrow gap region of the flow [24].

The first comprehensive study into the effect of fluid compressibility in Newtonian lubricants in journal bearing systems was performed by Bollada and Phillips [11]. In their investigation they used a log-density formulation, in which the governing equations for mass and momentum were re written in terms of log-density and then solved using a semi-Lagrangian discretisation in time and spectral elements in space. The numerical results showed that even at Mach numbers as low as 0.02 compressibility had a significant effect on the resultant load.

Despite these findings, only a small percentage of papers in the literature has considered the fully nonisothermal and compressible problem. To the author's knowledge, no investigations have been undertaken assessing the numerical predictions of compressible, nonisothermal and viscoelastic flows between eccentrically rotating cylinders.

This section will focus solely on the statically loaded bearing problem in which a cylinder, radius R_J rotates under a time dependent load inside a cylindrical container with radius R_B ($R_B - R_J > 0$). The centre of the journal is fixed at a distance, e, to the left of the centre of the bearing. The concentric configuration of this problem ($e = 0$) is known as the Taylor-Couette problem, which is one of the classical problems in fluid mechanics. For a Newtonian fluid, Taylor [86] showed that the purely azimuthal shearing flow that occurs at low speeds becomes unstable as the inertial forces increase. The flow then becomes fully 3D with steady toroidal roll cells forming. As a consequence, an upper limit exists to the Reynolds number if the assumption of 2D flow is to be used, which is given by the Taylor number

$$Ta = 2Re^2\left(\frac{R_B - R_J}{R_J}\right) \tag{6.2.1}$$

where R_B is the bearing radius, R_J is the journal radius and Re is the Reynolds number.

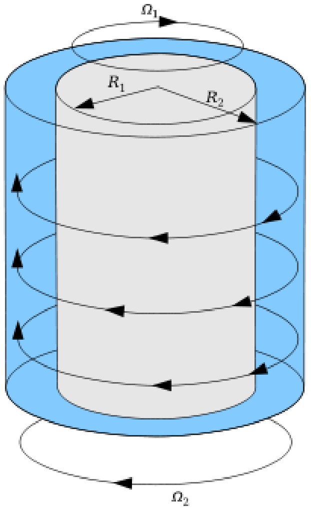

Figure 6.1: Taylor-Couette Problem. At lower Reynolds numbers the flow is steady and azimuthal. The laminar flow state is circular Couette flow (Image: Magasjukur2, Wikipedia).

We will analyse the flow predictions of two thermodynamically consistent viscoelastic models; the extended White-Metzner model and the FENE-P-MP model. Both models predict shear-thinning and the numerical results will provide an opportunity to compare predictions of the FENE-P-MP to those in the literature for the EWM model. In Sec. 6.4 we compute the flow predictions of the incompressible Oldroyd-B fluid within a tightly fitting journal bearing cavity. This is so that we can benchmark the results for journal bearing load and torque against those given by Phillips, Davies and Li [42, 69, 73]. In Sec. 6.5 the compressible flow of an (i) extended White-Metzner and (ii) FENE-P-MP fluid in a loosely fitting journal bearing cavity is analysed. In each case the governing equations are discretised and solved using Taylor-Galerkin/finite element schemes outlined in Sec. 4.2. Measurements of the reaction forces and torque on the rotating journal are assessed for $0 \leq We \leq 2.0$, $10 \leq Re \leq 100$ and $0 \leq Ma \leq 0.1$.

6.3 Computational Domain and Boundary Conditions

The computational domain is defined as follows:

$$\Omega = \{(x, y) : x^2 + y^2 \leq R_B^2 \wedge (x - e)^2 + y^2 \geq R_J^2\} \tag{6.3.1}$$

Using a long bearing approximation and the assumption that $Ta < Ta_{crit}$ the flow is modelled as 2D. The fluid occupies the region Ω between the two cylinders with boundaries.

$$\Gamma_J = \{(x, y) : x^2 + y^2 = R_J^2\} \qquad \Gamma_B = \{(x, y) : x^2 + y^2 = R_B^2\} \tag{6.3.2}$$

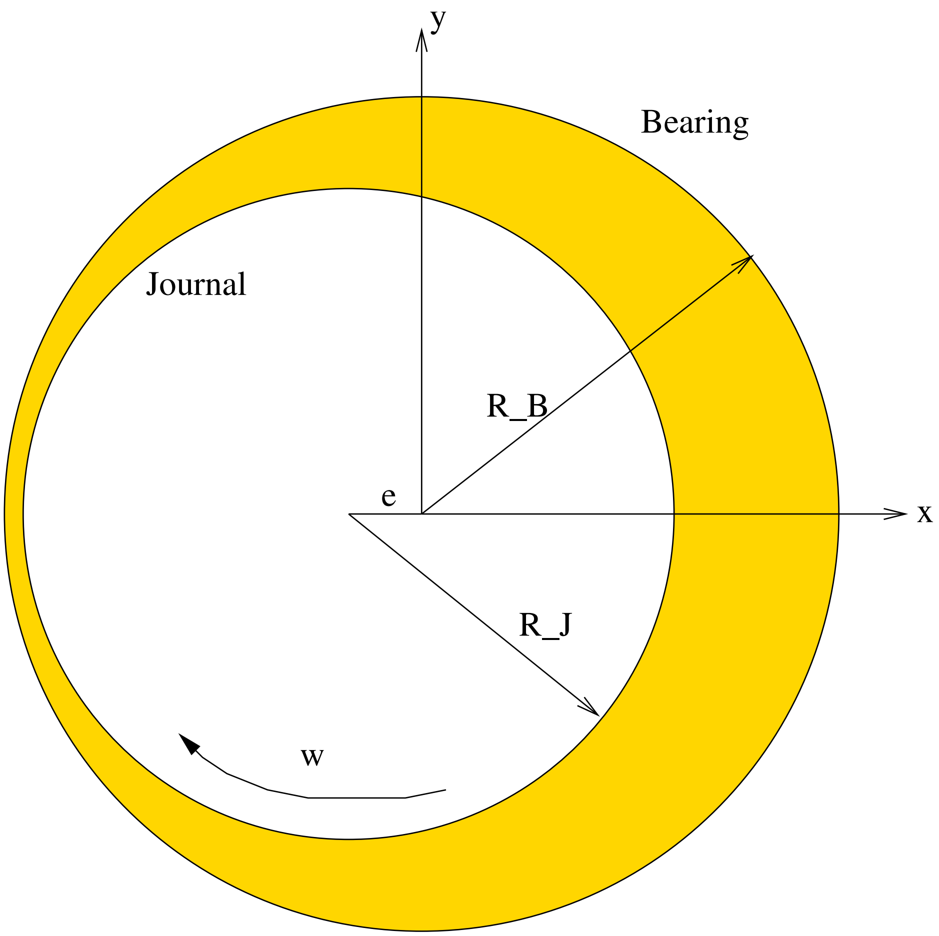

Figure 6.2: Journal Bearing Problem: Schematic diagram of Ω.

where e is the eccentricity. Fig. 6.2 gives a schematic diagram of the computational domain. On the journal we impose no-slip Dirichlet boundary conditions for the velocity and constant temperature

$$\mathbf{u} = \frac{\phi(t)}{\sqrt{x^2 + y^2}}(y, -x), \qquad T = T_0$$

on Γ_J where

$$\phi(t) = \frac{\omega}{2}(1 + \tanh(8(t - 0.5))) \tag{6.3.3}$$

and ω is the journal's angular rotation rate (rad/s). On Γ_B we impose no-slip conditions for the velocity and Neumann conditions for the temperature

$$\mathbf{u} = 0, \quad \frac{\partial T}{\partial \mathbf{n}} = -\frac{Bi}{h_c}T$$

where h_c is the characteristic thickness and the Biot number, Bi, is a nondimensional measure of the heat transfer at the outward facing boundary of the journal bearing. The eccentricity ratio, ϵ, and relative thickness, υ, are defined

$$\epsilon = \frac{e}{R_B - R_J} \qquad \upsilon = \frac{R_B - R_J}{R_J} \tag{6.3.4}$$

6.4 Incompressible Oldroyd-B Flow

In order to benchmark the numerical scheme we first consider the flow of an incompressible Oldroyd-B. Numerical results obtained using the scheme presented in Sec 4.7.1 are compared with those from the literature.

The finite element mesh used is shown in Fig. 6.3.

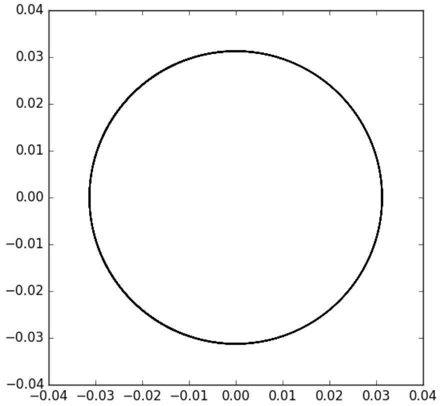

Figure 6.3: Finite element mesh of Ω for the incompressible problem. $R_J = 0.03125$m, $R_B = 0.03129$m, $\epsilon = 0.75$, $\upsilon = 0.00128$, cells= 3448, DoF= 216272

6.4.1 Governing Equations & Solution Method

In order to make a direct numerical comparison with the study by Li et al. [58] we compute the flow behaviour using the dimensional form of the governing equations. The governing equations of mass, momentum, temperature and extra stress are given by (4.1.4) with

$$\mathbf{g}_1(\mathbf{C}, \mathbf{I}) = \frac{\mu_p}{\lambda}(\mathbf{C} - \mathbf{I}) \qquad \mathbf{g}_2(\mathbf{C}, \nabla\mathbf{u}) = 0 \tag{6.4.1}$$

Additionally we assume that the flow is incompressible and isothermal i.e. $\nabla \cdot \mathbf{u} = 0$, $\lambda(T) = \lambda$ and $\mu_p(T) = \mu_p$. To solve the governing equations we use the numerical scheme outlined in Sec. 4.7.1 with $\Delta t = h_{min}^2$, $c_1 = 0.1$, $c_2 = 0.05$ and $\gamma_u = 1 - \beta_v$.

6.4.2 Results & Comparisons with Long Bearing Theory

Analytical solutions for the journal bearing problem can be obtained by invoking the lubrication approximation. In the thin bearing approximation $c = (R_B - R_J) \ll R_B$ the pressure field obeys Reynolds' equation

$$p = p_0 + \frac{6\mu\omega R_J^2}{c^2}\frac{\epsilon \sin\theta(2 + \epsilon\cos\theta)}{(2 + \epsilon^2)(1 + \epsilon\cos\theta)^2} \tag{6.4.2}$$

$$F_y = \frac{12\pi\mu\omega n R_J^3 \epsilon^2}{[c^2(1-\epsilon^2)(2+\epsilon^2)]^{\frac{1}{2}}} \quad C = \frac{2\pi\mu\omega n R_J^3}{c(1-\epsilon^2)^{\frac{1}{2}}} + \frac{F_y e}{2} \tag{6.4.3}$$

where $n > 1$ is the ratio of the length of the bearing to its diameter [58, 69]. This allows us to calculate the load and torque explicitly as a function of the viscosity, rotation speed and eccentricity. The solutions are generated using the nondimensionalised scheme and so dimensional factors are required in order to compare with predictions from the literature. Load and torque action on the bearing by fluid are calculated using the pressure, velocity and stress using the following formula

$$\mathbf{F} = \begin{pmatrix} F_x \\ F_y \end{pmatrix} = \left\{ \frac{L^3}{\mu_0 U} \right\} \int_{\Gamma_J} \boldsymbol{\sigma} \cdot \mathbf{n} \, dS \tag{6.4.4}$$

$$C = \left\{ \frac{L^4}{\mu_0 U} \right\} \int_{\Gamma_J} \mathbf{n}^T \cdot \boldsymbol{\sigma} \cdot \mathbf{t} \, dS \tag{6.4.5}$$

where the characteristic length and velocity are given by

$$L = R_J \qquad U = \omega R_J \tag{6.4.6}$$

	Current work	SEM (Li [58])	LBT	Current Work	SEM (Li [58])	LBT
ϵ	F_y	F_y	F_y	C	C	C
0.7	0.23×10^4	0.21×10^4	0.22×10^4	0.84×10^0	0.82×10^0	0.84×10^0
0.8	0.28×10^4	0.27×10^4	0.28×10^4	0.11×10^1	0.11×10^1	0.11×10^1
0.9	0.37×10^4	0.4×10^4	0.41×10^4	0.15×10^1	0.16×10^1	0.16×10^1
0.95	0.52×10^4	0.56×10^4	0.59×10^4	0.19×10^1	0.23×10^1	0.23×10^1

Table 6.1: Comparison of long bearing theory and SEM numerical results to TG finite element computed solutions for Newtonian flow;$\omega = 25$ rad/s, $\mu_p = 0 = \lambda$, $\mu_s = 5\times10^{-3}$Pa.s.

λ_1	F_x	F_y	C
0.0	0.0	38.20	0.77760
1.0×10^{-3}	1.9750	38.192	0.77756
1.0×10^{-2}	1.9760	38.190	0.77752
1.0×10^{-1}	1.9765	38.17	0.7741
5.0×10^{-1}	1.980	35.41	0.7200

Table 6.2: Load and torque values for a range of relaxation times ($\omega = 25$ rad/s, $\mu_s = \mu_p = 2.5 \times 10^{-3}$Pa.s, $t = 10$s)

Tables 6.1 and 6.2 show the results for $\mathbf{F}$ and C comparing the numerical scheme in Sec. 4.7.1 to both long bearing theory and numerical results from the literature. The difference between the LBT and numerical results for high eccentricities is almost certainly due to errors in the velocity solution in the narrow gap that occur as the two boundaries become closer. The large velocity gradients across the narrow gap may lead to significant differences between the theoretical result and the velocities computed on each cell. Despite this, for $\epsilon < 0.9$ the results demonstrate good agreement with the theory and numerical results in the literature. In the next section we analyse the numerical predictions for weakly compressible and nonisothermal flow.

6.5 Weakly Compressible and Nonisothermal Viscoelastic Flow

We now consider the flow of a compressible viscoelastic fluid between eccentrically rotating cylinders. The two suitable models chosen for the simulations are the extended White-Metzner (Eq. (3.1.39)) and FENE-P-MP (Eq. (3.3.21)).

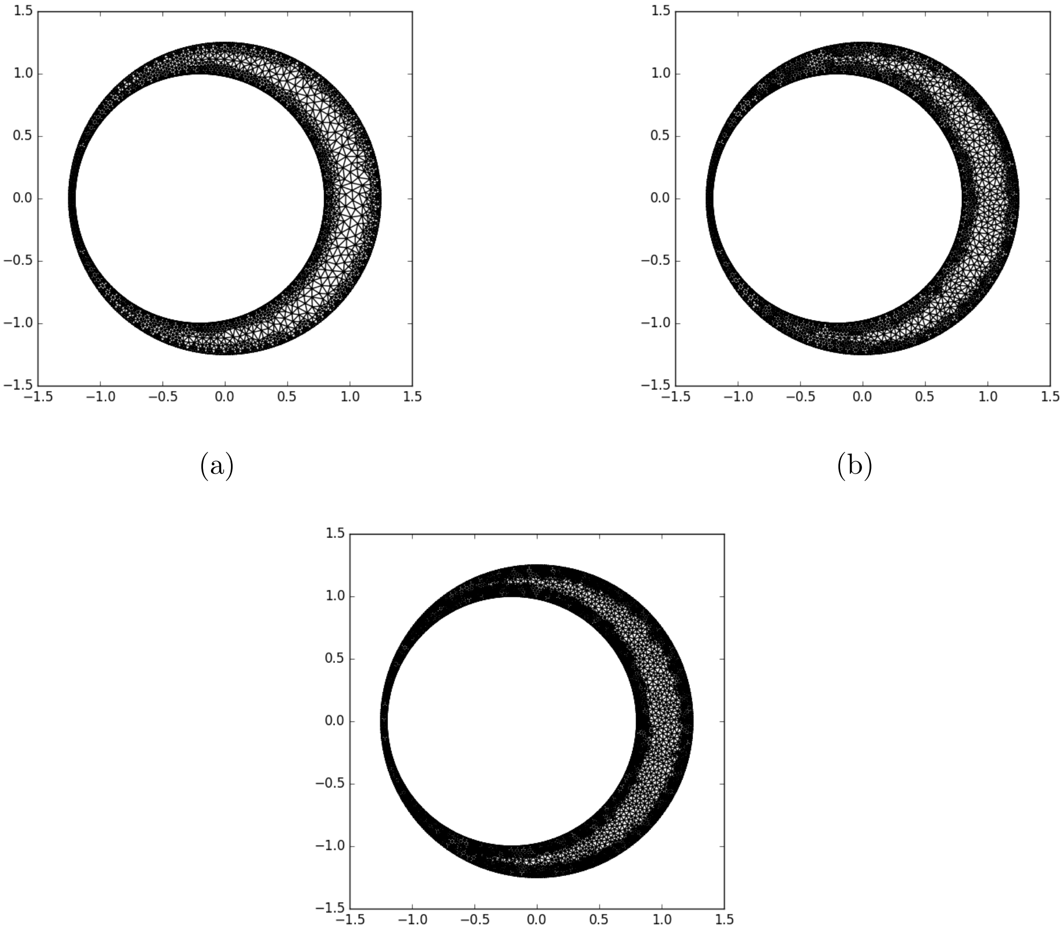

(a)

(b)

(c)

Figure 6.4: Finite element meshes for the flow between eccentrically rotating cylinders: (a) Coarse mesh ($M1$), (b) medium ($M2$) and (c) refined ($M3$)

6.5.1 Geometrical Data & Fluid Parameters

Mesh	Cells	h_{min}	h_{max}	$DoF(p)$	$DoF((\mathbf{u}, \mathbf{D}))$	$DoF(\mathbf{C})$
M1	4466	0.01446	0.09855	2745	33310	29868
M2	5704	0.01086	0.07136	3364	41976	37296
M3	11930	0.00883	0.04536	6447	85558	74652

Table 6.3: Flow between eccentrically rotating cylinders: Mesh characteristics $M1$-$M3$.

In order establish a clear relationship between the effects of viscoelasticity and compressibility we fix the geometry of the journal bearing as well as most of the fluid parameters. We can then analyse the effect of two important variables: the journal rotation rate, ω, and the relaxation time, λ.

Parameter	Value (S.I. Units)
R_J	4×10^{-2} m
R_B	5×10^{-2} m
e	8×10^{-3} m
ω	$100 - 1000$ rad/s
ρ	8.2×10^{2} kg/m^3
μ_s	1.25×10^{-2} Pa s
μ_p^0	1.25×10^{-2} Pa s
μ_p^∞	1.25×10^{-3} Pa s
μ^0	2.5×10^{-2}Pa s
λ_0	$0 - 10^{-3}$s
c_0	1500m/s
C_v	1.75×10^{3}J/K
K_0	5×10^{-10}
κ	0.14W/mK
T_0	300K
T_h	350K

Table 6.4: Geometrical data and fluid parameters

Table 6.4 gives the values of the parameters used in the simulations. The fluid density and viscosity are chosen to be that of 15W40 engine oil (data from Anton Paar Ltd). The journal bearing of radii 4cm (journal) and 5cm (bearing) are chosen so that the numerical results can be verifiable using a practical experiment. Furthermore the eccentricity is fixed at $\epsilon = 0.8$ as this was near the upper limit of the range of ϵ where the incompressible scheme produced reliable results. The scalings used for this problem are as follows:

$$
\begin{aligned}
&L = R_J, \quad U = \omega R_J, \\
&Re = \frac{\rho_0 U L}{\mu_0}, \quad We = \frac{\lambda_0 U}{L}, \quad Ma = U/c_0, \\
&Di = \frac{\kappa}{\rho_0 C_v U L}, \quad V_h = \frac{U \mu_0}{\rho_0 C_v L (T_h - T_0)}, \\
&\beta_s = \mu_s^0/\mu^0,
\end{aligned}
\tag{6.5.1}
$$

We can reduce the large number of nondimensional variables by fixing all fluid and experimental parameters to those given in Table 6.4. In this case Re and Ma are directly proportional to the angular frequency of the bearing, ω, and We is proportional to $\omega\lambda_0$

Nondimensional Parameter	Value
Re	$50 - 400$
We	$0 - 2.0$
Ma	$Re \times 10^{-4}$
ϵ	0.8
υ	0.2
Di	$\frac{1}{625} \times Re^{-1}$
V_h	$1.06 \times 10^{-6} \times Re$
Bi	0.2
β_s	0.5
B	0.1
k	-2

Table 6.5: Nondimensional parameters

With the speed of sound, zero-shear viscosity and density for the fluid fixed, the Mach number is directly proportional to the Reynolds number. Furthermore the Weissenberg number is directly proportional to the product of angular frequency and relaxation time. Both the diffusion number, Di, and viscous heating number, V_h, are small with the latter almost negligible.

6.5.2 Governing Equations & Boundary Conditions

The Extended White Metzner (EWM) Model

The generalisation of the Oldroyd-B model to capture variable relaxation time was proposed by White & Metzner [91]. The extended White Metzner (EWM) model [81] (Eq. (3.1.39)) is a thermodynamically derived constitutive equation with variable relaxation time. Importantly the dependence of λ on the conformation tensor and not the strain-rate and pressure avoids the potential loss of evolutionarity that can occur with the White-Metzner model ([8] p.230). The polymeric viscosity and relaxation time depend on both temperature and conformation stress. The nondimensional form of the EWM model is given by (4.1.14) with

$$\mathbf{g}_1 = \frac{(1-\beta_v)\hat{\psi}_p(\mathbf{C},\theta)}{We\tilde{\psi}_p(\mathbf{C},\theta)}(\mathbf{C}-\mathbf{I}) \qquad \mathbf{g}_2 = 0 \tag{6.5.2}$$

Combining both the EWM stress-thinning and temperature dependence we obtain the following functions for the viscosity and relaxation time alternative to Eq. (4.1.11)-(4.1.12)

$$\hat{\psi}_p(\mathbf{C},\theta) = \exp(-A_{p,0}\theta) \times \frac{1}{2}I_1(\mathbf{C})^k \tag{6.5.3}$$

and

$$\tilde{\psi}_p(\mathbf{C},\theta) = \exp(-A_{p,0}\theta)[\theta/\theta_s+1] \times \frac{1}{2}I_1(\mathbf{C})^k \tag{6.5.4}$$

where we define

$$\theta_s = T_0/(T_h - T_0)$$

and k is a power law index.

Note: the coefficient of $1/2$ *appears in the* $2D$ *formulation to ensure that* $\boldsymbol{\psi} = 1$ *when* $\boldsymbol{C} = \boldsymbol{I}$ *and* $\theta = 0$*. For the 3D case the coefficient is* $1/3$ *as presented in the literature [36, 81].* The values of the various parameters used in the simulations of the EWM model are given in Table 6.6.

Nondimensional Parameter	Value
β_v	0.5
$A_{p,0}$	0.1
θ_s	6
k	-0.7

Table 6.6: Nondimensional parameters in the viscosity relations for the EWM model.

FENE-P-MP Model

For simulations of the FENE-P-MP model we use (4.1.14) with

$$\begin{aligned} \mathbf{g}_1(\mathbf{C},\mathbf{I}) &= \frac{(1-\beta_v)\hat{\psi}(\mathbf{C},\theta)}{We\tilde{\psi}(\mathbf{C},\theta)}(\mathbf{f}(\mathrm{tr}\mathbf{C})\mathbf{C}-\mathbf{I}) \\ \mathbf{g}_2(\mathbf{C},\mathbb{D}) &= (\mathbf{f}(\mathrm{tr}\mathbf{C})-1)\mathbf{C} + We\tilde{\psi}_p(\mathbf{C},\theta)\psi(\dot{\epsilon})[\mathbf{C}\cdot\mathbb{D}+\mathbb{D}\cdot\mathbf{C}] \end{aligned} \tag{6.5.5}$$

with

$$\mathbf{f}(\mathrm{tr}\mathbf{C}) = \frac{b^2}{b^2-\mathrm{tr}\mathbf{C}} \tag{6.5.6}$$

6.5.3 Discretisation & Solution Method

To solve the governing set of equations we use the numerical scheme outlined in Sec. 4.7.2. Throughout the computations we use DEVSS (Sec. 4.6.1) and LPS (Sec. 4.6.4) with $\gamma_u = 1-\beta_v$, $c_1 = 0.1$, $c_2 = 0.05$.

6.5.4 Results & Discussion

The key measurements of the efficiency and effectiveness of a journal bearing lubricant are the torque and resultant load forces on the journal. Pressure dominates the forces around the journal. In the numerical simulation of an incompressible Newtonian fluid the pressure is perfectly anti-symmetric about the narrow gap [11, 69]. When either the Weissenberg or Mach number is non-zero, this asymmetry is broken leading to an inevitable non-zero component of force in the x direction. The resultant force, $\mathbf{F}$, and torque, C, acting on the journal are calculated from the solution of the pressure, velocity and stress by using

$$\mathbf{F} = \begin{pmatrix} F_x \\ F_y \end{pmatrix} = \int_{\Gamma_J} \boldsymbol{\sigma} \cdot \mathbf{n} \, dS \tag{6.5.7}$$

$$C = \int_{\Gamma_J} \mathbf{n}^T \cdot \boldsymbol{\sigma} \cdot \mathbf{t} \, dS \tag{6.5.8}$$

where

$$\boldsymbol{\sigma} = -p\mathbf{I} + 2\beta_v \mathbb{D} + \boldsymbol{\tau}_p \tag{6.5.9}$$

The ratio of the magnitude of horizontal and vertical forces, denoted by χ, can be used as a measurement of *rotational stability* [12]

$$\chi = \left| \frac{F_x}{F_y} \right| \tag{6.5.10}$$

We say that we have stability when $\chi \to \infty$ and increasing instability when $\chi \to 0$.

Mesh Convergence

First we compare the kinetic, elastic energy and torque for the different meshes shown in Fig. 6.4 in order to verify the independence of the numerical solution's on the mesh being used.

Figure 6.6 shows the convergence behaviour of the kinetic, elastic energy and torque with meshes $M1$, $M2$ and $M3$ for $We = 0.25$. We observe that the kinetic, elastic energy and torque tend to a constant value as the number of interpolation points increase.

Extended White Metzner Model

We now present the results for the EWM flow. As the journal begins to rotate a film of fluid close to the journal rotates in the same direction. The flow in the wider gap recirculates

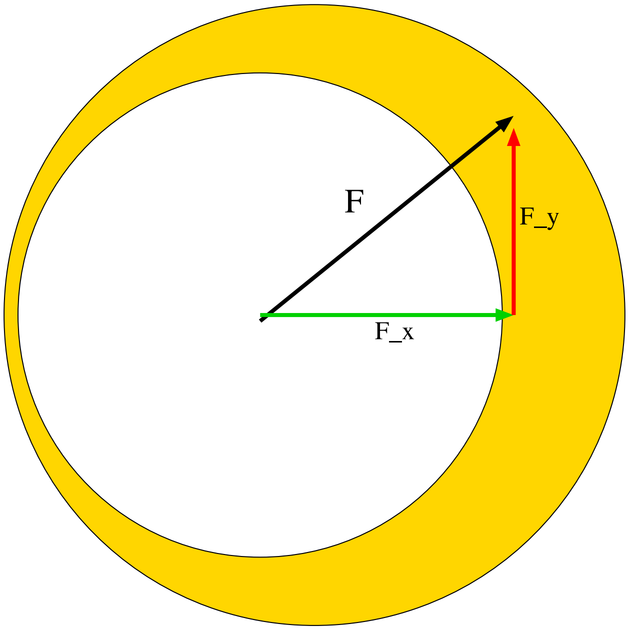

Figure 6.5: Journal bearing problem: Resultant force acting on the journal calculated using $\boldsymbol{\sigma}$.

with the centre of rotation just above the centre-line. The recirculation region occupies the majority of Ω, suggesting a mechanism for efficiency in that the journal does not drag all the fluid around when the rotation is eccentric [12]. The kinetic energy grows as the flow accelerates, reaches a maximum as the journal reaches its maximum speed, and then reduces significantly as the elastic energy grows. Similar to the lid-driven cavity and natural convection flows, the steady-state kinetic energy decreases as the Weissenberg number increases whilst the elastic energy grows.

Reference	ψ_{max}
Current work	0.0602
Germann et al. [36]	0.0627

Table 6.7: Flow between eccentrically rotating cylinders: Comparison of maximum value of stream function: $\beta_v = 0$ ($\gamma_u = 1$), $\epsilon = 0.8$, $\upsilon = 1$ $We = 1.0$, $k = -0.7$.

Table 6.7 compares the results from this work to those produced by Germann et al. [36]. Note that for this specific simulation we set $\epsilon = 0.8$ and $\upsilon = 1$ and not the values provided in Table 6.5.

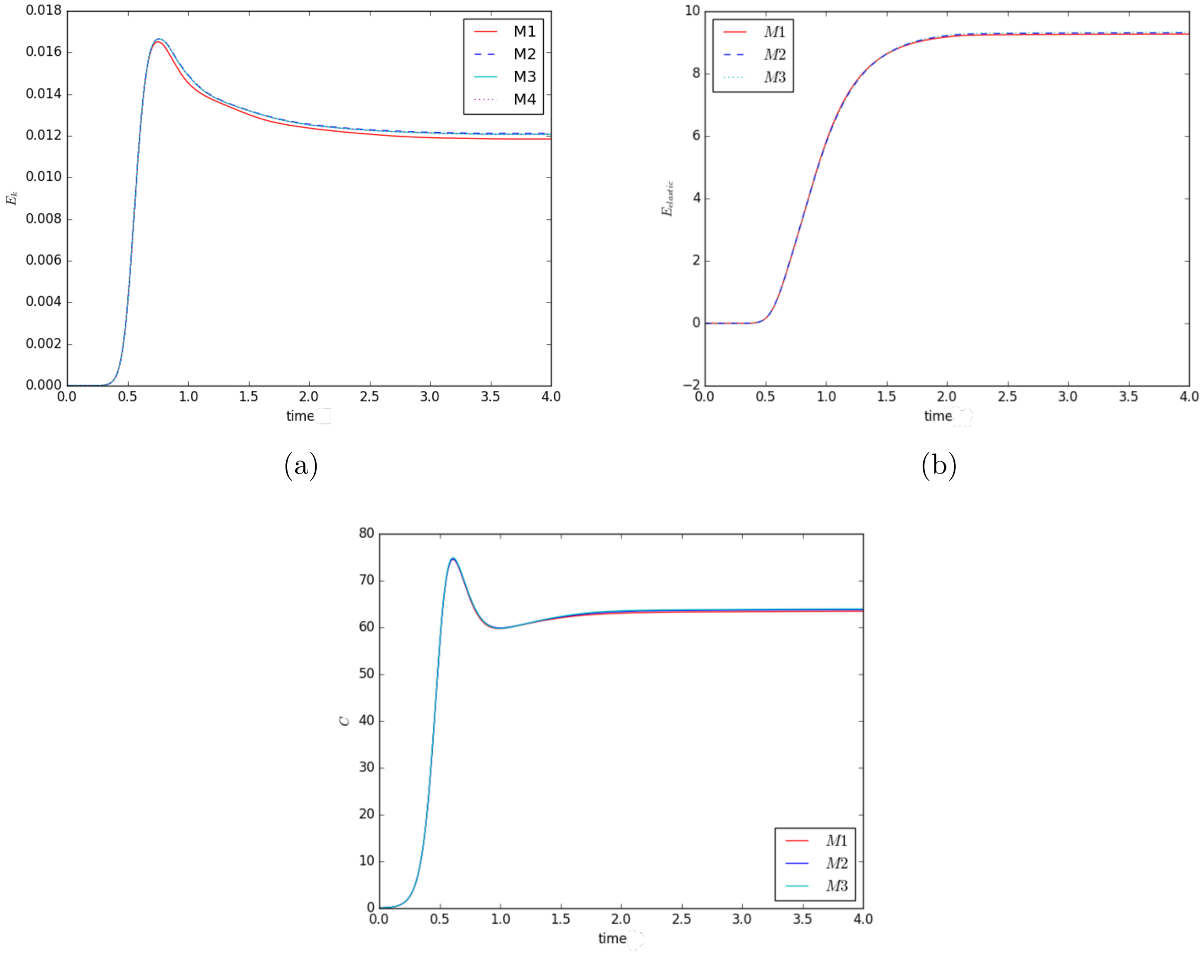

(a)

(b)

(c)

Figure 6.6: Flow between eccentrically rotating cylinders: (a) Kinetic , (b) elastic energy and (c) torque (EWM model), $Re = 50$ $We = 0.1$, $Ma = 0.001$

Figures 6.7-6.10 give a sample of the numerical simulation results. The flow recirculates in the region away from the journal with the strength of the recirculation increasing with Weissenberg number. For $We > 0$, a large build up of elastic stress occurs in the narrow gap. Crucially, the stress components are all asymmetric, with high values in the narrow gap resulting in a non-zero force component F_x.

Figures 6.8 (a) and (b) show the steady state temperature profile for journal bearing. The temperature of the fluid is maximum near the journal and in the region around the narrow gap. With an increase in eccentricity or zero shear fluid viscosity the viscous heating

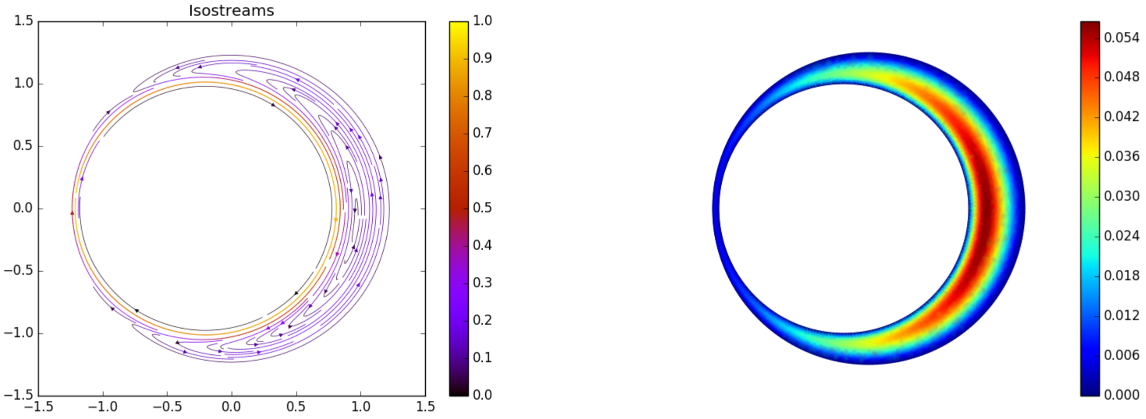

(a) (b)

Figure 6.7: Flow between eccentrically rotating cylinders: (a) Lubricant isostreams and (b) stream function for extended White-Metzner fluid: $We = 1.0$ $Re = 50$ $Ma = 10^{-4}Re$.

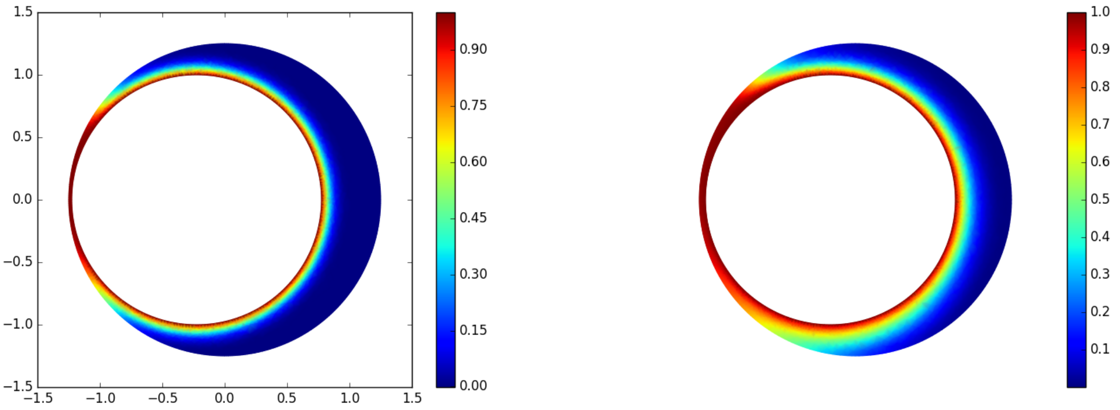

(a) (b)

Figure 6.8: Flow between eccentrically rotating cylinders: Steady-state temperature profile for extended White-Metzner Fluid (a) $We = 0.5$ and (b) $We = 1.0$ ($Re = 200$ and $Ma = 0.02$)

parameter, V_h would also increase and the impact on temperature may be more significant. Tables 6.8-6.9 show the values of the stability factor for various We, Re, Ma. There is a positive relationship between compressibility and stability. for Mach numbers in the range $0 \leq Ma \leq 0.05$ the stability factor shows a clear positive trend with Mach number. Fluid relaxation has a much larger impact on the stability factor. From We from $0.1 - 0.5$ the

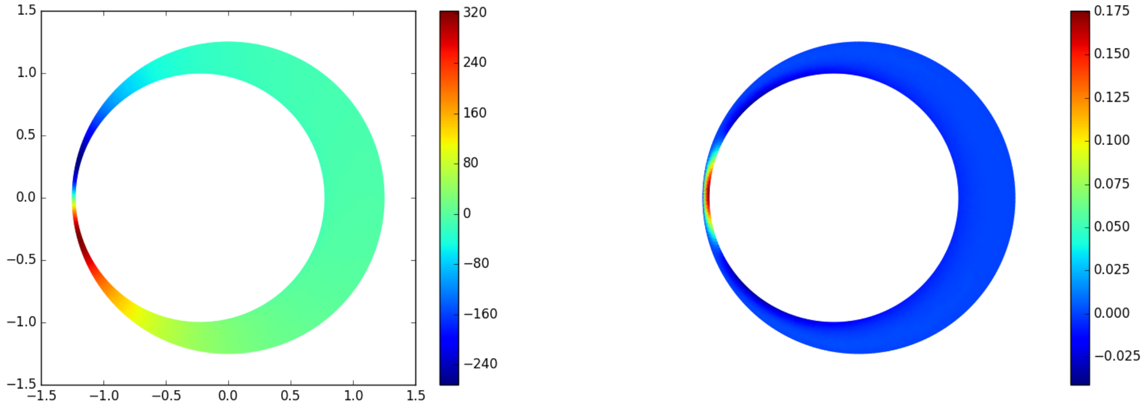

(a) (b)

Figure 6.9: Flow between eccentrically rotating cylinders: (a) Steady-state p and (b) $\nabla \cdot \mathbf{u}$ for extended White-Metzner model ($Re = 100$, $We = 0.5$ and $Ma = 0.01$)

stability factor increases from ≈ 0.1 to 4.23 ($Re = 50$) before decreasing. The cause of the reduction is that the, for Weissenberg numbers above 0.5 the direction of the vertical component of the resultant force reverses direction during the transient phase of the flow.

$Ma \backslash We$	0	0.1	0.25	0.5	1.0
0.001	0.315	0.358	2.862	7.492	5.212
0.01	0.364	0.392	2.916	7.893	5.411
0.1	0.392	0.510	3.521	10.920	7.633

Table 6.8: Flow between eccentrically rotating cylinders: Values of the stability factor, χ, for the extended White-Metzner fluid. $Re = 10^4 Ma$.

A trend observed is that the stability of the system increases with Weissenberg number

$Re \backslash We$	0	0.1	0.25	0.5	1.0
25	0.0261	0.0576	2.324	6.0208	4.214
50	0.0490	0.2227	3.384	8.227	4.894
100	0.0825	0.584	5.245	10.612	6.245
200	0.1162	0.788	6.945	36.62	-

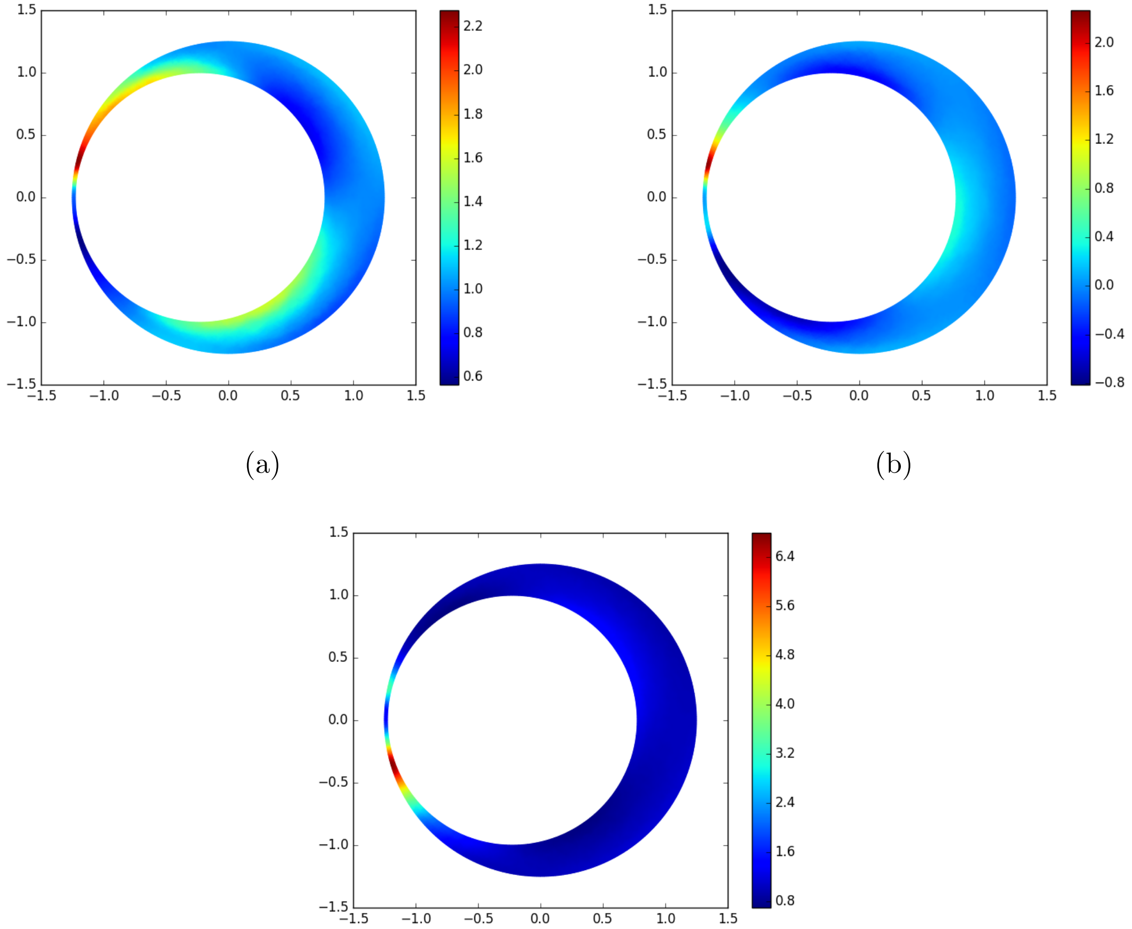

(a) (b)

(c)

Figure 6.10: Flow between eccentrically rotating cylinders: Steady-state polymeric stress profile (a) $\boldsymbol{\tau}_{xx}$ (b) $\boldsymbol{\tau}_{xy}$ and (c) $\boldsymbol{\tau}_{yy}$ for extended White-Metzner fluid ($t = 10$, $We = 0.2$, $Re = 50$ and $Ma = 0.02$).

Table 6.9: Flow between eccentrically rotating cylinders: Values of the stability factor, χ, $Ma = 10^{-4}Re$ (small), $We \in \{0, 0.1, 0.25, 0.5, 1.0\}$ $k = -0.7$.

FENE-P-MP Model

Figure 6.18 and Table 6.10 shows a sample of results for the FENE-P-MP model. The dissipation parameter, λ_D, has a very significant impact on the journal torque, C. At $Re = 50$, $We = 0.5$ we see that the steady-state value of F_y is reduced considerably by from

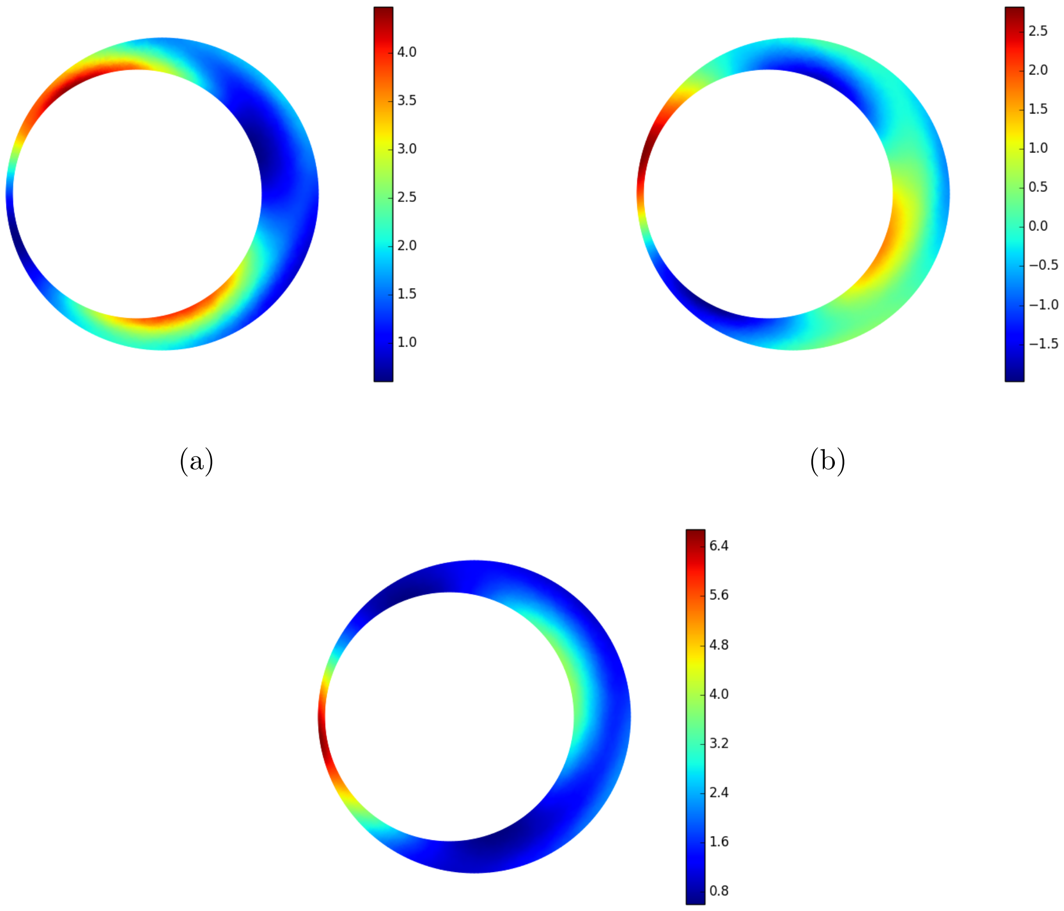

(a) (b)

(c)

Figure 6.11: Flow between eccentrically rotating cylinders: Steady-state polymeric stress profile $\boldsymbol{\tau}_{xx}$ (a) $\boldsymbol{\tau}_{xy}$ (b) $\boldsymbol{\tau}_{yy}$ (c) extended White-Metzner fluid ($t = 10$, $We = 1.0$, $Re = 50$ and $Ma = 0.02$)

$\lambda_D = 0$ to $\lambda_D = 0.2$ and at the same time the value of F_x is increased. As a result the stability factor rises from $\chi = 0.81$ to 21.25.

$\lambda_D \backslash We$	0	0.1	0.25	0.5
0	0.0494	1.256	3.384	8.227
0.1	2.325	3.64	4.4758	15.698
0.2	6.69	10.256	24.608	-

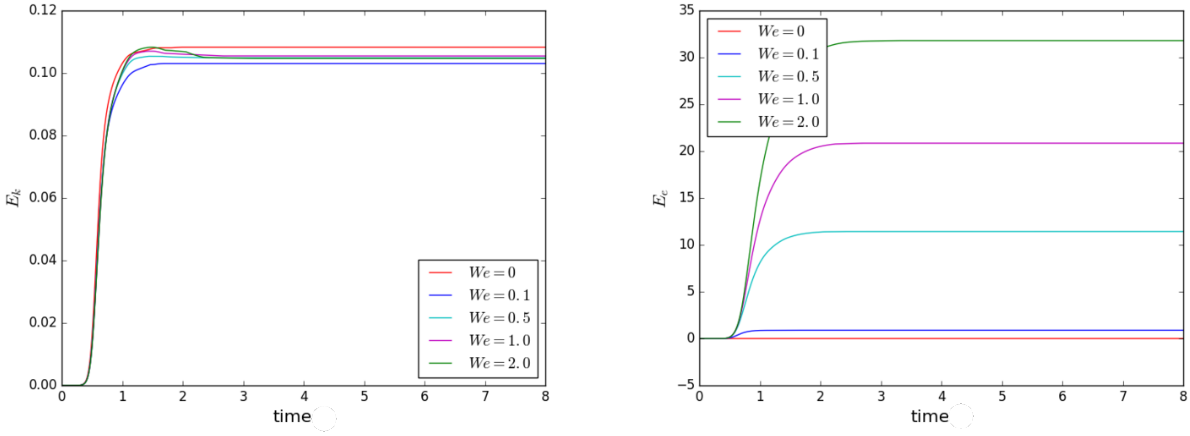

(a) (b)

Figure 6.12: Flow between eccentrically rotating cylinders: Kinetic & Elastic energies for extended White-Metzner fluid, $We \in \{0.1, 0.25, 0.5, 0.75, 1.0\}$, $\beta_v = 0.5$, $Re = 100$ $Ma = 0.1$.

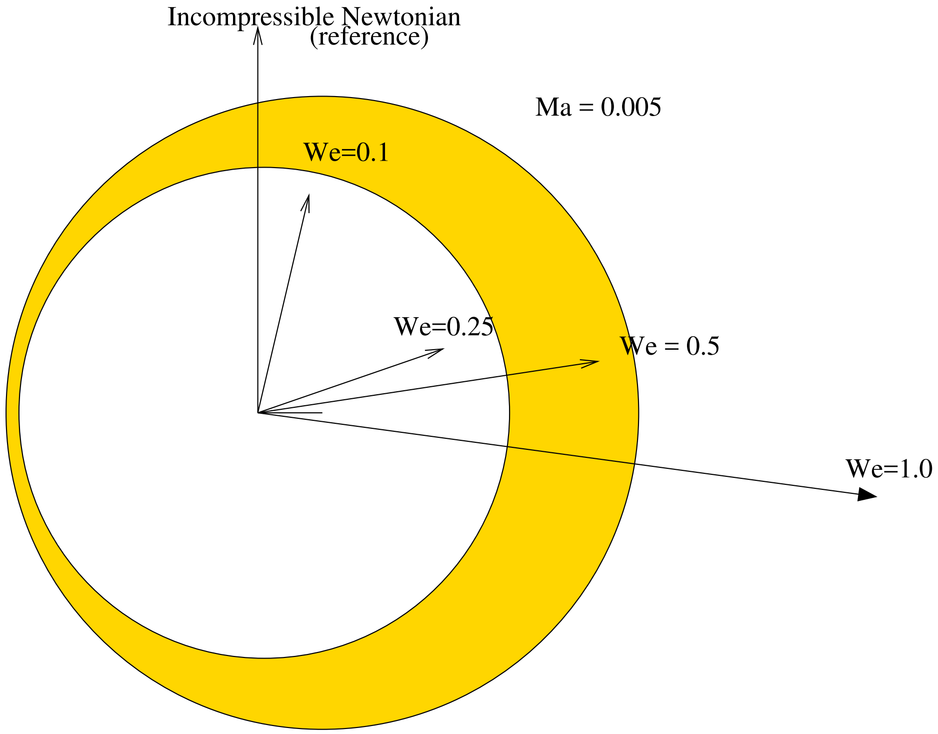

Figure 6.13: Flow between eccentrically rotating cylinders: Diagram of steady-state resultant force vector, **F**, varying with Weissenberg number for extended White-Metzner fluid, $\beta_v = 0.5$, $Re = 100$, $Ma = 0.005$.

Table 6.10: Flow between eccentrically rotating cylinders: Values of the stability factor, χ, $Ma = 10^{-4}Re$ (small), $We = 0.5$ $Re = 25$ $k = -0.7$, $Re = 50$.

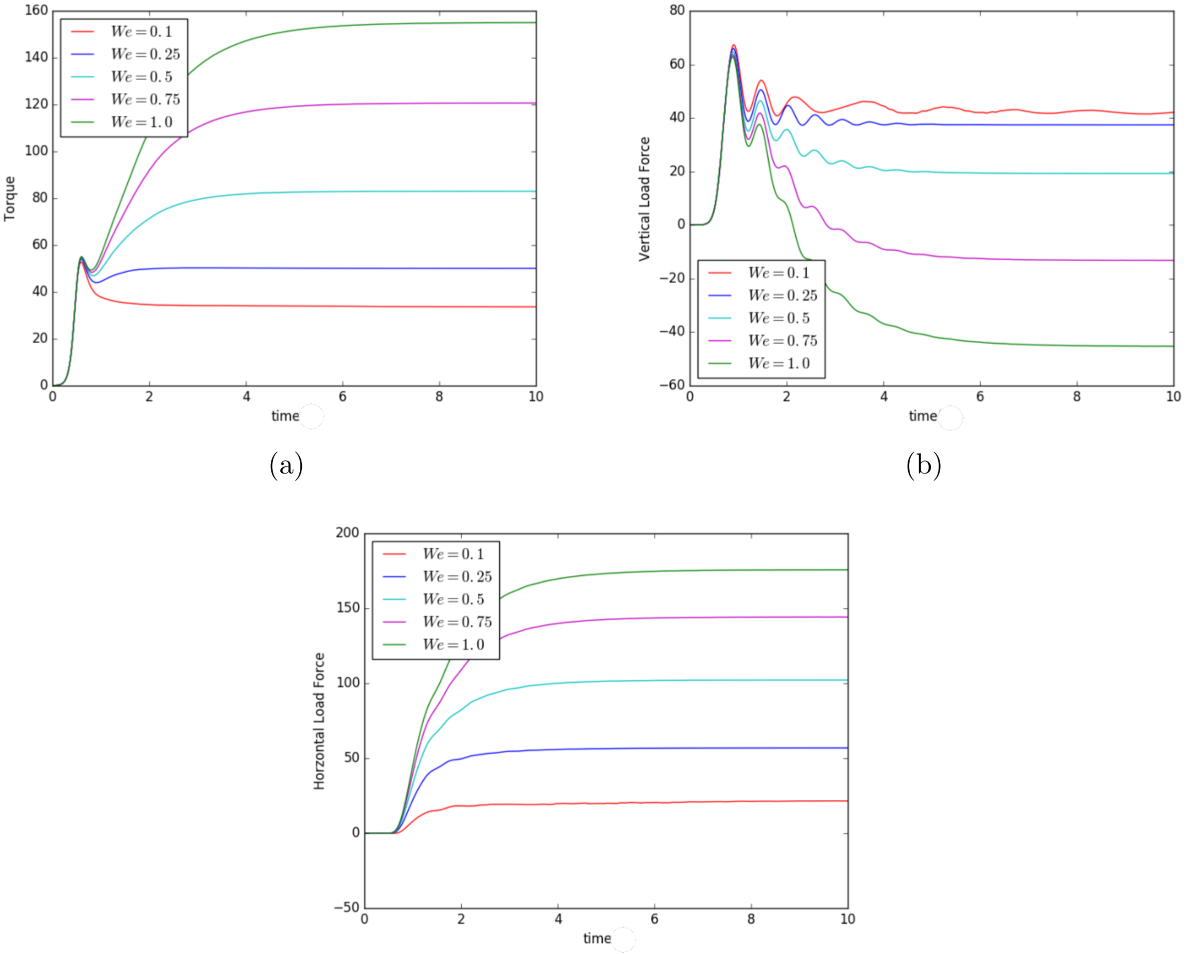

(a)

(b)

(c)

Figure 6.14: Flow between eccentrically rotating cylinders: (a) torque, (b) vertical load (F_y) and (c) horizontal load (F_x) for extended White-Metzner fluid, $We \in \{0.1, 0.25, 0.5, 0.75, 1.0\}$, $\beta_v = 0.5$, $Re = 100$ $Ma = 0.1$.

6.6 Summary

Numerical results for the viscoelastic flow between two cylinders have been presented. Both incompressible and compressible flow have been considered. Using χ as a measure of the rotational stability, we have shown that both elasticity and compressibility have a significant stabilising effect on the journal for the extended White-Metzner and FENE-P-MP models. The numerical results for viscoelastic flow suggest desirable and undesirable effects on the load bearing capacity and torque. For both EWM and FENE-P-MP fluids the torque in-

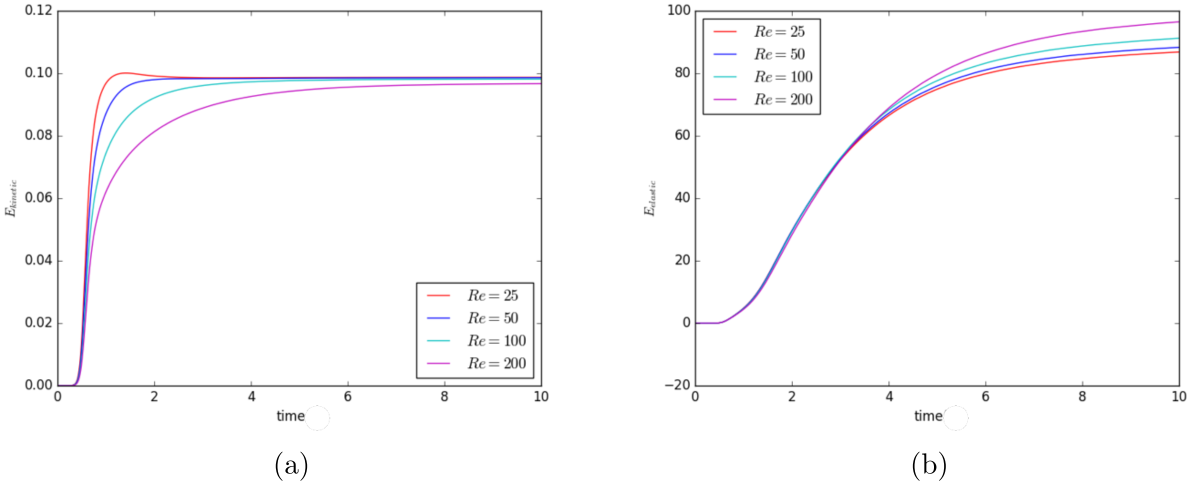

Figure 6.15: Flow between eccentrically rotating cylinders: (a) kinetic & (b) elastic energies for extended White-Metzner fluid, $Re \in \{25, 50, 100, 200\}$, $\beta_v = 0.5$, $We = 0.5$ $Ma = 10^{-4} \times Re$

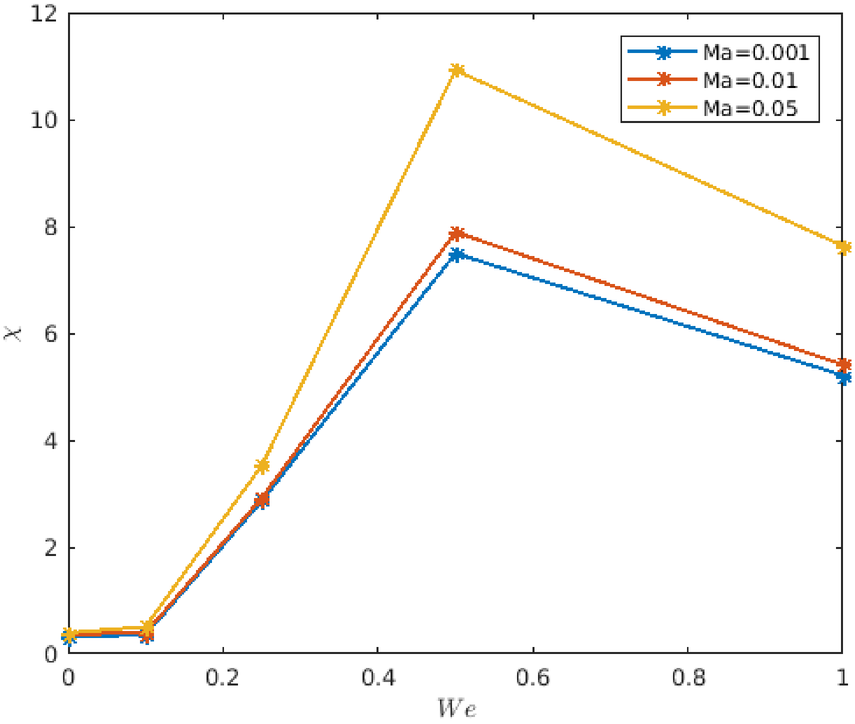

Figure 6.16: Flow between eccentrically rotating cylinders: Values of the stability factor, χ against We. $Ma \in \{0.001, 0.01, 0.05\}$

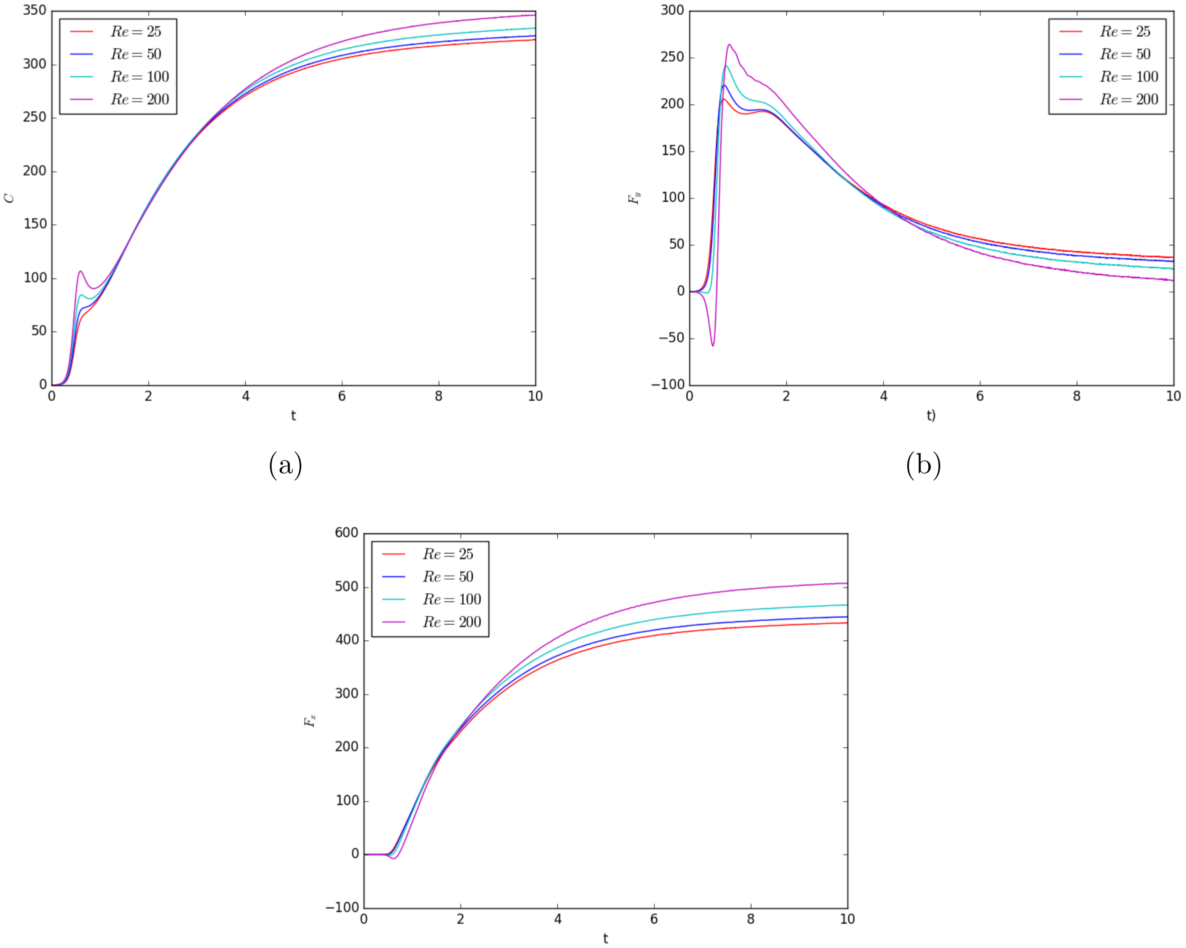

(a) (b)

(c)

Figure 6.17: Flow between eccentrically rotating cylinders: (a) torque, (b) horizontal load and (c) vertical load for extended White-Metzner fluid, $Re \in \{25, 50, 100, 200\}$, $\beta = 0.5$, $We = 0.5$ $Ma = 10^{-4} \times Re$.

creases with Weissenberg number whilst the stability factor also increases. This may be a surprising result as both models are technically *shear-thinning*. However, whilst it is true that the flow near the inner boundary near the journal is shear dominated, the flow becomes increasing extensional in the region near the small gap. Hence the viscosity response in the extensional region increases substantially as expected with both of these models. The selection of geometrical parameters (see Table 6.4) used in the simulations are similar to those in a standard rheometer (see [92]). The results presented in this chapter are qualitatively

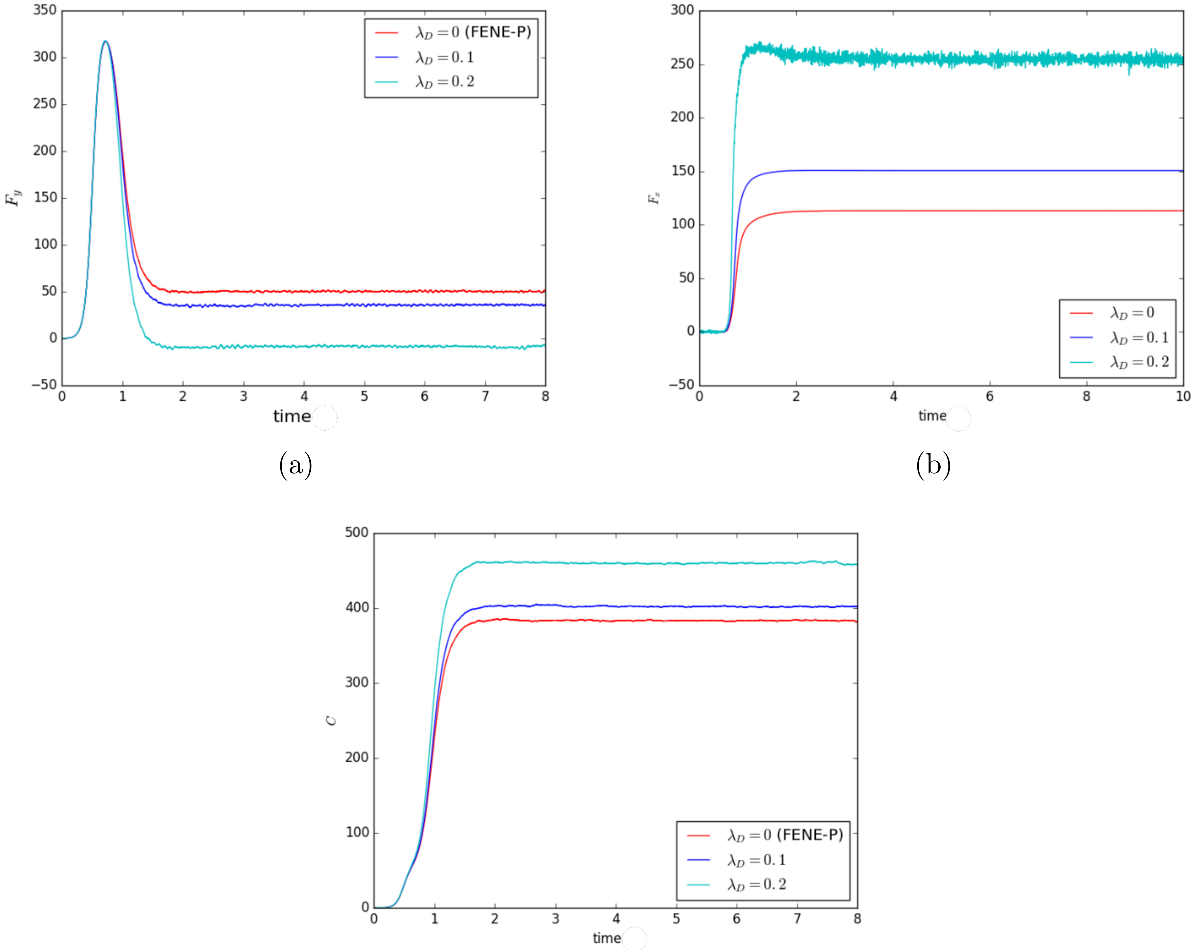

(a)

(b)

(c)

Figure 6.18: Flow between eccentrically rotating cylinders: The effect of dissipation parameter λ_D on (a) F_x, (b) F_y and (c) torque for FENE-P-MP fluid ($We = 0.5$, $\beta = 0.5$, $Re = 50$ $Ma = 0.005$).

verifiable and may give us stronger numerical insight into the nonisothermal flow between cylinders.

Future work should focus on the dynamic problem, where the centre of rotation of the inner moves as the inner cylinder is subject to the forces exerted on it by the fluid. This is a necessary step for developing a fully dynamic model of journal bearing lubrication.

Chapter 7

Drag Predictions for the FENE-P-MP Model

7.1 Introduction

The flow of a viscous fluid past a sphere at low Reynolds numbers is a classical problem and one of the oldest in theoretical fluid mechanics, dating back to the work of G.G. Stokes [83]. Stokes developed an analytical solution for non-inertial flow around a sphere in an unbounded fluid. The problem of mathematically modelling viscoelastic flow past a sphere has been studied since the 1970s, with the flow characteristics departing from the Newtonian case in several important ways.

The quantity of interest is the drag experienced by a sphere, radius R_s when falling through a cylindrical tube, radius, R. The drag correction factor, D^*, is used to normalise the results and is defined as the ratio of the drag in the current flow to that which would be experienced by the same sphere in an *unbounded expanse* of Newtonian fluid of the same viscosity. We define D^* as

$$D^* = \frac{F_d}{6\pi\mu R_s U} \tag{7.1.1}$$

where F_d is the drag force on the sphere, μ is the dynamic viscosity, R_s is the radius of the

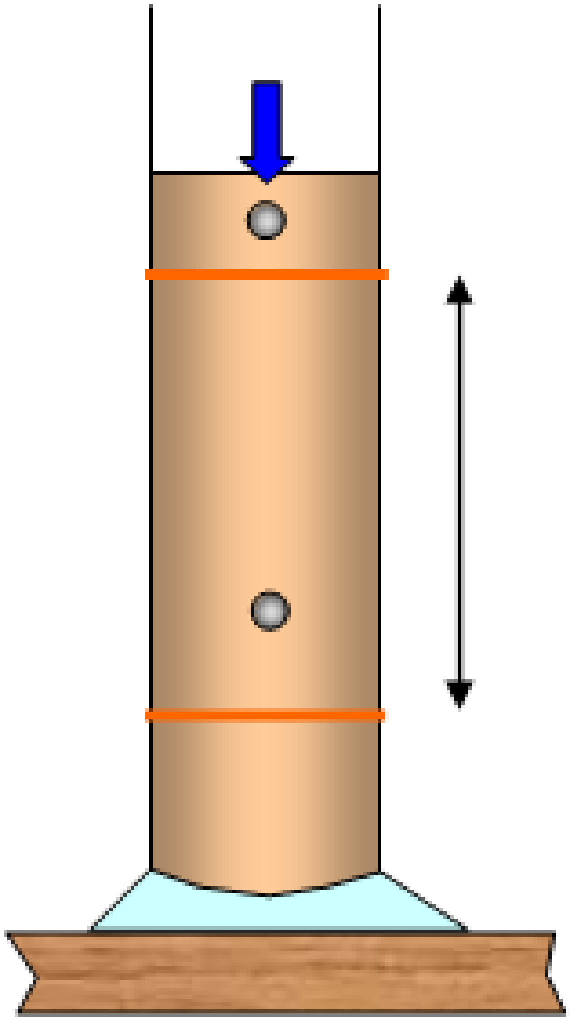

Figure 7.1: Schematic diagram of viscosity experiment: A sphere falling through a cylindrical tube.

sphere and U is the sphere velocity. Another measurement of the drag used in the literature is the normalised drag coefficient, K/K_N, defined

$$K/K_N := \frac{F_d}{F_{Newtonian}} \tag{7.1.2}$$

where $F_{Newtonian}$ is the Newtonian drag experienced by the sphere *falling through a cylinder with the same aspect ratio* R_{sphere}/R.

7.2 Literature Survey

In a study examining the influence of polymer properties (solvent quality and polymer molecular weight), Solomon and Muller [79] concluded that the steady-state drag on a sphere is determined by the interplay between the quality of the solvent, and the shear and extensional viscosity behaviour of the solutions.

Jones et al. [47] performed drag experiments with Type-I and Type-II Boger fluids: Type-I is a mixture of maltose syrup/water-based with 0.1% PAA (polyacrylamide) and Type-II containing a 0.19% PIB w/v (polyisobutylene) with a solvent consisting of polybutene (93%) and 2-chloropropane (7%). For the experimental set-up the drag was calculated by measuring the rate at which spheres of radius R_s fall through cylindrical tubes, radius R. The experiments were repeated varying the aspect ratio, $\beta_{sphere} = R_s/R$. Once the sphere achieves its terminal velocity the flow is considered to have reached a steady-state. Results for the Type-II drag predictions are shown in Fig. 7.2. The rheological properties show that both types of fluid exhibit constant shear viscosity, at low to moderate shear-rates, giving way to some slight shear-thinning at high shear-rates. Furthermore, it is reported that the first normal stress-difference, N_1, exhibits the classical quadratic behaviour [34, 47].

Until recently the most widely used continuum models for Boger fluids have been the Oldroyd-B and FENE-CR models, both predicting constant shear viscosity and extensional strain-hardening. However, both models fail to predict the level of drag enhancement observed in the flow past a solid sphere [17, 78]. Garduño et al [34] proposed the swanINNNF(q) class of viscoelastic models to capture the strain hardening behaviour that causes the drag enhancement observed in Type-II Boger fluids. They found that the extension rate dependent viscosity FENE-CR and White Metzner models proved capable of capturing the levels of enhanced drag, observed experimentally by Jones et al. [47] over comparable measures of deformation-rates.

In this section we describe numerical predictions of drag for the FENE-P-MP model (Eq. (3.3.21)) presented in Sec. 3.3.2. From the point of view of the underlying physics, the cause of the secondary strain hardening regime can be attributed to the non-affine polymer stick relative to the flow field which is captured by the stick/slip tensor, **L**, defined in Eq. (3.3.15).

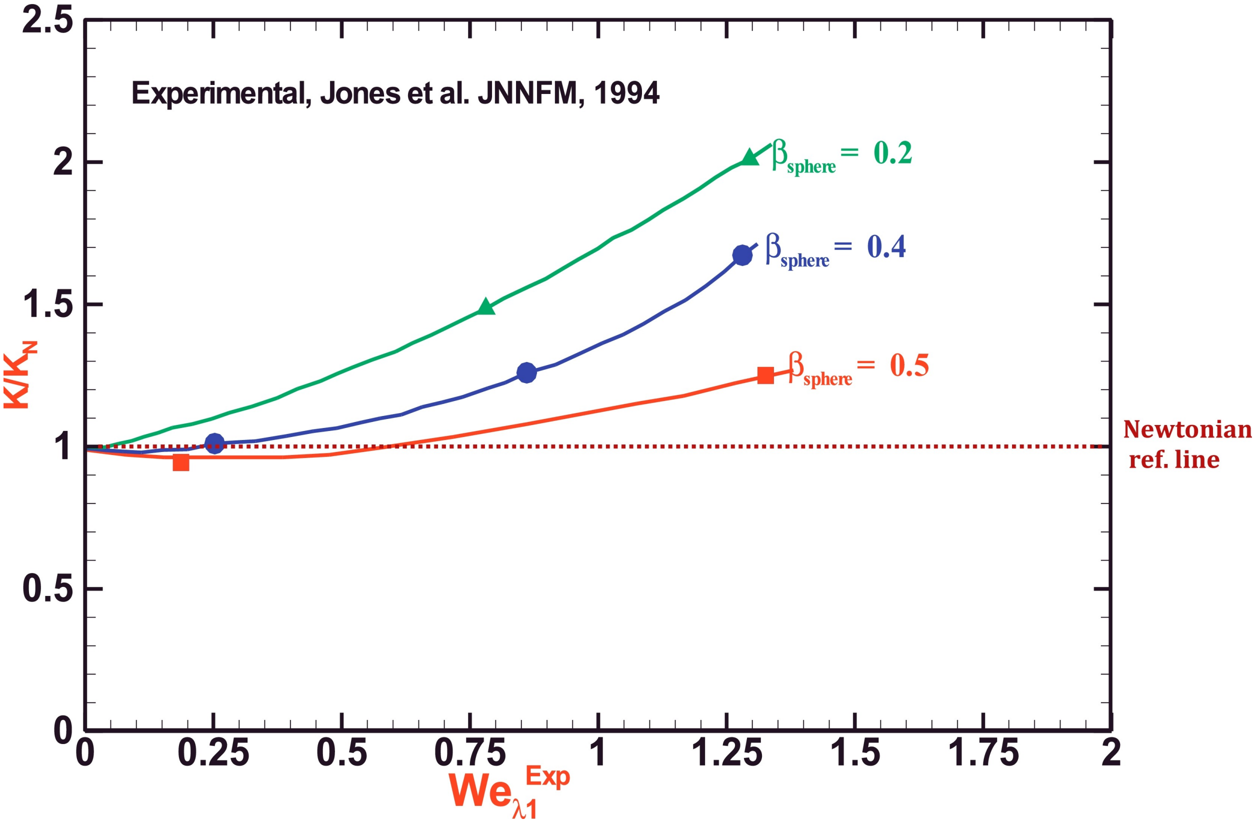

Figure 7.2: Empirical data for the normalised drag coefficient K/K_N of a Type-II Boger fluid with different aspect ratios ($\beta_{sphere} = 0.2, 0.4, 0.5$), Jones et al. [47] (Image: Garduño et al. [34])

7.3 Domain & Mesh

We consider a cylinder of length $40R_s$ and radius $5R_s$ ($\beta_{sphere} = 0.2$) or $2.5R_s$ ($\beta_s = 0.4$) or $2R_s$ ($\beta_s = 0.5$). The inflow boundary is located at $z = -20R_s$ and outflow at $z = 20R_s$. Uniform flow in the axial direction is imposed on both the inflow and outflow boundaries. Axisymmetric boundary conditions are imposed along the axis of symmetry and no-slip boundary conditions are imposed on the sphere. Finally, to take account of the moving frame, time-dependent moving wall boundary conditions are applied along the top wall matching the inflow and outflow velocity. The inflow and upper wall Dirichlet boundary conditions are ramped using a hyperbolic tangent ramping function so that the velocity at the top wall and inlet is given by

$$\mathbf{u} = (u, v) = (U(t), 0) \tag{7.3.1}$$

where $U(t) = \frac{U_{in}}{2}\tanh(8(t-0.5))$ and U_{in} is the terminal velocity of the sphere. At the outlet and along the line of symmetry we impose that the radial component of velocity is zero ($v = 0$).

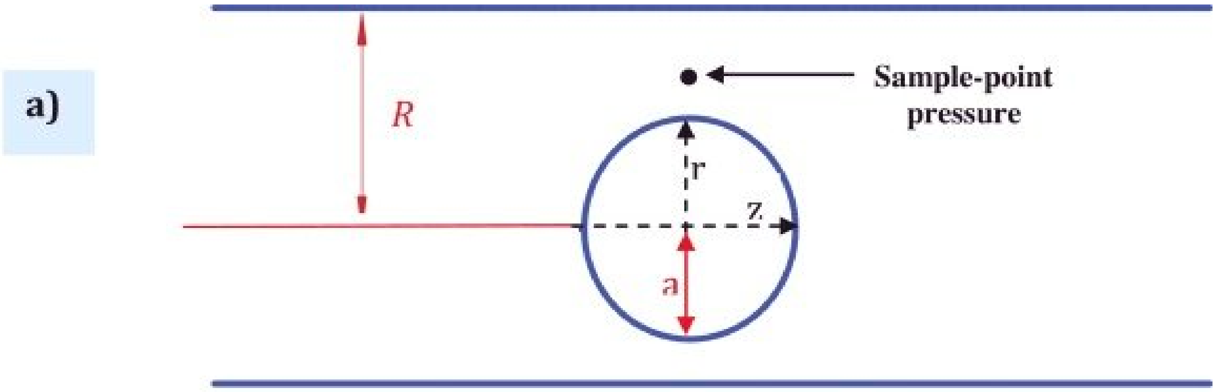

(a)

Figure 7.3: Flow past a sphere: Schematic diagram of the 2D domain. As the flow is axisymmetric it is only necessary to model a 2D flow in the plane extending from the centreline to the boundary along the length of the cylinder. Here R_{sphere} is denoted a (Image: Garduño et al. [34]).

Computations are performed on meshes with 3 levels of refinement: coarse ($M1$), medium ($M2$) and fine ($M3$). Details of the finite element meshes when $\beta_{sphere} = 0.5$ are given in Table 7.1.

Mesh	Cells	h_{min}	h_{max}	$DoF(p)$	$DoF(\mathbf{u})$	$DoF(\boldsymbol{\tau}_p)$
M1	3248	0.017425	0.744317	1879	14010	21015
M2	6362	0.017425	0.450238	3542	26890	40335
M3	8453	0.017425	0.37433	4606	35328	52992

Table 7.1: Flow past a shere: Mesh characteristics for coarse $M1$, medium $M2$ and fine $M3$ meshes for $\beta_{sphere} = 0.5$.

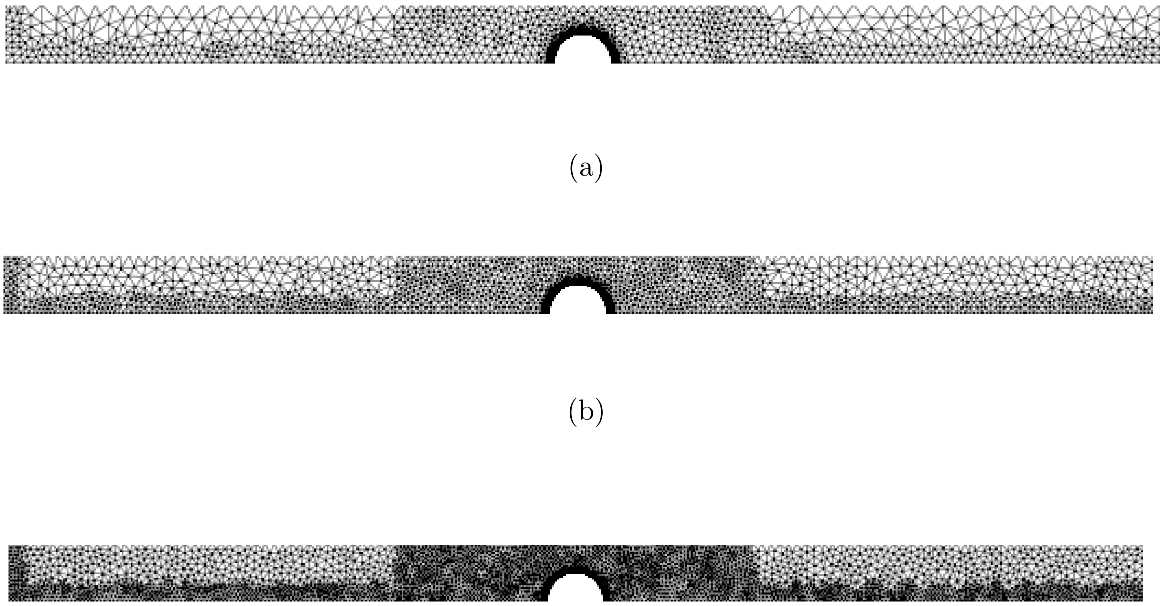

(a)

(b)

(c)

Figure 7.4: Flow past a sphere. Meshes (a) $M1$,(b) $M2$ and (c) $M3$ for $\beta_{sphere} = 0.5$.

Fig. 7.3 shows the 2D schematic of the flow geometry. As $Re \approx 0$ the flow is axisymmetric about the centreline we only compute the flow in a 2D plane extending radially outward from the sphere to reduce computational cost. Table 7.2 shows the characteristics of the meshes shown in Fig. 7.4. In each case the meshes are further refined in he region near the sphere boundary to maximise the solution accuracy.

β_{sphere}	Cells	h_{min}	h_{max}	$DoF(p)$	$DoF(\mathbf{u})$	$DoF(\boldsymbol{\tau}_p)$
0.2	8135	0.017377	0.52666	4434	34004	51006
0.4	6819	0.017402	0.50254	3689	28112	42668
0.5	6362	0.017425	0.450238	3542	26890	40335

Table 7.2: Flow past a sphere: Mesh characteristics $\beta_{sphere} = 0.2, 0.4, 0.5$.

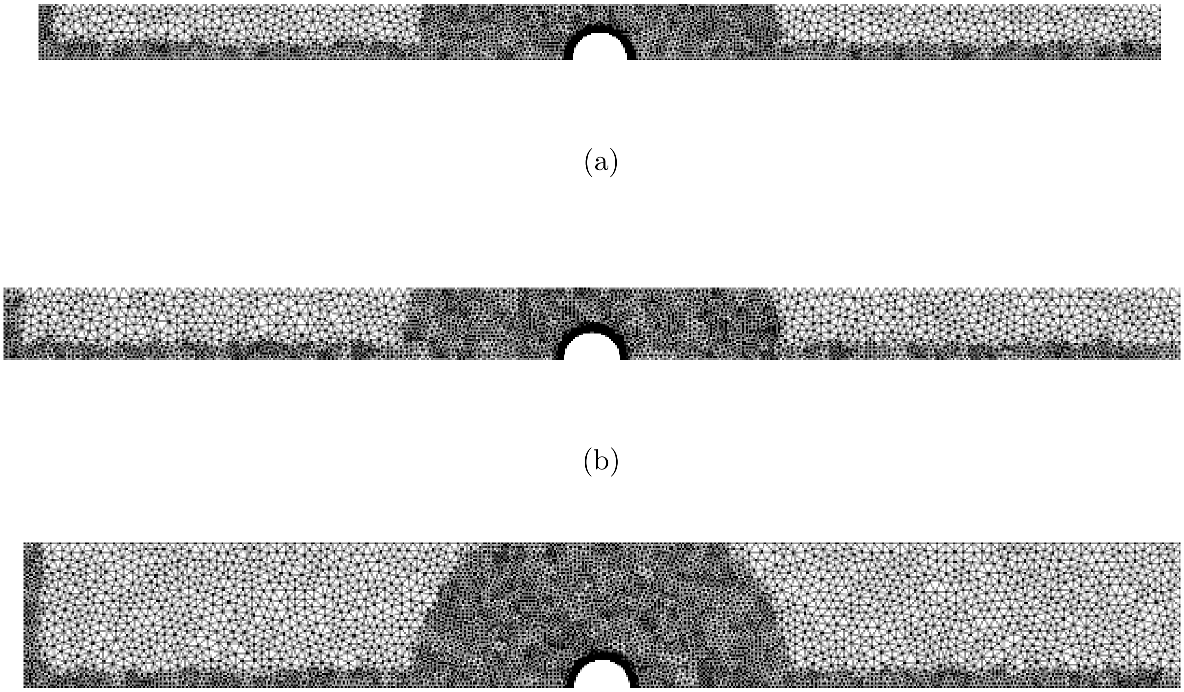

(a)

(b)

(c)

Figure 7.5: Flow past a sphere. Finite element meshes for different aspect ratios: (a) $\beta_{sphere} = 0.5$ (b) $\beta_{sphere} = 0.4$ and (c) $\beta_{sphere} = 0.2$ (medium refinement).

7.4 Calculating Drag on Sphere

The solution is used to approximate the drag experienced by the sphere as the fluid passes over it. The drag is calculated by computing the integral of $\boldsymbol{\sigma} \cdot \mathbf{n}$ over the sphere boundary

$$\begin{aligned} F_d &= 2\pi R_s^2 \int_{\Gamma_{sphere}} (1,0) \cdot \boldsymbol{\sigma} \cdot \mathbf{n} \sin\theta \, dS \\ &= 2\pi R_s^2 \int_{\Gamma_{sphere}} (\sigma_{zz}\cos\theta + \sigma_{rz}\sin\theta)\sin\theta \, dS \end{aligned} \tag{7.4.1}$$

where

$$\theta = \arctan\left(\left|\frac{r}{z}\right|\right) \tag{7.4.2}$$

and the sphere is centred at the origin. the Reynolds, Weissenberg and Mach numbers are defined

$$Re = \frac{\rho U_{in} L}{\mu_0}, \qquad We = \frac{\lambda U_{in}}{L}, \qquad Ma = \frac{U_{in}}{c_0}. \tag{7.4.3}$$

where U_{in} is the terminal velocity of the sphere, the characteristic length $L = R_{sphere}$ and μ_0 is the total viscosity.

7.5 Governing Equations

7.5.1 Oldroyd-B Model

In order to benchmark the results we first compute the flow of an Oldroyd-B fluid past a sphere and compare the drag predictions with those obtained by Kynch and Phillips [54]. A creeping flow is assumed and as such the effects of inertia and compressibility are negligible, therefore we set $Re = 0$, $Ma = 0$ ($\nabla \cdot \mathbf{u} = 0$). The governing equations are given by (4.1.15) with

$$\mathbf{g}_1(\mathbf{C}) = \frac{1-\beta_v}{We}(\mathbf{C} - \mathbf{I}) \quad \mathbf{g}_2(\mathbf{C}, \nabla\mathbf{u}) = 0 \tag{7.5.1}$$

The equations are solved using the numerical scheme for incompressible viscoelastic flow, outlined in Sections 4.3, 4.6 and 4.7.

7.5.2 FENE-P-MP Model

We consider creeping flow past a sphere of a FENE-P-MP fluid, setting $Re = 0$, $Ma = 0$ ($\nabla \cdot \mathbf{u} = 0$). For incompressible flow the governing equations are given by (4.1.15) with $\mathbf{g}_1$ and $\mathbf{g}_2$ defined

$$\mathbf{g}_1(\mathbf{C}) = \frac{1-\beta_v}{We}(\mathbf{f}(tr\mathbf{C})\mathbf{C} - \mathbf{I}) \tag{7.5.2}$$

$$\mathbf{g}_2(\mathrm{C}, \nabla \mathbf{u}) = (\mathbf{f}(\mathrm{tr}\mathbf{C}) - 1)\mathbf{C} + We\psi(\dot{\epsilon})[\mathbf{C} \cdot \mathbb{D} + \mathbb{D} \cdot \mathbf{C}] \tag{7.5.3}$$

where

$$\mathbf{f}(tr\mathbf{C}) = \frac{1}{1 - tr\mathbf{C}/b^2} \tag{7.5.4}$$

and ψ is defined by Eq. (3.3.16).

7.6 Results and Discussion

Results for low Reynold's number flow past a sphere of Oldroyd-B and FENE-P-MP fluids were computed for Weissenberg numbers in the range $0 \leq We \leq 2.5$ and aspect ratios $\beta_{sphere} \in \{0.2, 0.4, 0.5\}$. Results for the Oldroyd-B flow were quantitatively compared to results by Kynch & Phillips [53] and for the FENE-P-MP model are compared to numerical results by Garduño at. al [34] and empirical data by Jones et al. [47].

7.6.1 Grid Independence and Error Size

First we compare the kinetic energy for the different meshes shown in Fig. 6.4 to verify the independence of the solution to the mesh used.

Figure 7.6 shows the convergence behaviour of the kinetic energy and drag with meshes $M1$, $M2$ and $M3$ for $We = 0.2$. Mesh convergence is confirmed for both elastic energy and drag.

7.6.2 Oldroyd-B

Figure 7.7 shows steady state pressure and velocity contours. For the Newtonian fluid ($We = 0$) the pressure is symmetric about the mid-point of the channel. As the Weissenberg number is increased this symmetry is progressively broken. A significant pressure drop begins to occur in the wake of the sphere. The minimum and maximum pressures are not

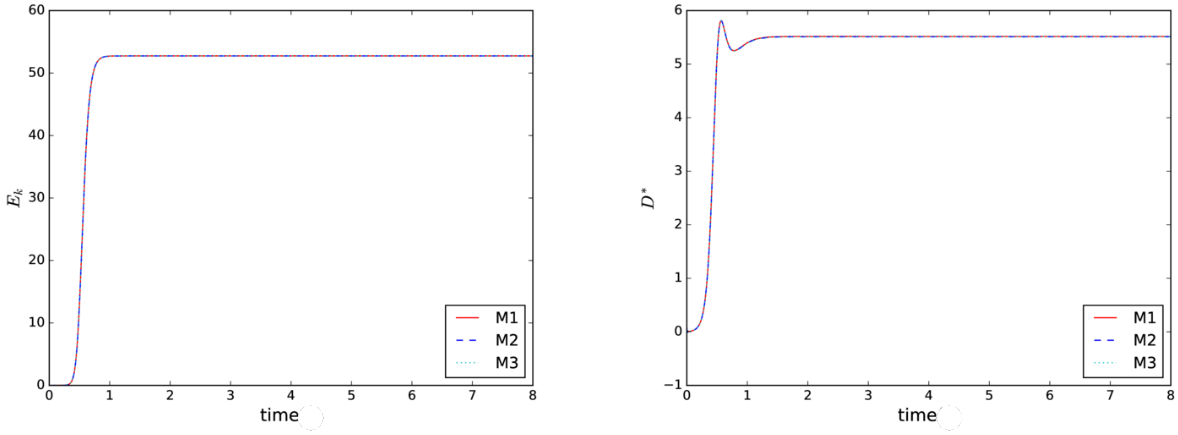

(a)

(b)

Figure 7.6: Flow Past a Sphere: (a) Kinetic energy and (b) Drag profiles (Oldroyd-B model) for meshes $M1$-$M3$ ($\beta_{sphere} = 0.5$), $Re = 1$ $We = 0.2$, $c_1 = 0.05$, $\gamma_u = 1 - \beta_v$.

largely affected by this for Weissenberg numbers in the range $0 \leq We \leq 1.0$. Furthermore the maximum flow speed in the region between the sphere and the wall remains effectively unchanged in the range $0 \leq We \leq 1.0$.

The first normal stress difference, $N_1 = \tau_{zz} - \tau_{rr}$, and shear stress, τ_{rz}, grow significantly in the wake of the sphere as the Weissenberg number increases. Figure 7.7 shows two cases ($We = 0.1$ and $We = 1.0$). It is in this region where the fluid experiences large extension rates and, as discussed in Sec. 3.4, the Oldroyd-B model risks predicting unphysical extensional viscosities. For this reason the fluctuation operator, κ_h, attains high values in the region just after the narrow gap.

We were able to compute values of the normalised drag coefficient for $We \leq 1.2$ as shown in Table 7.3. As the Weissenberg number is increased from 0, D^* decreases. Drag predictions computed using the Taylor-Galerkin finite element solution compare well in to those by Kynch & Phillips [53].

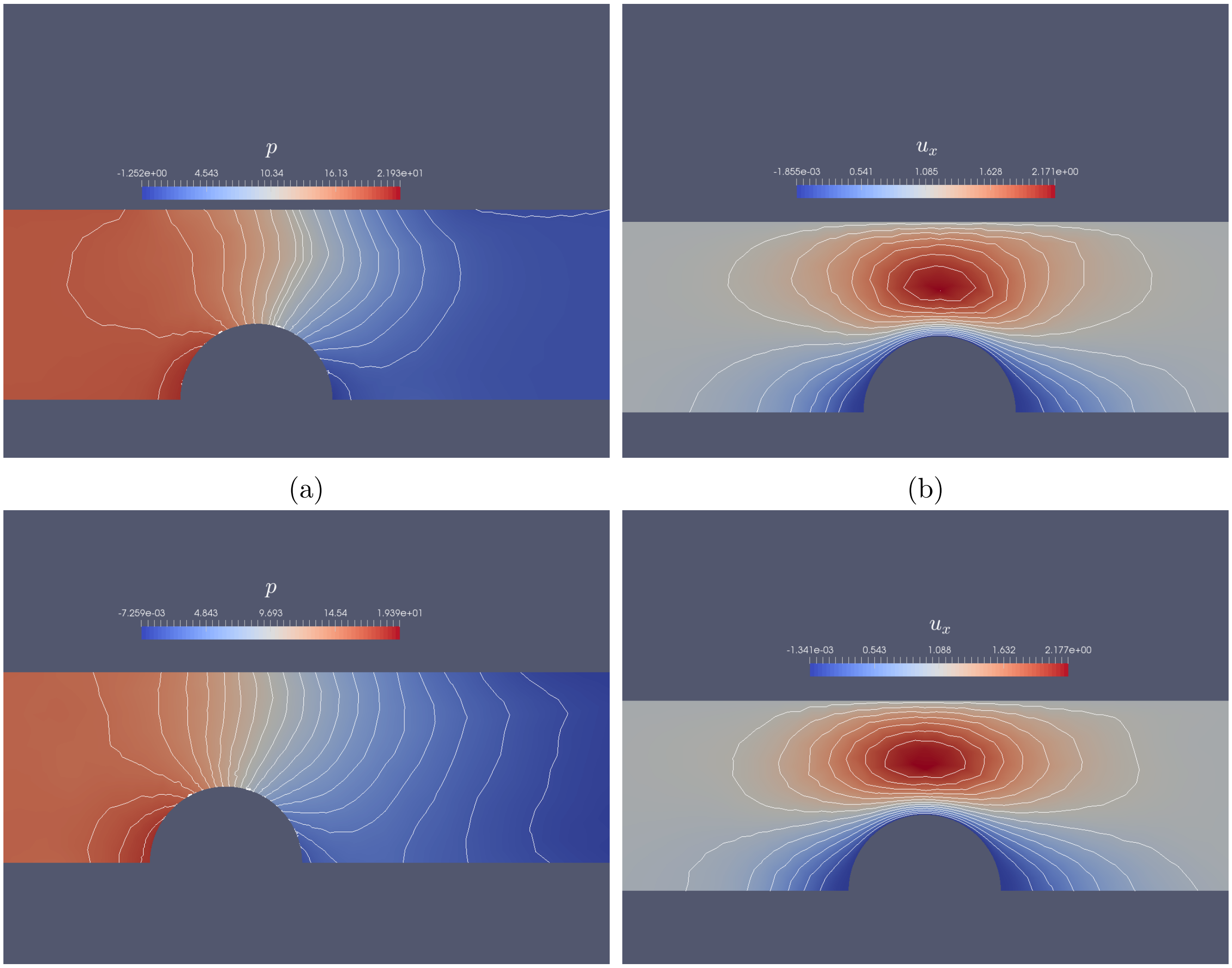

(a) (b)

(c) (d)

Figure 7.7: Flow past a sphere: Contours of steady state pressure and axial velocity of an Oldroyd-B fluid, $\beta_{sphere} = 0.5$ (a) and (b) $We = 0.5$ and (c) and (d) $We = 1.0$.

β_{Sphere}	We	Current study	Kynch & Phillips [54]
0.5	0.0	5.9379	5.9474
	0.5	5.8024	5.8494
	0.7	5.4133	5.3492
	1.0	5.2844	5.2277
	1.2	5.2021	5.1887

Table 7.3: Flow past a sphere: Values of the drag correction factor for Oldroyd-B fluid, $Re = 0$, $\beta_{sphere} = 0.5$, $\beta_{solvent} = 0.5$.

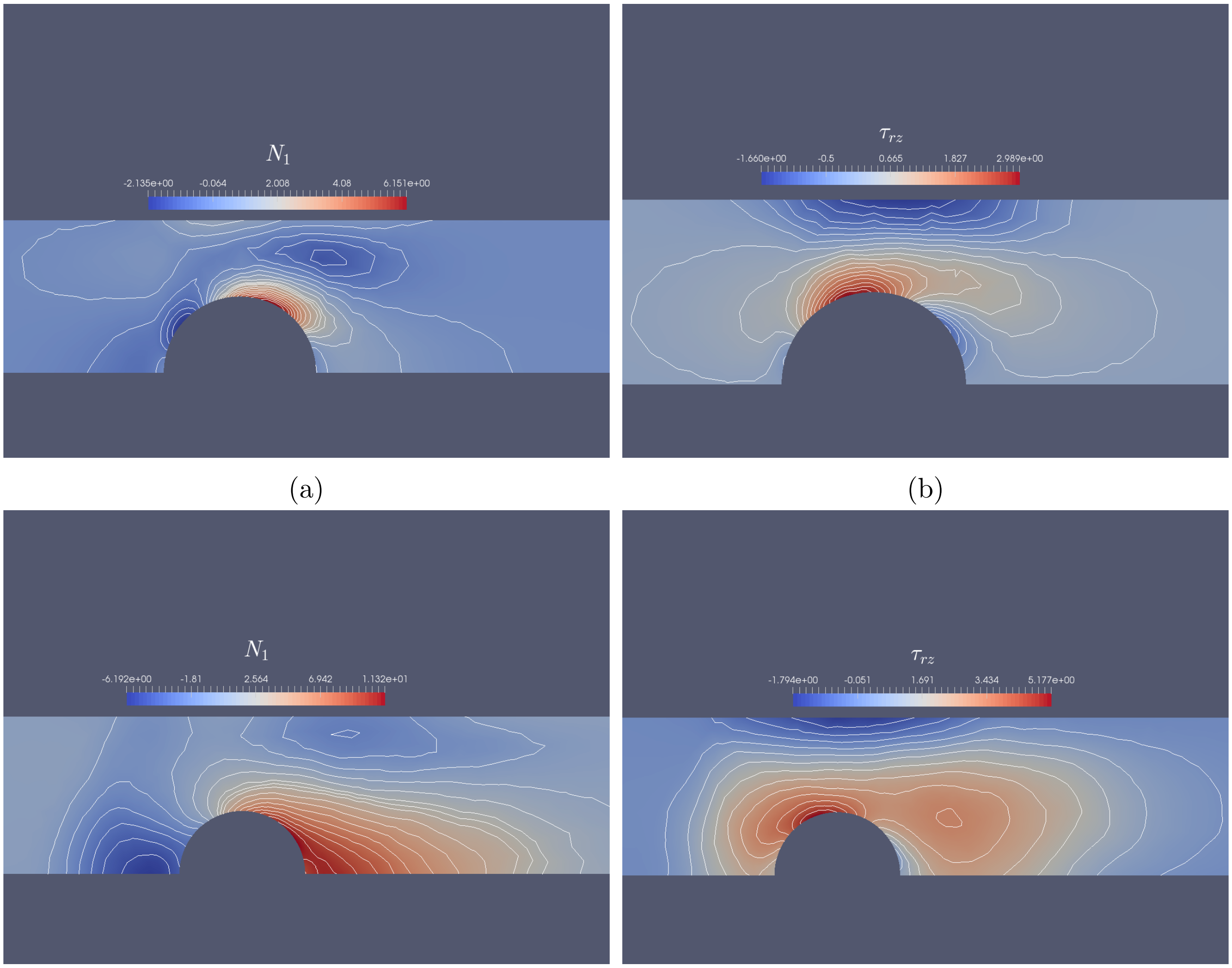

(a) (b)

(c) (d)

Figure 7.8: Flow past a sphere: Contours of Steady N_1 and τ_{rz} of an Oldroyd-B fluid $\beta_{sphere} = 0.5$ (a) and (b) $We = 0.2$, (c) and (d) $We = 1.0$.

7.6.3 FENE-P-MP

Now that the numerical scheme has been benchmarked for Oldroyd-B flow and exhibits a good level of agreement with results in the literature we numerically simulate FENE-P-MP flow past a sphere. For all of the computations we set $\Delta t = h_{min}^2$, $\gamma_u = 1 - \beta_v$, $c_1 = 0.05$ and $c_2 = 0.01$.

A sample of the results is displayed in Fig. 7.9 - Fig. 7.14 . During the first two seconds of the flow there is an initial overshoot in the drag before it reduces to a steady state value.

The time taken for D^* to reach a steady state increases with Weissenberg number however the peak value of drag during the transient phase is independent of We.

Comparisons of flow characteristics for varying λ_D are shown in Fig. 7.13 and 7.12. For $\beta_{sphere} = 0.4$, $\backepsilon= 5$, a *drag reduction* is observed for $We = 0.2$ and K/K_N stays below 1 for $0 \leq \lambda_D \leq 0.15$. The transient behaviour remains largely unchanged by varying λ_D. However, increases in the value of λ_D result in an increase in steady-state drag. The dissipation parameter, λ_D, has a significant effect on both K/K_N and E_e. Even for small values of λ_D a significant increase in the normalised drag coefficient is observed, reaching 1.4 for $\lambda_D = 0.2$ ($We = 0.5$, $\beta_{sphere} = 0.4$). Pressure at the mid point of the flow also varies significantly with λ_D, ranging from $P = 41.23$ for $\lambda_D = 0$ to $P = 56.27$ for $\lambda_D = 0.15$ ($We = 0.65$), a 36.4% increase. A sample of drag and energy results are displayed in Figures 7.12 and 7.14.

Table 7.4 provides a sample of calculated normalised drag coefficients for the FENE-P-MP fluid, comparing our results to (i) numerical predictions by Garduño et al. [34] and (ii) empirical data by Jones [47]. A lower value of the dissipation parameter is required in order to attain the empirically observed values of K/K_N and we are able to obtain good agreement with the empirical data for both $\beta_{sphere} = 0.2$ and $\beta_{sphere} = 0.4$. The value of κ_h required to stabilise solutions of the constitutive equation remains small over the range of fluid parameters considered. Figure 7.9 shows a typical plot of κ_h for $We = 1.0$ $Re = 0$ and $\lambda_D = 0.05$.

β_{Sphere}	We	K/K_N FENE-P-MP	K/K_N SwanINNF(q) (2016)	K/K_N Experimental (1994)
0.2	2.1	1.51 ($\lambda_D = 0.1$)	1.481 ($\lambda_D = 0.65$)	1.484
	3.5	-	2.041 ($\lambda_D = 0.65$)	2.009
0.4	0.65	1.018 ($\lambda_D = 0.09$)	1.004 ($\lambda_D = 0.62$)	1.012
	2.25	-	1.278 ($\lambda_D = 0.62$)	1.258

Table 7.4: Flow past a sphere: Drag prediction comparison of FENE-P-MP with swanINNF(q)-FENE-CR calculations ($Re = 0$, $b = 5$) and experimental data (Jones [47]).

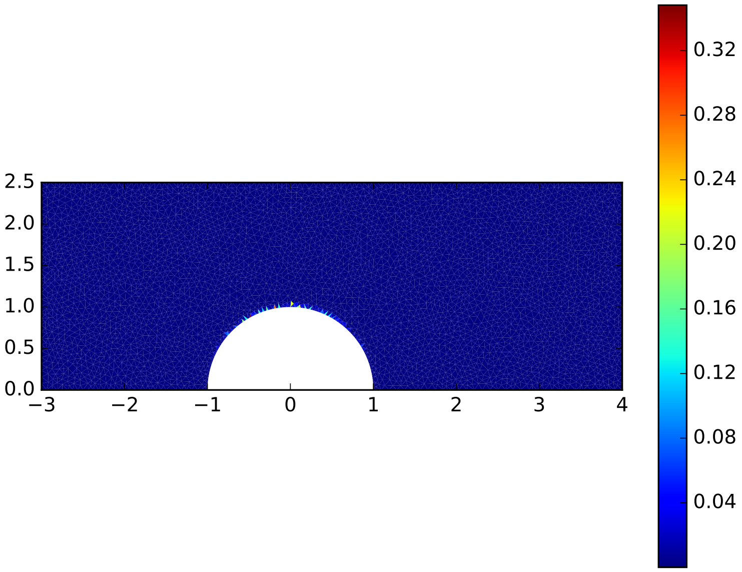

Figure 7.9: Flow past a sphere: Fluctuation operator κ_h: $\beta_{sphere} = 0.4$ $Re = 0$, $We = 1.0$, $\lambda_D = 0.05$, $t = 8.0$).

7.7 Summary

Numerical simulations of the inertia-free flow past a sphere using a stabilised Taylor-Galerkin finite element method have been presented. Results using the Oldroyd-B model show good agreement with results in the literature for attainable values of We. Computed values of the normalised drag coefficient for the FENE-P-MP model display good agreement with empirical data for the normalised drag coefficient of polyisobutylene/2-chloropropane solution (Type-II Boger fluid) in two cases where the Weissenberg number is below 2.0. Unfortunately, we were unable to achieve numerical convergence for high $We > 2.0$ for $\beta_{sphere} = 0.4$ and $We > 1.5$ for $\beta_{sphere} = 0.5$ ($\beta_v = 0.5$). Despite this disappointing result the overall qualitative behaviour of the model (increasing K/K_N with λ_D) implies that, with the right numerical stabilisation higher values of We can be attained and the drag increasing predictions of the FENE-P-MP can be further investigated. A suggested method for partial discretisation that could potentially yield mesh convergent results with better numerical stability could be the

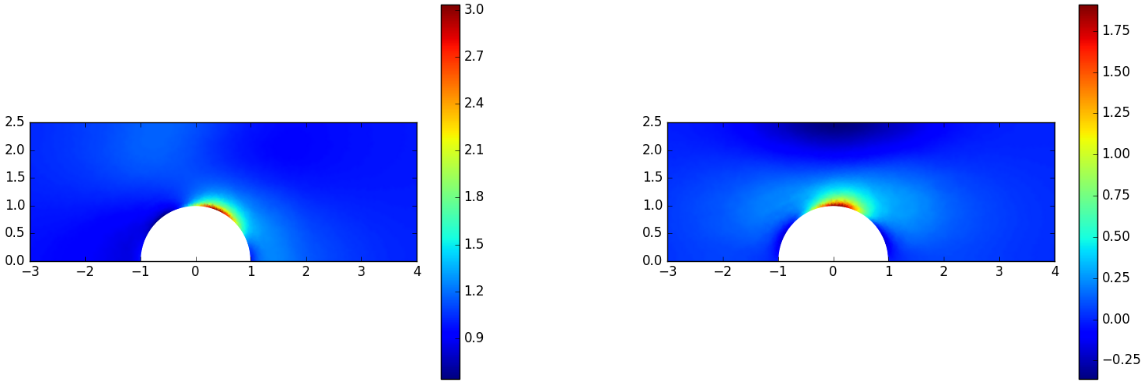

(a) τ_{rr}

(b) τ_{rz}

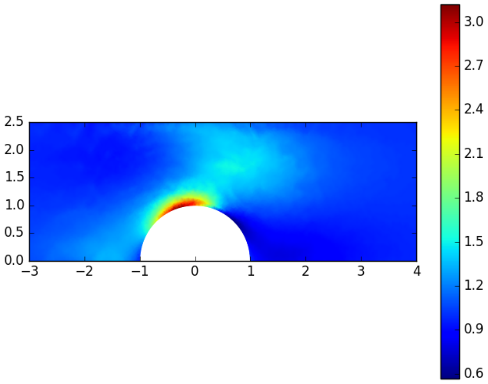

(c) τ_{zz}

Figure 7.10: Flow past a sphere: N_1, τ_{zz}, τ_{zr} and τ_{rr} for the FENE-P-MP fluid $\beta_{sphere} = 0.4$, $We = 0.5$, $b = 100$, $\lambda_D = 0.0$.

spectral element method developed by Kynch and Phillips [53, 54].

The stabilised Taylor-Galerkin finite element scheme for incompressible viscoelastic flow provides both an *efficient and easily implementable* method for simulating inertia free (axisymmetric) flow past a sphere. Computations were performed on a single CPU (quad-core) desktop and the numerical scheme (see Sec. 4.7.1) was programmed in Python using FEniCS/DOLFIN finite element libraries.

The derivation of the FENE-P-MP model using the generalised bracket method means that applications of the model to compressible and nonisothermal flows is straightforward and

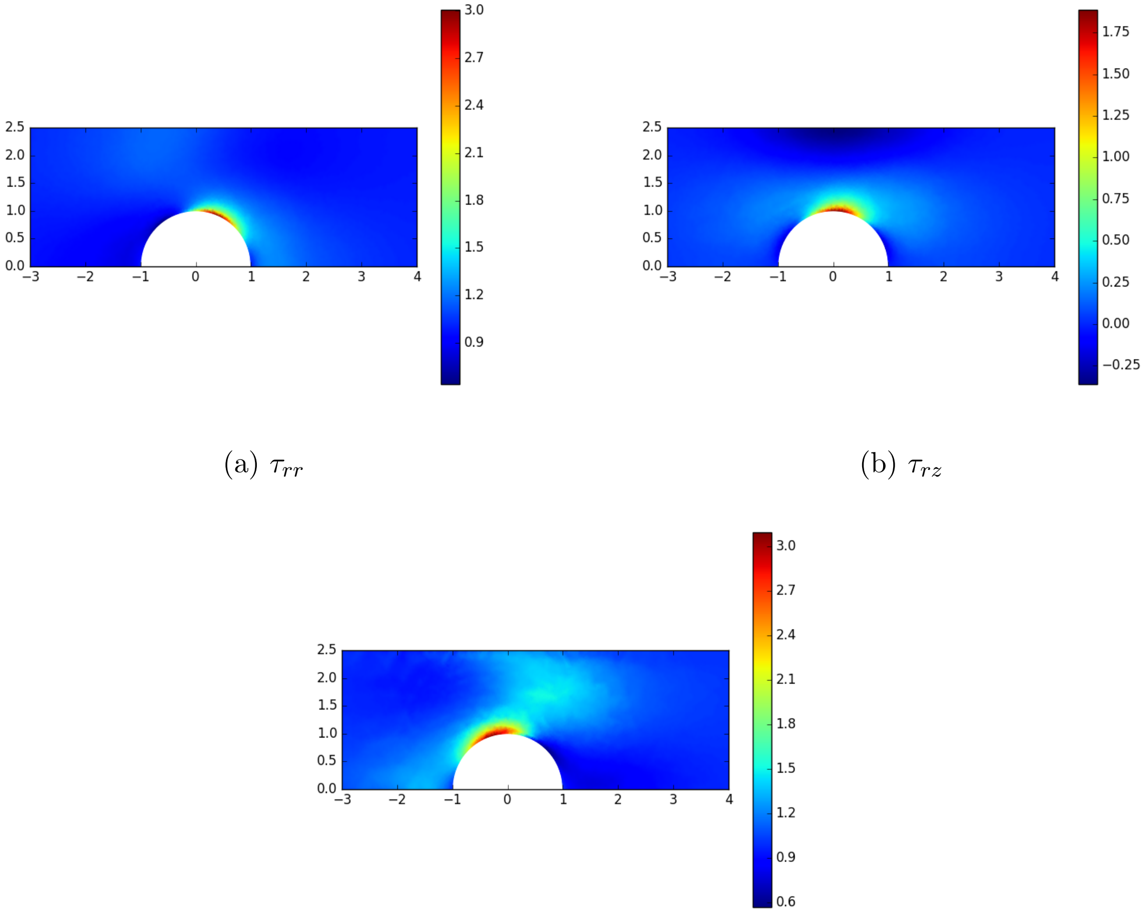

(a) τ_{rr}

(b) τ_{rz}

(c) τ_{zz}

Figure 7.11: Flow past a sphere: (a) τ_{zz}, (b) τ_{zr} and (c) τ_{rr} for the FENE-P-MP fluid, $\beta_{sphere} = 0.4$, $We = 0.5$, $b = 20$, $\lambda_D = 0.0$.

does not require ad-hoc modifications to the incompressible equations. This is an important advantage of the bracket method. When derived using the generalised bracket method and a nonzero **L** tensor, additional terms similar to the second term in Eq. (7.5.3) appear in the constitutive equation. The additional terms in the constitutive law (Eq. (3.3.19)) provide us with some physical insight into the material. A potential mechanism behind the observed drag enhancement that can be read from the equations is that, as the extensional flow rate increases, polymer entanglement causes the dissolved polymers to 'stick' relative to the flow field. However, this theory contradicts material assumption made when modelling

Boger fluids: that the polymer solution is *dilute* and therefore effects of polymer-polymer interaction are negligible. The exact physics behind the drag behaviour is still unclear and hence we are unable to determine the direct cause but numerical investigations such as this, using theoretically rigorous models, help provide strong insight into the possible explanations. It should be pointed out that the values of the phenomenological dissipation parameter, λ_D, required to predict the levels of empirically observed drag enhancement are lower in the FENE-P-MP model than those required in the swanINNF(q)-FENE-CR model. The reason for this is that the dissipation function, $\phi(\dot{\epsilon})$, appears in both the equation for the stress and the constitutive equation, increasing $\boldsymbol{\tau}_p$ both directly and indirectly as $\dot{\epsilon}$ increases. There are drawbacks to including these additional terms. The main two being increased numerical instability and computational cost associated with computing the conformation tensor. For small values of λ_D (≤ 0.2) the convergence is not affected although when $0.1 \leq \lambda_D \leq 0.2$ noticeable numerical oscillations occur in the stress solution. When $\lambda_D < 0.2$ such large values of c_1 are required to stabilise the computations that the (nonphysical) stabilisation terms dominate the constitutive equation in parts of the domain around the sphere boundary. As such we are unable (at the current moment) to obtain numerically convergent finite element solutions for $We > 2.0$ and $\lambda_D > 0.2$ for $\beta_{sphere} = 0.4$ and $\beta_{sphere} = 0.5$ using this particular stabilisation scheme.

Potential ways to overcome these numerical difficulties could be: (i) log-conformation tensor formulation (Fattal & Kupferman [31]) or (ii) adaptive mesh refinement methods (Berger & Oliver [5]). In each case the risk of of the blow-up errors in the region near the sphere can be mitigated. We intend to develop the numerical method and stabilisation methods further so that we can obtain K/K_N values for $We > 2.0$ when $\beta_{sphere} = 0.4$ and $\beta_{sphere} = 0.5$. Another suggested test for the accuracy of the FENE-P-MP model is the matching of rheometric and drag behaviour with a single choice of λ_D. This will ensure that λ_D is dependent on the fluid and not the length/time scale of the flow being modelled.

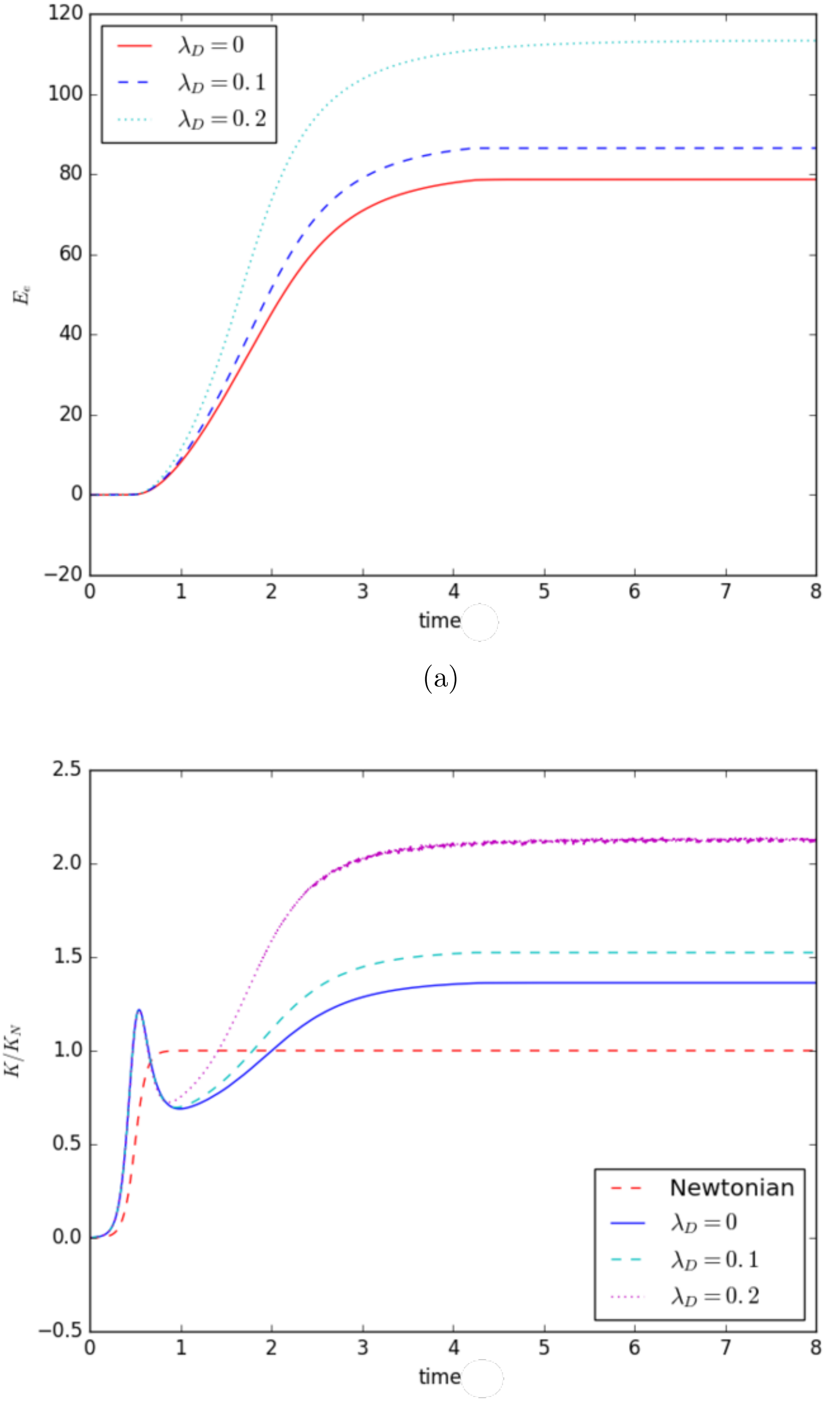

(a)

(b)

Figure 7.12: Flow past a sphere: The effect of dissipation parameter, λ_D, on elastic energy and normalised drag coefficient, $\beta = 0.5$, $Re = 0$, $We = 1.0$, $b = 5$, $\beta_{sphere} = 0.4$.

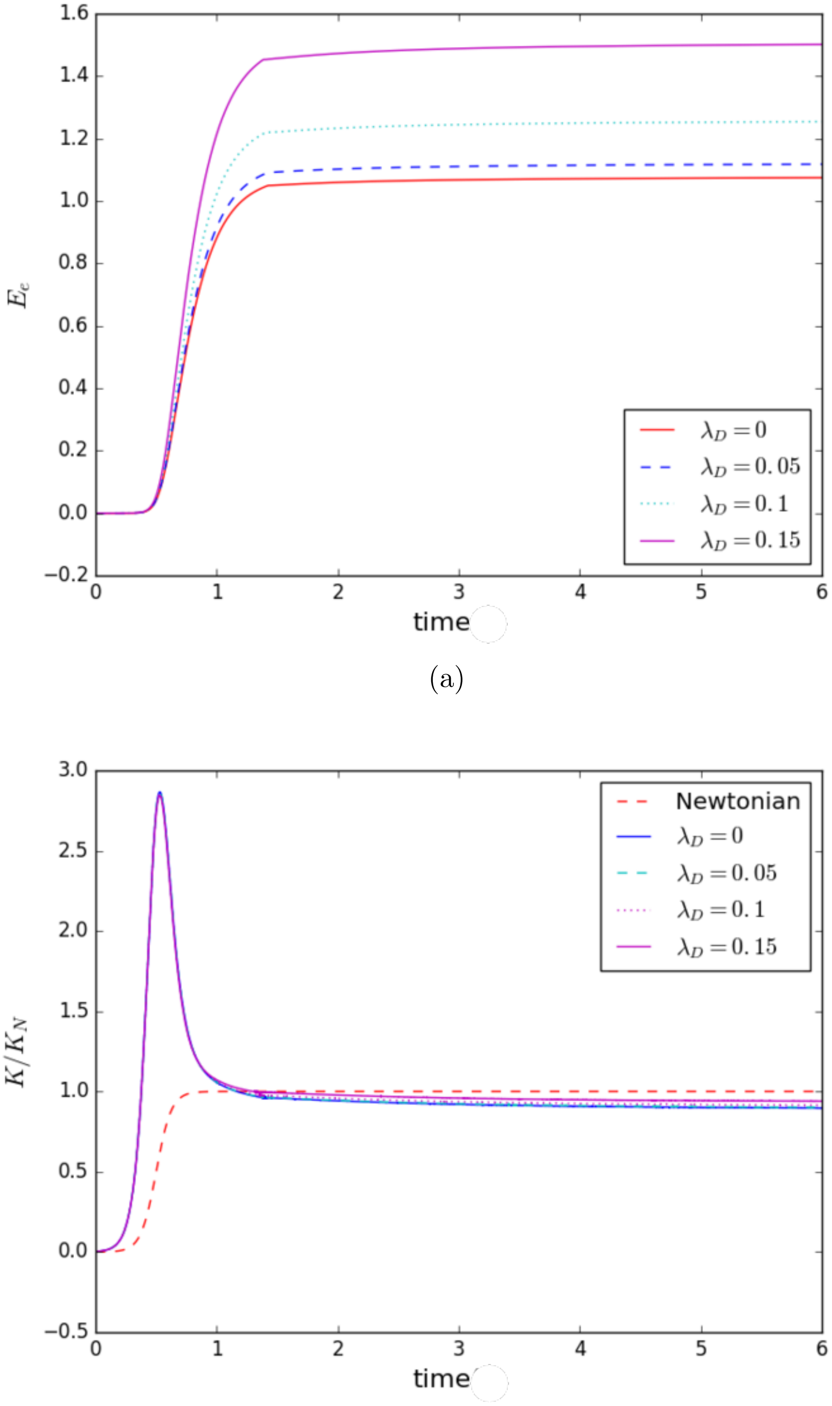

(a)

(b)

Figure 7.13: Flow past a sphere: The effect of dissipation parameter, λ_D, on (a) elastic energy and (b) normalised drag coefficient, $\beta = 0.5$, $Re = 0$, $We = 0.2$, $b = 5$, $\beta_{sphere} = 0.4$.

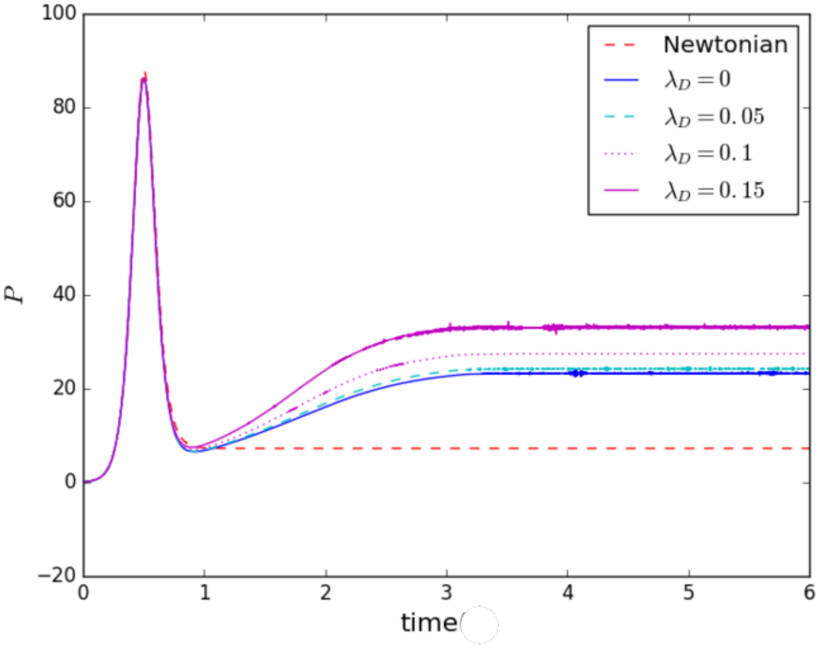

(a)

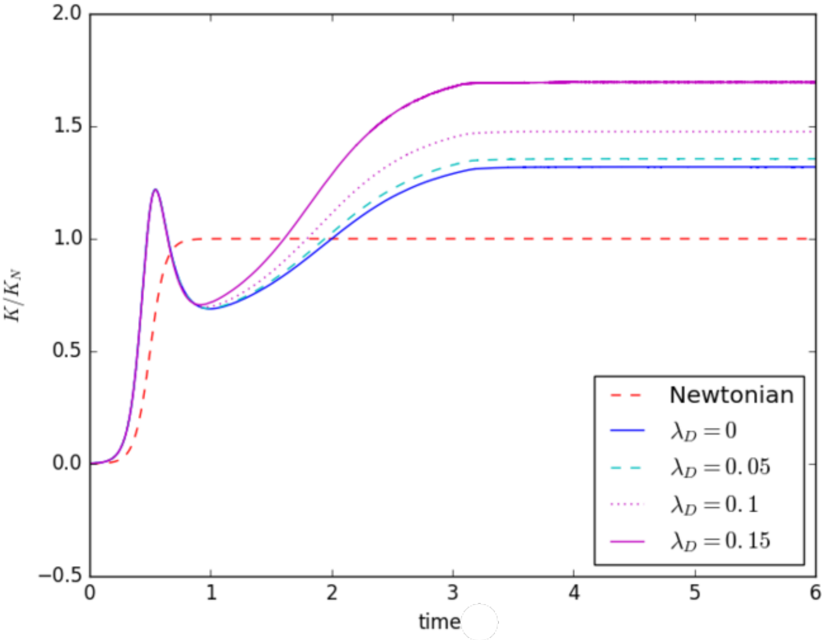

(b)

Figure 7.14: Flow past a sphere: The effect of dissipation parameter, λ_D, on (a) sample point pressure, (P=$p(0,(R_s+R)/2)$), and (b) drag, $\beta_{sphere} = 0.4$, $\beta = 0.5$, $Re = 0$, $We = 1.2$, $b = 5$.

Chapter 8

Conclusions

In this thesis we have conducted an investigation into the theoretical and computational modelling of compressible and nonisothermal viscoelastic fluids. The first principles that govern the dynamics of large particle systems are ignored too often in the literature on viscoelastic flow. Complex flows often occur under conditions where compressible and nonisothermal effects have to be accounted for. As such it is important to develop models that can accurately capture compressible, nonisothermal and viscoelastic behaviour whilst remaining consistent with the laws of thermodynamics. This thesis has contributed to the understanding of these important issues and valuable insights have been gained from the results. The generalised bracket method provides a suitable vehicle for the development of realistic viscoelastic models that can adequately describe nonisothermal and compressible behaviour. As such we have developed the FENE-P-MP dissipative model which, with some success has been able to capture features of Boger fluid flow such as drag enhancement for flow past a sphere.

Computing viscoelastic flow using numerical methods remains a very challenging problem. Alongside the new models we have developed, new techniques for obtaining approximate solutions to the governing equations over a range of input parameters have been constructed, which have worked with varying degrees of success. Furthermore, valuable insights have been gained about the competing influence of inertia, compressibility and viscoelasticity as measured by the Reynolds, Mach and Weissenberg numbers, respectively.

There are several valuable contributions this thesis. In Chapter 2 we gave an overview of the generalised bracket formulation. In Chapter 3 we used the single bracket formulation to derive a family of constitutive equations for compressible viscoelastic fluids. In particular, we have successfully derived the FENE-P-MP model, a strain-hardening and nonisothermal dissipative viscoelastic model for Boger fluids. The content from Chapters 2 and 3 have been submitted for publication in a JNNFM paper '*On the Derivation of Macroscopic Models for Compressible Viscoelastic Fluids using the Generalized Bracket Framework*'[72].

In addition to the development of the new generalised models we have presented a large number of numerical results for 2D compressible viscoelastic flows. In the development of the numerical scheme we have attempted to use well-established stabilisation methods in order to prevent numerical blow-up. The stabilised Taylor-Galerkin finite element scheme presented in Chapter 4 provided a robust means of computing viscoelastic flow, independent of the constitutive model being used and applicable to both incompressible and compressible flows.

In Chapter 5 we presented numerical solutions for both lid-driven cavity flow and natural convection flow of an Oldroyd-B fluid. In the case of the lid-driven cavity, the results displayed excellent agreement with those available in the literature for incompressible flow. For nonzero Mach numbers a range of numerical predictions were made varying Ma, We and Re. Numerical predictions for convection flow of an Oldroyd-B fluid using a Boussinesq approximation were presented, showing a clear negative impact that elasticity has on steady-state flow speed and thermal convection at low Rayleigh numbers. Failure to obtain solutions for the compressible flow scheme was somewhat disappointing, but we believe that these numerical issues can be overcome with a suitable problem-specific stabilisation methods.

In Chapter 6, eccentric Taylor-Couette flow of both the Extended White Metzner and FENE-P-MP fluids model have been presented. Both models predict very clear trends in the torque and load-bearing capacity for varying We and Ma, specifically that some reduction of effective shear viscosity due to shear thinning does not imply reduced levels of torque for eccentric flow. For an eccentricity of $\epsilon = 0.8$ viscosity increase in torque and load bearing capacity is observed as We is increased due to the extensional viscosity response in the narrow gap of the geometry. Moreover, the predictions presented in Chapter 6 are verifiable with a suitable Taylor-Couette flow experiment and has also been summarised in the paper '*Compressible Viscoelastic Flow between Eccentrically Rotating Cylinders*' (in preparation)[71].

In Chapter 7 we presented some numerical solutions to the inertia-free flow of a FENE-P-MP fluid past a sphere. The drag force on the sphere and pressure at the mid point of the flow were calculated over a range of Re, We and λ_D. The numerical scheme was benchmarked using the Oldroyd-B constitutive model, displaying good agreement with results in the literature. The drag force predictions for the FENE-P-MP model show very good agreement with the drag calculated using the swanINNF(q)-FENE-CR model as well as empirical data. This work represents a contribution to the development of viscoelastic constitutive equations that benefit from being consistent with the laws of thermodynamics (making them generally applicable to compressible and nonisothermal flows) whilst also being able to capture complex drag behaviour. Altogether the results are encouraging and help provide a roadmap for future developments.

8.1 Future Work

There are areas of this thesis related to modelling and numerical analysis that could be further developed. Future work should focus on applications of the FENE-P-MP model. A suggested benchmark problem is the 4:1 contraction flow, where a large body of both numerical and experimental data is available. Now that the Mackay-Phillips class of dissipative models has been established, similar extensions of models such as PTT and EPTT can be derived. There are many examples of 2D and 3D nonisothermal viscoelastic flows where pressure and temperature determine the flow behaviour. Models presented in this thesis could be useful in the quantitative modelling of these problems.

Further improvements to the numerical method should be considered as a major area for development. Additional deformation terms in the constitutive equation that appear in the derivation of the Mackay-Phillips class models make the scheme much more vulnerable to the high Weissenberg number problem. The stabilisation techniques for the finite element method need to be developed so that solutions can be obtained for a larger range of values of We. This is especially important for tackling the flow past a sphere and compressible natural convection flow problems, where results were somewhat hampered by numerical instability. A suggested method suitable for this task could be the DEVSS-G-DG stabilised spectral element method developed by Kynch and Phillips [53]. Furthermore, when $Ma > 0.3$ the flow is no longer considered to be weakly-compressible. In practice this means that alternatives to the equation of state that underpins the Taylor-Galerkin time-marching scheme will have to be considered. A possible solution method for computing higher Mach number compressible flows is the log-density formulation, which was described in Section 4.6.3.

Lastly, future numerical investigations using the models developed in this thesis should be conducted focussing on the combined effects of compressibility and viscoelasticity. The results from this thesis have shown that viscoelastic flow characteristics can vary drastically depending on Re, We and Ma and temperature. More work needs to be done to determine the relationship between these dimensionless parameters and their separate and combined influence on flow characteristics for 3D problems.

Appendices

Appendix A

A.1 Notation Statistical Mechanics

Sec. A.1.1 covers some basic concepts in statistical mechanics including the definition of the Poisson bracket for discrete particle systems. Sec. A.1.2 introduces the Lagrangian, Hamiltonian and Hamilton's equations of motion. In Sec. A.1.3 bracket notation is introduced along with the definition of the Volterra derivative.

A.1.1 Phase Space and Canonical Coordinates

For a collection of N particles in a system, Ω, we define configuration space.

Definition A.1.1 *A point in configuration space, $C = \mathbb{R}^{3N}$, corresponds to all of the positions of the N particles in order i.e $\boldsymbol{x} \in C$ is $\boldsymbol{x} = (x_1, y_1, z_1, x_2, y_2, z_2, ..., x_N, y_N, z_N)$ where (x_1, y_1, z_1) is the position of the 1st particle in $\mathbb{R}^3$, (x_2, y_2, z_2) is the position of the second etc.*

Phase Space, Γ, is the union of configuration space with an equivalent space that, instead gives the momenta of each particle instead of the position

$$\Gamma := \mathbb{R}^{6N}$$

Any point, $\mathbf{x} \in \Gamma$ is denoted $(q_1, ..., q_{3N}, p_1, ..., p_{3N})$ is called a *microstate.* For each microstate $(q_1, ..., q_{3N})$ are general coordinates and $(p_1, ..., p_{3N})$ is the general momenta where $p_1 = m_1 \frac{dx_1}{dt}$, $p_2 = m_2 \frac{dx_2}{dt}$ etc.

Definition A.1.2 *An* ***observable****,* $F : \Gamma \to \mathbb{R}$ *is a mapping (functional) that represents some quantity over the field* Γ

The Hamiltonian and Lagrangian are examples of observables, the Hamiltonian especially useful for the purposes of understanding energy[43].

Definition A.1.3 *Given two functionals dependent on time and the canonical coordinates of a system,* $f(p_i, q_i, t)$ *and* $g(p_i, q_i, t)$*, the* ***Poisson bracket*** *is a bilinear operator* $\{\cdot, \cdot\} : \mathbb{R} \times \mathbb{R} \to \mathbb{R}$

$$\{f, g\} = \sum_{i=1}^{N} \left(\frac{\partial f}{\partial q_i} \frac{\partial g}{\partial p_i} - \frac{\partial f}{\partial p_i} \frac{\partial g}{\partial q_i} \right) \tag{A.1.1}$$

A.1.2 The Lagrangian and Hamiltonian

Definition A.1.4 *The Lagrangian,* $\boldsymbol{L}$*, of a dynamical system is defined as the kinetic energy,* T*, minus the potential energy,* V*.*

$$L = T - V \tag{A.1.2}$$

In generalised coordinated the kinetic energy is given by the equation $T = \sum_{i=1}^{N} \frac{1}{2} m_i \dot{q}_i^2$ and the potential field is dependent on the external forces acting on the system.

Definition A.1.5 *The Euler Lagrange equation is a second order partial differential equation that gives the solutions to stationary 'points' of functionals. in generalised coordinates*

$$\boldsymbol{L}_q(t, q(t), \dot{q}(t)) - \frac{d}{dt} \boldsymbol{L}_{\dot{q}}(t, q(t), \dot{q}(t)) = 0$$

where $\boldsymbol{L}$ *is the Lagrangian of the system. Physically the Euler-Lagrange equation is the mathematical expression for the principle of least action.*

When applied to classical mechanics it becomes the mathematical statement for the principle of least action (i.e Newton's 1st law)[43]. The Euler-Lagrange equation is a powerful method determining the motion of N particles in a dynamical system given that we have worked out the relevant Lagrangian, **L**. A related functional, the Hamiltonian allows us to formulate the time evolution of a system in a much more straightforward way [43].

Definition A.1.6 *The Hamiltonian* $H(\boldsymbol{q}, \boldsymbol{p}, t)$ *is a functional can be thought of as the total energy of a system. but loosely we define* H *as follows*

$$H = \frac{\boldsymbol{p} \cdot \boldsymbol{p}}{2m} + V(\boldsymbol{q}, t) \tag{A.1.3}$$

where $\boldsymbol{p}$ *and* $\boldsymbol{q}$ *are the momenta and positions of the* N *particles in phase space.*

The first and second term corresponding to kinetic and potential energy respectively. Note that the potential energy has been very loosely defined here (as has the functional itself) and we will need to sharpen this formulation later.

Definition A.1.7 ***Hamilton's Equations*** *are a set of partial differential equations that uniquely determine the time evolution of a dynamical system.*

$$\frac{dq_i}{dt} = \frac{\partial H}{\partial p_i}(q_1(t), ..., q_N(t), p_1(t), ..., p_N(t)) \tag{A.1.4}$$

$$\frac{dp_i}{dt} = -\frac{\partial H}{\partial q_i}(q_1(t), ..., q_N(t), p_1(t), ..., p_N(t)) \tag{A.1.5}$$

where $H = H(\boldsymbol{p}, \boldsymbol{q}, t)$ *is the Hamiltonian of the system[43].*

These relations can be easily proved using the definition of the Hamiltonian given in (A.1.3)[43]. A key use for the Hamiltonian and the Poisson bracket is determining the time derivative of an observable along a phase space trajectory.

A.1.3 Bracket Notation

In order to understand the bracket formulation for fluids we must first take a moment to discuss some notation and calculus of functionals. Define an arbitrary function $f = f[a, b, ..]$ $a, b \in P$ where P is the operating space. Importantly, we need to establish a relation between the functional and its integral over a domain Ω.

Definition A.1.8 *For any given function, $f = f[a, b, ..]$ $(a, b \in P)$, we define a corresponding functional $F : f \to \mathbb{R}$ $F = F[a, b, \ldots]$*

$$F[a, b, \ldots] = \int_{\Omega} f(a, b, \ldots) d\Omega \tag{A.1.6}$$

Note that $d^3x = dx_1 dx_2 dx_3 (= d\Omega)$. Let us also introduce the definition of the **Volterra functional derivative** as it will become of great importance later when we need to do write dynamic relations in terms of integral equations.

Definition A.1.9 *The Volterra functional derivative of F (where $F : f \to \mathbb{R}$), denoted $\frac{\delta F}{\delta \cdot}$, is defined as the partial derivative of the function f w.r.t. $\cdot$, $\frac{\partial f}{\partial \cdot}$.*

$$\frac{\delta F}{\delta a} \equiv \frac{\partial f}{\partial a}$$

$$\frac{\delta F}{\delta b} \equiv \frac{\partial f}{\partial b}$$

The situation is more complex when the functional depends on not just a but ∇a. We write

$$F[a] = \int_{\Omega} f(a, \nabla a) d\Omega$$

The Volterra derivative of the functional F w.r.t. a becomes

$$\frac{\delta F}{\delta a} \equiv \frac{\partial f}{\partial a} - \nabla \cdot \frac{\partial f}{\partial (\nabla a)} \tag{A.1.7}$$

$$\implies \frac{dF}{dt} = \frac{d}{dt}\left[\int_\Omega f(a, \nabla a, b) d^3x\right] = \int_\Omega \frac{\partial}{\partial t} f(a, \nabla a, b) d\Omega$$

Hence

$$\frac{dF}{dt} = \int_\Omega \left[\frac{\delta F}{\delta a}\frac{\partial a}{\partial t} + \frac{\delta F}{\delta b}\frac{\partial b}{\partial t}\right] d\Omega \tag{A.1.8}$$

A.2 Derivation of the General Set of Governing Equations

A.2.1 Fundamental Concepts in Equilibrium Thermodynamics

To introduce the basics of thermodynamics we will simplify the problem by imagining a system enclosed by a boundary Ω. The system has an internal energy, U which, as we will see is directly related to the heat energy, Q, of the system. The change of internal energy of a system is given by the heat energy transmitted into the system plus work done, W, by the surroundings on the fluid body.

$$dU = dQ + dW \tag{A.2.1}$$

The infinitesimal change in heat energy is given by the temperature multiplied by change in entropy of the system $dQ = TdS$ and the work done by the system is equal to the pressure multiplied by the change in volume, $dW = -pdV$. Substituting these relations into (A.2.1) leads us to the **fundamental equation of thermodynamics**.

Definition A.2.1 *The fundamental equation of thermodynamics for a closed system, Ω, is given by the relation*

$$dU = TdS - pdV \tag{A.2.2}$$

where U is the internal energy, T is the temperature, S is the entropy, p is the pressure exerted onto the surrounding wall, $\partial\Omega$, and V is the volume of Ω.

The differential of internal energy depends directly on entropy, S and the volume of the system, V i.e. $U = U(S, V)$. Note that if there is 0 energy exchange between a system and its environment then

$$TdS = pdV$$

for a fixed volume of fluid. Additionally, the change in enthalpy, E is given by the change in internal energy plus the work done in order to expand the volume of the domain (pressure multiplied by volume)

$$dE = TdS + d(pV) = dU + (pdV + Vdp)$$

Eliminating dU using (A.2.2) gives

$$dE = TdS + Vdp$$

he enthalpy is dependent on S and p vary i.e. $E = E(s, p)$ It is useful at this point to go over some of Maxwell's fundamental thermodynamic relations.

$$\left(\frac{\partial S}{\partial V}\right)_T = \left(\frac{\partial P}{\partial T}\right)_V$$

$$\left(\frac{\partial S}{\partial P}\right)_T = \left(\frac{\partial V}{\partial T}\right)_P$$

The first relation states that the change in entropy with respect to volume at a constant temperature is equal to the change in pressure w.r.t temperature at constant volume. The second states that the change in entropy w.r.t pressure at a constant temperature is equal to the change in volume w.r.t temperature at constant pressure.

A.2.2 Lagrangian & Eulerian Poisson Bracket

In order to obtain working equations in the (Eulerian) form that we desire, we must convert our Lagrangian variables Γ, Π, ρ_0, for which the Poisson bracket was originally described in into spatial variables, ρ, $\mathbf{m}$, s and $\mathbf{C}$. Putting aside functional forms we can discuss a simple example of this transformation. Let $\dot{\Gamma}(\mathbf{r}, t)$ be the Lagrangian description of the **velocity** field. In the Eulerian description, we consider a fixed coordinate point in space (assumed to be Cartesian), $\mathbf{x}$, for which the (constant) volume element is given by $d^3x = d\Omega$. For the Eulerian description, dynamic variables of the body are functions of $\mathbf{x}$ and t, instead of $\mathbf{r}$. In particular the Eulerian specification for the flow field is given by

$$\mathbf{u}(\mathbf{x}, t)$$

where

$$\mathbf{x} = \Gamma(\mathbf{r}, t)$$

In terms of our functional defined variables the Lagrange to Euler transformation is a little more complex. First we start with a definition of the variables concerned using a Dirac delta function.

Definition A.2.2 $\delta^3[\Gamma(\boldsymbol{r}, t) - \boldsymbol{x}]$ *is a differential operator defined*

$$\int_{\Omega'} g(\Gamma)\delta^3[\Gamma(\boldsymbol{r}, t) - \boldsymbol{x}]d^3\Gamma = \begin{cases} g(\boldsymbol{x}) & ; \quad \Gamma(\boldsymbol{r}, t) = \boldsymbol{x} \\ 0 \quad ; & \Gamma(\boldsymbol{r}, t) \neq \boldsymbol{x} \end{cases} \tag{A.2.3}$$

where g is a function of suitable continuity.

$\delta^3[..]$ is defined as the Dirac operator. The usefulness of this notation will become more apparent as we move on. Additionally, defining the Lagrange to Euler map (transition) this way allows us to encode the initial conditions in the definition. The mass density in the Eulerian (spatial) frame is given by

$$\begin{aligned} \rho(\mathbf{x},t) &= \rho(\mathbf{F}(\mathbf{r},t),t) \\ \implies \rho(\mathbf{x},t) &= \int_\Omega \rho(\mathbf{F}(\mathbf{r},t),t)\delta^3[\Gamma(\mathbf{r},t)-\mathbf{x}]d^3\Gamma \\ \rho(\mathbf{x},t) &= \int_\Omega \rho_0(\mathbf{r})\delta^3[\Gamma(\mathbf{r},t)-\mathbf{x}]d^3r \end{aligned} \tag{A.2.4}$$

where $\mathbf{x}$ is the original location of the fluid body. Similarly the momentum field is

$$\mathbf{M}(\mathbf{x},t) = \int_\Omega \rho(\mathbf{F}(\mathbf{r},t))\dot{\Gamma}(\mathbf{r},t)\delta^3[\Gamma(\mathbf{r},t)-\mathbf{x}]d^3\Gamma$$

which can be simplified using (A.2.6)

$$\mathbf{M}(\mathbf{x},t) = \int_\Omega \rho_0\dot{\Gamma}(\mathbf{r},t)\delta^3[\Gamma(\mathbf{r},t)-\mathbf{x}]d^3r$$

where $\rho_0\dot{\Gamma}$ is simply the initial momentum field which we can denote by $\mathbf{p}_0$

$$\mathbf{M}(\mathbf{x},t) = \int_\Omega \mathbf{p}_0\delta^3[\Gamma(\mathbf{r},t)-\mathbf{x}]d^3r$$

Similarly

$$s(\mathbf{x},t) = \int_\Omega s_0(\mathbf{r})\delta^3[\Gamma(\mathbf{r},t)-\mathbf{x}]d^3r$$

At time $t = 0$, the fluid occupies a region Ω with surface $\partial\Omega$. We can view fluid body motion as a mapping $\Gamma : \Omega \times t \to \mathbb{R}^3$ denoted $\Gamma(\mathbf{r},t)$ (we may denote the codomain of Γ as Ω'). The mapping transforms the fluid body to fit in the domain Ω' at time time $t = t'$ with boundary $\partial\Omega'$ where $\partial\Omega' = \partial\Omega$

Each fluid particle is considered a volume element at $t = 0$, $d^3r \equiv dr_1dr_2dr_3$ where the vector $\mathbf{r} = (r_1, r_2, r_3)$. It is necessary now to introduce some key dynamic variables and notation.

Definition A.2.3 *The* ***deformation gradient*** $\boldsymbol{F} : \Omega' \times \Omega \to \mathbb{R}^{3\times 3}$ *is a second order tensor field that represents the derivative of each component of the deformed map,* Γ*, with respect to each component of the reference configuration,* $\boldsymbol{r}$

$$F_{ij} = \frac{\partial \Gamma_i}{\partial r_j} \tag{A.2.5}$$

Though the mass of the fluid must remain constant, the volume element may vary.

Definition A.2.4 *The* ***elemental volume change*** *for the continuum mapped from Ω to Ω' by Γ is given by the equation*

$$d^3\Gamma = J d^3 r$$

where $J = det\boldsymbol{F}$ and $\boldsymbol{F}$ is the deformation gradient.

Proposition A.2.1 *If the distribution of the mass of the fluid at time $t = 0$ can be described by the density function $\rho_0 = \rho_0(r)$, then* ***mass conservation*** *principle can simply be stated*

$$\rho d^3\Gamma = \rho_0 d^3 r \tag{A.2.6}$$

which implies

$$\rho = \frac{\rho_0(r)}{J}$$

meaning that the density, ρ depends on Γ though the Jacobian $\implies \rho = \rho(\mathbf{F}, t)$. This way of denoting fluid body modeling will make the relatively difficult mathematics much easier to read.

Definition A.2.5 *the momentum vector field, Π, for a continuum occupying Ω is given by*

$$\Pi(r,t) = \rho_0 \dot{\Gamma}(r,t)$$

where $\dot{\Gamma}$ is the velocity field.

Definition A.2.6 *The Left Cauchy-Green deformation tensor, $\boldsymbol{c} : \Omega \to \mathbb{R}^3$ is a second order tensor field*

$$c_{ij} = F_{ik}F_{jk} = \frac{\partial \Gamma_i}{\partial r_k}\frac{\partial \Gamma_j}{\partial r_k}$$

where $\boldsymbol{F} = F_{ij}$ *is the deformation gradient tensor. We define* $\boldsymbol{C}$ *as the density dependent finger tensor*

$$C_{ij}(\boldsymbol{x}, t) = \rho c_{ij}(\boldsymbol{x}, t)$$

Several different definitions for $\mathbf{C}$ exist in the literature [8]. Another that we will consider in later sections is the form based on kinetic theory where $\mathbf{C}$ is the *normalised* and *averaged* dyadic product of the end-to-end distance vector $\mathbf{Q}$ denoted $\langle \mathbf{Q}, \mathbf{Q} \rangle$.

Definition A.2.7 *The Hamiltonian for an elastic, inviscid continuum occupying* Ω *with boundary* $\partial\Omega$ *is given by the expression*

$$H[\Pi, \Gamma] = \int_\Omega \left[\frac{1}{2\rho_0}\Pi \cdot \Pi + \rho_0 e_p^v(\Gamma) + \rho_0 \hat{U}(\rho(\Gamma, t), s_0(r), \boldsymbol{C}(F, t)) \right] d^3r \tag{A.2.7}$$

In the Lagrangian framework the Poisson bracket representation for the time derivative of F can be written

$$\frac{dF}{dt} = \{F, H\}_L = \int_\Omega \left[\frac{\delta F}{\delta \Gamma}\frac{\delta H}{\delta \Pi} - \frac{\delta F}{\delta \Pi}\frac{\delta H}{\delta \Gamma} \right] d^3r \tag{A.2.8}$$

Using definition (A.2.7) we can write Hamilton's equations for an elastic continuum

$$\dot{\Gamma}_i(\mathbf{r}, t) = \frac{\partial H[\Pi, \Gamma]}{\partial \Pi} = \frac{1}{2\rho_0}\frac{\partial}{\partial \Pi}(\Pi \cdot \Pi) = \frac{\Pi(\mathbf{r}, t)}{\rho_0(\mathbf{r})}$$

$$\dot{\Pi}_i = -\frac{\partial H[\Pi, \Gamma]}{\partial \Gamma} = -\rho_0 \frac{\partial e_v^p}{\partial \Gamma_i} + \frac{\partial}{\partial r_j}\left(\rho_0 \frac{\partial \hat{U}}{\partial F_{ij}} \right)$$

Definition A.2.8 *The operating space for an observable on* Ω *with elastic dependence is given by*

$$\mathbb{P} = \begin{cases} \rho(\boldsymbol{x},t) \in \mathbb{R}^+ \\ \boldsymbol{M}(\boldsymbol{x},t) \in \mathbb{R}^+, \qquad \boldsymbol{n}\cdot\boldsymbol{M} = 0 \,\text{on}\, \partial\Omega \\ s(\boldsymbol{x},t) \in \mathbb{R}^+ \\ \boldsymbol{C}(\boldsymbol{x},t) \in \mathbb{R}^+ \end{cases} \tag{A.2.9}$$

Note the derivatives of $\mathbf{C}$

$$\frac{\delta \mathbf{C}_{ij}(\mathbf{x},t)}{\delta \Gamma_k(\mathbf{r},t)} = \rho_0 c_{ij} \frac{\partial \delta^3[\Gamma - \mathbf{x}]}{\partial \Gamma_k} - \frac{\partial}{\partial r_l}\left(\rho_0 \delta^3[\Gamma - \mathbf{x}] \frac{\partial C_{ij}}{\partial \mathbf{F}_{kl}}\right) \tag{A.2.10}$$

Making use of the Volterra derivative definition given in (A.1.7) $\frac{\delta F}{\delta a} = \frac{\partial f}{\partial a} - \nabla_i \frac{\partial f}{\partial(\nabla a_i)} \in \mathbb{P}$

$$\frac{\delta C_{ij}(\mathbf{x},t)}{\delta \Pi_k(\mathbf{r},t)} = 0 \tag{A.2.11}$$

A.2.3 Derivation of the Eulerian Poisson Bracket

By taking a continuum approximation ($N \to \infty$) of (A.1.1) we are able to derive a continuous form of the Poisson bracket, Eq. (A.2.8). However the traditional formulation of the Poisson bracket uses Lagrangian coordinates and hence the continuum approximation yields and equation for F in terms of In order to establish an expression for the Poisson bracket in Eulerian coordinates we need a change of variables. By substitution of F into (A.2.8) we have

$$\begin{aligned}\{F,G\}_E = \int_\Omega \Bigg[&\int_\Omega \left[\frac{\delta F}{\delta \rho}\frac{\delta \rho}{\delta \Gamma_i} + \frac{\delta F}{\delta M_j}\frac{\delta M_j}{\delta \Gamma_i} + \frac{\delta F}{\delta s}\frac{\delta s}{\delta \Gamma_i}\right] d^3y \int_\Omega \left[\frac{\delta G}{\delta \rho}\frac{\delta \rho}{\delta \Gamma_i} + \frac{\delta G}{\delta M_j}\frac{\delta M_j}{\delta \Gamma_i} + \frac{\delta G}{\delta s}\frac{\delta s}{\delta \Gamma_i}\right] d^3z \\ &- \int_\Omega \left[\frac{\delta F}{\delta \rho}\frac{\delta \rho}{\delta \Gamma_i} + \frac{\delta F}{\delta M_j}\frac{\delta M_j}{\delta \Gamma_i} + \frac{\delta F}{\delta s}\frac{\delta s}{\delta \Gamma_i}\right] d^3y \int_\Omega \left[\frac{\delta G}{\delta \rho}\frac{\delta \rho}{\delta \Gamma_i} + \frac{\delta G}{\delta M_j}\frac{\delta M_j}{\delta \Gamma_i} + \frac{\delta G}{\delta s}\frac{\delta s}{\delta \Gamma_i}\right] d^3z \Bigg] d^3x\end{aligned} \tag{A.2.12}$$

The notation d^3y, d^3z and d^3x expresses the fact that we are integrating over the domain for each functional and keeps the bracket bilinear. We now expand and regroup in a way that allows us to express the "spatial" bracket $\{,\}_E$ in terms of the Poisson (or "material") bracket $\{,\}_L$. Note that we can manipulate the integrands as long as we keep track of the x, y and z dependence of each functional derivative

$$\begin{aligned}
\{F,G\}_E = & \int_{\Omega'}\int_{\Omega'}\int_{\Omega'} \frac{\delta F}{\delta\rho}\frac{\delta G}{\delta M_j}\left[\frac{\delta\rho}{\delta\Gamma_i}\frac{\delta M_j}{\delta\Pi_i} - \frac{\delta\rho}{\delta\Pi_i}\frac{\delta M_j}{\delta\Gamma_i}\right] + \frac{\delta F}{\delta M_j}\frac{\delta G}{\delta\rho}\left[\frac{\delta M_j}{\delta\Gamma_i}\frac{\delta\rho}{\delta\Pi_i} - \frac{\delta M_j}{\delta\Pi_i}\frac{\delta\rho}{\delta\Gamma_i}\right] \\
& + \frac{\delta F}{\delta s}\frac{\delta G}{\delta M_j}\left[\frac{\delta s}{\delta\Gamma_i}\frac{\delta M_j}{\delta\Pi_i} - \frac{\delta s}{\delta\Pi_i}\frac{\delta M_j}{\delta\Gamma_i}\right] + \frac{\delta F}{\delta M_j}\frac{\delta G}{\delta s}\left[\frac{\delta M_j}{\delta\Gamma_i}\frac{\delta s}{\delta\Pi_i} - \frac{\delta M_j}{\delta\Pi_i}\frac{\delta s}{\delta\Gamma_i}\right] \\
& + \frac{\delta F}{\delta M_i}\frac{\delta G}{\delta M_j}\left[\frac{\delta M_i}{\delta\Gamma_i}\frac{\delta M_j}{\delta\Pi_i} - \frac{\delta M_j}{\delta\Gamma_i}\frac{\delta M_i}{\delta\Pi_i}\right] d^3z d^3x d^3y \\
& = \int_{\Omega}\int_{\Omega'}\left[\frac{\delta F}{\delta\rho}\frac{\delta G}{\delta M_j} - \frac{\delta F}{\delta M_j}\frac{\delta G}{\delta\rho}\right] \times \int_{\Omega}\left(\frac{\delta\rho}{\delta\Gamma_i}\frac{\delta M_j}{\delta\Pi_i} - \frac{\delta M_j}{\delta\Gamma_i}\frac{\delta\rho}{\delta\Pi_i}\right) \\
& + \left[\frac{\delta F}{\delta s}\frac{\delta G}{\delta M_j} - \frac{\delta F}{\delta M_j}\frac{\delta G}{\delta s}\right] \times \int_{\Omega}\left(\frac{\delta s}{\delta\Gamma_i}\frac{\delta M_j}{\delta\Pi_i} - \frac{\delta M_j}{\delta\Gamma_i}\frac{\delta s}{\delta P_i}\right) \\
& + \frac{\delta F}{\delta M_i}\frac{\delta G}{\delta M_j}\int_{\Omega}\left(\frac{\delta M_i}{\delta\Gamma_i}\frac{\delta M_j}{\delta\Pi_i} - \frac{\delta M_j}{\delta\Gamma_i}\frac{\delta M_i}{\delta\Pi_i}\right) d^3z d^3x
\end{aligned}$$

which can be written

$$\begin{aligned}
\{F,G\}_E = & \int_{\Omega'}\int_{\Omega}\left[\frac{\delta F}{\delta\rho(\mathbf{x},t)}\frac{\delta G}{\delta m_j(\mathbf{z},t)} - \frac{\delta G}{\delta\rho(\mathbf{x},t)}\frac{\delta F}{\delta m_j(\mathbf{z},t)}\right] \times \{\rho(\mathbf{x},t), m_j(\mathbf{z},t)\}_L d^3z d^3x \\
& + \int_{\Omega'}\int_{\Omega'}\left[\frac{\delta F}{\delta s(\mathbf{x},t)}\frac{\delta G}{\delta m_j(\mathbf{z},t)} - \frac{\delta G}{\delta s(\mathbf{x},t)}\frac{\delta F}{\delta m_j(\mathbf{z},t)}\right] \times \{s(\mathbf{x},t), m_j(\mathbf{z},t)\}_L d^3z d^3x \\
& + \int_{\Omega'}\int_{\Omega'}\left[\frac{\delta F}{\delta m_i(\mathbf{x},t)}\frac{\delta G}{\delta m_j(\mathbf{z},t)}\right] \times \{m_i(\mathbf{x},t), m_j(\mathbf{z},t)\}_L d^3z d^3x \\
& + \int_{\Omega'}\int_{\Omega'}\left[\frac{\delta F}{\delta C_{ij}(\mathbf{x},t)}\frac{\delta G}{\delta m_j(\mathbf{z},t)} - \frac{\delta G}{\delta\rho(\mathbf{x},t)}\frac{\delta F}{\delta m_j(\mathbf{z},t)}\right] \times \{C_{ij}(\mathbf{x},t), m_j(\mathbf{z},t)\}_L d^3z d^3x
\end{aligned} \tag{A.2.13}$$

where

$$\{\rho(x,t), M_j(z,t)\}_L = \int_{\Omega'} \left[\frac{\delta\rho(\mathbf{x},t)}{\delta\Gamma_j(\mathbf{r},t)} \frac{\delta M_j(z,t)}{\delta\Pi_j(\mathbf{r},t)} - \frac{\delta M_j(\mathbf{z},t)}{\delta\Gamma_j(\mathbf{r},t)} \frac{\delta\rho(\mathbf{z},t)}{\delta\Pi_j(\mathbf{r},t)} \right] d^3r$$

$$\{m_i(\mathbf{x},t), m_j(\mathbf{z},t)\}_L = \int_{\Omega'} \left[\frac{\delta\mathbf{m}_i(\mathbf{x},t)}{\delta\Gamma_j(\mathbf{r},t)} \frac{\delta\mathbf{m}_j(z,t)}{\delta P_j(\mathbf{r},t)} - \frac{\delta M_j(\mathbf{z},t)}{\delta\Gamma_j(\mathbf{r},t)} \frac{\delta\mathbf{m}_i(\mathbf{z},t)}{\delta P_j(\mathbf{r},t)} \right] d^3r$$

$$\{C_{ij}(\mathbf{x},t), M_j(\mathbf{z},t)\} = \int_{\Omega} \left[\frac{\delta C_{ij}(\mathbf{x},t)}{\delta\Gamma_i(\mathbf{r},t)} \frac{\delta M_k(\mathbf{z},t)}{\delta\Pi_i(\mathbf{r},t)} - \frac{\delta M_k(\mathbf{z},t)}{\delta\Gamma_i(\mathbf{r},t)} \frac{\delta C_{ij}(\mathbf{x},t)}{\delta\Pi_i(\mathbf{r},t)} \right] d^3r$$

Now $\frac{\delta C_{ij}(\mathbf{x},t)}{\delta\Gamma_i(\mathbf{r},t)}$ can be obtained using the Hamiltonian (A.2.7) and $\frac{\delta M_k(\mathbf{z},t)}{\delta\Pi_i(\mathbf{r},t)} = \delta^3[\Gamma - \mathbf{z}]$
Using (A.2.10) and (A.2.11)

$$\{C_{ij}(\mathbf{x},t), M_j(\mathbf{z},t)\} = \int_{\Omega} \left[\rho_0 c_{ij} \frac{\partial\delta^3[\Gamma - \mathbf{x}]}{\partial\Gamma_k} - \frac{\partial}{\partial r_l} \left(\rho_0 \delta^3[\Gamma - \mathbf{x}] \frac{\partial C_{ij}}{\partial\mathbf{F}_{kl}} \right) \right] \delta^3[\gamma - \mathbf{z}] d^3r$$

Using the product rule

$$\begin{aligned}
\{C_{ij}(\mathbf{x},t), M_j(\mathbf{z},t)\} &= \int_{\Omega} \left[\rho_0 c_{ij} \frac{\partial\delta^3[\Gamma - \mathbf{x}]}{\partial\Gamma_k} - \frac{\partial}{\partial r_l} \left(\frac{\rho J}{J} \delta^3[\Gamma - \mathbf{x}](F_{il}\delta_{jk} + F_{jl}\delta_{ik}) \right) \right] \delta^3[\gamma - \mathbf{z}] d^3\Gamma \\
&= \int_{\Omega} \left[\rho_0 c_{ij} \frac{\partial\delta^3[\Gamma - \mathbf{x}]}{\partial\Gamma_k} - \frac{\partial}{\partial r_l} \frac{1}{J} \left(\rho J \delta^3[\Gamma - \mathbf{x}](F_{il}\delta_{jk} + F_{jl}\delta_{ik}) \right) \right] \delta^3[\Gamma - \mathbf{z}] d^3\Gamma
\end{aligned} \tag{A.2.14}$$

Note we have used the fact that $\rho d^3\Gamma = \rho_0 d^3 r$. We can then write

$$\{C_{ij}(\mathbf{x},t), M_j(\mathbf{z},t)\} = \int_{\Omega} \left[\rho_0 c_{ij} \frac{\partial\delta^3[\Gamma - \mathbf{x}]}{\partial\Gamma_k} - \frac{\partial}{\partial r_l} \left(\rho F_{ml} \delta^3[\Gamma - \mathbf{x}](F_{il}\delta_{jk} + F_{jl}\delta_{ik}) \right) \right] \delta^3[\Gamma - \mathbf{z}] d^3\Gamma$$

The expression can be simplified to

$$\{C_{ij}(\mathbf{x},t), M_j(\mathbf{z},t)\}_L = C_{ij} \frac{\partial\delta^3[\mathbf{z} - \mathbf{x}]}{\partial\mathbf{z}} - \frac{\partial}{\partial z_m} (\rho\delta^3[\Gamma - \mathbf{x}](C_{ni}(\mathbf{z},t)\delta_{jk} + C_{nj}(\mathbf{z},t)\delta_{ik})) \tag{A.2.15}$$

Eq. (A.2.13) can be written as $\{F,G\}_E = \{F,G\}_E^{\rho} + \{F,G\}_E^{s} + \{F,G\}_E^{m} + \{F,G\}_E^{C}$ where the first, second and third term on the RHS correspond to the first, second and third terms on the RHS of equation (A.2.13), respectively.

$$\begin{aligned}
\frac{\delta\rho(\mathbf{x},t)}{\delta\Gamma_i(\mathbf{r},t)} &= \rho_0(\mathbf{r})\frac{\partial\delta^3[\Gamma(\mathbf{r},t)-\mathbf{x}]}{\partial\Gamma_i(\mathbf{r},t)} &\qquad \frac{\delta\rho(\mathbf{x},t)}{\delta\Pi(\mathbf{r},t)} &= \frac{\delta\rho(\mathbf{x},t)}{\delta\rho(\mathbf{r},t)\dot{\Gamma}(\mathbf{r},t)} = 0\\
\frac{\delta s(\mathbf{x},t)}{\delta\Gamma_i(\mathbf{r},t)} &= s_0(\mathbf{r})\frac{\partial\delta^3[\Gamma(\mathbf{r},t)-\mathbf{x}]}{\partial\Gamma_i(\mathbf{r},t)} &\qquad \frac{\delta s(\mathbf{x},t)}{\delta\Pi(\mathbf{r},t)} &= \frac{\delta s(\mathbf{x},t)}{\delta\rho(\mathbf{r},t)\dot{\Gamma}(\mathbf{r},t)} = 0\\
\frac{\delta m_j(\mathbf{x},t)}{\delta\Gamma_i(\mathbf{r},t)} &= \Pi_j(r,t)\frac{\partial\delta^3[\Gamma(\mathbf{r},t)-\mathbf{x}]}{\partial\Gamma_i(\mathbf{r},t)} &\qquad \frac{\delta m_j(\mathbf{x},t)}{\delta\Pi_i(\mathbf{r},t)} &= \delta_{ij}\delta^3[\Gamma(\mathbf{r},t)-\mathbf{x}]
\end{aligned}$$

where δ_{ij} denotes the Kronecker delta. We can obtain expressions for all the relevant material (Lagrangian) brackets by substituting these 6 partial derivatives into the definition of the Poisson bracket (A.1.1) [8].

$$\{\rho(\mathbf{x},t), M_j(\mathbf{z},t)\}_L = \rho(\mathbf{z},t)\frac{\partial\delta^3[\mathbf{z}-\mathbf{x}]}{\partial z_j} \tag{A.2.16}$$

$$\{s(\mathbf{x},t), M_j(\mathbf{z},t)\}_L = s(\mathbf{z},t)\frac{\partial\delta^3[\mathbf{z}-\mathbf{x}]}{\partial z_j} \tag{A.2.17}$$

$$\{m_i(\mathbf{x},t), m_j(\mathbf{z},t)\}_L = m_k(\mathbf{z},t)\frac{\partial\delta^3[\mathbf{z}-\mathbf{x}]}{\partial z_j} - m_j(\mathbf{x},t)\frac{\partial\delta^3[\mathbf{z}-\mathbf{x}]}{\partial x_j} \tag{A.2.18}$$

Substituting (A.2.16), (A.2.17) and (A.2.18) into (A.2.13) yields

$$\{F,G\}_E^{\rho} = \int_{\Omega'}\int_{\Omega'}\left[\frac{\delta F}{\delta\rho(\mathbf{x},t)}\frac{\delta G}{\delta M_j(z,t)} - \frac{\delta G}{\delta\rho(\mathbf{x},t)}\frac{\delta F}{\delta M_j(z,t)}\right]\times\rho(\mathbf{z},t)\frac{\partial\delta^3[\mathbf{z}-\mathbf{x}]}{\partial z_j}d^3z\,d^3x$$

Integrating by parts ($\int fg' = [fg] - \int f'g$ where f is the term in the '[...]' parenthesis and the g' term is the partial derivative in the integrand

$$\{F,G\}^{\rho}_{E} = \int_{\Omega'}\int_{\Omega'}\left\{\int_{\Omega'}\left[\left[\frac{\delta F}{\delta\rho(\mathbf{x},t)}\frac{\delta G}{\delta M_j(z,t)} - \frac{\delta G}{\delta\rho(\mathbf{x},t)}\frac{\delta F}{\delta M_j(z,t)}\right]\times n_j\delta^3[\mathbf{z}-\mathbf{x}]\right]_{\partial\Omega'} - \int_{\Omega}\left[\frac{\delta F}{\delta\rho(\mathbf{x},t)}\frac{\partial}{\partial z_j}\left(\rho(\mathbf{z},t)\frac{\delta G}{\delta M_j(\mathbf{z},t)}\right) - \frac{\delta G}{\delta\rho(\mathbf{x},t)}\frac{\partial}{\partial z_j}\left(\rho(\mathbf{z},t)\frac{\delta F}{\delta M_j(\mathbf{z},t)}\right)\right]\delta^3[\mathbf{z}-\mathbf{x}]\right\}d^3z d^3x$$

We must introduce key boundary conditions, the first being that n_j is zero on the boundary. The first term of the integrand is equal to zero.

$$\mathbf{n}\cdot\frac{\delta F}{\delta\mathbf{m}} = 0$$

which leaves us with the expression

$$\{F,G\}^{\rho}_{E} = -\int_{\Omega}\int_{\Omega'}\left[\frac{\delta F}{\delta\rho(\mathbf{x},t)}\frac{\partial}{\partial z_j}\left(\rho(\mathbf{z},t)\frac{\delta G}{\delta M_j(\mathbf{z},t)}\right) - \frac{\delta G}{\delta\rho(\mathbf{x},t)}\frac{\partial}{\partial z_j}\left(\rho(\mathbf{z},t)\frac{\delta F}{\delta M_j(\mathbf{z},t)}\right)\right]\delta^3[\mathbf{z}-\mathbf{x}]d^3z d^3x$$

$\delta^3[\mathbf{z}-\mathbf{x}]d^3z d^3x = d^3x$ and all $\mathbf{z}$ functions to $\mathbf{x}$ dependent in the integrand i.e $\int f(x)g(y)\delta[y-x]dxdy = \int f(x)g(x)dx$

$$\{F,G\}^{\rho}_{E} = -\int_{\Omega'}\left[\frac{\delta F}{\delta\rho(\mathbf{x},t)}\frac{\partial}{\partial x_j}\left(\rho(\mathbf{x},t)\frac{\delta G}{\delta M_j(\mathbf{x},t)}\right) - \frac{\delta G}{\delta\rho(\mathbf{x},t)}\frac{\partial}{\partial x_j}\left(\rho(\mathbf{x},t)\frac{\delta F}{\delta M_j(\mathbf{x},t)}\right)\right]d^3x \tag{A.2.19}$$

By the symmetry of the terms governing $s(\mathbf{x},t)$ in (A.2.20)

$$\{F,G\}^{s}_{E} = -\int_{\Omega'}\left[\frac{\delta F}{\delta\rho(\mathbf{x},t)}\frac{\partial}{\partial x_j}\left(s(\mathbf{x},t)\frac{\delta G}{\delta M_j(\mathbf{x},t)}\right) - \frac{\delta G}{\delta s(\mathbf{x},t)}\frac{\partial}{\partial z_j}\left(s(\mathbf{x},t)\frac{\delta F}{\delta M_j(\mathbf{x},t)}\right)\right]d^3x \tag{A.2.20}$$

and

$$\{F,G\}^{M}_{E} = -\int_{\Omega'}\left[\frac{\delta F}{\delta M_k(\mathbf{x},t)}\frac{\partial}{\partial x_j}\left(M_k(\mathbf{x},t)\frac{\delta G}{\delta M_j(\mathbf{x},t)}\right) - \frac{\delta G}{\delta M_k(\mathbf{x},t)}\frac{\partial}{\partial x_j}\left(M_k(\mathbf{x},t)\frac{\delta F}{\delta M_j(\mathbf{x},t)}\right)\right]d^3x \tag{A.2.21}$$

Note that $\frac{\partial}{\partial x_j} = \nabla_j = \nabla\cdot$ is the divergence operator. The conformation tensor terms in the bracket can be written

$$\{F,G\}^C_E = I_1 + I_2 + I_3 \tag{A.2.22}$$

where

$$\begin{aligned} I_1 =& \int_{\Omega'}\int_{\Omega'}\left[\frac{\delta F}{\delta C_{ij}(\mathbf{x},t)}\frac{\delta G}{\delta M_j(\mathbf{z},t)} - \frac{\delta G}{\delta C_{ij}(\mathbf{x},t)}\frac{\delta F}{\delta M_j(\mathbf{z},t)}\right] C_{ij}(\mathbf{z},t)\frac{\partial\delta^3[\mathbf{z}-\mathbf{x}]}{\partial z_k} d^3z d^3x \\ =& \int_{\Omega'}\left\{\int_{\partial\Omega'} C_{ij}(\mathbf{z},t)\left[\frac{\delta F}{\delta C_{ij}(\mathbf{x},t)}\frac{\delta G}{\delta M_j(\mathbf{z},t)} - \frac{\delta G}{\delta C_{ij}(\mathbf{x},t)}\frac{\delta F}{\delta M_j(\mathbf{z},t)}\right] \times n_j\delta^3[\mathbf{z}-\mathbf{x}]d^3x\right\}d^3z \\ &- \int_{\Omega'}\int_{\Omega'}\left[\frac{\delta F}{\delta C_{ij}(\mathbf{x},t)}\frac{\partial}{\partial z_j}\left(C_{ij}\frac{\delta G}{\delta M_j(\mathbf{z},t)}\right) - \frac{\delta G}{\delta C_{ij}(\mathbf{x},t)}\frac{\partial}{\partial z_j}\left(C_{ij(\mathbf{x},t)}\frac{\delta F}{\delta M_j(\mathbf{z},t)}\right)\right]\delta^3[\mathbf{z}-\mathbf{x}]d^3xd^3z \end{aligned}$$

where n_j is the unit normal to the surface. The first term vanishes as $\mathbf{n}\cdot\frac{\delta F}{\delta \mathbf{M}(\mathbf{z},t)} = n_j\frac{\delta F}{\delta M_j(\mathbf{z},t)} = 0$ on the surface/boundary and so we are left with

$$I_1 = \int_{\Omega'}\left[\frac{\delta F}{\delta C_{ij}(\mathbf{x},t)}\frac{\partial}{\partial z_j}\left(C_{ij}\frac{\delta G}{\delta M_j(\mathbf{z},t)}\right) - \frac{\delta G}{\delta C_{ij}(\mathbf{x},t)}\frac{\partial}{\partial z_j}\left(C_{ij(\mathbf{x},t)}\frac{\delta F}{\delta M_j(\mathbf{z},t)}\right)\right]d^3x \tag{A.2.23}$$

Noting again that $\int_{\Omega'} g(\mathbf{z})\delta^3[\mathbf{z}-\mathbf{x}]d^3xd^3z = g(\mathbf{x})$ when $\mathbf{x}=\mathbf{z}$ and 0 otherwise. The second and third of the extra three integrals can be derived using integration by parts

$$\begin{aligned} I_2 =& -\int_{\Omega'}\int_{\Omega'}\left[\frac{\delta F}{\delta C_{ij}(\mathbf{x},t)}\frac{\delta G}{\delta M_j(\mathbf{z},t)} - \frac{\delta G}{\delta C_{ij}(\mathbf{x},t)}\frac{\delta F}{\delta M_j(\mathbf{z},t)}\right]\frac{\partial}{\partial z_k}(\rho\delta^3[\Gamma-\mathbf{x}]C_{ni}(\mathbf{z},t)\delta_{jk})d^3zd^3x \\ &- \int_{\Omega'} C_{ki}\left[\frac{\delta G}{\delta C_{ij}}\nabla_k\left(\frac{\delta F}{\delta M_j}\right) - \frac{\delta F}{\delta C_{ij}}\nabla_k\left(\frac{\delta G}{\delta M_j}\right)\right]d^3x \end{aligned}$$

And similarly for the third integral

$$\begin{aligned} I_3 =& -\int_{\Omega'}\int_{\Omega'}\left[\frac{\delta F}{\delta C_{ij}(\mathbf{x},t)}\frac{\delta G}{\delta M_j(\mathbf{z},t)} - \frac{\delta G}{\delta C_{ij}(\mathbf{x},t)}\frac{\delta F}{\delta M_j(\mathbf{z},t)}\right]\frac{\partial}{\partial z_k}(\rho\delta^3[\Gamma-\mathbf{x}]C_{nj}(\mathbf{z},t)\delta_{jk})d^3zd^3x \\ &- \int_{\Omega'} C_{ki}\left[\frac{\delta G}{\delta C_{ij}}\nabla_k\left(\frac{\delta F}{\delta M_j}\right) - \frac{\delta F}{\delta C_{ij}}\nabla_k\left(\frac{\delta G}{\delta M_j}\right)\right]d^3x \end{aligned}$$

Combining the three we arrive at the spatial bracket counterpart to the Poisson bracket for continuous media

$$
\begin{aligned}
\{F, H\}_E = &-\int_{\Omega'} \left[\frac{\delta F}{\delta \rho}\nabla_j\left(\rho\frac{\delta H}{\delta m_j}\right) - \frac{\delta H}{\delta \rho}\nabla_j\left(\rho\frac{\delta F}{\delta m_j}\right)\right] d^3x \\
&-\int_{\Omega'} \left[\frac{\delta F}{\delta m_k}\nabla_j\left(m_k\frac{\delta H}{\delta m_j}\right) - \frac{\delta H}{\delta m_k}\nabla_j\left(m_k\frac{\delta H}{\delta m_j}\right)\right] d^3x \\
&-\int_{\Omega'} \left[\frac{\delta F}{\delta \rho}\nabla_j\left(s\frac{\delta H}{\delta m_j}\right) - \frac{\delta H}{\delta s}\nabla_j\left(s\frac{\delta F}{\delta m_j}\right)\right] d^3x \\
&-\int_{\Omega'} \left[\frac{\delta F}{\delta C_{ij}}\nabla_k\left(C_{ik}\frac{\delta H}{\delta m_k}\right) - \frac{\delta H}{\delta C_{ij}}\nabla_k\left(C_{ij}\frac{\delta F}{\delta m_k}\right)\right] d^3x \\
&-\int_{\Omega'} C_{ki}\left[\frac{\delta H}{\delta C_{ij}}\nabla_k\left(\frac{\delta F}{\delta m_j}\right) - \frac{\delta F}{\delta C_{ij}}\nabla_k\left(\frac{\delta H}{\delta m_j}\right)\right] d^3x \\
&-\int_{\Omega'} C_{ki}\left[\frac{\delta H}{\delta C_{ij}}\nabla_k\left(\frac{\delta F}{\delta m_j}\right) - \frac{\delta F}{\delta C_{ij}}\nabla_k\left(\frac{\delta H}{\delta m_j}\right)\right] d^3x
\end{aligned}
\tag{A.2.24}
$$

which can be written in the form

$$
\begin{aligned}
\{F, H\}_E = -\int_{\Omega'} &\left[\frac{\delta F}{\delta \rho}\nabla_j\left(\rho\frac{\delta H}{\delta m_j}\right) + \frac{\delta F}{\delta m_i}\left(\rho\nabla_i\left(\frac{\delta H}{\delta \rho}\right) + \nabla_j\left(\frac{\delta H}{\delta m_j}m_i\right) + m_j\nabla_i\left(\frac{\delta H}{\delta m_j}\right)\right.\right. \\
&+ s\left(\frac{\delta H}{\delta s}\right) + C_{ij}\nabla_k\left(\frac{\delta H}{\delta C_{ij}}\right) - \nabla_k\left(C_{ki}\frac{\delta H}{\delta C_{ij}}\right) - \nabla_k\left.\left(C_{kj}\frac{\delta H}{\delta C_{ij}}\right)\right) + \nabla_j\left(s\frac{\delta H}{\delta m_j}\right) \\
&\left.+ \frac{\delta F}{\delta C_{ij}}\left(\nabla_k\left(C_{ij}\frac{\delta H}{\delta m_k}\right) - C_{ki}\nabla_k\left(\frac{\delta H}{\delta m_j}\right) - C_{kj}\nabla_k\left(\frac{\delta H}{\delta m_i}\right)\right)\right] d^3x
\end{aligned}
\tag{A.2.25}
$$

We can also establish, by the chain rule, that

$$
\frac{dF}{dt} = \int_{\Omega'}\left[\frac{\delta F}{\delta \rho}\frac{\partial \rho}{\partial t} + \frac{\delta F}{\delta m_i}\frac{\partial m_i}{\partial t} + \frac{\delta F}{\delta s}\frac{\partial s}{\partial t}\right] d\Omega \tag{A.2.26}
$$

Comparing coefficients in both equations Eq. (A.2.26) and Eq. (A.2.25) and evaluating the

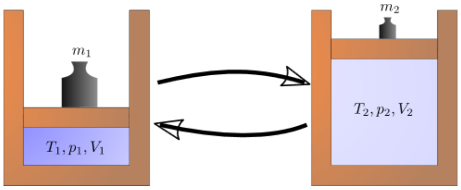

Figure A.1: Reversible process. Here $dW = -pdV$. One can theoretically interchange between the two states with no energy being 'wasted'.

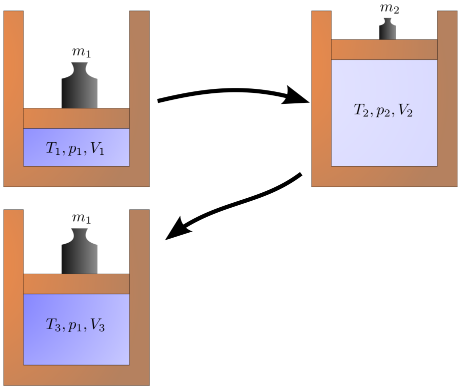

Figure A.2: Irreversible Process: Here some energy is wasted and thus the final temperature and volume do not return to their initial values.

Volterra derivatives of H (see Eq. (2.2.8)) we obtain the system of governing equation given by (2.2.9).

A.2.4 Fundamental Concepts in Nonequilibrium Thermodynamics

At the most fundamental level we will have to change the assumption made in (A.2.2) $dW = -pdV$ (equilibrium process). A.2 and A.1 demonstrate the distinction between reversible (theoretical) and irreversible (real) processes.

The new equation relating work, pressure and volume in for a system surrounded by a flexible adiabatic wall is

$$dW = -pdV + dW_i$$

Here dW_i represents the work lost recovering the initial deformation [8]. The second law of thermodynamics restricts this new term: $dW \geq 0$. The pressure difference between the outside and inside of this flexible wall $p_\alpha - p < 0$.

$$dW_i = (p - p_\alpha)dV$$

To ensure mechanical stability we have to guarantee that.

$$\left(\frac{\partial V}{\partial p}\right)_s < 0 \implies \kappa_s > 0$$

where κ_s is the isentropic compressibility coefficient. In addition thermal stability means

$$\left(\frac{\partial U}{\partial T}\right)_v > 0 \implies C_v > 0$$

which also means $C_p > 0$. The second law can be extended to the Gibbs relation [8]

$$dQ \leq TdS \tag{A.2.27}$$

where Q is the heat energy. All of this leads us to the fundamental equation for an irreversible process

$$dU \leq TdS - pdV \tag{A.2.28}$$

Beris and Edwards [8] provide a uniform formulation of fluid modelling incorporating both conservative and dissipative phenomena known as the **The Generalized Bracket**.

Proposition A.2.2 *The internal dynamics of an isolated system is* ***completely described*** *by the equation*

$$\frac{dF}{dt} = \{[F, H]\} = \{F, H\} + [F, H] \tag{A.2.29}$$

where F is an observable over Ω and H is the Hamiltonian.

A.3 Derivation of the Compressible & Nonisothermal Maxwell Models

In Section 3.1 we derive the closed form equations for the generalised Maxwell models. Note that $\mathbf{C} \equiv \rho\mathbf{c}$ where ρ is the density and $\mathbf{c}$ is the kinematic conformation tensor. For the purposes of clarity, here presented is the derivation of the governing equations. Starting from the conservation of mass, which can be written

$$\frac{D\rho}{Dt} + \rho(\nabla \cdot \mathbf{u}) = 0, \tag{A.3.1}$$

Substituting Eq. (3.1.8) into (2.3.6) and (2.3.10) we obtain the evelution equation for the kinematic conformation tensor

$$\lambda(T) \overset{\triangledown}{\mathbf{c}} + \mathbf{c} = \frac{k_b T}{K(T)}\mathbf{I}, \tag{A.3.2}$$

and polymeric extra stress

$$\boldsymbol{\tau}_p = \alpha\rho K(T)\mathbf{c} - \alpha\rho k_b T\mathbf{I}, \tag{A.3.3}$$

where $\mathbf{c}$ - kinematic conformation tensor, $\boldsymbol{\tau}_p$ - extra-stress tensor, $\lambda(T)$ - relaxation time, α - mass fraction, ρ - density, T - temperature, k_b - Boltzmann constant. which can also be written in terms of $\mathbf{C}$ as

$$\boldsymbol{\tau}_p = \alpha K(T)\mathbf{C} - \alpha\rho k_b T\mathbf{I} \tag{A.3.4}$$

Isothermal and Incompressible - α, ρ, $K(T) = K$, $\lambda(T) = \lambda$, T - constant
Take upper convected derivative of (A.3.3)

$$\overset{\triangledown}{\boldsymbol{\tau}}_p = \alpha\rho K \overset{\triangledown}{\mathbf{c}} - \alpha\rho k_b T \overset{\triangledown}{\mathbf{I}}. \tag{A.3.5}$$

Multiply (A.3.2) by $\alpha\rho K$

$$\lambda \underbrace{\alpha\rho K \overset{\triangledown}{\mathbf{c}}}_{\text{(A.3.5)}} + \underbrace{\alpha\rho K\mathbf{c}}_{\text{(A.3.3)}} = \alpha\rho K\frac{k_b T}{K}\mathbf{I}$$

$$\lambda(\overset{\triangledown}{\boldsymbol{\tau}}_p + \alpha\rho k_b T \overset{\triangledown}{\mathbf{I}}) + (\boldsymbol{\tau}_p + \alpha\rho k_b T\mathbf{I}) = \alpha\rho k_b T\mathbf{I}$$

Using the fact that $\overset{\triangledown}{\mathbf{I}} = -\nabla\mathbf{u} - \nabla\mathbf{u}^T = -2\mathbb{D}$

$$\lambda \overset{\triangledown}{\boldsymbol{\tau}}_p + \boldsymbol{\tau}_p = 2\lambda\alpha\rho k_b T\mathbb{D} = 2\mu_p\mathbb{D} \tag{A.3.6}$$

where we have used the definition of polymeric viscosity $\mu_p = \lambda\alpha\rho k_b T$.

Isothermal and Compressible - α, $K(T) = K$, T - constant, ρ - variable

Take upper convected derivative of (A.3.3)

$$\overset{\triangledown}{\boldsymbol{\tau}}_p = \alpha\frac{D\rho}{Dt}K\mathbf{c} + \alpha\rho K \overset{\triangledown}{\mathbf{c}} - \alpha\rho k_b T \overset{\triangledown}{\mathbf{I}} - \alpha\frac{D\rho}{Dt}k_b T\mathbf{I} \tag{A.3.7}$$

Substituting Eq. (A.3.1)

$$\overset{\triangledown}{\boldsymbol{\tau}}_p = \alpha\rho K \overset{\triangledown}{\mathbf{c}} - \alpha\rho k_b T \overset{\triangledown}{\mathbf{I}} - \alpha\rho(\nabla\cdot\mathbf{u})K\mathbf{c} + \alpha\rho(\nabla\cdot\mathbf{u})k_b T\mathbf{I},$$

$$\overset{\triangledown}{\boldsymbol{\tau}}_p = \alpha\rho K \overset{\triangledown}{\mathbf{c}} - \alpha\rho k_b T \overset{\triangledown}{\mathbf{I}} - (\nabla\cdot\mathbf{u})[\alpha\rho K\mathbf{c} - \alpha\rho k_b T\mathbf{I}].$$

Using Eq. (A.3.3) we obtain

$$\overset{\triangledown}{\boldsymbol{\tau}}_p = \alpha\rho K \overset{\triangledown}{\mathbf{c}} - \alpha\rho k_b T \overset{\triangledown}{\mathbf{I}} - (\nabla\cdot\mathbf{u})\boldsymbol{\tau}_p$$

$$\overset{\triangledown}{\boldsymbol{\tau}}_p + (\nabla\cdot\mathbf{u})\boldsymbol{\tau}_p = \alpha\rho K \overset{\triangledown}{\mathbf{c}} - \alpha\rho k_b T \overset{\triangledown}{\mathbf{I}} \tag{A.3.8}$$

$$\lambda \underbrace{\alpha\rho K \overset{\triangledown}{\mathbf{c}}}_{\text{(A.3.8)}} + \underbrace{\alpha\rho K \mathbf{c}}_{\text{(A.3.3)}} = \alpha\rho K \frac{k_b T}{K}\mathbf{I}$$

$$\lambda(\overset{\triangledown}{\boldsymbol{\tau}}_p + (\nabla\cdot\mathbf{u})\boldsymbol{\tau}_p + \alpha\rho k_b T \overset{\triangledown}{\mathbf{I}}) + (\boldsymbol{\tau}_p + \alpha\rho k_b T\mathbf{I}) = \alpha\rho k_b T\mathbf{I}$$

$$\lambda\left(\overset{\triangledown}{\boldsymbol{\tau}}_p + (\nabla\cdot\mathbf{u})\boldsymbol{\tau}_p\right) + \boldsymbol{\tau}_p = 2\lambda\alpha\rho k_b T\mathbb{D} = 2\mu_p\mathbb{D} \tag{A.3.9}$$

Nonisothermal and Compressible - α - constant, ρ, $K(T)$, T - variable

Take upper convected derivative of (A.3.3)

$$\overset{\triangledown}{\boldsymbol{\tau}}_p = \alpha\frac{D\rho}{Dt}K\mathbf{c} + \alpha\rho\frac{DK(T)}{Dt}\mathbf{c} + \alpha\rho K \overset{\triangledown}{\mathbf{c}} - \alpha\rho k_b T \overset{\triangledown}{\mathbf{I}} - \alpha\frac{D\rho}{Dt}k_b T\mathbf{I} - \alpha\rho k_b\frac{DT}{Dt}\mathbf{I} \tag{A.3.10}$$

Use conservation of mass (eq.)

$$\overset{\triangledown}{\boldsymbol{\tau}}_p = \alpha\rho K \overset{\triangledown}{\mathbf{c}} - \alpha\rho k_b T \overset{\triangledown}{\mathbf{I}} - (\nabla\cdot\mathbf{u})[\alpha\rho K\mathbf{c} - \alpha\rho k_b T\mathbf{I}] + \frac{D\ln K(T)}{Dt}\alpha\rho K\mathbf{c} - \frac{D\ln T}{Dt}\alpha\rho k_b T\mathbf{I}$$

$$\overset{\triangledown}{\boldsymbol{\tau}}_p = \alpha\rho K \overset{\triangledown}{\mathbf{c}} - \alpha\rho k_b T \overset{\triangledown}{\mathbf{I}} + \left(-(\nabla\cdot\mathbf{u}) + \frac{D\ln K(T)}{Dt}\right)[\alpha\rho K\mathbf{c} - \alpha\rho k_b T\mathbf{I}] + \left(\frac{D\ln K(T)}{Dt} - \frac{D\ln T}{Dt}\right)\alpha\rho k_b T\mathbf{I}$$

Using Eq. (A.3.3)

$$\overset{\triangledown}{\boldsymbol{\tau}}_p + \left((\nabla\cdot\mathbf{u}) - \frac{D\ln K(T)}{Dt}\right)\boldsymbol{\tau}_p - \left(\frac{D\ln K(T)}{Dt} - \frac{D\ln T}{Dt}\right)\alpha\rho k_b T\mathbf{I} = \alpha\rho K \overset{\triangledown}{\mathbf{c}} - \alpha\rho k_b T \overset{\triangledown}{\mathbf{I}} \tag{A.3.11}$$

Using the same technique as in the last section

$$\lambda(T)\,\underbrace{\alpha\rho K\,\overset{\triangledown}{\mathbf{c}}}_{\text{(A.3.11)}}+\underbrace{\alpha\rho K\mathbf{c}}_{\text{(A.3.3)}}=\alpha\rho K\frac{k_bT}{K}\mathbf{I}$$

$$\lambda(T)\left(\overset{\triangledown}{\boldsymbol{\tau}}_p+\left((\nabla\cdot\mathbf{u})-\frac{D\ln K(T)}{Dt}\right)\boldsymbol{\tau}_p+\alpha\rho k_bT\,\overset{\triangledown}{\mathbf{I}}\right)+(\boldsymbol{\tau}_p+\alpha\rho k_bT\mathbf{I})=\alpha\rho k_bT\mathbf{I}+\left(\frac{D\ln K(T)}{Dt}-\frac{D\ln T}{Dt}\right)\alpha\rho$$

$$\lambda(T)\,\overset{\triangledown}{\boldsymbol{\tau}}_p+\left[1+\lambda(T)\left(\nabla\cdot\mathbf{u}-\frac{D\ln K(T)}{Dt}\right)\right]\boldsymbol{\tau}_p=G(\rho,T)\lambda(T)\left[2\mathbb{D}+\left(\frac{D\ln K(T)}{Dt}-\frac{D\ln(T)}{Dt}\right)\mathbf{I}\right] \tag{A.3.12}$$

where

$$G(\rho,T)=\alpha\rho k_bT=\mu(\rho,T)/\lambda(T) \tag{A.3.13}$$

is the elastic modulus. Note that in the subsequent chapters Eq. (...) is not used. Instead the used for computing viscoelastic flow is not the closed form expressions but those in terms of $\mathbf{C}$.

A.4 Derivation of the Energy equation

As outlined in Sec. 2.3 the Helmholtz free energy is given by

$$A=H-ST==\int_\Omega \hat{a}(\rho,\mathbf{u},s,T,\mathbf{C})\,d\Omega \tag{A.4.1}$$

where

$$\hat{a}=\frac{\mathbf{m}\cdot\mathbf{m}}{2\rho}+w(\mathbf{C})+\hat{u}(\rho,s,T)-s(\rho,\mathbf{C})T \tag{A.4.2}$$

Taking the derivative w.r.t. t gives

$$\begin{aligned}\frac{\partial \hat{a}(\rho, s, \mathbf{C})}{\partial t} =& \frac{\partial \hat{a}}{\partial \rho}\frac{\partial \rho}{\partial t} + \frac{\partial \hat{a}}{\partial s}\frac{\partial s}{\partial t} + \frac{\partial \hat{a}}{\partial \mathbf{C}} : \frac{\partial \mathbf{C}}{\partial t} \\ =& \frac{\partial \hat{a}}{\partial \rho}\Bigg(- \nabla \cdot (\rho \mathbf{u})\Bigg) \\ & + \frac{\partial \hat{a}}{\partial s}\Bigg(-\nabla \cdot (s\mathbf{u}) + \frac{1}{T}\mathbf{Q} :: \Bigg(\nabla \mathbf{u} \otimes \nabla \mathbf{u}\Bigg) + \frac{1}{T}\nabla \cdot (\boldsymbol{\alpha} T \nabla T) + \frac{1}{T}\boldsymbol{\Lambda} :: \Bigg(\frac{\delta A}{\delta \mathbf{C}} \otimes \frac{\delta A}{\delta \mathbf{C}}\Bigg)\Bigg) \\ & + \frac{\partial \hat{a}}{\partial \mathbf{C}} : \Bigg(- \nabla \cdot (\mathbf{u}\mathbf{C}) + \nabla \mathbf{u} \cdot \mathbf{C} + \mathbf{C} \cdot \nabla \mathbf{u}^T - \boldsymbol{\Lambda} : \frac{\delta A}{\delta \mathbf{C}} + \mathbf{L} : \nabla \mathbf{u}\Bigg)\end{aligned} \tag{A.4.3}$$

Given that $\frac{\partial a}{\partial t} = T$ and $\frac{\partial \hat{a}}{\partial \mathbf{C}} =: \frac{\delta A}{\delta \mathbf{C}}$, Eq. (A.4.3) can be re-arranged to give

$$\begin{aligned}\frac{\partial \hat{a}}{\partial t} =& - \frac{\partial \hat{a}}{\partial \rho}\nabla \cdot (\rho \mathbf{u}) - \frac{\partial \hat{a}}{\partial s}\nabla \cdot (s\mathbf{u}) - \frac{\partial \hat{a}}{\partial \mathbf{C}} : \nabla \cdot (\mathbf{u}\mathbf{C}) \\ & + \nabla \cdot (\boldsymbol{\alpha} T \nabla T) + \boldsymbol{\Lambda} :: \Bigg(\frac{\delta A}{\delta \mathbf{C}} \otimes \frac{\delta A}{\delta \mathbf{C}}\Bigg) \\ & + \frac{\delta A}{\delta \mathbf{C}} : (\nabla \mathbf{u} \cdot \mathbf{C} + \mathbf{C} \cdot \nabla \mathbf{u}^T) - \frac{\delta A}{\delta \mathbf{C}} : \boldsymbol{\Lambda} : \frac{\delta A}{\delta \mathbf{C}} + \frac{\delta A}{\delta \mathbf{C}} : \mathbf{L} : \nabla \mathbf{u}\end{aligned} \tag{A.4.4}$$

It can be shown, using the definition of the pressure given by Eq. (2.3.11) that

$$\frac{\partial \hat{a}}{\partial \rho}\nabla \cdot (\rho \mathbf{u}) + \frac{\partial \hat{a}}{\partial s}\nabla \cdot (s\mathbf{u}) + \frac{\partial \hat{a}}{\partial \mathbf{C}} : \nabla \cdot (\mathbf{u}\mathbf{C}) = \nabla \cdot (\mathbf{u}\hat{a}) + p(\nabla \cdot \mathbf{u}) \tag{A.4.5}$$

Furthermore, because all indices are being summed over, terms 5 and 7 in (A.4.4) cancel and

$$\frac{\delta A}{\delta \mathbf{C}} : (\nabla \mathbf{u} \cdot \mathbf{C} + \mathbf{C} \cdot \nabla \mathbf{u}^T) = 2\mathbf{C} \cdot \frac{\delta A}{\delta \mathbf{C}} : \nabla \mathbf{u} \tag{A.4.6}$$

and

$$\frac{\delta A}{\delta \mathbf{C}} : \mathbf{L} : \nabla \mathbf{u} = \mathbf{L} \cdot \frac{\delta A}{\delta \mathbf{C}} : \nabla \mathbf{u} \tag{A.4.7}$$

Substitution of Eq. (A.4.5), (A.4.6) and (A.4.7) into (A.4.4) gives the energy equation

$$\frac{D\hat{a}}{Dt} + (\nabla \cdot \mathbf{u})\hat{a} = \nabla \cdot (\boldsymbol{\alpha} T \nabla T) - p(\nabla \cdot \mathbf{u}) + \hat{\mathbb{T}} : \nabla \mathbf{u} \tag{A.4.8}$$

where

$$\hat{\mathbb{T}} = \mathbb{T} - \mathbf{L} \cdot \frac{\delta A}{\delta \mathbf{C}} \tag{A.4.9}$$

and $\mathbb{T}$ is given by (2.3.10).

8.5 GitHub

Scripts used to generate the data used in Chapters 5-7 are available from the GitHub repository

https://github.com/mackaya1/FEniCS

Bibliography

[1] AM Afonso, FT Pinho, and MA Alves. The kernel-conformation constitutive laws. *J. Non Newtonian Fluid*, 167:30–37, 2012.

[2] N Balci, B Thomases, M Renardy, and CR Doering. Symmetric factorization of the conformation tensor in viscoelastic fluid models. *J. Non Newtonian Fluid*, 166(11):546–553, 2011.

[3] G Barrenechea, E Castillo, and R Codina. Time-dependent semidiscrete analysis of the viscoelastic fluid flow problem using a variational multiscale stabilized formulation. *IMA J. Num. Anal.*, page 18, 2018.

[4] G Batchelor. Heat transfer by free convection across a closed cavity between vertical boundaries at different temperatures. *Q. Appl. Math.*, 12(3):209–233, 1954.

[5] MJ Berger and J Oliger. Adaptive mesh refinement for hyperbolic partial differential equations. *J. Comp. Phys.*, 53(3):484–512, 1984.

[6] A Beris, R Armstrong, and R Brown. Finite element calculation of viscoelastic flow in a journal bearing: I: Small eccentricities. *J. Non Newtonian Fluid*, 16(1-2):141–172, 1984.

[7] A Beris, R Armstrong, and R Brown. Finite element calculation of viscoelastic flow in a journal bearing: Ii: Moderate eccentricity. *J. Non Newtonian Fluid*, 19(3):323–347, 1986.

[8] AN Beris and BJ Edwards. *Thermodynamics of flowing systems: with internal microstructure*. Number 36. Oxford University Press, 1994.

[9] RB Bird, RC Armstrong, and O Hassager. Dynamics of polymeric liquids. vol. 1: Fluid mechanics. 1987.

[10] PB Bochev, MD Gunzburger, and JN Shadid. Stability of the supg finite element method for transient advection–diffusion problems. *Comp. Method Appl. M.*, 193(23):2301–2323, 2004.

[11] PC Bollada and TN Phillips. On the effects of a compressible viscous lubricant on the load-bearing capacity of a journal bearing. *Int. J. Numer. Meth. Fl.*, 55(11):1091–1120, 2007.

[12] PC Bollada and TN Phillips. An anisothermal, compressible, piezoviscous model for journal-bearing lubrication. *Int. J. Numer. Meth. Fl.*, 58(1):27–55, 2008.

[13] PC Bollada and TN Phillips. On the mathematical modelling of a compressible viscoelastic fluid. *Arch. Rat. Mech. An.*, 205(1):1–26, 2012.

[14] AN Brooks and TJR Hughes. Streamline upwind/petrov-galerkin formulations for convection dominated flows with particular emphasis on the incompressible navier-stokes equations. *Comp. Method Appl. M.*, 32(1-3):199–259, 1982.

[15] RA Brown, MJ Szady, PJ Northey, and RC Armstrong. On the numerical stability of mixed finite-element methods for viscoelastic flows governed by differential constitutive equations. *Theor. Comp. Fluid Dyn.*, 5(2):77–106, 1993.

[16] E Castillo and R Codina. Numerical analysis of a stabilized finite element approximation for the three-field linearized viscoelastic fluid problem using arbitrary interpolations. *ESAIM-Math. Model Num.*, 51(4):1407–1427, 2017.

[17] MD Chilcott and JM Rallison. Creeping flow of dilute polymer solutions past cylinders and spheres. *J. Non Newtonian Fluid*, 29:381–432, 1988.

[18] PG Ciarlet. *Lectures on the finite element method*, volume 49. Tata Institute of Fundamental Research Bombay, 1975.

[19] A A Cocci Jr and J J C Picot. Rate of strain effect on the thermal conductivity of a polymer liquid. *Polym. Eng. Sci.*, 13(5):337–341, 1973.

[20] BD Coleman and W Noll. An approximation theorem for functionals, with applications in continuum mechanics. *Arch. Ration. Mech. An.*, 6(1):355–370, 1960.

[21] BD Coleman and W Noll. The thermodynamics of elastic materials with heat conduction and viscosity. *Arch. Ration. Mech. An.*, 13(1):167–178, 1963.

[22] R Courant. Variational methods for the solution of problems of equilibrium and vibrations. *B. Am. Math. Soc.*, 49(1):1–23, 1943.

[23] MJ Crochet and V Legat. The consistent streamline-upwind/petrov-galerkin method for viscoelastic flow revisited. *J. Non Newtonian Fluid*, 42(3):283–299, 1992.

[24] AR Davies and XK Li. Numerical modelling of pressure and temperature effects in viscoelastic flow between eccentrically rotating cylinders. *J. Non Newtonian Fluid*, 54:331–350, 1994.

[25] M Dressler, BJ Edwards, and Hans Christian Öttinger. Macroscopic thermodynamics of flowing polymeric liquids. *Rheol. Acta*, 38(2):117–136, 1999.

[26] A Drozdov. *Finite elasticity and viscoelasticity: a course in the nonlinear mechanics of solids*. World Scientific, 1996.

[27] T Dupont, J Hoffman, C Johnson, RC Kirby, MG Larson, A Logg, and LR Scott. *The FEniCS project*. Chalmers Finite Element Centre, Chalmers University of Technology, 2003.

[28] I E Dzyaloshinskii and G E Volovick. Poisson brackets in condensed matter physics. *Annals of Physics*, 125(1):67–97, 1980.

[29] BJ Edwards and AN Beris. Unified view of transport phenomena based on the generalized bracket formulation. *Ind. Eng. Chem. Res.*, 30(5):873–881, 1991.

[30] R Fattal and R Kupferman. Constitutive laws for the matrix-logarithm of the conformation tensor. *J. Non Newtonian Fluid*, 123(2-3):281–285, 2004.

[31] R Fattal and R Kupferman. Time-dependent simulation of viscoelastic flows at high weissenberg number using the log-conformation representation. *J. Non Newtonian Fluid*, 126(1):23–37, 2005.

[32] M Fortin and A Fortin. A new approach for the fem simulation of viscoelastic flows. *J. Non Newtonian Fluid*, 32(3):295–310, 1989.

[33] S Ganesan, G Matthies, and L Tobiska. Local projection stabilization of equal order interpolation applied to the stokes problem. *Math. Comput.*, 77(264):2039–2060, 2008.

[34] IE Garduño, HR Tamaddon-Jahromi, and MF Webster. The falling sphere problem and capturing enhanced drag with boger fluids. *J. Non Newtonian Fluid*, 231:26–48, 2016.

[35] IE Garduño, HR Tamaddon-Jahromi, and MF Webster. Flow past a sphere: Predicting enhanced drag with shear-thinning fluids, dissipative and constant shear-viscosity models. *J. Non Newtonian Fluid*, 244:25–41, 2017.

[36] N Germann, M Dressler, and EJ Windhab. Numerical solution of an extended white–metzner model for eccentric taylor–couette flow. *J. Comput. Phys.*, 230(21):7853–7866, 2011.

[37] M Grmela. Bracket formulation of dissipative fluid mechanics equations. *Phys. Lett. A*, 102:355–358, 1984.

[38] M Grmela. Hamiltonian mechanics of complex fluids. *J. Phys. A*, 22(20):4375, 1989.

[39] R Guénette and M Fortin. A new mixed finite element method for computing viscoelastic flows. *J. Non Newtonian Fluid*, 60(1):27–52, 1995.

[40] RK Gupta and AB Metzner. Modeling of nonisothermal polymer processes. *J. Rheol.*, 26(2):181–198, 1982.

[41] S Gupta, J Schieber, and D Venerus. Anisotropic thermal conduction in polymer melts in uniaxial elongation flows. *J. Rheol.*, 57(2):427–439, 2013.

[42] D Rh Gwynllyw, AR Davies, and TN Phillips. On the effects of a piezoviscous lubricant on the dynamics of a journal bearing. *J. Rheol.*, 40(6):1239–1266, 1996.

[43] WR Hamilton. *The Mathematical Papers of Sir William Rowan Hamilton.* CUP Archive, 2000.

[44] MR Hestenes and E Stiefel. *Methods of conjugate gradients for solving linear systems*, volume 49. NBS Washington, DC, 1952.

[45] CO Horgan. The remarkable gent constitutive model for hyperelastic materials. *Int. J. Nonlin. Mec.*, 68:9–16, 2015.

[46] MA Hulsen. A sufficient condition for a positive definite configuration tensor in differential models. *J. Non Newtonian Fluid*, 38(1):93–100, 1990.

[47] WM Jones, AH Price, and K Walters. The motion of a sphere falling under gravity in a constant-viscosity elastic liquid. *J. Non Newtonian Fluid*, 53:175–196, 1994.

[48] Gi Bin K, Jae Min H, and Ho Sang K. Transient buoyant convection of a power-law non-newtonian fluid in an enclosure. *Int. J. Heat Mass Trans.*, 46(19):3605–3617, 2003.

[49] AN Kaufman. Dissipative hamiltonian systems: a unifying principle. *Phys. Lett. A*, 100(8):419–422, 1984.

[50] IJ Keshtiban, F Belblidia, and MF Webster. Compressible flow solvers for low mach number flows—a review. 2004.

[51] IJ Keshtiban, F Belblidia, and MF Webster. Numerical simulation of compressible viscoelastic liquids. *J. Non Newtonian Fluid*, 122(1):131–146, 2004.

[52] R Keunings. On the peterlin approximation for finitely extensible dumbbells. *J. Non Newtonian Fluid*, 68(1):85–100, 1997.

[53] RM Kynch and TN Phillips. A high resolution spectral element approximation of viscoelastic flows in axisymmetric geometries using a devss-g/dg formulation. *J. Non Newtonian Fluid*, 240:15 – 33, 2017.

[54] Ross Kynch. *Numerical investigation of sedimentation in viscoelastic fluids using spectral element methods*. PhD thesis, Cardiff University, 2013.

[55] AI Leonov. Nonequilibrium thermodynamics and rheology of viscoelastic polymer media. *Rheol. Acta*, 15:85–98, 1976.

[56] A Leygue, A Beris, and R Keunings. A constitutive equation for entangled linear polymers inspired by reptation theory and consistent with non-equilibrium thermodynamics. *J. Non Newtonian Fluid*, 101(1-3):95–111, 2001.

[57] XK Li, AR Davies, and TN Phillips. A transient thermal analysis for dynamically loaded bearings. *Comput. Fluids*, 29(7):749–790, 2000.

[58] XK Li, D Rh Gwynllyw, AR Davies, and TN Phillips. Three-dimensional effects in dynamically loaded journal bearings. *Int. J. Numer. Meth. Fl.*, 29(3):311–341, 1999.

[59] X. L. Luo and R. I. Tanner. A computer study of film blowing. *Polym. Eng Sci.*, 25:620–629, 1985.

[60] JM Marchal and MJ Crochet. A new mixed finite element for calculating viscoelastic flow. *J. Non Newtonian Fluid*, 26(1):77–114, 1987.

[61] G Marrucci. The free energy constitutive equation for polymer solution from the dumbbell model. *Trans. Soc. Rheol.*, 16:321–330, 1972.

[62] MA McClelland and BA Finlayson. Heat transfer effects in extrudate swell of elastic liquids. *J. Non Newtonian Fluid*, 27:363—-374, 1988.

[63] G Meurant and Z Strakoš. The lanczos and conjugate gradient algorithms in finite precision arithmetic. *Acta Numerica*, 15:471–542, 2006.

[64] PJ Morrison. The maxwell-vlasov equations as a continuous hamiltonian system. *Phys. Lett. A*, 80(5):383–386, 1980.

[65] PJ Morrison. Bracket formulation for irreversible classical fields. *Phys. Lett. A*, 100(8):423–427, 1984.

[66] S Ostrach. Laminar flows with body forces. *Theory of laminar Flows*, pages 528–718, 1964.

[67] S Ostrach. Completely confined natural convection. *Developments in Mechanics*, 1968.

[68] S Ostrach. Natural convection in enclosures. *J. Heat Transfer*, 110(4-B):1175–1190, 1988.

[69] RG Owens and T N Phillips. *Computational Rheology*, volume 2. World Scientific, 2002.

[70] Tsorng-Whay P, Jian H, and R Glowinski. On the simulation of a time-dependent cavity flow of an oldroyd-b fluid. *Int. J. Numer. Meth. Fl.*, 60(7):791–808, 2009.

[71] TN Phillips and AT Mackay. Compressible viscoelastic flow between eccentrically rotating cylinders. 2018 (in preparation).

[72] TN Phillips and AT Mackay. On the derivation of macroscopic models for compressible viscoelastic fluids using the generalized bracket framework. *J. Non Newtonian Fluid*, 2018 (under review).

[73] TN Phillips and GW Roberts. The treatment of spurious pressure modes in spectral incompressible flow calculations. *J. Comput. Phys.*, 105(1):150–164, 1993.

[74] JFT Pittman, JF Richardson, and CP Sherrard. An experimental study of heat transfer by laminar natural convection between an electrically-heated vertical plate and both newtonian and non-newtonian fluids. *Int. J. Heat Mass Trans.*, 42(4):657–671, 1999.

[75] DJ Plazek. Temperature dependence of the viscoelastic behavior of polystyrene. *J. Phys. Chem-US*, 69(10):3480–3487, 1965.

[76] D Rajagopalan, RC Armstrong, and RA Brown. Finite element methods for calculation of steady, viscoelastic flow using constitutive equations with a newtonian viscosity. *J. Non Newtonian Fluid*, 36:159–192, 1990.

[77] RS Rivlin. Review of *The Non-Linear Field Theories of Mechanics* by C. Truesdell and W. Noll. *J. Acoust. Soc. Am.*, 40:1213, 1966.

[78] JV Satrape and MJ Crochet. Numerical simulation of the motion of a sphere in a boger fluid. *J. Non Newtonian Fluid*, 55(1):91–111, 1994.

[79] MJ Solomon and SJ Muller. Flow past a sphere in polystyrene-based boger fluids: the effect on the drag coefficient of finite extensibility, solvent quality and polymer molecular weight. *J. Non Newtonian Fluid*, 62(1):81–94, 1996.

[80] RG Sousa, RJ Poole, AM Afonso, FT Pinho, PJ Oliveira, A Morozov, and MA Alves. Lid-driven cavity flow of viscoelastic liquids. *J. Non Newtonian Fluid*, 234:129–138, 2016.

[81] A Souvaliotis and AN Beris. An extended white–metzner viscoelastic fluid model based on an internal structural parameter. *J. Rheol.*, 36(2):241–271, 1992.

[82] EM Sparrow, R Eichhorn, and JL Gregg. Combined forced and free convection in a boundary layer flow. *The Physics of Fluids*, 2(3):319–328, 1959.

[83] GG Stokes. *On the effect of the internal friction of fluids on the motion of pendulums*, volume 9. Pitt Press Cambridge, 1851.

[84] F Sugeng, N Phan Thien, and RI Tanner. A study of non-isothermal non-Newtonian extrudate swell by a mixed boundary element and finite element method. *J. Rheol.*, 31:37–58, 1987.

[85] H Tautz. Bestimmung der warmeleifahigkeit von kautschukvulkanisaten in abhangigkeit von der dehnung. *Exp. Tech. Phys*, 7:1–14, 1959.

[86] GI Taylor. Stability of a viscous liquid contained between two rotating cylinders. *Philosophical Transactions of the Royal Society of London. Series A, Containing Papers of a Mathematical or Physical Character*, 223(605-615):289–343, 1923.

[87] B Van den Brule and P Slikkerveer. Anisotropic conduction of heat caused by molecular orientation in a flowing polymeric liquid. *Rheol. Acta*, 29(3):175–181, 1990.

[88] J Venkatesan and S Ganesan. A three-field local projection stabilized formulation for computations of oldroyd-b viscoelastic fluid flows. *J. Non Newtonian Fluid*, 247:90–106, 2017.

[89] NJ Wagner, HC Öttinger, and BJ Edwards. Generalized doi–ohta model for multiphase flow developed via generic. *AIChE J.*, 45(6):1169–1181, 1999.

[90] MF Webster, IJ Keshtiban, and F Belblidia. Computation of weakly-compressible highly-viscous liquid flows. *Eng. Computation*, 21(7):777–804, 2004.

[91] JL White and AB Metzner. Development of constitutive equations for polymeric melts and solutions. *J. Appl. Polym. Sci.*, 7(5):1867–1889, 1963.

[92] JM White and SJ Muller. Experimental studies on the effect of viscous heating on the hydrodynamic stability of viscoelastic taylor–couette flow. *J. Rheol.*, 47(6):1467–1492, 2003.

[93] JM Wiest. Time-temperature superposition in nonisothermal flow. *J. Non Newtonian Fluid*, 27:127–131, 1988.

[94] JM Wiest and N Phan-Thien. Nonisothermal flow of polymer melts. *J. Non Newtonian Fluid*, 27(3):333–347, 1988.